MOLECULAR ECOLOGY AND PHYSIOLOGY OF MICROBIOLOGICALLY-INFLUENCED CORROSION IN THE DEEP SEA

YEO YEE PHAN

Interdisciplinary Graduate Programme
Singapore Centre for Environmental Life Sciences
Engineering (SCELSE)

2023

MOLECULAR ECOLOGY AND PHYSIOLOGY OF MICROBIOLOGICALLY-INFLUENCED CORROSION IN THE DEEP SEA

YEO YEE PHAN

Interdisciplinary Graduate Programme
Singapore Centre for Environmental Life Sciences
Engineering (SCELSE)

A thesis submitted to the Nanyang Technological University in partial fulfilment of
the requirement for the degree of Doctor of Philosophy

2023

Statement of Originality

I hereby certify that the work embodied in this thesis is the result of original research, is free of plagiarised materials, and has not been submitted for a higher degree to any other University or Institution.

21/08/2023

. . . .
Date

Yeephan

. . . .
Yeo Yee Phan

Supervisor Declaration Statement

I have reviewed the content and presentation style of this thesis and declare it is free of plagiarism and of sufficient grammatical clarity to be examined. To the best of my knowledge, the research and writing are those of the candidate except as acknowledged in the Author Attribution Statement. I confirm that the investigations were conducted in accord with the ethics policies and integrity standards of Nanyang Technological University and that the research data are presented honestly and without prejudice.

21/08/2023

. . . .
Date

. . . .
Assc Prof Federico M. Lauro

Authorship Attribution Statement

This thesis **does not** contain any materials from papers published in peer-reviewed journals or from papers accepted at conferences in which I am listed as an author.

21/08/2023

. . . .
Date

Yeephan

. . . .
Yeo Yee Phan

Acknowledgments

First of all, I would like to express my gratitude to my former supervisor A/Prof Scott for providing me with this invaluable opportunity to pursue my Ph.D. candidature in SCELSE and for involving me in this challenging yet wonderful PhD project. Although he has since departed from his position, his professional supervision and mentorship laid a strong foundation for my research. I owe a debt of gratitude to him for his mentorship and encouragement, which paved the way for my progress.

Next, I extend my sincere thanks to my current supervisor A/Prof Federico Lauro who has selflessly assumed the role after the departure of my former supervisor. I am deeply grateful for his supervision and support, which are indispensable in shaping the success of this thesis. Every critical discussion with him propelled me closer to my research goal and honed my abilities as an independent researcher.

I would like to express my gratitude to my co-supervisor A/Prof Sridhar Idapalapati, my TAC mentor A/Prof Daniel Blackwood, and my former co-supervisor Asst Prof Matteo Seita. Their countless constructive comments extended beyond my area of expertise and many of the experiments would not have been possible without their support.

My deep appreciation goes to Dr. Pauliina Rajala for her mentorship and the guidance she gave, extending even after her departure. The experienced and insightful inputs that she shared have been pivotal in shaping my thesis plan. I am also thankful for her help in collecting deep-sea samples for my experiment and her thoughtful opinion on establishing enrichment cultures. Her contributions to my work are indispensable.

My sincere thanks also go to my lab colleague Dr. Astorga Solange Elizabeth for her insightful discussion and helpful advice; to Dr. Tony Ruiliang Liu for his helps and advices on material analysis; to Nicholas John Tan Jie Hao for his administrative support and willingness to lend a helping hand in my experiment; to Nicolo Ivanovich for fruitful idea exchanges and collaborative discussions; to Winona Wijaya and Dr. Dong Qiang for their bioinformatics supports; and to Dr. Guo Xue from A*Star Functional Proteomic Laboratory for her assistance in conducting proteomic analysis and the subsequent discussion and interpretation.

I would also like to acknowledge the support of my SCELSE friends and my former lab colleague from Scott’s team, whose invaluable support and their companionship have turned my PhD journey into a profoundly enriching and enjoyable experience.

Last but not least, I want to express my deepest gratitude to my wife, Ms. Chong Hai Tarng, for her constant support and encouragement, which has significantly contributed to the successful completion of this endeavor.

This project is funded by the National Research Foundation under Competitive Research Programme award CRP21-2018-0102 and supported by the Interdisciplinary Graduate Programme, Nanyang Technological University.

Table of Contents

List of Figures

List of Abbreviations

ACN	Acetonitrile
ASV	Amplicon Sequence Variants
ASW	Artificial Seawater
ATP	Adenosine Triphosphate
CAA	Chloroacetamide
CMIC	Chemical-MIC
CR	Corrosion Rate
DNA	Deoxyribonucleic Acid
DO	Dissolved Oxygen
DSMZ	German Collection of Microorganisms and Cell Cultures GmbH
EDS	Energy-dispersive X-ray spectroscopy
EDTA	Ethylenediaminetetraacetic Acid
EMIC	Electric-MIC
EPS	Extracellular polymeric substance
ETC	Electron Transport Chain
FA	Formic Acid
gDNA	Genomic DNA
HHP	High Hydrostatic Pressure
KEGG	Kyto Encyclopedia of Gene and Genomes
LC-MS/MS	Liquid Chromatography coupled with Tandem Mass Spectrometry
MC	Mooring Chain
MIC	Microbiologically-Influenced Corrosion

mm/y	Millimeter per year
MOPS	3-(*N*-morpholino) propanesulfonic acid
MPa	Megapascal
NCMA	National Center for Marine Algae and Microbiota
NMDS	Non-Metric Multi-Dimensional Scaling
PBS	Phosphate Buffered Saline
PC	Polycarbonate
PCA	Principal Component Analysis
PMSF	Phenylmethylsulfonyl Fluoride
qPCR	Quantitative Polymerase Chain Reaction
rRNA	Ribosomal Ribonucleic Acid
RT	Room Temperature
SD	Standard Deviation
Sd	Sediment
SEM	Scanning Electron Microscope
SRB	Sulfate-Reducing Bacteria
TCEP	Tris (2-carboxyethyl) phosphine
TEAB	Triethylammonium Bicarbonate Buffer
TFA	Trifluoroacetic Acid
UV	Ultraviolet

Abstract

Corrosion poses a significant challenge to deep-sea operations, given the harsh and remote conditions of this environment. Mild steels, widely utilized for their affordability and favorable mechanical properties in marine applications, have not been extensively studied regarding microbiologically-influenced corrosion (MIC) in the deep sea. By employing hydrostatic pressure vessels and pump to replicate deep-sea conditions, the MIC of the marine-grade mild steel AH36 was investigated. Here, it was found that the hydrostatic pressure may influence the severity of the MIC induced by shallow-water and deep-sea sulfate-reducing bacteria (SRB). Further comparative proteomic analysis of the selected deep-sea SRB *P. piezophilus* indicates that differential enrichment of proteins associated with the energy metabolism pathway when incubated with mild steel. Interestingly, elevated hydrostatic pressures do not significantly alter the total proteome of deep-sea SRB, suggesting that changes in MIC behaviors may be linked to protein activity rather than the abundance of specific proteins. To validate the deep-sea MIC, enrichment cultures from field samples collected from deep sea at a depth of 1988 m. The enrichment culture established from a corroding mooring chain exhibits aggressive MIC, causing localized corrosion attacks primarily at the edges of mild steel coupons. This corrosive microbial community comprises SRB and elemental sulfur metabolizing bacteria, hinting at a potential role of elemental sulfur in mediating deep-sea MIC. Overall, this dissertation underscores the persistent threat of MIC to mild steels, even in the extreme conditions of the deep sea. While exact mechanism remains unclear, the findings here suggest that enhanced MIC is associated with stimulating anodic reaction

rather than cathodic hydrogen reduction, with a potential involvement of the formation of corrosive sulfur species.

Chapter 1

Current state of knowledge on microbiologically-influenced corrosion in the deep sea

1.1 Introduction

Deep sea (depth ≥ 1000 m) hosts a huge reserve of oil and natural gas, as well as valuable minerals such as polymetallic nodules, massive sulfide deposits, and manganese-iron nodules. This has attracted global interest to exploit the deep sea to feed the ever-growing global demands on energy and mineral resources (Koschinsky et al. 2018). However, corrosion remains a major challenge for infrastructures and equipment installed or deployed to the deep sea due to the hostility, remoteness, and inaccessible nature of the environment (Traverso and Canepa 2014). The loss of material integrity from corrosion may lead to catastrophic failure or accident, that not only inflict economic loss but also brought about severe safety as well as environmental consequences (Cordes et al. 2016, Muehlenbachs et al. 2013). Mild steels stand out for their exceptional mechanical properties and cost-effectiveness, making them highly appealing as structural materials for deep-sea applications. This is especially true for extensive offshore infrastructures. Yet, it too is not immune to corrosion when submerged in seawater (Traverso and Canepa 2014). Therefore, protective measures such as coating, cathodic polarization as well as sacrificial anodes are often applied singly or in combination to reduce the corrosion of mild steel for marine applications (Hou et al. 2018, Popoola et al. 2013). However, most of the protective efforts require proper application for effective protection and frequent re-application, which is hindered by the inaccessibility and their associated cost, not to mention that their effectiveness in deep-sea environments remained questionable (Liu et al. 2013, Price and Figueira 2017, Winning et al. 2010). The use of biocides for protection against biofouling has raised environmental concerns and is often limited to closed systems such as within the pipeline, leaving the external surface vulnerable (Winning et al. 2010). To manage the corrosion risk, corrosion engineers will conduct environmental assessments for material design and lifetime prediction (Abbas and Shafiee 2020). However, the presence of microorganisms and their activity may influence the corrosion process and the surrounding environment, which in turn may lead to unexpected corrosion acceleration (or in some cases, inhibition) in a process known as microbiologically-influenced corrosion (MIC) (Kip and van Veen 2015). More details will be discussed later in Chapter 1.3. MIC is estimated to contribute to 10 – 20% of the total cases of corrosion, posing a large threat to the oil & gas sectors (Jia et al. 2019, Marciales et al. 2019). Unlike abiotically-driven corrosion, MIC is extremely difficult to predict and is often localized, making the detection difficult and almost impossible for large infrastructures (Marciales et al. 2019). While past research has provided some rudimentary understanding on MIC, the impact of extreme environments of deep-sea on MIC remains unexplored. Knowledge of deep-sea MIC would be essential to understand and reduces the adverse economic, safety, and environmental impacts associated with deep-sea corrosion.

1.2 Principles of metallic corrosion

Corrosion refers to the deterioration process of, usually metal, but also other materials such as concrete and stones, which the detail process varies according to different types of materials (Kip and van Veen 2015). For the context of this dissertation, I will discuss specifically metallic corrosion, with a particular focus on mild steels unless otherwise stated. Most active metals, including iron and its alloys, are thermodynamically unstable and have a natural tendency to revert to their oxidized state and hence, corrode (Umoren et al. 2022). Corrosion is an electrochemical process that consists of three principal components: i) the corroding metal, ii) an electron acceptor, and iii) the electrolyte (Figure 1.1). The metal dissolution occurs at the anode, where the zero-valent iron oxidizes into aqueous ferrous ions (Eq. 1), leading to metal loss. A reduction reaction occurs at the cathode where the liberated electrons are acquired by an electron acceptor, thereby sustaining the corrosion reaction. Oxygen is often the preferred electron acceptor (Eq. 2) while in anoxic or acidic environments, the hydrogen ions (H^+) form from the water dissociation may act as alternative electron acceptor (Eq. 3) (Frankel 2016):

Eq. 1 $Fe^0 \rightarrow Fe^{2+} + 2\ e^-$ $(E^0 = -0.44\ V)$

Eq. 2 $O_2 + 2\ H_2O + 4\ e^- + \rightarrow 4OH^-$ $(E^0 = 0.4\ V)$

Eq. 3 $2\ H^+ + 2\ e^- \rightarrow H_2$ $(E^0 = 0\ V)$

Eq. 4 $Fe^{2+} + 2\ OH^- \rightarrow Fe(OH)_2$

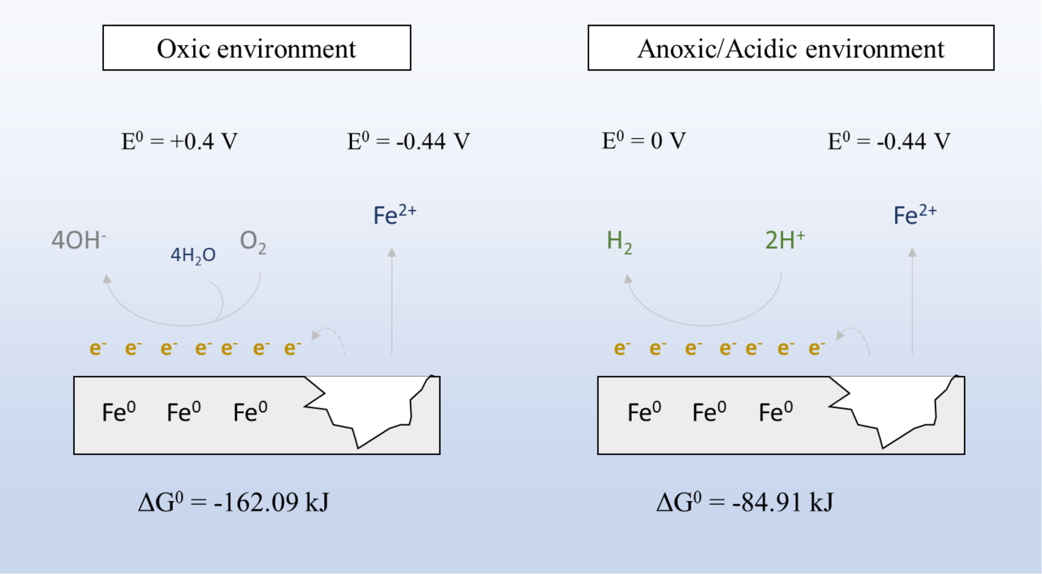

Figure 1.1. Schematic diagram of the electrochemical corrosion process in oxic environment and anoxic/acidic environment.

From a thermodynamic perspective, the coupling of iron oxidation with oxygen reduction (ΔG^0 = -162.09 kJ) and hydrogen reduction (ΔG^0 = -84.91 kJ) are energetically favorable and hence will occur spontaneously. However, the actual corrosion behavior may change depending on the pH and redox potential, as well as with the corrosion products formed and deposited on the surface (Beverskog and Puigdomenech 1996, Popov 2015, Refait et al. 2020). The role of the corrosion products in the corrosion of steels has been reviewed in detail elsewhere (Refait et al. 2020, Tamura 2008, Wang et al. 2019). Iron hydroxide, or $Fe(OH)_2$, is often the initial corrosion products formed upon corrosion (Eq. 4), which is then rapidly oxidized into other corrosion products (Liu et al. 2019, Wang et al. 2019). In aerated seawater, the corrosion of mild steels often produces a variety of oxides and hydroxides such as goethite (α-FeOOH), lepidocrocite (γ-FeOOH), magnetite (Fe_3O_4) (Pusparizkita et al. 2023, Refait et al. 2020). In addition, green rusts (consist of a mixture of Fe^2+ and Fe^{3+}) including sulfate green rust, carbonate green rust, chloride green rust are often formed as an intermediate transition product due to the presence of sulfate, carbonate, and chloride, respectively, in seawater (Refait et al. 2020, Wang et al. 2019). The development of a compact corrosion product layer, such as goethite, may passivate the surface by acting as a physical barrier that impede mass transport (Popov 2015, Wang et al. 2019). The depletion of oxygen in the corrosion product layer creates an anoxic environment that favors the growth of MIC microorganism including sulfate-reducing bacteria, which will be discussed in Chapter 1.3 (Refait et al. 2020). The presence of microorganism may alter the corrosion product composition (Stipaničev et al. 2013). For example, sulfide production by the sulfate-reducing bacteria may drive the formation of tightly-adhered yet conductive iron sulfide film that depend on the condition, may either enhance or suppress the corrosion (El Mendili et al. 2014, Zhang et al. 2021). This will be discussed further in Chapter 1.3.2.2.

Generally, mild steels corrode in a uniform manner known as general corrosion or uniform corrosion, where the corrosion cells (anode-cathode pairs) are distributed randomly. However, the presence of imperfections on the surface, either from physical or chemical irregularity such as local heterogeneity, grain boundary, inclusion, or impurities, will cause the anodes to be preferentially localized (Li et al. 2022b). With the remaining metal body now serving as the cathode, the large cathode-to-anode surface area will promote a sustained and concentrated corrosion of the anode, leading to devastating material loss known as localized corrosion, often manifested as pitting (Akpanyung and Loto 2019, Li et al. 2022b). One typical example of this is the local breakdown of the chromium oxide passive layer in the case of stainless steel, that leads to localized corrosion. Similar phenomenon can also be observed in mild steel when there is a defective coating layer, underneath deposits such as soils and corrosion products, or colonization by microorganisms (Akpanyung and Loto 2019, Eklund 1974, Sliem et al. 2021). The high chloride (Cl^-) content of seawater also helps creating a favorable condition for corrosion, particularly pitting corrosion. Chloride ions migrate into the pit cavity, neutralizing the electrical charges from the high concentration of positively charged ferrous ions and, at the same time, weakening the protective film via the formation of soluble ferrous chloride (Akpanyung and Loto 2019, Wang et al. 2015). The hydrolysis of ferrous ions and ferrous chloride will contribute to acidification within the pit cavity (Eq. 5 – 7) and further aggravating the corrosion (Lee 2004, Sweeton and Baes 1970). A schematic showing the effects of chloride on pitting corrosion is shown in Figure 1.2.

Eq. 5 $Fe^{2+} + H_2O \rightarrow FeOH^+ + H^+$

Eq. 6 $FeCl_2 + 2H_2O \rightarrow Fe(OH)_2 + 2HCl$

Eq. 7 $HCl \rightarrow H^+ + Cl^-$

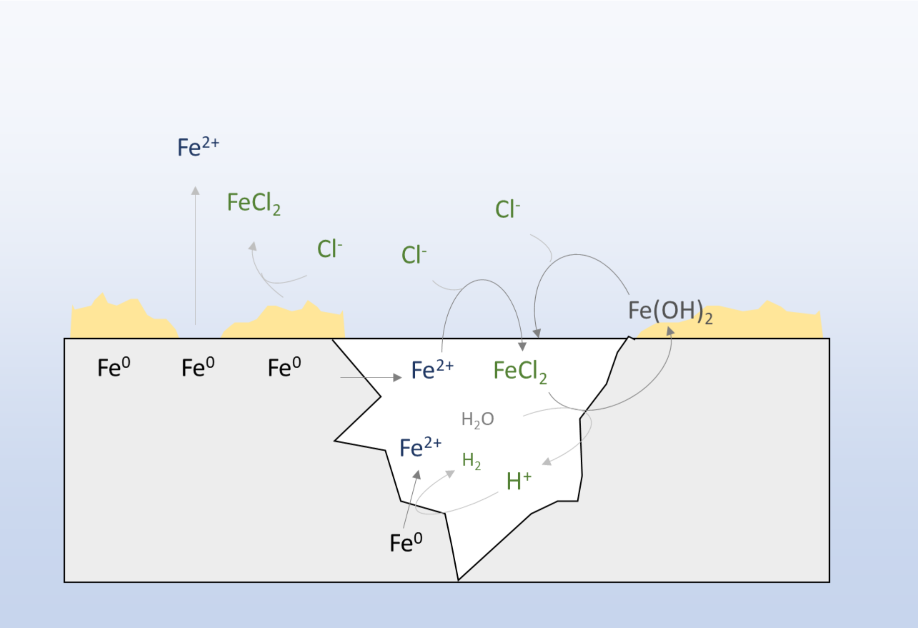

Figure 1.2. Schematic diagram of the role of chloride ions on pitting corrosion. Chloride ions facilitate corrosion via charge neutralization, formation of soluble $FeCl_2$ species, dissolving protective corrosion products film, and acidification of the pit cavity.

1.3 Microbiologically-influenced corrosion

The involvement of microorganisms in the process of corrosion has been described as early as 1910 and is now collectively grouped under the term microbiologically-influenced corrosion (also sometimes called microbial-induced corrosion or biofouling) (Gaines 1910, Puentes-Cala et al. 2022). MIC is attributed to the metabolic versatility of the microorganisms and their ability to colonize virtually all types of surfaces, which changes the surface properties and the surrounding micro-environments, or through production of reactive chemicals that interact with the surface to favor or inhibit the corrosion process (Kip and van Veen 2015). While many microorganisms, including archaea or even fungi, have the potential to cause MIC, bacteria of some groups are infamously associated with MIC, including but not limited to sulfate-reducing bacteria, iron-oxidizing bacteria, iron-reducing bacteria, acid-producing bacteria, and slime-forming bacteria (Kip and van Veen 2015, Stott and Abdullahi 2018). Bacteria in nature often adopt a surface-associated lifestyle known as biofilm and colonizing all kinds of surfaces through secreting and encasing themselves in a matrix known as extracellular polymeric substance (EPS) (Flemming et al. 2016). The attached biofilm community can often be found not only on natural but also engineered surfaces such as pipelines, ship hulls, and storage tanks, causing serious damage to the surface underneath the biofilm (Puentes-Cala et al. 2022). This is particularly problematic in anoxic conditions where, in the absence of MIC, the abiotic corrosion is expected to be lower. Yet, diagnosing corrosion as MIC has been proven difficult due to the ubiquitous nature of microbes as well as their complex interactions with the metals and their environments (Puentes-Cala et al. 2022).

1.3.1 Sulfate reducing bacteria as a model MIC microorganism

Sulfate-reducing bacteria (SRB) is a phylogenetically diverse group of bacteria that carry out dissimilatory sulfate reduction, using sulfate (SO_4^{2-}) as terminal electron acceptor in their respiration process (Barton and Fauque 2009). Sulfide (HS^-), a reactive reduced sulfur species, is produced as the respiratory end-product. SRB thrive in diverse anoxic environments and play an important role in the biogeochemical cycling of carbon and sulfur (Jørgensen 1982, Jørgensen et al. 2019, Muyzer and Stams 2008). Metabolically, they are versatile and capable of growing heterotrophically on various substrates including short-chain fatty acids, amino acids, sugars, alcohols, hydrocarbons, and aromatic compounds as well as molecular hydrogen (H_2) as electron donors for respiration. While they primarily reduce sulfate for energy metabolism, thiosulfate, sulfite, sulfur, nitrate, nitrite, and organic compounds such as fumarate may also serve as alternative electron acceptors in some species. While not coupled to growth, the reduction of transition metals was also reported (Joo et al. 2015). Some species may also grow fermentatively or through sulfur disproportionation (Barton and Fauque 2009, Muyzer and Stams 2008).

SRB has gained the most attention in the field of MIC as they are commonly isolated from corrosion sites and are often portrayed as the culprit for MIC under anoxic conditions (Enning and Garrelfs 2014). Plenty of research has demonstrated the MIC capability of this group of microbes both in pure culture as well as in mixed-species cultures (Batmanghelich et al. 2017, Beech and Campbell 2008, Eduok et al. 2019, Li et al. 2022c, Lyles et al. 2014, Unsal et al. 2019, Wang et al. 2021a). The severity of corrosion varies depending on the specific species presence, but a corrosion penetration rates as high as 0.71 mm/y induced by the SRB has been documented on carbon steels (Enning et al. 2012). Other than mild steels, SRB have been reported to interact with a diverse range of metals, including stainless steel, copper, nickel, and titanium, but also used in the bioremediation of toxic metal ions such as cadmium, nickel, and chromium (Joo et al. 2015, Tran et al. 2021, Unsal et al. 2023, Wang et al. 2021a). However, an overwhelming proportion of studies to date focused on a very limited number of SRB from the genus *Desulfovibrio* that cause severe corrosion in laboratory tests such as *D. vulgaris*, *D. desulfuricans*, and *D. ferrophilus.* The reason why certain SRB species causes more aggressive corrosion compared to others remain unclear. Understanding the mechanism of how SRB causes MIC might shed light on this question, which will be discussed in the next section.

1.3.2 Current understanding on MIC mechanisms

MIC is a complex process that involves the interaction between microorganisms, metals, and the surrounding environments. Past research has refined our knowledge of MIC but to date, the exact mechanism of how microorganism mediate MIC remains poorly understood. Several theories on MIC mechanisms have been proposed and reviewed in the past, with special attention focused (but not restricted to) on SRB. These include the consumption of cathodic hydrogen (cathodic depolarization theory), secretion of corrosive chemicals (chemical-MIC, CMIC), and direct electron uptake from metals (electric-MIC, EMIC).

1.3.2.1 Cathodic Depolarization Theory

During the anoxic corrosion of steel, an adsorbed hydrogen film will be developed from the hydrogen reduction (Eq. 3), which polarizes the surface and impedes further iron dissolution. Removal of cathodic hydrogen will "depolarize" the surface and cause uninterrupted anodic dissolution resulting in aggressive corrosion. The cathodic depolarization theory conjectures that the presence of hydrogenase-possessing microbes, such as SRB, consume the cathodic hydrogen (Eq. 8) as a result of their respiration process, allowing the corrosion to progress unimpeded (Figure 1.3A) (Iverson 1966, Kühr and Van der Vlugt 1934, Pankhania et al. 1986).

Eq. 8 $8H_2 \rightarrow 8H^+ + 8e^-$

While this theory provides a mechanistic explanation of MIC, there are still "flaws" challenging the credibility of this theory. Electrochemical studies on the hydrogen evolution process have revealed that the removal of cathodic hydrogen is not the ratelimiting step of anoxic corrosion and hydrogen overpressure does not prevent or may even stimulate the anoxic corrosion (Blackwood 2020). Therefore, consumption of cathodic hydrogen does not explain the severe corrosion often observed in the MIC cases. On the other hand, the role of hydrogenase in MIC remained controversial where one study found only one out of 26 hydrogen-consuming microbes isolated from a crude oil tank is capable of causing iron corrosion (Mori et al. 2010). However, it is noteworthy that there have been some findings reported in recent years that support the cathodic depolarization theory. Using a genetic mutant model, Woodlard *et. al.* demonstrated that a deletion mutant of all hydrogenase genes in *Desulfovibrio vulgaris*, one of the most studied MIC species, failed to grow on pure iron as electron donor (a pre-requisite for EMIC theory, which will be discussed in the next subsection), while its growth in lactate medium was not affected (Woodard Trevor et al. 2023). Another highly corrosive SRB, *Desulfovibiro ferrophilus* which was previously claimed to use pure iron as electron donor, was, instead, shown to be incapable of corroding through EMIC but rather more likely to be based on H_2 consumption (Liang et al. 2021, Ueki et al. 2022). Similarly, another study reported a mutant of a corrosive methanogen *Methanococcus maripaludis* strain OS7 loses its corrosiveness after a 12 kb chromosomal deletion, in the region coding for an extracellular [NiFe] hydrogenase (Tsurumaru et al. 2018). Collectively, these experimental observations imply that the hydrogen utilization by SRB may still play a role in MIC.

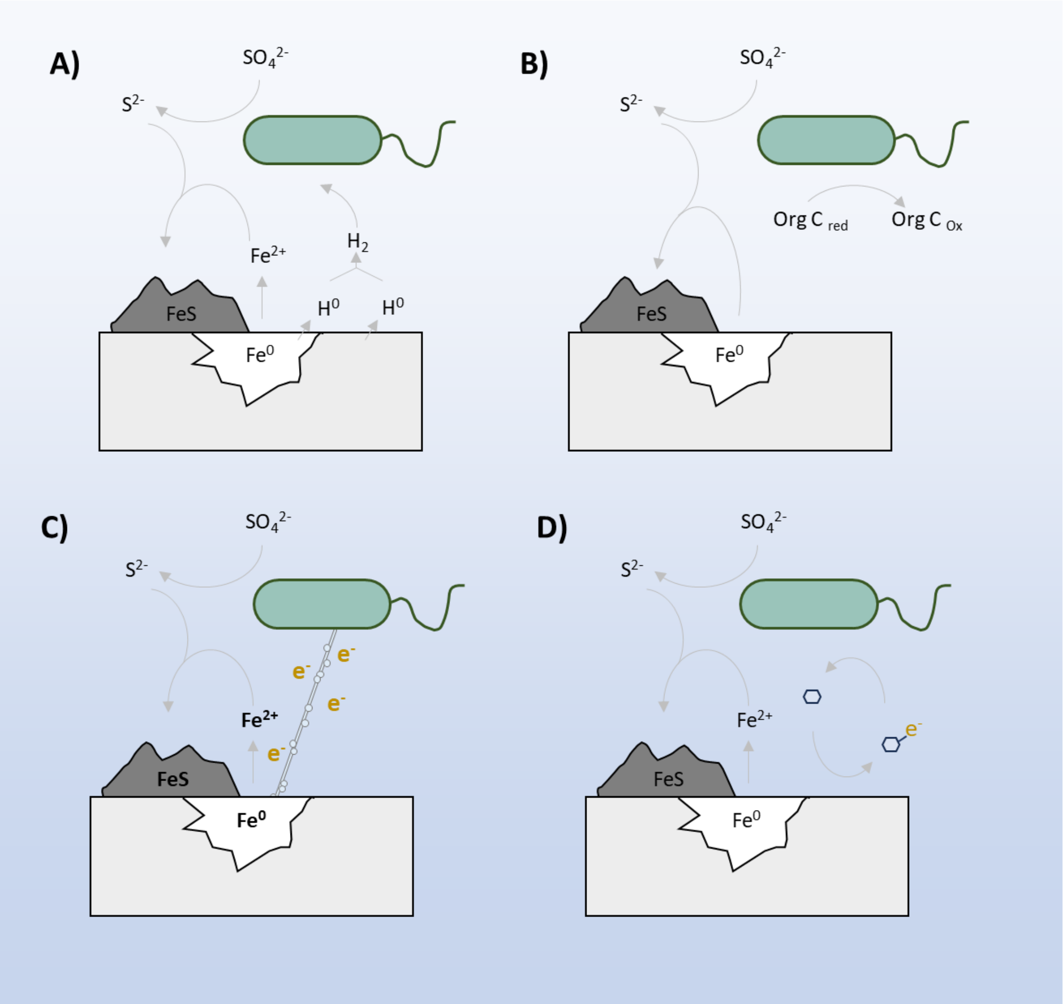

Figure 1.3. Schematic diagram of the commonly reported MIC mechanism of SRB. Cathodic depolarization theory proposed SRB enhanced corrosion via consuming cathodic hydrogen (A) whereas CMIC theory proposed SRB released corrosive metabolites that facilitate MIC (B). In EMIC theory, SRB is believed to acquire electron from the iron either directly via membrane proteins or appendages (C) or indirectly via soluble electron shuttle (D), thereby resulting in MIC.

1.3.2.2 Chemical-MIC (CMIC) Theory

CMIC theory proposes that the corrosive chemical/metabolites secreted by the MIC microbes as the causative agents for MIC. The corrosion attack may be uniform if the corrosive chemical/metabolite(s) is released into bulk liquid or localized if the chemical/metabolite(s) is trapped underneath a biofilm. One such often-discussed chemical is the hydrogen sulfide produced by SRB from sulfate reduction, which is an aggressive chemical that is capable of stimulating anodic iron dissolution (Eq. 9) and cathodic hydrogen evolution (Eq. 3, Figure 1.3B) (Edyvean 1991).

Eq. 9 $Fe^0 + H_2S \rightarrow FeS + H_2$

Hydrogen sulfide-induced corrosion is often reported in oil and gas pipelines where the anoxic environment and availability of (hydro)carbon sources create a favorable environment for SRB growth, resulting in the production of a significant amount of hydrogen sulfide (Kvarekvål and Moloney 2017). Due to its semi-conductive nature, the iron sulfide corrosion products formed in this corrosion process can act as a cathode allowing the hydrogen reduction to continue. With the progress of corrosion, more iron sulfide corrosion products built up and the large cathode-to-anode ratio will in turn, further accelerate the corrosion process in a self-promoting manner (Kvarekvål and Moloney 2017). Depending on the environmental conditions however, iron sulfide corrosion products may serve a protective role rather than promoting corrosion. At pH >7 or high sulfide concentration, the tightly-adhered iron sulfide corrosion products formed under this condition often act as a physical barrier protecting the metal from further dissolution (Ma et al. 2000, Zhang et al. 2021). However, severe corrosion by sulfide species are often reported in acidic environment which prevent the building up of the protective layer (Ma et al. 2000). In addition, the ingress of oxygen from the environment may oxidize the sulfide turning it into a corrosive sulfur species which could trigger detrimental localized attacks to carbon steels that are in direct contact (Erfanian et al. 2022, Kvarekvål and Moloney 2017, Zhang et al. 2021). Other than sulfide-induced MIC which is mediated mainly by SRB, production of organic or inorganic acid from acid-producing bacteria could induce aggressive corrosion by creating an acidic environment with a surplus supply of hydrogen ions. Organic acids are common by-products of microbial metabolism. An environmental isolate of *Acetobacter aceti* has been shown to induce carbon steel corrosion through fermenting ethanol into acetic acid (Sowards and Mansfield 2014). Another study demonstrated that the presence of acid-producing bacteria, *Citrobacter farmer*, enhances the corrosion of carbon steel in an artificial seawater medium, as evidenced by a 3.2-fold increase in the corrosion current density (Tian et al. 2020) .

1.3.2.3 Electric-MIC (EMIC) Theory

EMIC is a promising yet highly debated theory to explain the MIC mechanism that has received increased attention in recent years. This theory attempts to explain the highly corrosive nature of MIC with the capability of bacteria to carry out extracellular electron transfer (EET) to harvest electrons directly from the metals, hypothetically through membrane proteins, redox-active compounds, or conductive appendages such as pili or “nanowire” structures. EMIC microbes are the so-called “electrotroph” that derive energy from coupling the oxidation of metals and the reduction of an intracellular electron acceptor. In other words, the EMIC microbes take part in the anodic dissolution process by drawing electrons from the metals, and the metals corroded as the microbe grows.

Shewanella and *Geobacter* are iron-reducing bacteria that have an unconventional EET strategy to transfer electrons to insoluble ferric (hydr)oxides directly using redox-active membrane cytochrome, electroconductive “nanowire”, or indirectly through secretion of redox-active compounds (Figures 1.3C and 1.3D) (Brutinel and Gralnick

2012, Lovley and Walker 2019, Pirbadian et al. 2014). There are also some preliminary studies in recent years that suggest the EET system in these microbes can be operated in the reverse direction to draw electrons from metals hence causing corrosion (Chang et al. 2022, Tang et al. 2021). Inferring from the model EET bacteria, EMIC theory proposes that this mechanism is believed to be widespread in MIC microbes, and unlike the cathodic depolarization theory, participating in anodic reaction will not be kinetically controlled and hence results in enhanced corrosion. It is commonly believed that similar EET system might be present in SRB, as the coupling of iron oxidation (Eq. 1) with the reduction of sulfate (Eq. 10) is energetically favorable (ΔG^0 = -180.62 kJ) (Deng et al. 2015, Li et al. 2015a, Liang et al. 2021). In fact, many microbes (mainly SRB from the genus *Desulfovibrio*) isolated using Fe^0 as pure electron donor are also capable of inducing severe MIC and many SRB possess multiple *c*-cytochrome genes encoded in their genome that may potentially participate in EET function (Chatterjee et al. 2021, Enning et al. 2012, Kato et al. 2015). Carbon starvation and the addition of exogenous electron shuttles such as riboflavin have been shown to enhance corrosion, where in both situations, the electron uptake from metals is encouraged (Guan et al. 2021, Wang et al. 2021a, Xu and Gu 2014).

Eq. 10 $SO_4^{2-} + 9H^+ + 8e^- \rightarrow HS^- + 4H_2O$ $(E^0 = -0.21\ V)$

Like other MIC theories, EMIC theory has also been criticized. While the EET-induced corrosion is thermodynamically and kinetically favorable, there is a lack of consensus on how the liberated electrons could be transported across cell membranes without reacting with the environments (Blackwood 2020). The evidence of EET growth is sometimes controversial, and the identity of proteins and/or redox compounds involved in EET remains unclear despite many studies (Deng et al. 2015, Liang et al. 2021). Also, the growth on iron as sole electron donor should not be taken as an indicator of EET, as the microbes can utilize the di-hydrogen formed during the abiotic corrosion process to support growth. In fact, as mentioned above, some of the MIC microbes failed to grow after the deletion of hydrogenases gene or when replacing iron with stainless steel, which is more corrosion resistant and hence produces less dihydrogen (Liang et al. 2021, Woodard Trevor et al. 2023). Also, some works claiming EET or "higher-than-expected corrosion" were conducted in test medium with organic carbon sources serving as electron donors, which reduced the credibility of their claim (Li et al. 2015a, Wang et al. 2020).

In summary, the field of MIC is dynamic and complex and there is still a lack of understanding of the core metabolic and chemical processes that cause the corrosion because much of the knowledge is generalized from a limited number of model species/groups. The inter-species interactions within the nature biofilm, biofilm as a physical barrier creating differential aeration cells, and complexation of metal ions by EPS could also contribute to the MIC and have been discussed elsewhere (Beech and Campbell 2008, Blackwood 2020, Chan et al. 2002, Knisz et al. 2023, Liu et al. 2017, Zhou et al. 2020). It is likely that MIC is caused by not one but a combination of different mechanisms. However, there is no doubt that understanding the mechanism may provide valuable insight for developing a better model for service lifetime prediction and mitigation strategies to address MIC.

1.4 Deep-sea environments

Ocean is a vast body of water covering 70% of the Earth's surface. The average depth of the ocean is 3788 m and the deep sea, which is loosely defined as the ocean interior with a depth below 1000 m, is estimated to constitute roughly 99% of the ocean by volume (Costello et al. 2010). The deep sea is a hostile environment characterized by the permanent darkness due to lack of sunlight, cold (2 – 4 °C), oligotrophy, and extreme hydrostatic pressure, posing unique challenges to microbial life and conditions related to the corrosion process (NOAA , Pawlowicz 2013). With the exception of localized hotspot such as hydrothermal vents or underwater volcanoes, the deep sea maintains a remarkable homogeneity and stability. This contrasts with the ocean surface, where the conditions undergo seasonal or diurnal fluctuations in sunlight availability and atmospheric conditions.

1.4.1 Microbial adaptation to the deep-sea environments

The deep sea is a very challenging environment for life. Despite the harsh conditions, microbial life has not only adapted but also thrives in this hostile environment. Deep-sea environments are highly energy-starved due to the limited reserves of utilizable organic carbon available to the microbes (Dittmar et al. 2021, Jiao et al. 2018, Jørgensen and Boetius 2007). Due to the lack of sunlight, photosynthesis is not possible in the deep sea, and the primary production is restricted to limited areas such as hydrothermal vents that support chemolithoautotrophic lifestyles (Felbeck and Somero 1982). Recent studies reported a $\leqslant$ 40 μM dissolved organic carbon was measured in the deep sea as compared to 80 – 100 μM reported at the ocean surface (Ge et al. 2022, Hansell and Orellana 2021). The fallen organic matter (in the form of particulate organic matter or “marine snow”, or occasionally, animal corpses) originates from the ocean surface constitutes the main carbon source for deep-sea communities. These organic matters are consumed by the micro- and/or macroorganisms along the water column through its descent. As a result, the organic matter reserve in the deep sea is a mixture of extremely dilute but diverse molecules or is recalcitrant in nature that resist degradation (Cai and Jiao 2023, Dittmar et al. 2021, Giering et al. 2020). Many deep-sea microbes have adapted to this energy-limiting environment by possessing a reduced metabolic activity and growth or becoming metabolically versatile and able to utilize a wide range of nutrients that are available to them (Dittmar et al. 2021, Jiao et al. 2018). Without the warming effect from the sunlight, the ocean interior is extremely cold (~2 – 4°C). At this near-freezing temperature, many deep-sea microbes survive at a metabolically dormant state due to the reduced enzymatic kinetics, and experience reduced membrane fluidity similar to the effect of hydrostatic pressure (which will be discussed in subsection below) (D'Amico et al. 2006). Dissolved oxygen (DO) is another important determinant for animals and microbes that carry out aerobic respiration, however it’s distribution in the ocean is not constant across vertical gradients (NOAA). In general, the DO decreases with the depth increases, reaching a minimum at ~200 – 1000 m depth where the DO could drop to as low as <0.5 mg/L in some regions (Erbacher and Nelskamp 2006). Beyond this depth however, the deep sea is ventilated by the deep ocean circulation from the cold, dense, oxygen-rich polar water, typically at ~ 2 – 4 mg/L DO (NOAA). Yet, oxygen can be depleted quickly underneath a microbial biofilm or when going several centimeters down the sediments, where the anaerobes such as SRB and methanogen prevail (Emerson et al. 1985, Treude et al. 2009).

Hydrostatic pressure, the pressure exerted from the weight of overlying water, is arguably the most defining environmental factor of the deep sea. The hydrostatic pressure increases by 0.1 MPa (equivalent of one atmospheric pressure) with every ten meters increased in depth, reaching 110 MPa (equivalent of 1100 atmospheric pressure) at the deepest point of the ocean in Mariana Trench. Hydrostatic pressure has a broad effect on microorganisms, from cell growth and morphology, membrane properties and composition, macromolecules interactions to even the catalytic parameters of enzymes (Abe 2007). Taking the mesophilic *E. coli* as an example, high hydrostatic pressure has been shown to reduce motility (10 MPa), disrupt membrane protein function (25 – 50 MPa), induce filamentous growth (40 – 50 MPa), and inhibition of transcription (50 – 100 MPa) and translation (50 MPa) (Abe 2007). The bacterial cell membrane is where nutrient uptake and respiration take place but is susceptible to the perturbation of hydrostatic pressure.

Increased hydrostatic pressure compresses the lipid membrane and reduces its fluidity, therefore disrupting the liquid-crystalline phase which is crucial for membrane protein functions, cellular homeostasis, and metabolic activities (Abe 2013, Bartlett and Bidle 1999). To counteract the adverse effects of hydrostatic pressure, bacteria in the deep sea maintain their membrane fluidity by adjusting their membrane composition which includes increasing unsaturated fatty acid, increasing branched fatty acid, and increasing acyl chain length. These behaviors are known as homeoviscous adaptation and have been reviewed elsewhere (Abe 2013, Fang et al. 2010, Tamby et al. 2022). Another approach which piezophilic bacteria cope with hydrostatic pressure is through the accumulation of solutes (termed osmolytes or piezolytes) to offset the disruptive effects of hydrostatic pressure on macromolecular interaction. This is observed in

Photobacterium profundum which accumulates *β*-hydroxybutyrate and its oligomer when it is cultured at 28 MPa whereas *Desulfovibrio hydrothermalis* increased glutamate accumulation at 26 MPa as compared to the atmospheric pressure (Amrani et al. 2014, Martin et al. 2002). As the bacterial respiratory apparatus resides in the cell membrane and is susceptible to the influence of hydrostatic pressure, some deep-sea bacteria differentially regulate their respiratory proteins at different pressures. For example, *Shewanella benthica* expresses cytochrome *c*-551 at 0.1 MPa to 60 MPA whereas cytochrome *c*-552 was only expressed at 0.1 MPa. In addition, the expression of *cbb*-type quinol oxidase increased with hydrostatic pressure (Qureshi et al. 1998). Amano et. al. reported that the in-situ overall heterotrophic activities of deep-sea prokaryotic communities were suppressed at 4000 m (40 MPa) to only one-third of the atmospheric pressure. Interestingly, they also measure the single-cell leucine uptake activity and revealed that most of the bathypelagic community members are piezotolerant (~85%) rather than piezophilic (~5%) (Amano et al. 2022). Similarly, another study from Brown also reported that the deep-sea mesocosms exhibited a reduced and more constrained response to the nutrient amended when compared to the epipelagic and mesopelagic counterparts (Brown et al. 2022). They reasoned that the slower responses from the deep-sea community could be due to the dormancy under the nutrient-limiting environment. Nevertheless, these studies suggest that hydrostatic pressure plays an inhibitory role even in the native deep-sea community.

1.4.2 Field observation & laboratory tests on deep-sea corrosion

Seawater in general, is an excellent electrolyte conducive for corrosion. Steel, when submerged in seawater, experiences rapid and severe corrosion. The corrosion process is under heavy influence of the physicochemical properties of seawater, which varies with depth. In general, the corrosion in deep sea is kinetically slower (< 0.1 mm/y) as compared to the shallow seawater (0.1 – 0.5 mm/y) (Reinhart 1976, Venkatesan et al. 2002). Oxygen availability is a major determinant of corrosion in seawater. High dissolved oxygen level contributes to significant corrosion where the anodic dissolution is stimulated to match the cathodic reduction by oxygen (Eq. 2). For regions with anoxic or low dissolved oxygen levels, hydrogen ions generated from water dissociation (Eq. 3) may serve as alternative electron acceptor, which is a slow process in the circumneutral pH of seawater. It is therefore expected that corrosion is more severe in surface waters where oxygen is higher, and lower in the deep sea where dissolved oxygen is lower. This is demonstrated by a comprehensive corrosion study conducted by Reinhart, which he reported that the corrosion of steel at different depths of seawater resembles the dissolved oxygen distribution, which the highest corrosion rate of 0.178 mm/y observed at a depth of 1.5 m (DO = ~18 ml/l) , corresponding to where the oxygen concentration is highest. In the same study, he also reported that the corrosion rate decreases with the exposure time increase. For example, the corrosion rate decreases with longer exposure time from 0.272 mm/y at 181 days to 0.147 mm/y at 588 days (Reinhart 1976). The progressive development of the corrosion products might be responsible for the decreased in the corrosion rate as explained earlier in Chapter 1.2. In another field study conducted in the Indian Ocean, Venkatesan et. al. also reported similar observations where the corrosion rate of mild steel from 500 m to 5100 m depth corresponds to the dissolved oxygen concentration, 0.05 – 0.06 mm/y at a depth of 1000 m (DO = 160 µg/kg) as compared to ~0.09 mm/y measured at the 500 m depth (DO = 230 µg/kg), in addition to also reporting that no observable macro and micro-fouling at the deeper depth (Venkatesan et al. 2002). In addition to participating in the corrosion reaction, oxygen may also contribute to the formation of corrosion products (i.e., rust) which may accelerate or inhibit further corrosion depending on the local conditions and the properties of the corrosion products (Gaius et. al., 2016, Fang X et. al., 2018). Chloride ion is the major contributor to the salinity and hence, the electrical conductivity of the seawater (NOAA , Traverso and Canepa 2014). Seawater is an aggressive electrolyte for corrosion due to the presence of a high concentration of ions (Zakowski et al. 2014). It's role in pitting corrosion has been described earlier in Chapter 1.2. The salinity of the surface seawater is subject to hydrological cycle (e.g., run-off, evaporation and precipitation), whereas the seawater conductivity is remarkably uniform beyond 1000 m (Sena Martins et al. 2015, Tyler et al. 2017). On the other hand, temperature has a complex effect on corrosion. In general, the cold temperature in the deep-sea water suppressed corrosion by slowing down the corrosion kinetics (Melchers 2005). However, temperature also affects oxygen solubility, conductivity and could potentially suppress the growth of microbes involved in fouling or MIC. Several studies have investigated the effect of hydrostatic pressure with simulated environments in the laboratory. Sun et al., reported that high hydrostatic pressure (35 MPa) enhanced corrosion of low alloy steel during initial immersion by promoting chloride adsorption to the surface (Sun et al. 2013). The increased hydrostatic pressure also promotes pitting and hydrogen-induced stress corrosion cracking at 10 MPa (1000 m depth) compared to 0.1 MPa (atmospheric pressure) (Yang et al. 2017). Another study, however, pointed out that high hydrostatic pressure enhances corrosion by thinning of Helmboltz layer rather than through chloride adsorption (Liu et al. 2021). In apparent contrast to the laboratory studies, both the field studies by Reinhart and Venkatesan reported that hydrostatic pressure does not seem to affect significantly the corrosion of the metal deployed to the fields (Reinhart 1976, Venkatesan 2005).

Whether MIC is involved in deep-sea corrosion is largely understudied. While deep-sea microbes might be mostly dormant due to energy limitation, the introduction of metals could serve as potential energy sources via dihydrogen production or direct electron uptake hence triggering MIC (as discussed earlier in Chapter 1.3.2). White to reddish-brown stalactites-like corrosion products termed "rusticles" are commonly observed on deep-sea shipwrecks and are commonly believed to be formed as a result of the activity of MIC microbes by iron extraction from the steels (Cullimore and Johnston 2008, Miller et al. 2012). Using the corrosion of the *RMS Titanic* as an example, Melcher argued that rusticle-related corrosion can be explained without the involvement of MIC after accounting for the long-term, sustained corrosion under low oxygen levels (Melchers 2021). The author also argued that MIC is unlikely in low temperatures and low dissolved inorganic nitrogen seawater. While the low temperature could indeed potentially reduce the MIC activity, there is no clear relationship between MIC severity and dissolved inorganic nitrogen level in the deep sea (as discussed in Chapter 1.4.1, deep-sea microbes are carbon/energy-limited rather than dissolved inorganic nitrogen, which play a bigger role in supporting the primary production in surface water) (Gruber 2008). A more detailed investigation of MIC comes from a recent study that combines microbiome and corrosion analysis conducted on a corroding mild steel mooring chain retrieved from the Japan Sea at ~2000 m depth after 10 years of immersion (Rajala et al. 2022). The mooring chain was covered in a thick layer of black-colored corrosion products and the surface exhibited intensive pitting corrosion which resembles the MIC by SRB. The metagenomic analysis revealed that the genus *Desulfocapsa* (sulfur-disproportionating bacteria) and *Desulfovibrio* (SRB) constitute >50% of the total microbial community on the surface, while present in low abundance in the surrounding sediments. This finding suggests that sulfur-cycling microbial consortia are involved in accelerating the mooring chain corrosion.

In brief, our current understanding of deep-sea MIC remains limited. MIC is often neglected in most laboratory tests testing and modeling corrosion under simulated deep-sea environments, while many of the field corrosion tests lack follow-up examinations of the potential involvement of MIC. Integrating modern molecular techniques and -omics tools, microscopic observation or even the traditional culture isolation with the corrosion test would help address the most pressing questions in the field: i) Which are bacterial groups are involved in deep-sea MIC? ii) How do natural microbial communities respond to metals? Iii) What are the mechanisms through which they cause MIC?

1.5 Perspective & Future Outlooks

Deep-sea MIC research is particularly challenging for several reasons: i) inaccessibility due to the remoteness of deep sea, whether to conduct *in-situ* test or sample deployment/retrieval, ii) technical expertise and equipment, iii) slow and progressive nature of corrosion, iv) complexity and sensitivity of microbial response and v) the cross-disciplinary nature of study that demands expertise, communication, and cooperation from corrosion engineers, metallurgists, electrochemists, and microbiologists. With increasing technological capabilities and growing interest in deep-sea exploration for space and resource utilization, a more comprehensive understanding of deep-sea MIC will be crucial to minimize the cost of corrosion associated with human deep-sea activities.

Through extensive literature review, several fundamental yet unaddressed research questions have been identified among others, which are crucial to improve our current understanding of deep-sea MIC. Firstly, there are insufficient examples and evidence to raise the concern of deep-sea MIC. Most MIC studies focused on conventional bacteria, whereas the deep-sea harbors microbial communities with unique adaptations both in terms of physiology and genetics. While model MIC microbes have been studied extensively, it is not known that their deep-sea counterparts possess similar MIC behaviors. To date, several deep-sea SRB species have been isolated from different depths, including *D. hydrothermalis*, *Pseudodesulfovibrio profundus* (formerly *D. profundus*), *Pseudodesulfovibrio indicus* (formerly *D. indicus*) and *Pseudodesulfovibrio piezophilus* (formerly *D. piezophilus*) which are closely related to the well-studied model SRB (Alazard et al. 2003, Bale et al. 1997, Cao et al. 2016, Khelaifia et al. 2011). It is interesting to investigate whether they possess similar MIC behaviors as other marine SRB.

Secondly, it is typically assumed that corrosion in deep sea proceeds similarly to conventional marine corrosion albeit at a slower rate. However, there are substantial studies demonstrating the impact of hydrostatic pressure on deep-sea microbial physiologies such as energetic and membrane properties, hence affecting how they interact with and causing corrosion to the metals. Microbial membrane and membrane protein complexes play a role in metal interaction and EET mechanism, yet these biomolecules are particularly susceptible to hydrostatic pressure. Hydrostatic pressure also affects enzymatic parameters particularly when gaseous substrates/products are involved, this includes the respiratory and dihydrogen utilization efficiency, which

MIC is dependent on. As a result, the impact of hydrostatic pressure on microbial physiologies which contributes to the MIC is not known.

Lastly as discussed above, the MIC studies in the literature are overwhelmingly represented by SRB. In contrast, biofilm in nature is predominantly multispecies, with inter- and intra-species communications, competition, and cooperation between biofilm members, and is functionally diverse as well as spatially and temporally dynamic. It is therefore important to study not only single-species MIC, but also microbial consortia, particularly of deep-sea origin.

1.6 Research Objectives

Based on the identified research gap, several general research objectives have been formulated and will be addressed accordingly in this dissertation. These research objectives will be presented in a more specific manner in the respective chapters.

Objective 1

Examine and compare the MIC mediated by shallow-water marine SRB and deep-sea SRB at 0.1 MPa (atmospheric pressure), 15 MPa and 30 MPa, respectively. (Chapter 2)

Objective 2

Identify the underlying physiology of deep-sea SRB under corroding environment at 0.1 MPa (atmospheric pressure), 15 MPa and 30 MPa using comparative shotgun proteomic. (Chapter 3)

Objective 3

Investigate the progression and development MIC induced by deep-sea microbial enrichment cultures under simulated deep-sea conditions (Chapter 4)

In Chapter 2, I will first examine how the deep-sea high hydrostatic pressure environments affect the MIC process. The MIC of mild steel AH36 (ASTM 131, UNS K01806) by shallow-water marine SRB (*D. alaskensis* and *D. ferrophilus*) and deep-sea isolated SRB (*P. profundus* and *P. piezophilus*) in artificial seawater will be examined and compared at atmospheric (0.1 MPa) and high hydrostatic pressures (15 MPa and 30 MPa) environment. The corrosion will be evaluated based on weight-loss test and microscopy method and combined with biochemical and molecular analysis to interpret the effect of hydrostatic pressure on conventional marine as well as deep-sea SRB. Once the MIC behaviors have been examined, the underlying MIC-related physiologies of deep-sea SRB *P. piezophilus* at atmospheric and high hydrostatic pressures will be investigated using a proteomic approach in Chapter 3. The protein expressed when incubated with mild steel and an inert epoxy surface will be compared to identify the potential MIC-related proteins and study how their expression changes with pressures. To be more aligned with the field MIC, Chapter 4 will work on two mixed-species microbial consortiums established from the deep-sea samples collected from KAIREI 18-15 expedition, which will be subjected to a four-week MIC test on mild steel AH36 in artificial seawater at 15 MPa. The changes in overall microbial composition and potential MIC microbes will be tracked over four weeks using 16S rDNA amplicon sequencing, along with the corrosion examination and biochemical tests, in order to provide a more comprehensive understanding of the onset of deep-sea MIC. Lastly, the findings from the previous chapters will be reviewed and concluded in Chapter 5, where I will discuss the contribution of this dissertation to the MIC research and the potential future direction of this project.

Chapter 2

Deep-sea MIC: Impact of hydrostatic pressure on shallow- and deep-sea SRB

2.1 Introduction

Approximately 10 – 20% of corrosion is attributed to microbiologically-influenced corrosion (MIC), in which the corrosion is accelerated (or inhibited, in some cases) by the presence and/or activities of microorganisms, such as bacteria and fungi (Jia et al. 2019, Kip and van Veen 2015). Sulfate-reducing bacteria (SRB) are the most well-studied MIC bacteria and are widespread in diverse anoxic environments, including deep-sea sediments (Enning and Garrelfs 2014, Muyzer and Stams 2008). Several species of SRB have been described as model MIC microorganisms and have been repeatedly demonstrated corrosive behaviors in many laboratory studies (Eduok et al. 2019, Enning et al. 2012, Ueki and Lovley 2022). These include SRB from marine origin *D. alaskensis* and *D. ferrophilus*, which were isolated from producing oil well in Ventura County, California, and from marine sediment collected near Wilhelmshaven, North Sea, respectively (Dinh et al. 2004, Weimer Paul et al. 1988). However, the MIC behaviors of-deep-sea SRB are relatively unexplored. For example, Bale isolated and characterized a deep-sea SRB *Pseudodesulfovibrio profundus* (formerly *Desulfovibrio profundus*) from marine sediment from 900 m depth (+518 m below seafloor) of the Japan Sea and Khelaifia isolated *Pseudodesulfovibrio piezophilus* (formerly *Desulfovibrio piezophilus*) from wood falls in the Mediterranean Sea at 1693 m (Bale et al. 1997, Khelaifia et al. 2011). Whether these deep-sea SRB possess a similar MIC capability as the model SRB remains unknown.

MIC may be affected by the extreme conditions of deep sea. Hydrostatic pressure, an important characteristic of the deep sea, has been shown to influence both the corrosion process as well as microbial physiology and activity (see Chapter 1.4.1). However, bacteria adapted to the deep-sea environments might respond differently to their shallow-water counterparts when exposed to elevated hydrostatic pressure (Abe 2007, Lauro and Bartlett 2008). Using *P. piezophilus* as an example, this bacterium has been reported to increase membrane fatty acid lengths to maintain membrane fluidity, increased energy metabolism efficiency, and increased glutamate accumulation as "piezolytes" to counteract the effect of hydrostatic pressure (Amrani et al. 2016, Khelaifia et al. 2011). On the other hand, most bacteria tolerate moderate hydrostatic pressure, resulting in an inhibitory effect rather than lethality (Huang et al. 2014). For example, *D. alaskensis* shows a ~25% reduction in growth rate when incubated at 14 MPa, while similar test has not been performed in *D. ferrophilus*(Williamson et al. 2018). There is therefore a need to understand the changes in the MIC process caused by deep-sea as well as shallow-water marine SRB under high hydrostatic pressure in order to address deep-sea corrosion.

This chapter aims to address the research gap by investigating and comparing the MIC behaviors of shallow-water marine SRB *D. alaskensis* (isolated from oil well) and *D. ferrophilus* (isolated form coastal sediment), as well as deep-sea SRB *P. profundus* (isolated from deep-sea sediment) and *P. piezophilus* (isolated from wood fall) at 0.1 MPa (corresponding to atmospheric pressure), 15 MPa (corresponding to the hydrostatic pressure of where the two deep-sea SRB were isolated), and 30 MPa (above the optimal hydrostatic pressure for the deep-sea SRB). The hydrostatic pressure of the test environments was reproduced by employing a hydrostatic pressure reactor and pump. Marine-grade mild steel AH36 will be used in this study for its relevance in marine industrial applications. The corrosion (MIC) tests will be conducted in oligotrophic artificial seawater to simulate the deep-sea environment.

2.2 Materials and Methods

2.2.1 SRB culture preparation

The model SRB *Desulfovibrio alaskensis* G20 (DSM 17464), *Desulfovibrio ferrophilus* IS5 (DSM 15579), *Pseudodesulfovibrio profundus* 500-1 (DSM 11384), and *Pseudodesulfovibrio piezophilus* C1TLV30 (DSM 21447) were obtained from the German Collection of Microorganisms and Cell Cultures GmbH (DSMZ) and were routinely cultured in DSMZ 195c medium at 30°C. Details characterization of the SRB species can be found in the literature (Bale et al. 1997, Dinh et al. 2004, Khelaifia et al. 2011, Weimer Paul et al. 1988). The DSMZ 195c medium was prepared as instructed except resazurin was omitted due to its interference with OD600 measurement. The medium was sparged with N_2/CO_2 gas (95:5) and before inoculation, Na_2S solution was added at a final concentration of 0.04% (w/v) to scavenge residual oxygen. The medium pH was adjusted using filter-sterilized 1 M NaOH to 7.2. Manipulations of the SRB cultures were performed in an anaerobic chamber (Bactron) under $N_2/CO_2/H_2$ (91:4:5) atmosphere and their growth was monitored with optical density using a spectrophotometer at 600 nm. High-pressure incubations were performed in stainless steel pressure vessels (HiP) and a pump controller (Teledyne ISCO) was used to pressurize the pressure vessel using Milli-Q water (Figure 2.1A). A compressible and heat-sealable ProAmpac FoilPak Pouch (VWR), which allows hydrostatic pressure transmission (pre-sterilized with 70%

ethanol and dried), was used for culturing the SRB in the pressure vessel. For high-pressure experiments (15 MPa and 30 MPa), the SRB cultures were first acclimatized by transferring an active culture into fresh DSMZ 195c and allowed to grow into exponential phase at the respective pressure at room temperature before using them for MIC experiments.

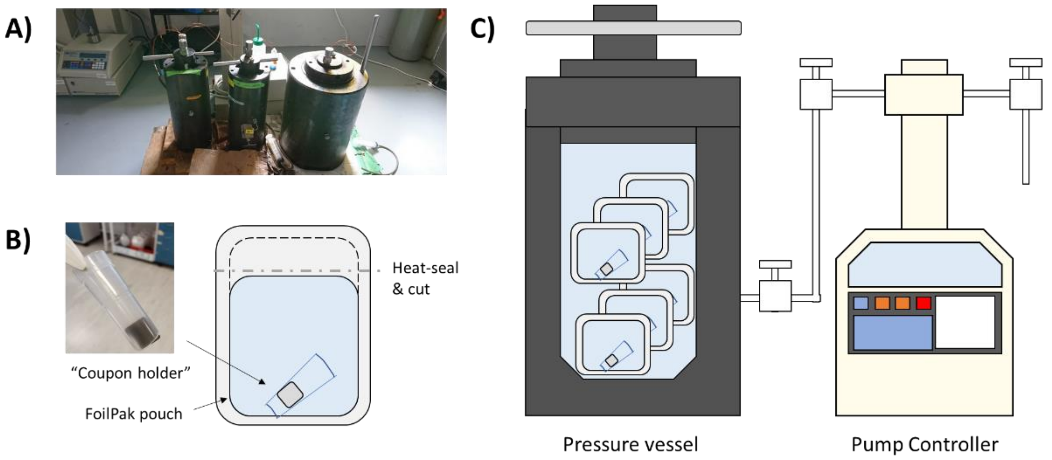

Figure 2.1. Experimental setup for the high-pressure incubation. A photograph of the pressure vessels and pump controller (A). Schematic of a MIC test sample with the mild steel AH36 placed in a coupon holder (B). Schematic of a pressure vessel filled with the samples for MIC test (C).

2.2.2 Mild steel specimen preparation

Mild steel ASTM A131, grade AH36 (UNS K01806) were obtained from Ebenezer NDT Services Pte Ltd with a dimension of 10 mm (width) x 10 mm (length) x 2 mm (height). The nominal composition of the mild steel AH36 is as follow (weight %): C ≤ 0.18, Mn 1.33, Si 0.2, P 0.013, S 0.001, Al 0.034, V 0.02, Ti 0.01, Cu 0.1, Cr 0.01, Ni 002, Mo 0.08 with Fe as the balance. The coupons were sequentially abraded with P420 (46 µm), P800 (22 µm), and P2000 (10 µm) sandpaper on all sides, degreased with acetone and absolute ethanol, and dried under a stream of N_2 gas. The initial coupon weight was obtained using XP2U weighting scale (Mettle Toledo) to a precision of ± 0.01 mg. Before the corrosion test, coupons were sterilized by ultraviolet (UV) light on both sides for 20 min each.

2.2.3 Immersion Test and corrosion analysis

Artificial seawater was chosen as the test medium to investigate deep-sea MIC. The artificial seawater test medium (MOPS-ASW) was prepared according to national center for marine algae and microbiota (NCMA) medium 1 (composition, per liter: NaCl 27.5 g, $MgCl_2$.6H2O 11.47 g, $MgSO_4.7H_2O$ 6.78 g, KCl 0.72 g, NH_4Cl 1.0 g, $CaCl_2.2H_2O$ 1.4 g, K_2HPO4 0.05 g, NaHCO3 0.84 g, mineral solution 0.1% (v/v), Wolfe's vitamin solution 0.1% (v/v)). Bicarbonate provides the pH buffering capacity for natural seawater but its supply in batch experiment is limited. Therefore, 3-(*N*-morpholino) propanesulfonic acid (MOPS) was added at a final concentration of 40 mM for pH buffering. Similarly, the oligotrophic condition in the deep sea is characterized by a low but continuous supply of nutrient from the water column (Chapter 1.4.1). However, the supply of nutrients in batch experiment is also limited to the beginning of the experiment. Therefore, 1 mM Na-*DL*-lactate (common carbon substrate for SRB) was chosen as carbon sources to compromise for the aforementioned limitation. The test medium was sparged with N_2/CO_2 gas (95:5) and pH was slowly adjusted to 7.8 ± 0.2 with anoxic 1 M NaOH before use. The typical concentration of dissolved oxygen after sparging was < 0.5 mg/L. Cysteine-HCl was often used in the literature to scavenge residual dissolved oxygen in the medium (Unsal et al. 2019, Wang et al. 2021a). However, the SRB cultures used in this test were able to grow without the addition of oxygen scavenger. In addition, *D.*

ferrophilus, *P. profundus* and *P. piezophilus* were found to be sensitive to cysteine-HCl, which delayed their growth significantly (Supplementary Figure 1). Therefore, no oxygen scavenger was used in the test medium. To initiate the MIC test, the acclimatized SRB cultures were harvested by centrifugation at 6000 x *g* for 10 min, washed once with the MOPS-ASW. The SRB cells were resuspended in MOPS-ASW and inoculated into MOPS-ASW at a final OD_{600} 0.02. The resuspended SRB cultures were transferred into FoilPak containing one mild steel AH36 coupon secured in a coupon holder (autoclaved and cut-5 ml pipette tip) to prevent the FoilPak pouch compressed directly onto the coupon surface upon pressurization (Figure 2.1B). After mixing, the bulk liquid was sampled for pH measurement, iron assay, sulfate assay, sulfide assay, as well as DNA extraction to determine planktonic biomass with a qPCR assay on the 16S gene (see Chapter 2.2.4 and 2.2.5). The final volume for the immersion test is 60 ml (volume-to-surface area ratio = ~0.24 ml/mm^2). The FoilPaks were heat-sealed twice using the impulse sealer before incubating at the respective pressures at room temperature (25 °C) for 14 days (Figure 2.1C). On Day 14, the FoilPaks were retrieved from the pressure vessel and opened aseptically. The bulk liquid was sampled for pH measurement, iron assay (Fe_{bulk}), sulfate assay, sulfide assay as well as DNA extraction to determine planktonic biomass. The coupons were washed once with sterile 1x PBS to remove loosely attached cells, before cleaning in filter-sterilized 1% HCl with 0.35% hexamethylenetetramine with the aid of ElmaP waterbath sonicator (37 kHz, 80% Pwr for 10 min). The coupons were washed three times with Milli-Q water and dried under a stream of air. The coupons were kept in a dry cabinet until measuring the final weight using XP2U weighting scale (Mettle Toledo). The cleaning solution was sampled for iron assay ($Fe_{surface}$) and DNA extraction to determine the biomass of the biofilm with a qPCR on the 16S gene. The experiment was repeated three times for independent biological replicates. General corrosion was calculated based on the weight-loss method according to ASTM G1 (ASTM 2003) using the Eq. 11:

Eq. 11 Corrosion rate (millimeter per year, mm/y) = K x W/ (A x T x D)

where K = constant, 8.76×10^4 for conversion to mm/y, W = initial weight – final weight, corrected to a treatment control coupon (g), A = surface area (cm^2), measured by ImageJ, T = test duration (h), and D = 7.86 (g/cm^3) for mild steel.

Localized corrosion was assessed using 3D Laser Scanning Microscope VK-X1000 (Keyence) under a 150 x magnification lens and analyzed using MultiFileAnalyzer software (Keyence). Briefly, a 3 x 3 stitched 3D image was taken in five randomly selected regions on the coupon surface. The stitched images were then tilt-corrected using Process Image function. Pits were manually selected using Vol & Area function, with the following criteria: i) a localized depression with more or less circular features, ii) deepest depth >0.25 μm, iii) pit surface area >10 μm^2, iv) distinguish itself from the polishing mark or scratches, and v) for merged pit, only count as a single pit. Five stitched images were used for pit quantification and depth measurement. The maximum pitting penetration rate, and pitting density of each replicate (i.e., five 3 x 3 stitched images) were calculated using the Eq. 12 and Eq. 13, respectively:

Eq. 12 Maximum pitting penetration rate (mm/y) = Deepest pit depth (mm) x 365 days/14days

Eq. 13 Pitting density (pits/mm^2) = total pit count from five stitched images ÷ total surface area counted (5 x 0.05357 mm^2)

The immersion tests presented in Supplementary Table 1 were prepared similarly except with some slight modification. MOPS-ASW with 6.4 mg/L was prepared without sparging with N_2/CO_2 gas. When indicated, a filter-sterilized stock of sodium sulfide, sodium-*DL*-lactate, and cysteine-HCl were added at a final concentration of 1 mM, 20 mM (or omitted), and 3.2 mM, respectively. Sterile anoxic NaOH solution was used to adjust the pH back to 7.8 after addition of cysteine. Culture filtrate of *P. piezophilus* culture (OD_{600} ~ 0.1) was prepared by filtering *P. piezophilus* culture the through 0.22 µm acrodisc syringe filter and 0.6 ml (1% v/v) was added to 60 ml MOPS-ASW with the mild steel AH36.

2.2.4 Chemical analysis

The samples for sulfate and sulfide measurement were fixed with zinc acetate at a final concentration of 0.2 M and immediately stored at -20°C to prevent sulfide oxidation. Sulfate and sulfide were measured using the barium chloride and the copper sulfate method, respectively (Bernardez et al. 2013). Sodium sulfate and sodium sulfide prepared using anoxic Milli-Q water and fixed with zinc acetate were used as the calibration standards for sulfate and sulfide assay, respectively (2.5 mM, 5 mM, 10 mM, 15 mM, 20 mM, 25 mM, and 30 mM). Sulfate consumption was determined by subtracting the final sulfate concentration measured on Day 14 from the initial sulfate concentration measured on Day 0. To determine the total iron concentration in the bulk liquid (Fe_{bulk}), 30 µl of 37% HCl was added to 1 ml bulk liquid samples and digested overnight before reduced with hydroxylamine and assayed using 1,10-

phenanthroline method (Pyenson and Tracy 1945). The total iron concentration in the corrosion product ($Fe_{surface}$) was measured with a similar method from the spent 1% HCl cleaning solution. Whenever necessary, the samples were diluted appropriately in 1% HCl. Iron (II) sulfate prepared in 1% HCl was used as the calibration standards (0.698 µg $_{Fe}$/ml, 1.396 µg $_{Fe}$/ml, 2.792 µg $_{Fe}$/ml, 5.585 µg $_{Fe}$/ml, 11.169 µg $_{Fe}$/ml, 22.338 µg $_{Fe}$/ml, and 44.676 µg $_{Fe}$/ml). The total iron (µg) was calculated by multiplying the measured concentration by the total volume of incubation (60 ml for Fe_{bulk} and 5 ml for $Fe_{surface}$).

2.2.5 DNA extraction and qPCR

Four milliliters of the bulk liquid (planktonic fraction) and spent 1% HCl cleaning solution (biofilm fraction) were centrifuged at 6000 x *g* for 10 min. The cell pellets were washed once in nucleic acid preservation buffer (Camacho-Sanchez et al. 2013) followed by PBS to remove excess iron in the samples which may inhibit downstream PCR. DNA extraction was performed on the cell pellet using PureLink^{TM} Genomic DNA mini kit (Thermo Fischer Scientific) according to the manufacturer's protocol and the DNA concentration was measured using the Qubit^{TM} dsDNA HS assay kit (Thermo Fischer Scientific). Quantitative PCR (qPCR) was then performed on the eluted samples in two technical duplicates using KAPA SYBR® Fast qPCR Master Mix (2x) ABI Prism^{TM}, targeting V1 variable region of 16S rRNA gene using primer pair P1 and P2 (Cocolin et al. 2001). Each qPCR reaction consists of 5 µl 2x master mix, 0.2 µl 10 µM forward primer (P1, 5'- GCG GCG TGC CTA ATA CAT GC -3'), 0.2 µl 10 µM reverse primer (P2, 5'- TTC CCC ACG CGT TAC TCA CC -3') 3.6 µl ultrapure water, and 1 µl extracted DNA as template. The PCR reaction was run with the thermal cycle setting recommended in the kit's manufacturer protocol (Initial denaturation: 95 °C, 3 min; Amplification cycle: 95 °C, 3 s and 60 °C, 20 s for 40 cycles).

2.2.6 Scanning electron microscope

Coupons for SEM were fixed in 5 ml ice-cold anoxic 0.1 M Sorensen's phosphate buffer, pH 7.8 with 2.5% glutaraldehyde (EM-grade) overnight. The coupons were washed twice in the Sorenson's buffer, before sequentially dehydrated in a series of anoxic ethanol concentration (30% 5 min, 50% 5 min, 70% 5 min, 80% 5 min, 90% 15 min, 95% 15 min, and 100% 30 min, twice) and dried under gentle stream of N_2. The coupons were stored in 15 ml tubes in an air-tight compact plastic pouch (Oxoid) containing silica desiccant under 100% N_2 atmosphere. Before SEM imaging, the samples were coated with gold (10 mA for 1 min, ~ 5 nm coating thickness) using sputter coater SC7620 (Quorum). SEM was performed using JEOL FE-SEM 7600F with 15 kV accelerating voltage.

2.3 Results

2.3.1 Formation of black-color corrosion products in the presence of SRB

Figure 2.2 shows the representative macrograph of the mild steel coupons after the immersion test, incubated in sterile MOPS-ASW or with different SRB at 0.1 MPa (Figure 2.2). A layer of black-colored corrosion product was observed on all mild steel coupons incubated with the SRB and were visually similar at all three pressures. The black corrosion product layer appeared homogeneous and firmly adhered to the surface except for *D. ferrophilus* samples which the corrosion product layer was rough and fragile, and detached easily during handling. Mild steel coupons incubated under sterile condition do not form any visible corrosion product.

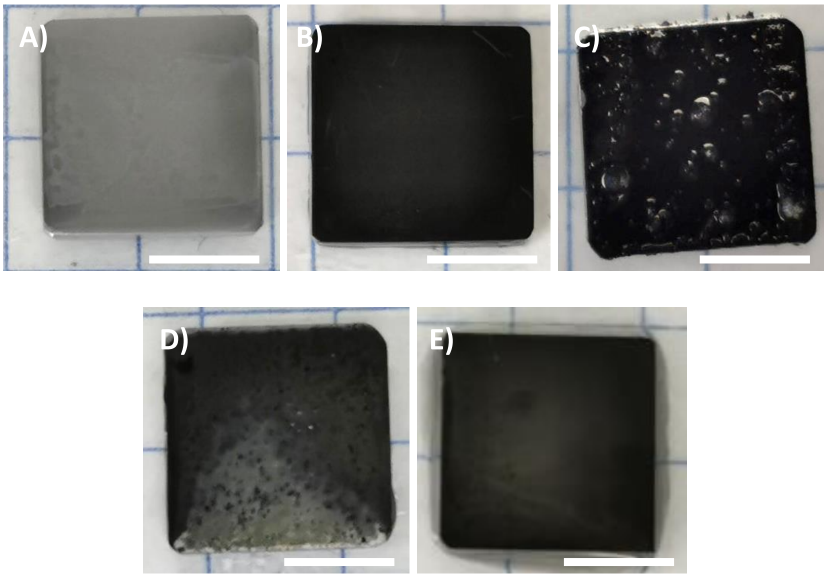

Figure 2.2. Macrograph of the mild steel coupons after the immersion test. The mild steel coupons were incubated in MOPS-ASW (A), or in the presence of *D. alaskensis* (B), *D. ferrophilus* (C), *P. profundus* (D), or *P. piezophilus* for 14 days at 0.1 MPa. Black colour corrosion products were observed on the mild steel coupons incubated with SRB. Scale bar = 0.5 mm. Replicates, n = 4

2.3.2 Hydrostatic pressure influences the weight-loss corrosion induced by SRB

The corrosion products were removed by cleaning the mild steel coupons in 1% HCl with corrosion inhibitor before corrosion assessment. The corrosion of mild steel coupons was evaluated based on the weight-loss method for corrosion rate calculation (Figure 2.3). The corrosion rate of mild steel coupons incubated under sterile conditions were 0.0164 ± 0.002 mm/y, 0.0153 ± 0.001 mm/y, and 0.0152 ± 0.03 mm/y at 0.1 MPa, 15 MPa, and 30 MPa, respectively. When incubated with *D. ferrophilus*, the corrosion rate of mild steels was ~10 x higher than the sterile samples with 0.1455 ± 0.063 mm/y and 0.1643 ± 0.058 mm/y at 0.1 MPa and 15 MPa respectively. At 30 MPa, the corrosion rate decreased to 0.0345 ± 0.048 mm/y. On the other hand, the corrosion rate of mild steel coupons incubated with *D. alaskensis*, *P. profundus*, and *P. piezophilus* were lower than the sterile samples with a corrosion rate of < 0.01 mm/y, regardless of hydrostatic pressure. A similar reduction of weight-loss corrosion could also be observed by the addition of exogenous sodium sulfide (1 mM) or culture filtrate (1% v/v) to the mild steel coupons incubated in sterile MOPS-ASW (Supplementary Table 1). Neither increasing nor decreasing the initial cell density, or the inclusion of 20 mM sodium lactate as carbon source, increased the weight loss induced by these SRB (Supplementary Table 1). Notably, the addition of 3.2 mM cysteine-HCl increased weight loss in *P. piezophilus* samples, however as shown in Supplementary Figure 1, cysteine-HCl delayed the growth of *P. piezophilus*. In addition, it was previously reported that cysteine may act as a corrosion inhibitor (Farahati et al. 2020, Fu et al. 2011). Therefore, cysteine was not included in the experimental setup.

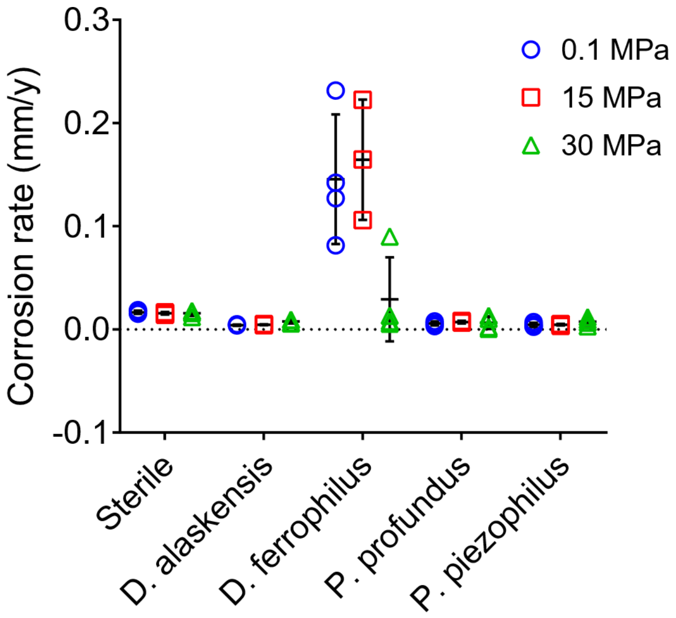

Figure 2.3. Corrosion rate of the mild steel coupons after 14 days incubation in MOPS-ASW at 0.1 MPa, 15 MPa, and 30 MPa derived from weight-loss results. Data

points represent replicates from four independent experiments and mean ± standard deviation is shown.

2.3.3 Formation of insoluble corrosion products species in the presence of SRB

The corroded iron loss into the bulk liquid (Fe bulk) or converted into corrosion products (Fe surface) was measured to complement the weight-loss results, also to monitor the distribution of corroded iron. In general, the total iron loss (Fe bulk + Fe surface) shows a good agreement with the weight-loss results (Figure 2.4). Aligning with the macroscopic observation, incubation with SRB results in a substantial amount of corroded iron detected on the surface as corrosion products, which comprised ~95% of the total corroded iron in the *D. alaskensis*, *P. profundus* and *P. piezophilus* samples. This contrasts with the mild steel coupons incubated in sterile MOPS-ASW where ~80% of the corroded iron was found in the bulk liquid of the test medium instead. Incubation with *D. ferrophilus* at 0.1 MPa and 15 MPa resulted in a roughly equal distribution of corroded iron in bulk test medium and on the surface as corrosion products. Black-colored fine particles of iron sulfide were found in the bulk liquid of the test medium in these two samples, which probably detached from the loosely attached corrosion products or formed by the dissolved ferrous ions reacting with the sulfide produced by the SRB.

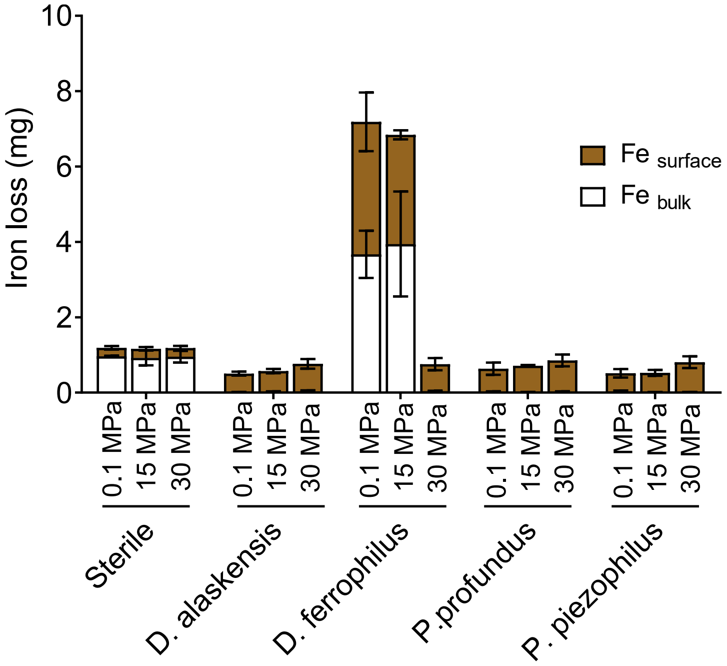

Figure 2.4. Total iron loss of mild steel coupons after 14 days incubation in MOPS-ASW at 0.1 MPa, 15 MPa, and 30 MPa. Fe $_{\text{bulk}}$ = dissolved and particulate (if any) iron. Fe $_{\text{surface}}$ = corrosion products. Bar chart is presented in mean ± standard deviation from independent replicates.

2.3.4 Hydrostatic pressure influences the pitting severity induced by the SRB

After removing corrosion products, the mild steel coupons were examined under the microscope for surface irregularities and identification of localized corrosion, which is difficult to detect by the weight-loss method (Figure 2.5 – 2.10). The coupons incubated in sterile seawater were uniformly corroded, displayed by general roughening of the surface in all three pressures tested, with very few micron-sized pits observed (Figure 2.5). The mild steel coupons incubated with *D. alaskensis*, *P. profundus* and *P. piezophilus,* showed little sign of general corrosion where the polishing lines remained visible in most regions. However, pitting corrosion was prominent in those samples (Figures 2.6, 2.8, and 2.9). Particularly, both the pitting penetration rate and pitting density were significantly higher in *P. profundus* and *P.*

piezophilus samples when incubated at 15 MPa, which corresponds to the hydrostatic pressure at the isolation depth, and when compared to the sterile sample at the respective pressure (Figure 2.10 and Supplementary Figure 2). On the other hand, mild steel incubated with *D. ferrophilus* exhibits the most severe surface damage from a combination of general and localized corrosion at 0.1 MPa and 15 MPa (Figure 2.7). Due to the overlapping general and localized corrosion features and without a pristine surface as a reference, it is not possible to quantitatively analyze the localized corrosion in these samples. At 30 MPa, however, the severe surface corrosion was no longer observed in *D. ferrophilus* samples, while pitting corrosion persisted. Mild steel samples in sterile media added with 1 mM sodium sulfide produced a visually similar corrosion product layer to those incubated with SRB samples but no pitting was observed (Supplementary Figure 3).

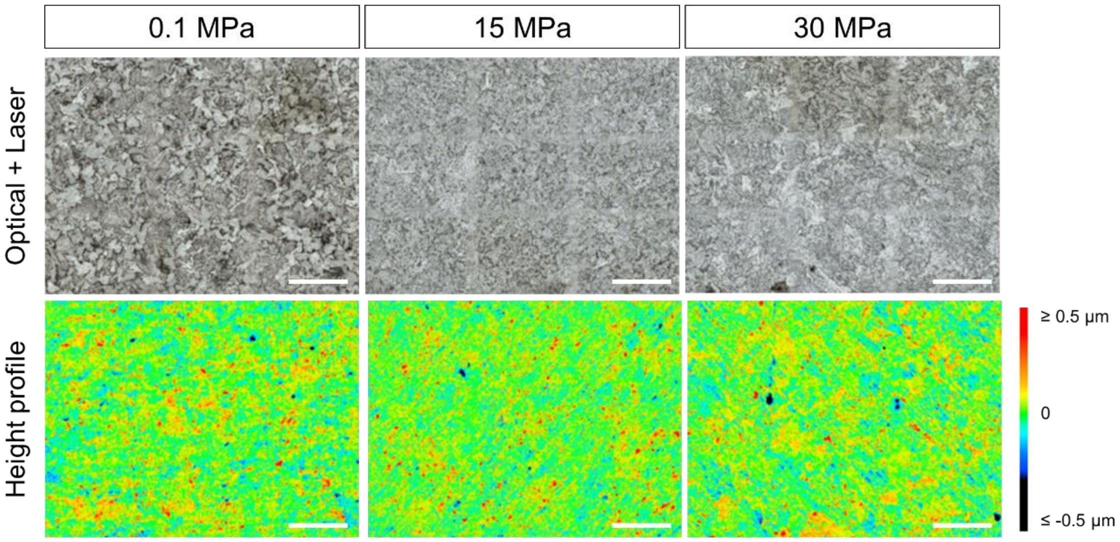

Figure 2.5. Surface of mild steel coupons after 14 days incubation in sterile MOPS-ASW at 0.1 MPa, 15 MPa, and 30 MPa. Five randomly selected field of views from four independent replicates were analyzed and consistent with these observations. Optical image (top) and height profile (bottom) of a representative field of view are shown. Scale bar = 50 µm.

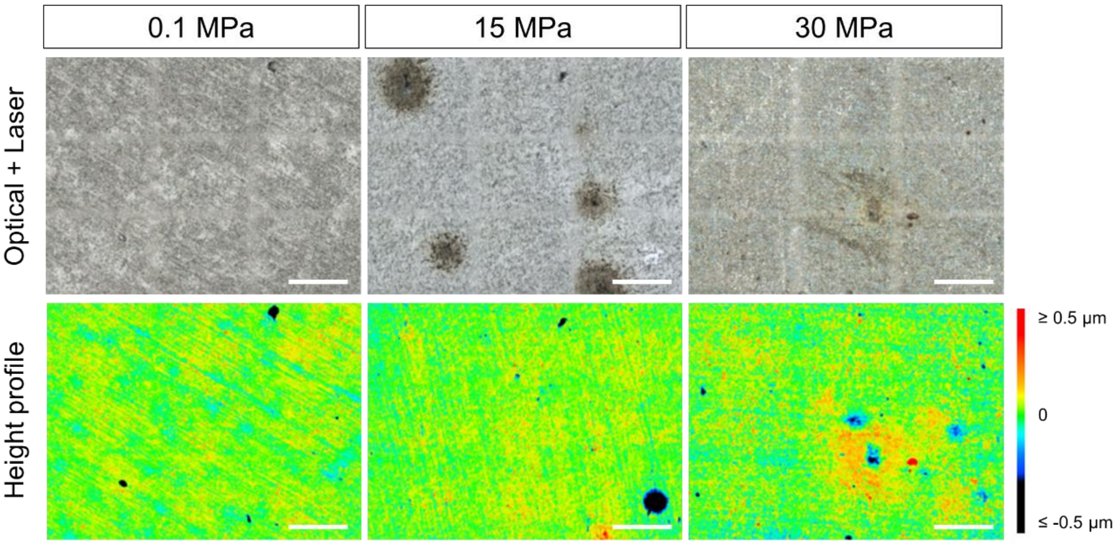

Figure 2.6. Surface of mild steel coupons after 14 days incubation with *D. alaskensis* in MOPS-ASW at 0.1 MPa, 15 MPa, and 30 MPa. Five randomly selected field of views from four independent replicates were analyzed and consistent with these observations. Optical image (top) and height profile (bottom) of a representative field of view are shown. Scale bar = 50 µm.

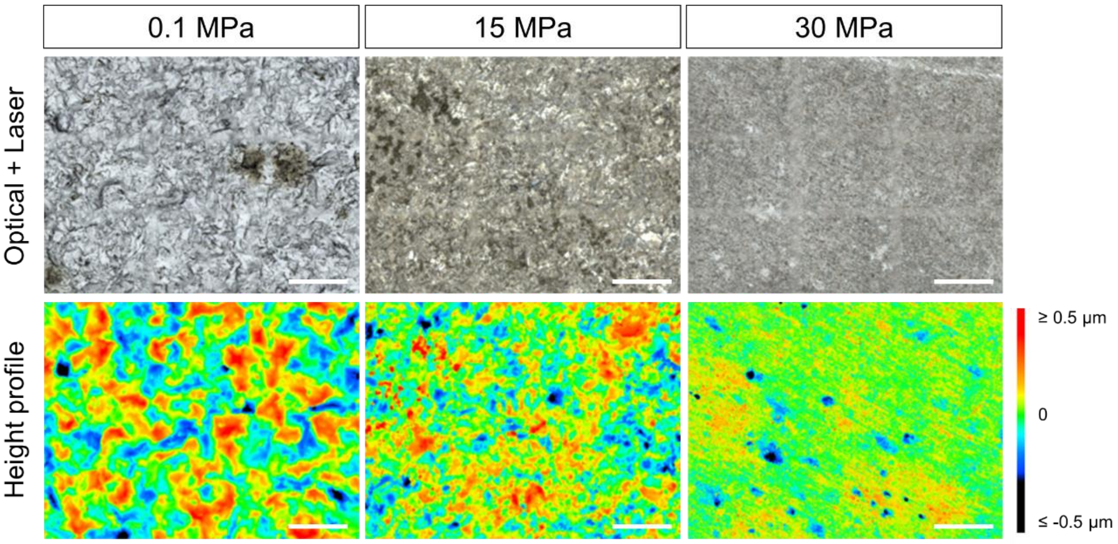

Figure 2.7. Surface of mild steel coupons after 14 days incubation with *D. ferrophilus* in MOPS-ASW at 0.1 MPa, 15 MPa, and 30 MPa. Five randomly selected field of views from four independent replicates were analyzed and consistent with these observations. Optical image (top) and height profile (bottom) from a representative field of view are shown. Scale bar = 50 µm.

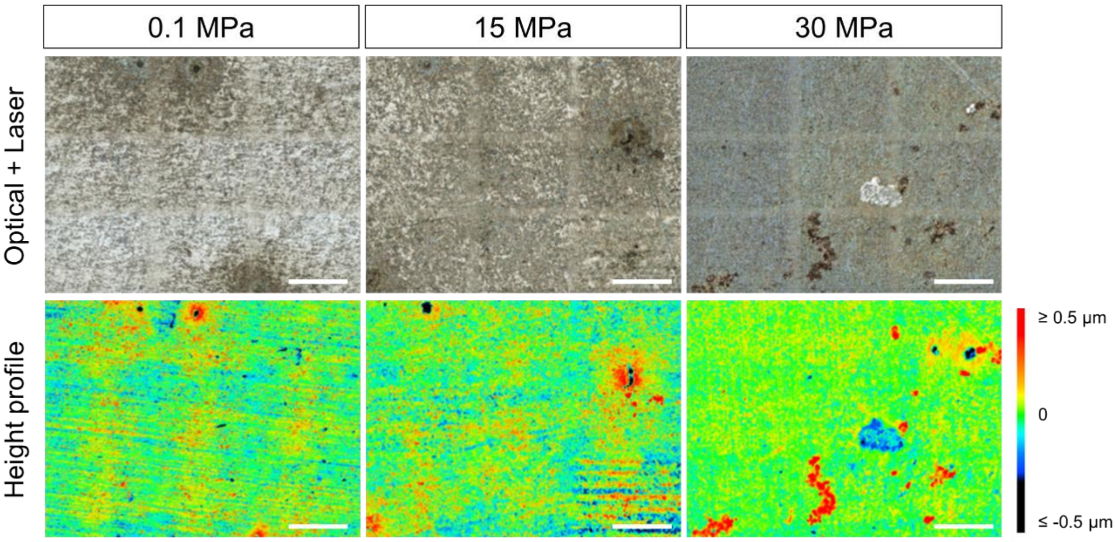

Figure 2.8. Surface of mild steel coupons after 14 days incubation with *P. profundus* in MOPS-ASW at 0.1 MPa, 15 MPa, and 30 MPa. Five randomly selected field of views from four independent replicates were analyzed and consistent with these observations. Optical image (top) and height profile (bottom) from a representative field of view are shown. Scale bar = 50 µm.

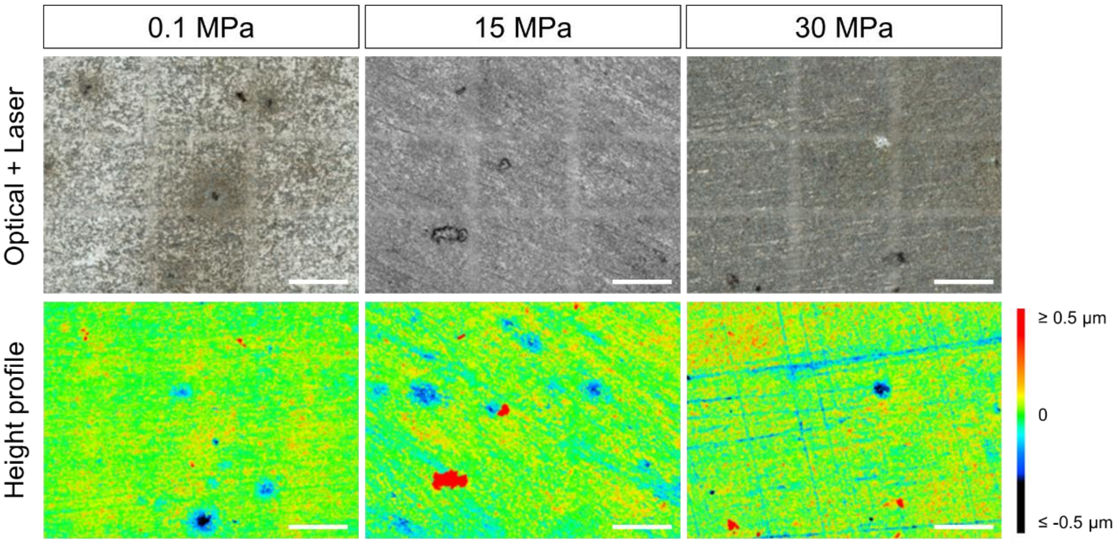

Figure 2.9. Surface of mild steel coupons after 14 days incubation with *P. piezophilus* in MOPS-ASW at 0.1 MPa, 15 MPa, and 30 MPa. Five randomly selected field of views from four independent replicates were analyzed and consistent with these observations. Optical image (top) and height profile (bottom) from a representative field of view are shown. Scale bar = 50 µm.

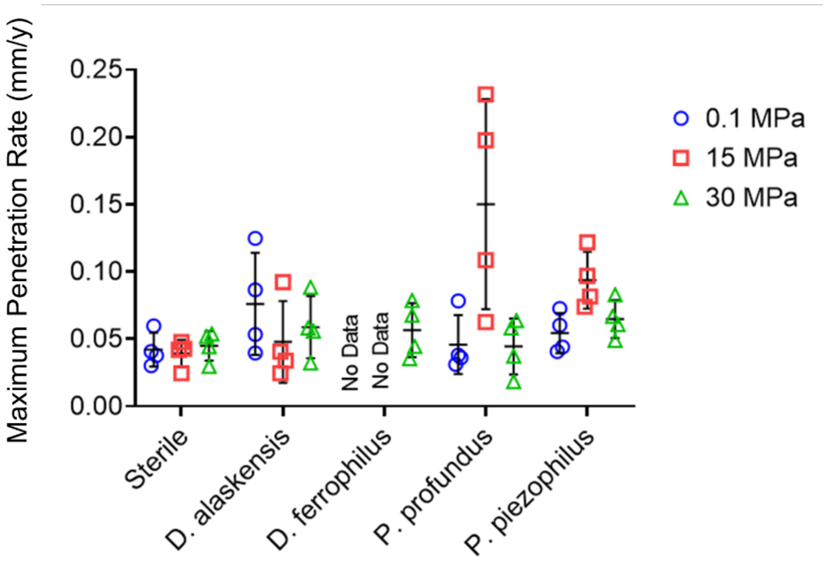

Figure 2.10. Analysis of the maximum pitting penetration rate of mild steel incubated with different SRB at 0.1 MPa, 15 MPa, and 30 MPa. Data points represent the maximum penetration rate from each independent replicates. Data are presented in mean ± standard deviation of the maximum pitting penetration rate of the independent replicates.

2.3.5 Corrosion severity does not depend on the microbial biomass and sulfate-reduction activity

Chemical and biomass analyses were also performed after the immersion test. Sulfide was detected only in the samples incubated with SRB; however, a high sulfide level does not necessarily correspond to greater corrosion severity (Table 2-1). In fact, a very low sulfide level (< 0.3 mM) was detected in the bulk liquid of *D. ferrophilus* samples, which displayed the highest weight-loss corrosion. However, it should be noted that some sulfide might have participated in the reaction with the dissolved iron and precipitated as corrosion products, therefore, was not detected by the test. Neither the sulfate consumption, planktonic biomass nor the biofilm biomass appeared correlated to the severity of the mild steel corrosion (Table 2-1). Nevertheless, interpretation from the chemical and biomass analysis is difficult as the results show high variability across replicates, potentially due to the prolonged incubation under low nutrients conditions. The pH of the buffered test medium shifted very little after the 14 days immersion test (Table 2-1).

Table 2-1. Biochemical assay, pH and biomass estimation based on 16S rRNA genes copy numbers.

Samples	**Hydrostatic Pressure**	**Sulfate consumed (mM)**	**Sulfide production (mM)**	**Planktonic biomass (16S rRNA genes copies/ml)**	**Biofilm biomass (16S rRNA genes copies/cm^2)**	**pH**
Sterile	0.1 MPa	-1.03 ± 1.48	-0.05 ± 0.06	< 100	< 100	7.78 ± 0.04
	15 MPa	2.00 ± 2.05	0.00 ± 0.01	< 100	< 100	7.75 ± 0.06
	30 MPa	0.50 ± 1.73	0.04 ± 0.11	< 100	< 100	7.77 ± 0.08
D. alaskensis	0.1 MPa	6.39 ± 2.35	2.08 ± 0.65	5.97 ± 3.83 x 10^6	1.18 ± 1.24 x 10^4	7.67 ± 0.05
	15 MPa	3.03 ± 2.32	1.73 ± 1.46	5.15 ± 1.06 x 10^6	0.77 ± 1.13 x 10^4	7.70 ± 0.04
	30 MPa	4.95 ± 0.67	3.03 ± 1.23	3.98 ± 1.77 x 10^6	1.80 ± 1.14 x 10^6	7.65 ± 0.06
D. ferrophilus	0.1 MPa	2.62 ± 0.90	0.13 ± 0.24	2.61 ± 0.96 x 10^5	1.00 ± 1.47 x 10^4	7.95 ± 0.13
	15 MPa	3.39 ± 1.35	0.26 ± 0.25	1.30 ± 1.54 x 10^6	2.42 ± 2.99 x 10^4	7.88 ± 0.13
	30 MPa	3.04 ± 1.84	0.25 ± 0.32	1.69 ± 0.89 x 10^4	4.98 ± 8.14 x 10^3	7.77 ± 0.07
P. profundus	0.1 MPa	1.89 ± 1.14	2.57 ± 0.52	3.36 ± 2.39 x 10^6	0.85 ± 1.44 x 10^5	7.71 ± 0.01
	15 MPa	2.83 ± 2.07	0.43 ± 0.25	1.52 ± 1.24 x 10^6	2.70 ± 2.77 x 10^3	7.73 ± 0.08
	30 MPa	1.39 ± 0.85	0.33 ± 0.21	2.44 ± 0.29 x 10^6	2.48 ± 2.90 x 10^3	7.72 ± 0.06
P. piezophilus	0.1 MPa	1.87 ± 1.38	1.96 ± 0.92	2.79 ± 3.03 x 10^7	8.84 ± 7.60 x 10^5	7.71 ± 0.06
	15 MPa	4.95 ± 1.58	2.54 ± 0.19	1.01 ± 0.36 x 10^7	3.33 ± 2.09 x 10^5	7.70 ± 0.03
	30 MPa	2.49 ± 1.83	0.68 ± 0.48	9.70 ± 4.72 x 10^6	7.03 ± 1.05 x 10^5	7.72 ± 0.07

2.3.6 Hydrostatic pressure influences the corrosion morphology of the SRB

The corrosion products and/or biofilm morphology of mild steel coupons incubated in sterile MOPS-ASW or with different SRB were examined under a scanning electron microscope (Figure 2.11). The mild steel surfaces incubated under sterile condition were similar at 0.1 MPa, 15 MPa and 30 MPa, the corrosion products deposited on the surface are tiny mineral flakes, characterized by Fe, O, and trace amounts of C, Ca, and Mg. Incubation with SRB produce corrosion products with different morphology, however the overall composition detected with EDS were similar which consist of mainly Fe, S, O and C. In *D. alaskensis* samples, the base metal surfaces were uniformly covered with bacterial cells and corrosion products. Spherical and fibrous-shaped corrosion products film were the main corrosion products deposited on the surface whereas at 0.1 MPa, some cells and corrosion products were covered by another layer of sub-micron size needles-like minerals. The coupon surface of *D. ferrophilus* sample at 0.1 MPa was covered by biofilm with “mushroom-shaped” three-dimensional structures, with cells and corrosion products buried within. The 3D structures were no longer observed at 15 MPa but rather in some regions, cracks were observed with cell and corrosion products found underneath, indicating the presence of outer crust and inner crust of the corrosion products. Incubation with *P. profundus* produces a layer of iron sulfide crust which was covered by fibrous-shaped corrosion products or dehydrated EPS. The bacterial cells and clumps of corrosion products are scattered on the surface, and more corrosion products were observed at higher hydrostatic pressures. A very dense S-rich corrosion products layer was found on the coupon surfaces incubated with *P. piezophilus* which has a more organic-like appearance. Micron-sized cracks were observed on the corrosion crust at 0.1 MPa and 15 MPa with sizes resembling the pits observed under 3D laser scanning microscope.

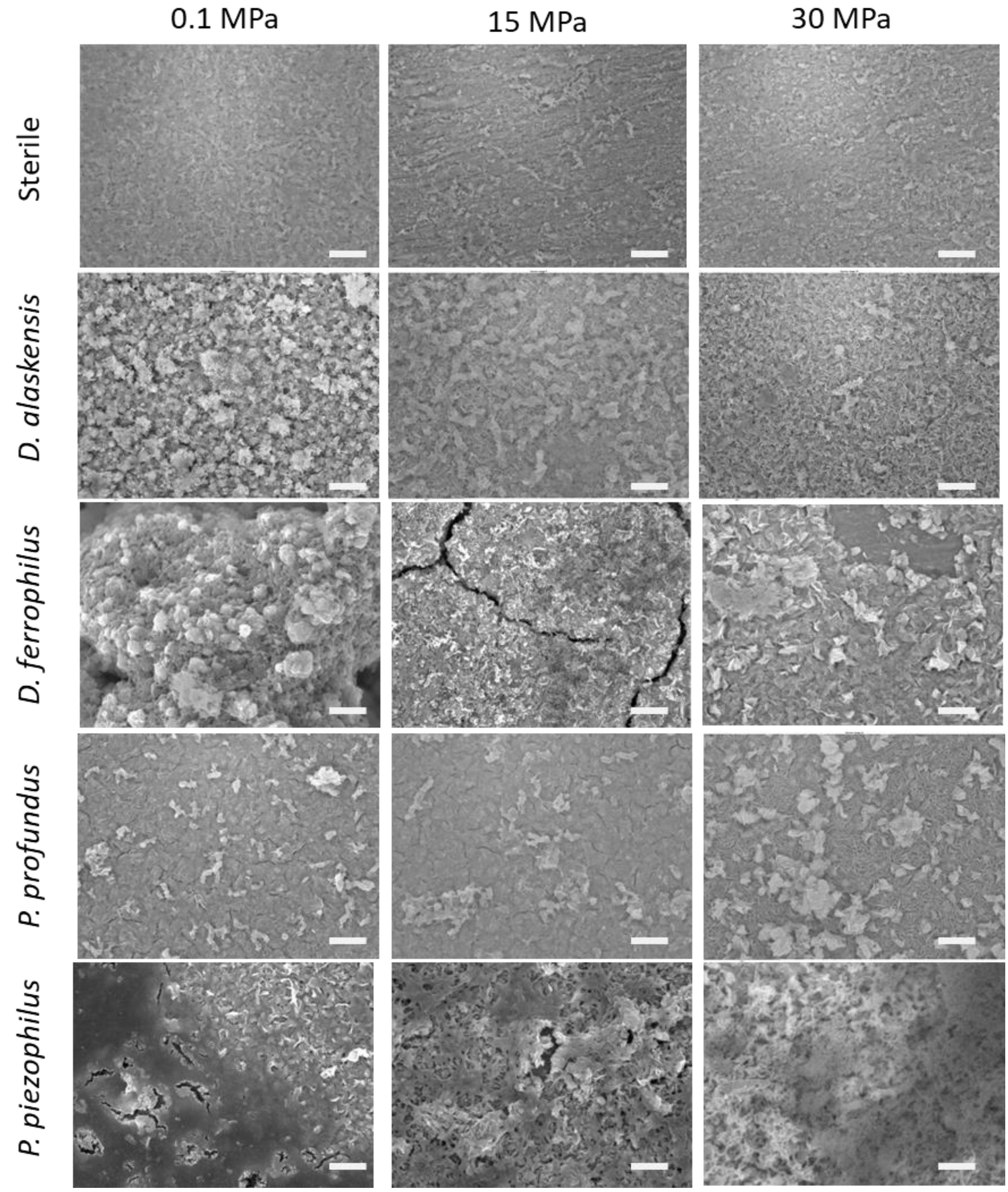

Figure 2.11. Scanning electron micrographs of biofilm and corrosion products morphology observed on the mild steel surface after 14 days incubation in MOPS-ASW at 0.1 MPa, 15 MPa, and 30 MPa. Scale bar = 5 μm.

2.4 Discussion

In this study, the influence of hydrostatic pressure on the short-term (14 days) MIC behaviors has been studied in the closely-related species of shallow-water marine SRB and deep-sea SRB in a simulated deep-sea environment using a low nutrient, pH-buffered artificial seawater. In the literature, the reported MIC induced by *D. ferrophilus* vary greatly from 0.3 mm/y to 1.31 mm/y depending on the test condition and the grade of mild steels used (Beese et al. 2013, Wang et al. 2021a, Wang et al. 2022). Similarly, the reported corrosion rate for *D. alaskensis* ranged from 0.05 mm/y to 0.20 mm/y (Padilla-Viveros et al. 2006, Wikieł et al. 2014). However, comparison with these studies has been proven to be difficult as the corrosion rate of a sterile control is not available in many of the studies. There is also a lack of MIC study done using the deep-sea SRB *P. profundus* and *P. piezophilus*. In agreement with the literature, incubation with *D. ferrophilus* greatly enhanced the corrosion of mild steel in artificial seawater. On the other hand, the presence of *D. alaskensis*, *P. profundus* and *P. piezophilus* resulted in a lower weight loss as compared to the sterile control (Figure 2.3). The reduction of weight loss is associated with the formation of a compact iron sulfide corrosion products that firmly adhered to the surface, which helps suppressing the anodic dissolution of the base metal (Ma et al. 2000, Zhou et al. 2013). This was demonstrated by the addition of Na_2S as well as culture filtrate as shown in Supplementary Table 1. On the other hand, the corrosion product film on the *D. ferrophilus* samples is porous and detached easily, hence offering less protection against the aggressive MIC behavior of the SRB (Figure 2.11). Our results suggest that the compactness, and hence the protectiveness, of the iron sulfide film is related to the $[HS^-]$: $[Fe^{2+}]$ ratio at the corrosion site, which the relationship was described in Figure 2.12. The high $[HS^-]$: $[Fe^{2+}]$ environment in *D. alaskensis*, *P. profundus* and *P. piezophilus* samples favor the formation of a tightly-adhered and compact iron sulfide film, whereas the low $[HS^-]$: $[Fe^{2+}]$ ratio in *D. ferrophilus* samples allows the iron sulfide layer to form more distantly from the steel surface, resulting in a thicker but porous FeS layer that failed to impede anodic dissolution. This is in agreement with the previous studies reporting that while sulfide is a common corrosive agent in oil and gas sector (where it is called “sour corrosion”), high sulfide level at pH > 6 actually promotes the formation of protective iron sulfide corrosion products that inhibit iron dissolution (El Mendili et al. 2014, Liu et al. 2023, Zhang et al. 2021). Cathodic reduction of hydrogen ions (Eq. 3), on the other hand, was not impeded as the electrons may migrate through the conductive iron sulfide layer (Kvarekvål and Moloney 2017). According to the cathodic depolarization theory, SRB may enhance the corrosion by the consumption of the cathodic-formed hydrogen (see Chapter 1.3.2.1). While all of the SRB used in this study is known to utilize hydrogen as electron donor, yet only the incubation with *D. ferrophilus* enhanced the weight loss of the mild steel specimens. Therefore, our findings suggest that the cathodic depolarization does not enhance the corrosion.

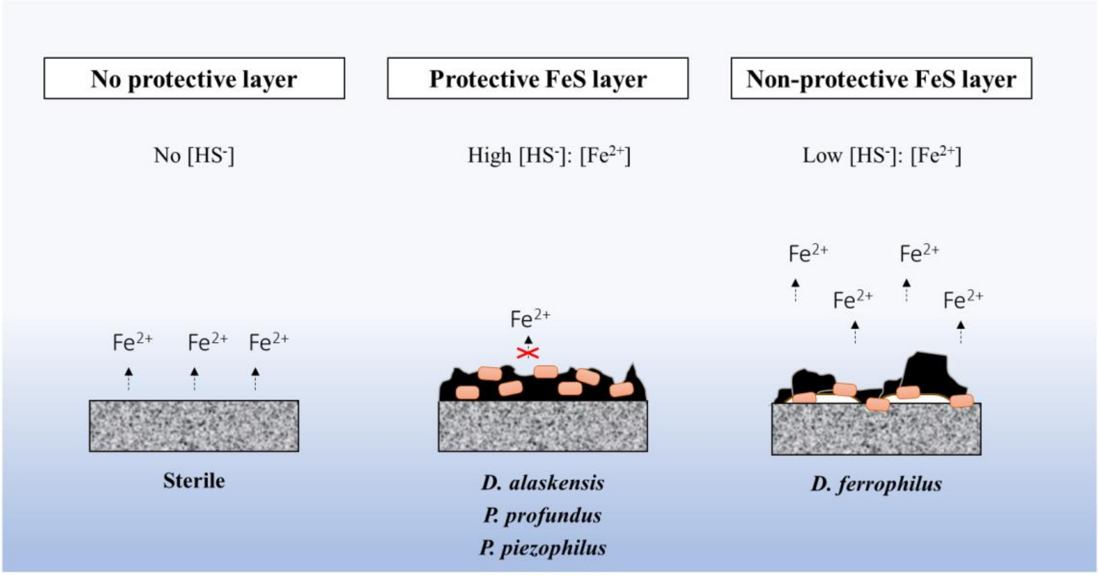

Figure 2.12. Schematic diagram describing the relationship between the $[HS^-]$: $[Fe^{2+}]$ ratio and the protective properties of FeS layer. High $[HS^-]$: $[Fe^{2+}]$ ratio favours the

formation of protective FeS layer whereas low [HS^-]: [Fe^{2+}] ratio favours the formation of porous, non-protective FeS layer.

The incubation with SRB induced the formation of micron-sized pits as a result of their activity, as the addition of exogenous Na_2S did not lead to such pitting (Figure 2.10 and Supplementary Figure 3). Pitting is a more devastating form of corrosion and is often initiated at sites where a local breakdown of passive/protective layer occurs, creating an environment encouraging localized dissolution (see Chapter 1.2). The pitting corrosion by the deep-sea SRB *P. profundus* and *P. piezophilus* was most severe at 15 MPa, which roughly corresponds to the in-situ pressure of where these two bacteria were isolated, and the pitting corrosion was lowest at 0.1 MPa. Given that these two SRB induced pitting corrosions but did not result in a higher weight loss (i.e., general corrosion), it is possible that the weight loss and pitting corrosion were caused by different MIC mechanisms. Depending on the conditions, the pit growth might become self-sustaining and continue to propagate ("stable pits"), while some pit growth might be ceased and re-passivated ("metastable pits") (Akpanyung and Loto 2019, Caines et al. 2013). As the test medium consists of only 1 mM lactate (carbon sources), the experiment ended on Day 14 when most of the SRB population is expected to become dormant/dead. Whether these pits propagate under oligotrophic condition in long-term requires further investigation and requires a continuous flow setup. When cultured in nutrient-rich media (DSMZ 195c), the growth of these two deep-sea SRB at 15 MPa is similar or even lower than 0.1 MPa and was lowest at 30 MPa (Supplementary Figure 4). This suggests that the MIC behaviors of these two bacteria were directly impacted by the hydrostatic pressure rather than through growth. Deep-sea bacteria cope with the high-pressure environment through adapting membrane composition, production of solutes (piezolytes), and differentially express specific proteins at increased hydrostatic pressure (Chapter 1.4.1). In a previous transcriptomic study on *P. piezophilus*, several genes involved in energy-conservation as well as membrane-associated proteins were previously reported to be differentially regulated in response to hydrostatic pressure (Amrani et al. 2016). The current observation suggests that MIC-related pathways/physiology may be differentially regulated or become more active at elevated pressures than at 0.1 MPa, which will be investigated in greater detail in the next chapter. To our surprise, a mildly piezo-tolerant trait was observed in *D. ferrophilus* since it survived and retained its corrosiveness up to 15 MPa. This raised the concern of the materials deployed to the deep sea should consider not only MIC mediated by the deep-sea bacteria but also the hitchhiking MIC microbes of shallow water origin during the installation or handling process.

2.5 Conclusion

In this chapter, the MIC induced by shallow-water marine SRB and deep-sea SRB at 0.1 MPa, 15 MPa, and 30 MPa hydrostatic pressure was investigated. To the author's knowledge, this is the first comparative MIC study investigating the impact of hydrostatic pressure on the MIC behaviors of shallow-water marine SRB and deep-sea SRB. Importantly, this study confirmed the MIC mediated by deep-sea SRB, and showed that even in closely-related SRB, the bacteria may exhibit different biofilm morphology on the metals, different MIC behaviors, as well as respond differently to the hydrostatic pressure. The underlying reason is unclear at the moment, and it was postulated to be related to the presence of different MIC pathways in different SRB species. Notably, the findings also suggest that the corroding microenvironment (particularly, the balance of [HS^-]: [Fe^{2+}] ratio) has a huge impact on the corrosion outcome by affecting the protective properties of the corrosion products layer. These findings highlight the importance of designing the MIC experiment in application-relevant environments and the need of expanding the MIC research to more diverse species rather than focusing on a selected and highly corrosive SRB.

The findings of this chapter suggest that consumption of cathodic hydrogen (cathodic repolarization theory) and via sulfide production (CMIC) are not the main MIC mechanism. On the other hand, hydrostatic pressure stimulates pitting corrosion behaviors in deep-sea SRB, and the mechanism is likely independent of weight-loss (general) corrosion. The observed changes in pitting behaviors may involve differential expression of MIC proteins under elevated hydrostatic pressure (either directly or indirectly related), which will be explored in the Chapter 3 using the proteomic approach. In the future with more deep-sea SRB species isolated and commercially available, it will be interesting to investigate their MIC at >30 MPa, as the current pressure tested is still lower than the pressure at the average depth of the ocean (~38 MPa). Another crucial finding in this chapter is that while the most severe MIC is often observed at their optimal hydrostatic pressure, the SRB may retain the ability to cause MIC even at sub-optimal hydrostatic pressure. The shallow-water marine SRB *D. ferrophilus* can be piezo-tolerant and preserves growth and metabolic activity as well as retaining MIC capability in moderate (15 MPa) hydrostatic pressure. This implies elevated hydrostatic pressure alone has limited effect on inhibiting MIC, and the potential MIC from bacteria of shallow-water origin should not be neglected. However as noted earlier in the discussion, it will be interesting to investigate the long-term corrosion behaviors of these SRB under high hydrostatic pressure environments. Overall, this chapter provided insights into how high hydrostatic pressure environment might impact MIC using axenic culture. However, natural biofilms often consist of diverse members which their interactions and cooperations shape their community composition and function. This will be explored in Chapter 4 where I will address this research gap by studying deep-sea MIC using microbial consortium enriched from deep sea.

Chapter 3

Physiological insights into deep-sea MIC: A comparative proteomic approach on deep-sea SRB Pseudodesulfovibrio piezophilus

3.1 Introduction

The involvement of sulfate-reducing bacteria (SRB) in anoxic MIC is well-documented and studied in laboratory settings (Kip and van Veen 2015). Several MIC mechanisms have been proposed, reviewed, and criticized over the decades of study, as none of these hypotheses were successfully generalized to explain the corrosion phenomenon incurred (discussed in Chapter 1.3.2) (Blackwood 2020, Gu et al. 2019). This is partly due to the existing MIC theories are derived mainly from corrosion thermodynamic perspective with limited emphasis on the physiological aspect. For example, hydrogen consumption is a pivotal factor in the MIC mechanism according to the cathodic depolarization theory (Iverson 1966). However, the expression level of hydrogenases has rarely been assessed (Iverson 1966, Liang et al. 2021, Mori et al. 2010). Similarly, EMIC theory proposed SRB induces MIC via EET, yet such electron transfer protein has not been identified (Deng et al. 2020, Deng et al. 2015, Li et al. 2015a). The lack of understanding of SRB physiology under such corroding environments hindered the deciphering and reconstruction of MIC mechanisms and progression. Traditionally, the study of MIC-related physiology has been challenged by the complexity of the interactions between the microbes and metal, and the spatial and temporal unpredictability of MIC. The advancement of modern “omics” techniques have overcome the challenges and have been demonstrated on a few models SRB such as *D. vulgaris* and *D. ferrophilus* (Chatterjee et al. 2021, Tripathi et al. 2021, Ueki and Lovley 2022).

Understanding the MIC caused by deep-sea bacteria is crucial to protect assets deployed in the deep ocean. Chapter 2 demonstrated that the deep-sea SRB *P. profundus* and *P. piezophilus* exhibited more severe MIC behaviors in artificial seawater supplemented with one millimolar lactate as carbon source when exposed to elevated hydrostatic pressure, corresponding to their isolation depth. How the simulated deep-sea condition altered the SRB physiology and contributed to enhanced MIC is an important missing piece of information that is crucial to shed light on the observed phenomenon. It was previously reported that *P. piezophilus* cope with the elevated hydrostatic pressure by adapting their membrane lipid composition and accumulates glutamate intracellularly as "piezolytes" to maintain cellular functions, and has a more efficient bioenergetic yield from lactate oxidation at their optimal hydrostatic pressure as compared to suboptimal hydrostatic pressure at 0.1 MPa and 26 MPa (Amrani et al. 2016, Khelaifia et al. 2011). However, these studies focused on the planktonic culture of *P. piezophilus* that was grown in a nutrient-rich medium, which the condition does not accurately represent the real environments. Furthermore, the biofilm formation, rather than the planktonic cells, is believed to be a prerequisite step for MIC (Puentes-Cala et al. 2022). To address this, a proteomic analysis was conducted on *P. piezophilus* culture incubated with marine grade mild steel AH36 to investigate the physiological changes at 0.1 MPa, 15 MPa and 30 MPa. The proteomic profile was compared with the *P. piezophilus* culture incubated with an inert surface subjected to the same hydrostatic pressure environment. Due to the tendency of SRB to corrode various metals, epoxy polymer was chosen as the control inert surface

(Huang et al. 2004, Pu et al. 2023, Unsal et al. 2023). This allow us to identify the proteins that are highly enriched under corroding environments and monitor their protein levels at 0.1 MPa, 15 MPa and 30 MPa.

3.2 Materials and Methods

3.2.1 SRB culture preparation

Deep-sea SRB *Pseudodesulfovibrio piezophilus* C1TLV30 (DSM 21447) was obtained from German Collection of Microorganisms and Cell Cultures GmbH (DSMZ) and was routinely cultured in the recommended medium DSMZ 195c medium at 30°C. The DSMZ 195c medium was prepared as instructed except resazurin was omitted. The medium was sparged with N_2/CO_2 gas (95:5) and before inoculation, Na_2S solution was added at a final concentration of 0.04% (w/v) to scavenge residual oxygen. The medium pH was adjusted using filter-sterilized 1 M NaOH to 7.2. Manipulations of the SRB cultures were performed in anaerobic chamber (Bactron) under $N_2/CO_2/H_2$ (91:4:5) atmosphere and their growth were monitored with optical density using spectrophotometer at 600 nm. High-pressure incubations (15 MPa and 30 MPa) were performed in stainless steel pressure vessels (HiP) and a pump controller (Teledyne ISCO) was used to pressurize the stainless-steel pressure vessel using Milli-Q water. A compressible and heat-sealable ProAmpac's Kapak FoilPAK (VWR) which allows hydrostatic pressure transmission (pre-sterilized with 70% ethanol and dried), was used for culturing the SRB at elevated hydrostatic pressure.

3.2.2 Specimen preparation

Mild steel ASTM A131, grade AH36 (UNS K01806) was obtained from Ebenezer NDT Services Pte Ltd with a dimension of 20 mm (width) x 30 mm (length) x 4 mm (height). The mild steel coupons were sequentially abraded with P420 (46 µm), P800 (22 µm), and P2000 (10 µm) sandpaper on all sides, degreased with acetone and absolute ethanol, and dried with stream of N_2 gas. Epoxy resin (Epofix) was obtained from Electron Microscopy Sciences and was prepared by gently mixing the resin solution and hardener in 6:1 (w/w) ratio. Two milliliters of the mixture were dispensed into a mounting cup through a syringe to remove bubbles and the resins were allowed to cure overnight at room temperature. After curing, the epoxy coupons were polished with P800 and P2000 sandpaper on all sides, cleaned with ethanol and dried. Before the immersion test, both the mild steel and epoxy coupons were sterilized by ultraviolet (UV) light on both sides for 20 min each.

3.2.3 Bacterial samples preparation for proteomic analysis

The experiment setup is illustrated in Figure 2.1. Briefly, the incubations were initiated by inoculating *P. piezophilus* into FoilPaks containing 20 ml of DSMZ 195c medium at a final OD600 of 0.02. Each FoilPak contained one piece of mild steel coupon or two pieces of epoxy coupons and was incubated for 48 h at RT to allow initial biofilm formation. Afterward, 90% volume of the spent DSMZ195c medium was replaced by MOPS-ASW with 1 mM sodium lactate and the samples were pressurized to 0.1 MPa, 15 MPa, and 30 MPa accordingly to initiate the incubation simulating deep-sea condition (three mild steel samples and three epoxy samples at each pressure). The FoilPaks were retrieved after 72 h of incubation. Three technical replicates from each pressure were pooled to ensure sufficient biomass for proteomic analysis. The planktonic cells were harvested by centrifuging the pooled bulk medium at 6000 x *g* for 10 min at 4 °C. Pellets were washed once with ice-cold wash buffer (0.1 M citrate buffer pH 5, 0.3 M NaCl, 0.05 M EDTA, 5 mM Na-pyrophosphate, 0.005% tween-20) to remove iron particles, and washed once with ice-cold 1x PBS before freezing the pellets at -80 °C until protein extraction. To harvest the biofilm cells, the mild steel coupons (three pieces per pressure) and epoxy coupons (six pieces per pressure) were shaken in 20 ml ice-cold wash buffer for 15 min and sonicated in ElmaP sonicator at 37 kHz, 80% Pwr for 2 min to detach the corrosion products and biofilm. The supernatant, now containing the detached biofilm cells, was transferred into a new canonical tube and centrifuged at 6000 x *g* for 10 min at 4 °C. Pellets were washed once with ice-cold 1x PBS before freezing at -80 °C until protein extraction. The experiment was repeated three times to obtain independent biological replicates.

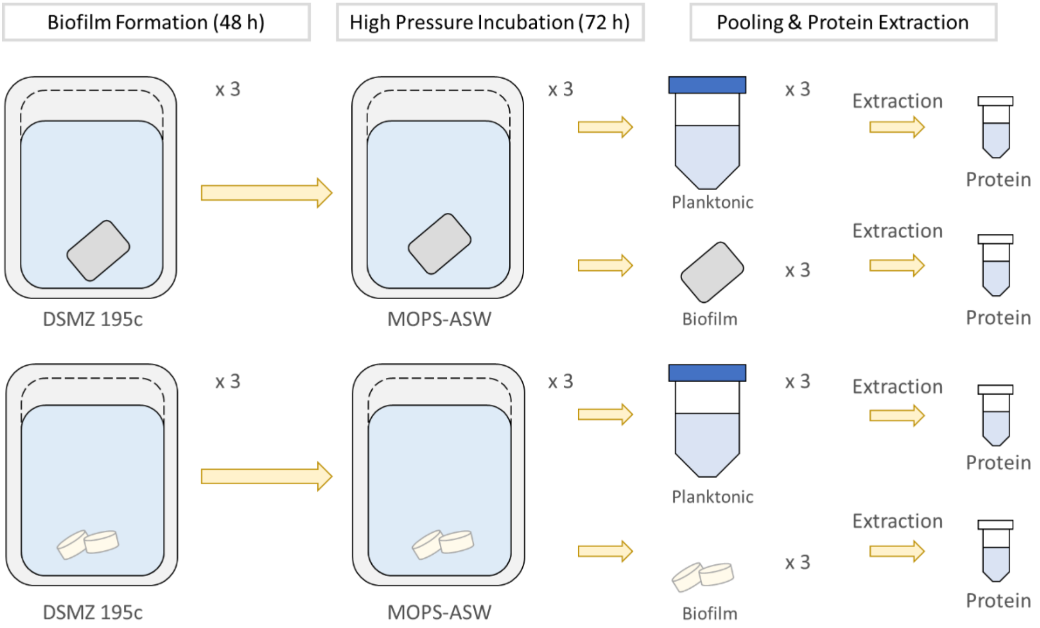

Figure 3.1. Schematic of the experiment workflow for total protein extraction. Each Foilpak contain one piece of mild steel coupon or two pieces of epoxy coupons. For each replicate, the planktonic and biofilm samples from three Foilpaks were pooled for protein extraction. The experiment was repeated for a total of three time for independent replicates.

3.2.4 Protein samples preparation

Cell pellets were resuspended in 0.5 ml lysis buffer (50 mM Tris-HCl, pH 8, 8 M Urea, 1 mM phenylmethylsulfonyl fluoride, PMSF) and incubated on ice for 30 min with intermittent vortex (Wiśniewski et al. 2009). Lysate was further disrupted using a probe sonicator (VibraCell CVX, 750W) on ice bath at 40% amplitude for 3 min at 10 s on-off intervals to increase lysis efficiency and shearing of genomic DNA to reduce the sample viscosity. To concentrate the proteins for analysis, 150 µl of 100% trichloroacetic acid was added to 450 µl of the crude lysate and the samples were incubated on ice for at least 60 min (Koontz 2014). The protein samples were centrifuged at 18000 x *g* at 4°C for 10 min and the supernatant was discarded. Protein pellets were washed twice in 0.8 ml ice-cold acetone, before air dried in a biosafety cabinet for 15 min. The precipitated proteins were reconstituted in lysis buffer without PMSF, and the concentration was measured using Pierce BCA Protein Assay Kit. Peptide samples for LC-MS/MS analysis were prepared as previously described (Guo et al. 2020). A total of 50 µg reconstituted proteins were reduced with 10 mM Tris (2-carboxyethyl) phosphine (TCEP) for 20 min followed by alkyalation with 55 mM chloroacetamide (CAA) for 30 min at room temperature in the dark. Seven volumes of the 100 mM triethylammonium bicarbonate buffer (TEAB) were added to the protein samples prior to the in-solution digestion of the proteins to dilute the urea. The protein samples were first digested with lys-C (1: 20 w/w) for 2 h, followed by a second digestion with trypsin (1: 40 w/w) overnight at room temperature. The digested peptide samples were desalted using HLB PriME 96-well C18 plate (Waters) and eluted with 250 µl of 65% acetonitrile (I), 0.1% formic acid (FA) buffer. The digested and desalted peptide samples were quantified using Pierce™ Quantitative Peptide Assays & Standards (Thermo Fischer Scientific). Two micrograms of the peptides were dried using a vacuum concentrator SpeedVac (Thermo Fischer Scientific) and reconstituted with 3% I, 0.1% acetic acid, and 0.06 trifluoroacetic acid (TFA).

3.2.5 Label-free mass spectrometry

LC-MS/MS and the subsequent analysis were prepared as previously described (Guo et al. 2020). Briefly, the reconstituted peptides were subjected to liquid chromatography coupled with tandem mass spectrometry (LC-MS/MS) analysis using an EASY-nLC™ 1200 system coupled to Orbitrap Fusion™ Lumos™ Tribrid™ Mass Spectrometer (Thermo Fisher Scientific). Peptide mixtures were separated using an EASY-Spray 75 μm × 50 cm column packed with PepMap C18, 3 μm, 100 Å (Thermo Fisher Scientific) at 50 °C and a flow rate of 300 nl/min. Mobile phase A (0.1% FA) and mobile phase B (0.1% FA in 95% I) were used for the peptide separation with the following gradients: 2−27% B for 45 min, 27−50% B for 15 min, 50−90% B for 5 min, and 90% B for 5 min. The separated peptides were analyzed with electron-spray potential of 2.1 kV and a full MS scan ranging from 350 to 1550 m/z was obtained at a resolution of 60,000 and a maximum injection time of 100 ms. The resolution of the higher collision-induced dissociation spectra was applied for fragmentation. Automatic gain control setting of 100% and 150% were applied to the full MS scan and the MS2 scan, respectively. Peptide identification was performed using data-dependent acquisition of MS2, and single and unassigned charged ions were omitted.

3.2.6 Proteome database search and analysis

Label-free quantification was carried out using Proteome Discoverer software (Thermo Fisher Scientific). The precursor tolerance and fragment ion tolerance were set as 20 ppm and 0.8 Da, respectively. Sequest was used for the database search, with the deamidation of asparagine and glutamine, and the oxidation of methionine were set at dynamic modifications whereas carbamidomethylation of cysteine was set as fixed modification. Protein identification was performed by matching searching the generated MS/MS spectra to the UniProt organism database of *Pseudodesulfovibrio piezophilus* and exported to RStudio for further analysis. Principal component analysis of each of the proteomic samples was performed by imputing the missing value (undetected proteins) in the samples with 0. Binary comparisons using the two-sided Welch Student's t-test were conducted. Enriched and depleted proteins were identified based on a p-value < 0.05 and a differential abundance fold change (relative to the inert material epoxy) of $\geqslant 1.5$ or ≤ -1.5, respectively (Supplementary Figures 4 – 8, Supplementary Tables 2 - 11). Pathway enrichment analyses were performed on the differentially abundant proteins in RStudio using clusterProfiler package and mapped to Kyto Encyclopedia of Gene and Genomes (KEGG) pathway database (Kanehisa et al. 2023, Wu et al. 2021).

3.3 Results

Proteomic analyses were conducted to study the physiologies of deep-sea SRB *P. piezophilus* incubated with mild steel (compared to epoxy coupon as an inert material control), from both planktonic and biofilm cells, and at 0.1 MPa, 15 MPa, and 30 MPa (3 hydrostatic pressures x 2 material types x 2 cell populations x 3 independent replicates = 36 proteomic samples). A total of 2295 proteins were identified in at least one of the sample/replicates and 1966 proteins were identified in at least half of the sample/replicate. The total proteomic profiles of the samples were separated into three distinct clusters on the PCA plot, where the biofilm from two materials formed two clusters separated from each other, whereas the planktonic populations from both materials were clustered together (Figure 3.2).

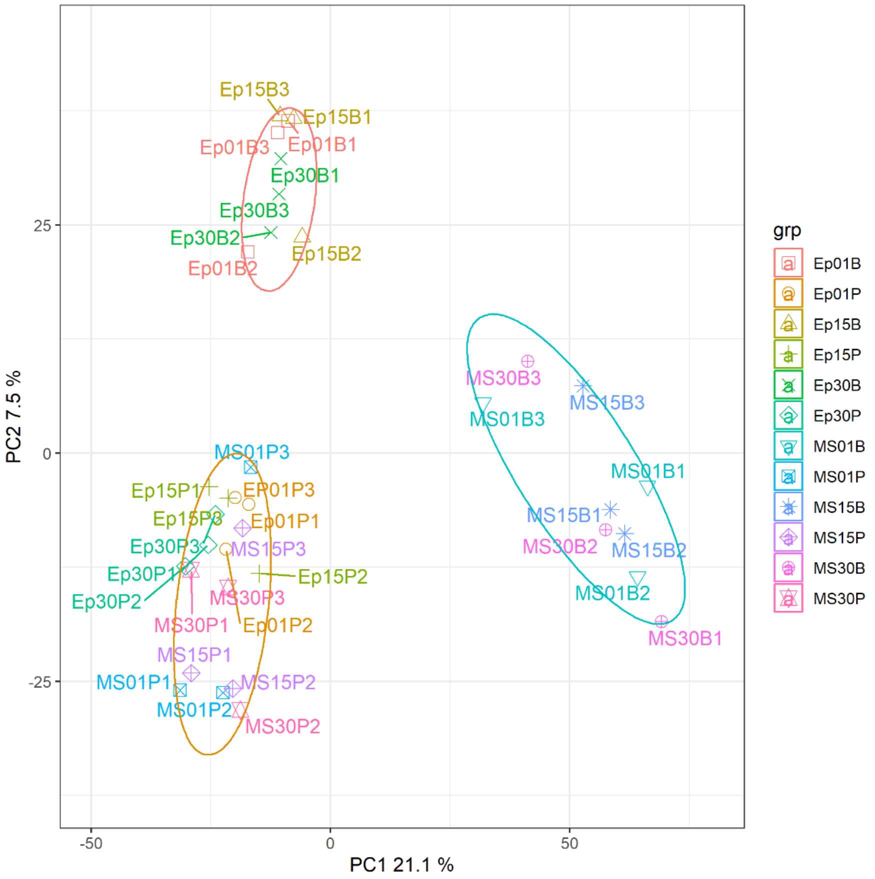

Figure 3.2. Principal component analysis of the proteomic profiles of *P. piezophilus* incubated with mild steel and epoxy coupons. MS = Mild steel, Ep = Epoxy; 01 = 0.1 MPa, 15 = 15 MPa; 30 = 30 MPa; P = Planktonic, B = Biofilm; 1, 2, and 3 = Replicate 1, 2 and 3, respectively. Ellipses were drawn to visually separate the data points with PC1<0, PC1>0, and PC2>20.

3.3.1 Differential abundant protein analysis

The differentially abundant proteins in the planktonic and biofilm population incubated with mild steel at 0.1 MPa, 15 MPa, and 30 MPa were identified using cut-off of fold change > |1.5| and *p*-value < 0.05 (relative to the inert material epoxy)

(Supplementary Figure 5 and 6). When incubated with mild steel, 48, 31, and 23 proteins were enriched whereas 44, 35, and 51 proteins were depleted in the planktonic population at 0.1 MPa, 15 MPa, and 30 MPa, respectively (Supplementary Tables 2, 3 and 4). More differentially abundant proteins were found in the biofilm population, with 107, 137, and 129 proteins enriched, and 276, 377, and 348 proteins depleted in the biofilm cells incubated with mild steel at 0.1 MPa, 15 MPa, and 30 MPa, respectively (Supplementary Tables 5, 6 and 7). A Venn diagram was plotted to show the number of overlapping proteins that are differentially abundant at 0.1 MPa, 15 MPa, and 30 MPa (Figure 3.3).

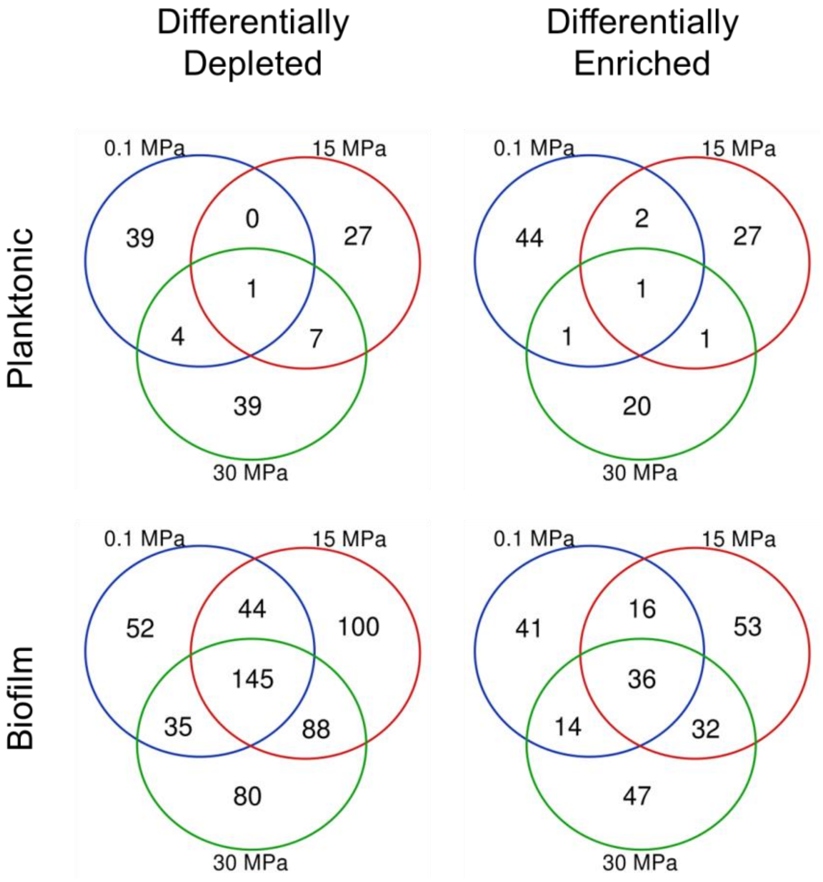

Figure 3.3. Venn diagram showing the number of differentially abundant proteins of *P. piezophilus* incubated with mild steel in the planktonic and biofilm population at 0.1 MPa, 15 MPa, and 30 MPa, respectively.

KEGG enrichment pathway analysis revealed that bacterial chemotaxis (dpi02030), two-component system (dpi02020), and flagellar assembly (dpi02040) were significantly enriched in the biofilm population at all three hydrostatic pressures tested (Figure 3.4). Oxidative phosphorylation (dpi00190) was significantly enriched at 0.1 MPa and 15 MPa, and ABC transporters (dpi02010) were significantly enriched only at 0.1 MPa (Figure 3.4). Many of the metabolism pathways such as biosynthesis of amino acids (dpi01230), biosynthesis of phenylalanine, tyrosine and tryptophan (dpi00400), carbon metabolism (dpi01200) and TCA cycles (dpi00020) were differentially depleted in the biofilm incubated with mild steel (Figure 3.5). While some of the pathways were statistically enriched/depleted in the planktonic population, there were relatively few proteins mapped to each of the pathways, therefore, was not further analyzed (Supplementary Table 12).

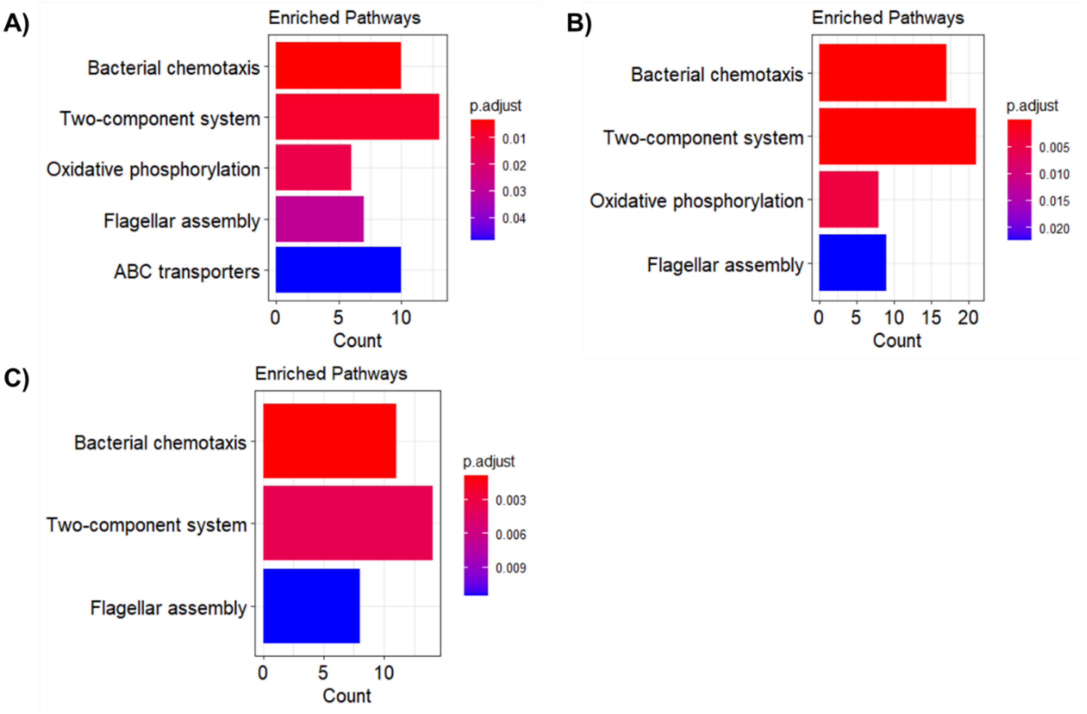

Figure 3.4. Pathway enrichment analysis of differentially enriched proteins in the biofilm population of *P. piezophilus* incubated with mild steel. The count and *p*-value of the enriched pathway at 0.1 MPa (A), 15 MPa (B), and 30 MPa (C) were shown.

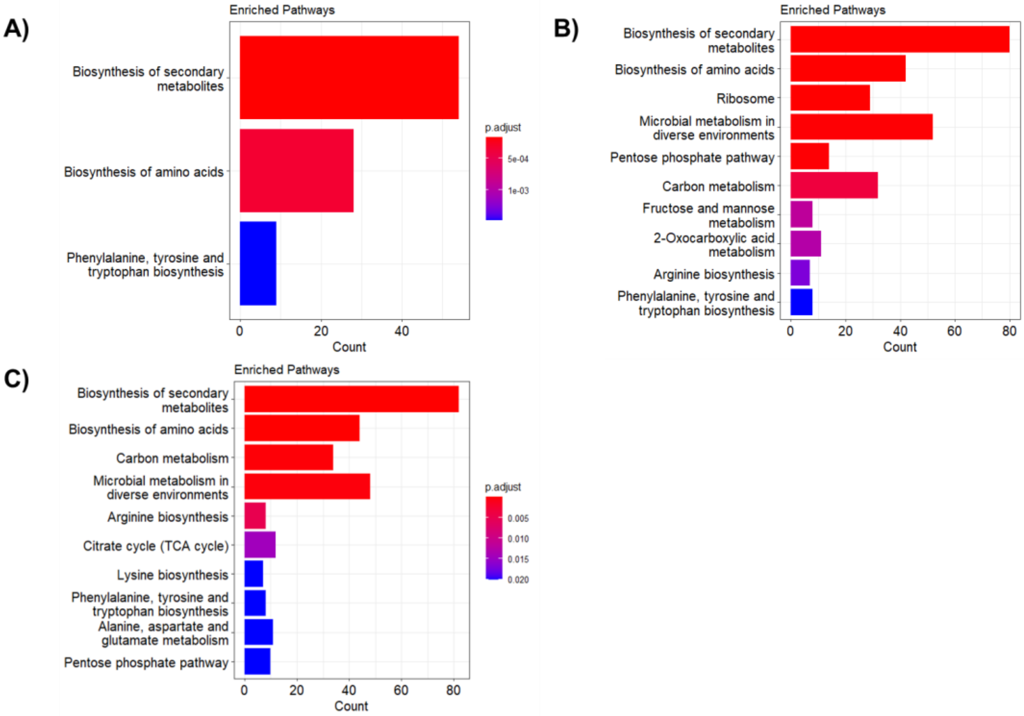

Figure 3.5. Pathway enrichment analysis of differentially depleted proteins in the biofilm population of *P. piezophilus* incubated with mild steel. The count and p-value of the enriched pathway at 0.1 MPa (A), 15 MPa (B), and 30 MPa (C) were shown.

3.3.2 Flagellar Motility were enriched in the *P. piezophilus* biofilm incubated with mild steel

Multiple proteins related to flagellar motility were enriched in the *P. piezophilus* biofilm incubated with mild steel (Supplementary Tables 5, 6, 7 and 13). These proteins include flagella assembly components (e.g., M1WXN9, M1WUY5, and M1WJ78) and several flagellar hook-associated proteins (e.g., M1WL21, M1WRE9, and M1WJJ2) as well as membrane protein MotA/TolQ/ExbB (M1WJ94). Along with the motility, chemotaxis sensors such as methyl-accepting chemotaxis sensors (e.g., M1WP26, M1WWC3, M1WK58 with Pas/Pac-sensor domain, and M1WYH8 with Cache-sensor domain), which transduced the environmental signal through CheA (M1WUB4), and CheW (M1WNQ0) were also enriched in the *P. piezophilus* biofilm incubated with mild steel. While some of these proteins were differentially expressed at different hydrostatic pressure, some of these proteins were commonly enriched at all three hydrostatic pressures tested, which include three flagellar component proteins, four methyl-accepting chemotaxis sensors, MotA/TolQ/ExbB proton channel, as well as CheA.

3.3.3 Energy-conservation pathway was enriched in the *P. piezophilus* biofilm incubated with mild steel

Oxidative phosphorylation is another highly enriched pathway and many proteins involved in the SRB electron transport chain were enriched in the *P. piezophilus* biofilm incubated with mild steel (Supplementary Table 5, 6, 7 and 13). At 0.1 MPa, three subunits of the electron transport chain complex I NADH-quinone oxidoreductase (M1WR22, M1WV01, and M1WP51), cytochrome C oxidase subunit 2 (M1WM78) as well as adenosine triphosphate (ATP) synthase subunit β (M1WRT9) were enriched (Supplementary Table 5). While the KEGG pathway analysis detected only aerobic electron transport chain proteins (dpi00190), several anaerobic respiratory complexes were differentially enriched at 15 MPa and 30 MPa (Supplementary Tables 6 and 7). These proteins including subunits of Rnf complex (M1WYD9 and M1WKW2 at both 15 MPa and 30 MPa; M1WN81 and M1WSN1 at 15 MPa only; and M1WND0 at 30 MPa only), Qmo complex subunit C (M1WK61, at both 15 MPa and 30 MPa), Qrc complex (M1WQS5 and M1WJG4, at 15 MPa only), transmembrane cytochrome (M1WPA1, at both 15 MPa and 30 MPa) as well as membrane-bound dissimilatory sulfite reductase complex subunit M (M1WXH5). Inorganic diphosphatase (M1WLF6) that regenerates ATP precursor phosphate was also highly enriched in the *P. piezophilus* biofilm incubated with mild steel at all three hydrostatic pressures tested (Supplementary Tables 5, 6 and 7). Both Rnf and NADH-quinone oxidoreductase receive reducing equivalents from the cytoplasm, in which Rnf reduces NAD^+ to NADH with ferredoxin whereas NADH-quinone oxidoreductase transfers the electrons from NADH to the membrane quinone pool (Wang et al. 2016). On the other hand, Qrc, DsrMKJOP, and Tmc complexes are believed to receive electrons from the periplasmic space (*cycA* for example, which is not differentially abundant in this study) and, directly or indirectly through the Qmo complex, transfer the electron back to the cytoplasmic DsrAB and DsrC for sulfate reduction. These membrane complexes are part of the electron transport chain in sulfate-reducing bacteria to establish proton/Na^+ gradient that power the ATP synthesis via ATP synthase (Price et al. 2014). However, the cytoplasmic dissimilatory sulfite reductase DsrA (M1WMP4, at 30 MPa only), DsrB (M1WKM5, at both 0.1 MPa and 15 MPa), and DsrC (M1WL82, at all three hydrostatic pressures) that involved in sulfate reduction were found depleted in the *P. piezophilus* biofilm incubated with mild steel (Supplementary Tables 5, 6, and 7). No membrane-bound or secreted cytochromes that may be involved in extracellular electron uptake were found to be differentially abundant.

3.3.4 Reduced biosynthesis pathway in *P. piezophilus* biofilm incubated with mild steel

Many of the proteins involved in various carbon metabolism pathways such as TCA cycle and pentose phosphate pathway, were found depleted in the *P. piezophilus* biofilm when incubated with mild steel (Figure 3.5). Biosynthesis of various amino acids were also differentially depleted in the biofilm, and an overall reduction in the protein synthesis were also observed where 12, 29, and 15 ribosomal proteins were differentially depleted at 0.1 MPa, 15 MPa, and 30 MPa, respectively (Figure 3.5, Supplementary Tables 5, 6, and 7). Instead, the biofilm potentially acquires amino acid from the environment, as several of the amino acid transporter (e.g., M1WUG6, M1WUG6, and M1WSX2) and dipeptide ABC transporters (M1WJS0) and metalloproteases (e.g., M1WP62, M1WUF4, and M1WP62) were also differentially enriched in at least one of the hydrostatic pressures tested (Supplementary Tables 5, 6, and 7). Carbon starvation protein CstA (M1WSP1), a protein that induces peptide utilization in *Campylobacter jejuni*, was found enriched in the *P. piezophilus* biofilm incubated with mild steel at both 15 MPa and 30 MPa (Supplementary Tables 6 and 7).

3.3.5 Membrane adaptation in *P. piezophilus* biofilm incubated with mild steel

A substantial portion of the enriched proteins in the *P. piezophilus* biofilm incubated with mild steel were predicted to be membrane-associated according to GO annotation in the Uniprot database and were predicted to be involved in (apart from the electron transport complexes) nutrient/ions exchange functions, cell envelope maintenance and osmoregulation (Supplementary Tables 5, 6 and 7). Some of the membrane proteins involved in nutrient acquisition and inorganic ions exchange which include, for example, amino acid ABC transporter for polar amino acids (e.g., M1WUG6, M1WUS8, and M1WLG9), glutamine (M1WJG3), and branched-chain amino acids (M1WSX2), sulfate exporter family transporter (M1WMA7), nickel transport complex (M1WR57), zinc transporter (M1WTI8), and molybdenum transport system permease (M1WSJ9). There are also several putative ABC transporters (M1WM46), outer membrane trimeric porin (M1WJL4), and efflux proteins (M1WSG8 and M1WUH3) that their transport substrate were not known. PEP-CTERM protein-sorting domain-containing protein (M1WU68, also enriched in the planktonic fraction of mild steel samples), inner membrane protein ybhL (M1WKP6), membrane protein insertase YidC (M1WLY2), as well as several membrane lipoproteins (M1WQ50, M1WX13, and M1WTG5) that serve to maintain the membrane integrity were also found enriched. Glucans biosynthesis protein G (M1WLT9) and YggT family protein (M1WUM6) were involved in osmoregulation. There are also a number of extracellular ligand-binding receptors (e.g., M1WUA2, M1WS10, and M1WLE6) which their cognate ligand were not known but were consistently enriched in the *P. piezophilus* biofilm incubated with mild steel.

3.3.6 Differential abundant proteins in respond to hydrostatic pressure

There is only a mild effect of hydrostatic pressure on the proteomic profile of *P. piezophilus* samples incubated with mild steel. Most of the proteins that are differentially abundant when incubated with mild steel at 15 MPa and 30 MPa but not at 0.1 MPa were not statistically significantly enriched when compared directly to 0.1 MPa (Supplementary Figure 7 and 8). There are 26 and 46 proteins that were identified to be differentially abundant at 15 MPa and 30 MPa, respectively in the planktonic population from samples incubated with mild steels (Supplementary Tables 8 and 9). On the other hand, only nine and sixteen proteins were identified to be differentially abundant in the *P. piezophilus* biofilm incubated with mild steel at 15 MPa and 30 MPa, respectively (Supplementary Tables 10 and 11). Of which, a response regulator receiver protein (M1WJ48) was found commonly enriched at both hydrostatic pressures (Supplementary Tables 10 and 11). Four proteins, ATP-dependent Clp protease ATP-binding subunit ClpA (M1WLB4), leucine carboxyl methyltransferase (M1WLU5), N-acylneuraminate-9-phosphate synthase (M1WXS5) and a transcriptional regulatory protein zraR (M1WQU8) were commonly enriched at both 15 MPa and 30 MPa whereas an ABC transporter related protein (M1WLH9), oxidoreductase FAD/NAD(P)-binding domain protein (M1WQP9) and a flagellin protein (M1WK85) were commonly depleted in the planktonic population at both 15 MPa and 30 MPa (Supplementary Tables 10 and 11).

3.4 Discussion

MIC induced by sulfate-reducing bacteria has been studied extensively, yet there is very limited understanding of the underlying physiology that contributes to the MIC. In the previous chapter, it was demonstrated that the deep-sea SRB *P. pieozophilus* induced a more severe pitting corrosion at elevated hydrostatic pressures. To correlate the MIC phenomenon with the physiological changes at elevated hydrostatic pressure, the proteomic changes in *P. piezophilus* when incubated with mild steel at 0.1 MPa, 15 MPa, and 30 MPa was investigated.

The electron transport pathway In SRB is complex and involves electron transfer between cytoplasm, cell membrane, and periplasm (Price et al. 2014). Recently, Chatterjee et al. identified an extracellular *c*-cytochrome along with several other electron transfer proteins were enriched in the highly aggressive *D. ferrophilus* cells when incubated with a mild steel coupon which is potentially crucial for the EET mechanism (Chatterjee et al. 2021). While similar extracellular cytochrome protein was not found enriched in this study, *P. piezophilus* biofilm exhibits active energy production, with increased electron transport chain (ETC) proteins such as Rnf, Qmo, Qrc, the membrane-bound DsrMJKOP complex, and the Tmc complex (Figure 3.6) These findings strongly suggest the involvement of the energy-active biofilm population in MIC. NADH-quinone oxidoreductase is seldomly reported and is poorly characterized in genus *Desulfovibrio* whereas Rnf, Qmo, and Tmc were found crucial for *Desulfovibrio alaskensis* to grow on H_2, which may generated through the abiotic corrosion of mild steel (Wang et al. 2016). The enrichment of Rnf, Qrc, Tmc, and membrane-bound DsrMJKOP complex hence indicates that H_2 utilization may play an important role in sustaining ATP production in the *P. piezophilus* biofilm incubated with mild steel. No lactate or pyruvate dehydrogenase/oxidoreductase proteins (as 1 mM lactate was used as a carbon source in this study) were found enriched suggest that the energy production is not driven by the lactate provided in the test medium. At the same time however, the hydrogenases and formate dehydrogenase were either unchanged (periplasmic hydrogenase, Hyn), differentially reduced (periplasmic hydrogenase, Hyd), or inconclusive due to lacking sufficient detection from the mass-spectrometry in the replicates (membrane-bound hydrogenase Ech and Coo, and formate dehydrogenase Fdh). Despite the sulfate was supplied in excess relative to the electron donor, the depletion of cytoplasmic dissimilatory sulfite reductase DsrB and DsrC that are part of the sulfate reduction pathway suggest that an alternative path of electron flow was utilized for energy production (Figure 3.6). The lack of any membrane-bound or secreted cytochrome that are differentially abundant or potentially involved in the extracellular electron uptake indicates that electric-MIC (EMIC) is not the primary MIC pathway in *P. piezophilus*.

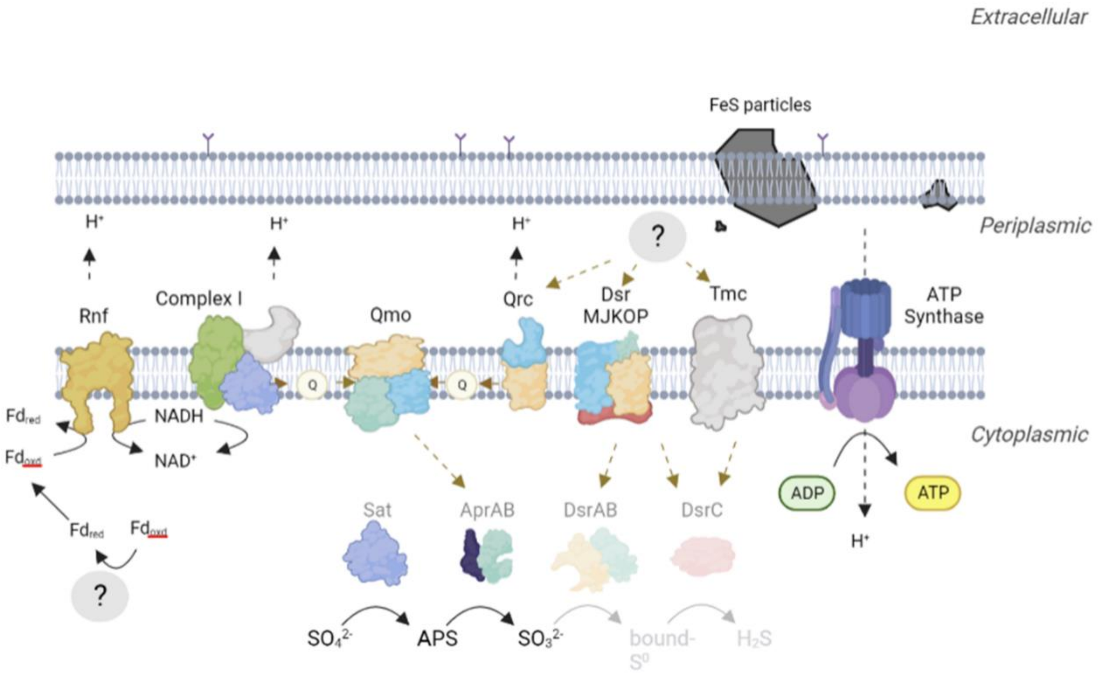

Figure 3.6. Schematic diagram summarizing the differentially enriched proteins involved in the energy-conservation pathway in the *P. piezophilus* biofilm incubated with mild steel. An unknown cytoplasmic protein/pathways that produce reduced ferredoxin for Rnf complex, and an unknown periplasmic electron sources that transfer electron to Qrc, Qmo and Tmc complex remains unidentified in this study. The cytoplasmic sulfate reduction pathway was shown where the Sat and AprAB proteins were not differentially abundant but were indicated to demonstrate the potential electron flow whereas DsrAB and DsrC were differentially depleted. The schematic was created with Biorender.com. Q = quinones, Fd = ferredoxin.

Despite the increased abundance in the energy production pathway, the proteomic results suggest that *P. piezophilus* biofilm incubated with mild steel was in fact metabolically suppressed, potentially due to the nutrient-limitation and environmental stresses. Many carbon metabolism and ribosomal proteins were differentially depleted in the *P. piezophilus* biofilm incubated with mild steel (Supplementary Tables 5, 6 and 7). The ribosome concentration have been reported to be tightly linked to the growth rate as well as the activation of starvation reaction (Bosdriesz et al. 2015, Rasmussen et al. 2013). The depletion of ribosomal proteins hence indicates that the biofilm cells entered a maintenance state under the oligotrophic test condition despite the apparent enrichment of the energy production pathway. The reduced abundance of amino acid biosynthesis proteins can be compensated by the enriched amino acid ABC transporter to scavenge amino acids from the environment (probably from membrane-compromised, or lysed cells). Yet, the reduction in ribosomal proteins suggests that increased amino acid uptake was not directed for protein synthesis (Figure 3.7). The ability to scavenge a wide range of organic compounds, including amino acids, is crucial for the deep-sea microbes to survive in the electron donor-limiting environment (Li et al. 2015b, Torres-Beltrán et al. 2021). For SRB, growth supported by amino acid has been demonstrated in *Desulfovibrio aminophilus* in which the amino acids can be fermented (serine, glycine, cysteine, and threonine) or coupled to sulfate reduction (alanine, aspartate, leucine, isoleucine, valine, and methionine) (Baena et al. 1998). Similar metabolism strategy has been reported in *Clostridium sticklandii* where this bacteria can utilize amino acids via fermentation and Stickland reaction (in which an amino acid pair where one was used as an electron donor and another as an electron acceptor) and coupled to energy conservation through Rnf complex (Fonknechten et al. 2010). While both the energy conservation pathway (including Rnf subunits) and amino acids uptake proteins were found enriched in *P. piezophilus* biofilm incubated with mild steel, it is difficult to conclude if a similar amino acid utilization pathway exist in this bacterium as the pathway is poorly characterized among the SRB.

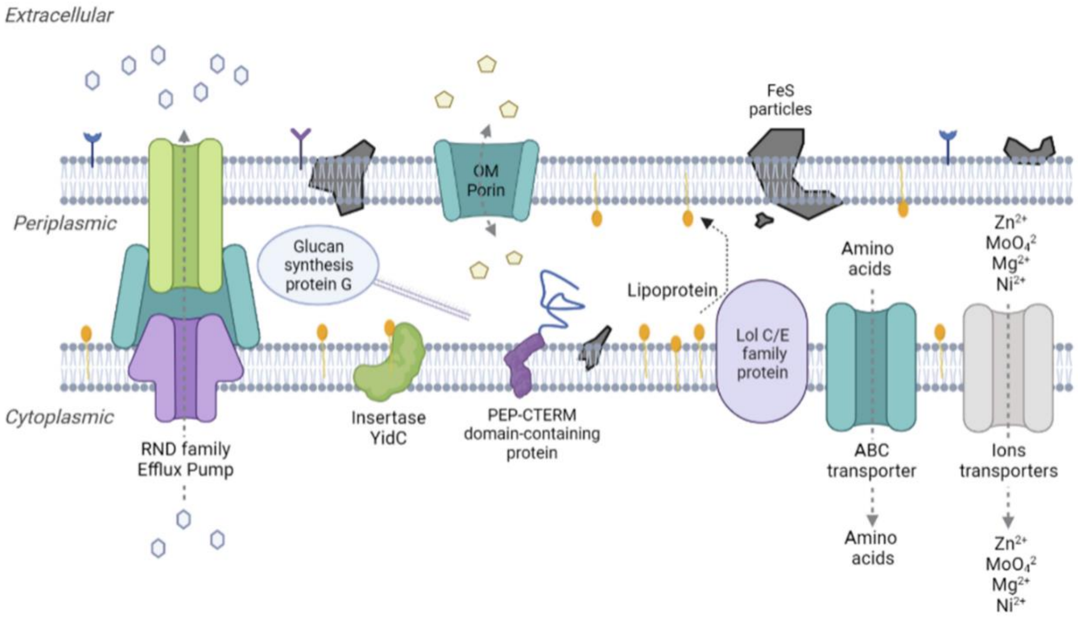

Figure 3.7. Schematic diagram summarizing the differentially enriched proteins involved in the membrane adaptation and nutrient/ions acquisition under corroding environment in the *P. piezophilus* biofilm incubated with mild steel. The schematic was created with Biorender.com.

Many of the differentially abundant proteins were related to membrane homeostasis, suggesting that the corroding mild steel might impose envelope stress on the biofilm (Figure 3.7). RND efflux transporter has been reported to counteract the heavy metal toxicity which may be present in the corroding environment (Alvarez-Ortega et al. 2013). At the same time, zinc, nickel, and molybdenum were actively transported, which may serve as cofactors for many of the enzymes, for example, the metalloprotease and hydrogenases (Fukasawa et al. 2011, Ogata et al. 2016). Excess molybdate however may inhibit the growth of SRB by jamming the sulfate reduction pathway due to its structural analogues to the sulfate, therefore, its concentration required to be tightly regulated by the transporter proteins (Nair et al. 2015). In Chapter 2, the SEM micrograph shows that *P. piezophilus* formed a thick biofilm intermixed with inorganic minerals (i.e., corrosion products) on the mild steel (Figure 2.11). In addition, it was previously reported that when *Desulfovibrio vulgaris* incubated in the presence of ferrous ions, FeS nanoparticles were formed both on the cell surfaces and intracellularly, causing periplasm enlargement while presumably serves as a conduit for extracellular electron transfer (Deng et al. 2020). These observations suggest that the corroding environment may impose envelope stress on the biofilm cells and compromising of membrane integrity. Here, an increased abundant in a number of membrane lipoproteins and membrane remodeling proteins such as membrane protein insertase and LolC/E family transporter for outer membrane lipoprotein trafficking was observed, which is potentially required to maintain the cellular integrity under such environments (May Kerrie et al. 2019, Sharma et al. 2021).

Flagella have been previously found to be the main structural component of biofilm in *D. alaskensis* and *D. vulgaris* (Clark et al. 2007, Krumholz et al. 2015). An increased abundance of a number of flagella components and chemotaxis proteins was observed in *P. piezophilus* biofilm incubated with mild steel (Figure 3.8). It was postulated that these protein filaments serve as an anchor to the SRB biofilm and the biofilm formation can be prevented by proteases treatment (Clark et al. 2007). At the same time, *Desulfovibrio* chemotaxis has been demonstrated to respond to a variety of stimulus such as different organic carbons, sulfate (and other sulfur electron acceptor), sulfide, and even ferrous ions (Eschemann et al. 1999, Li et al. 2022a, Sass et al. 2002). The corroding environment consists of rather diverse microenvironments (e.g., metal ions, electron donor/acceptors, and redox gradients), in which motility may be needed for the bacteria to establish itself in a niche environment and escape mineralization. In fact, point breakages were often observed in the thick corrosion products/biofilm layer of *P. piezophilus* in the SEM micrograph (Figure 2.11). In contrast to fracture cracks which result from the dehydration step or during SEM imaging, these point breakages resemble void spaces left by detached cells and were not observed in the samples incubated at 30 MPa or with other SRB (Figure 2.11). Unlike the highly corrosive SRB such as *D. ferrophilus*, incubation with *P. piezophilus* does not lead to significant weight loss of the mild steel but rather causes micron-size pitting on the surface after 14 days of incubation (Figure 2.9). These localized corrosion attacks could have resulted from the disruption of the protective iron sulfide layer due to bacterial motility. Confirmation with fluorescence microscope might provide further insight, however, is proven to be difficult due to the presence of a thick layer of corrosion products and the need for maintenance of anoxic conditions during imaging to prevent rusting and iron sulfide oxidation.

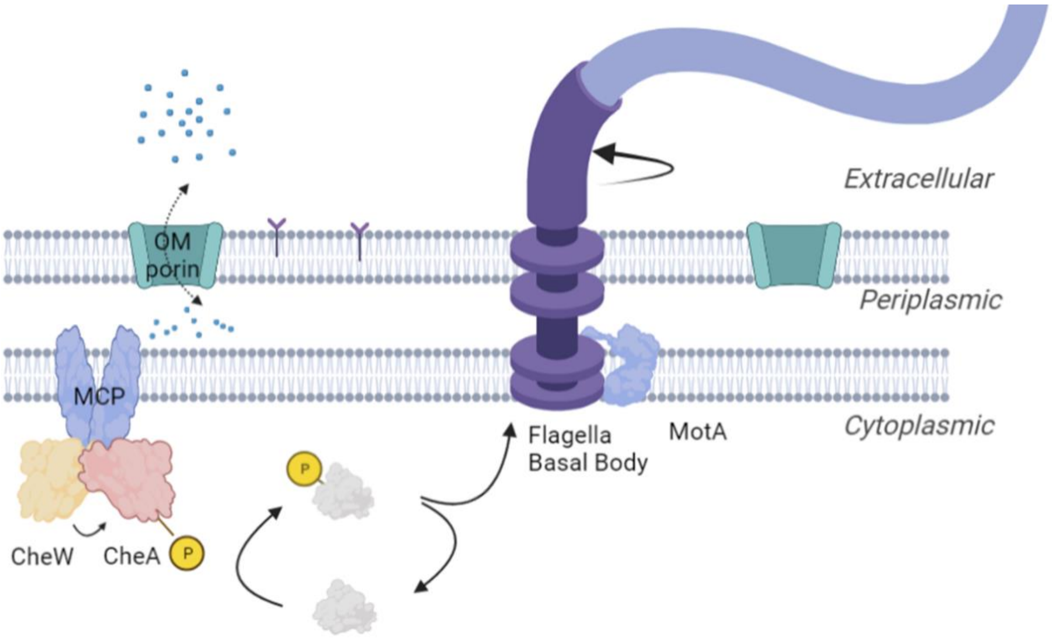

Figure 3.8. Schematic diagram summarizing the differentially enriched proteins involved in the flagellar motility in the *P. piezophilus* biofilm incubated with mild steel. The schematic was created with Biorender.com.

While incubating with mild steel resulted in many differentially abundant proteins, hydrostatic pressure alone has little impact on the *P. piezophilus* proteomic profile (Supplementary Figures 7 and 8). This seems to contradict with the findings from Chapter 2 where *P. piezophilus* induced a more severe pitting corrosion at elevated hydrostatic pressure (Figure 2.10). It was also previously found that *P. piezophilus* cope with the elevated hydrostatic pressure by accumulating glutamate intracellularly and the transcripts of glutamate synthase as well as the uptake gene were upregulated at elevated pressure in the planktonic culture of *P. piezophilus* grown in lactate/thiosulfate medium (Amrani et al. 2014). The corresponding proteins, however, were not found to be differentially abundant with increased hydrostatic pressure in this study. Other than serving as “piezolytes” that helps with maintaining the osmolarity at elevated hydrostatic pressure, glutamate is a central metabolite of carbon and nitrogen pathway to the cells and its accumulation requires a significant allocation of organic carbon (Commichau et al. 2008). Therefore, it may not be feasible for the cells to synthesize and accumulate glutamate under the carbon-limited test condition used in this study. The failure to identify potential MIC proteins that are differentially abundant at 15 MPa and 30 MPa suggests that the increased pitting severity may not be associated with protein abundance but rather may lie in the changes of protein activities. Hydrostatic pressure has a complex effect on protein via affecting reaction kinetics and thermodynamics, as well as adversely impact on protein-protein interactions which destabilizes the protein complexes (Gross and Jaenicke 1994). Piezophilic adaptations allowed the proteins from deep-sea bacteria to retain or increase activity at elevated hydrostatic pressure (up to a threshold) as compared to the homolog proteins from their counterpart from atmospheric pressure (Ichiye 2018). The coding sequence of *P. piezophilus* has a substantial number of amino acids substitutions (mainly replaced by alanine, histidine, and arginine) compared to other SRB which may be linked to the piezophilic adaptation of the proteins in this bacteria (Pradel et al. 2013). This adaptation at the genomic level may contribute to the increased protein activity and results in the increased pitting severity at elevated hydrostatic pressure as observed in Chapter 2 (Figure 2.10). Similarly, no membrane proteins were consistently enriched under high hydrostatic pressure conditions, despite the important role that membrane adaptation plays in coping with a high-pressure environment. Therefore, the *P. piezophilus* may cope with the increased hydrostatic pressure primarily through modifying the acyl chain length (alternatively, saturation and/or branching level) of the membrane fatty acid to maintain membrane fluidity as previously described by Khelaifia (Khelaifia et al. 2011).

3.5 Conclusion

While identifying the physiological changes under a corroding environment could offer valuable insights into MIC mediated by deep-sea sulfate-reducing bacteria, there has been limited research on this aspect in the past. Many MIC studies claiming EMIC proposed that SRB may benefits from a corroding metal due to the direct electron uptake (Gu et al. 2019, Kato 2016). However, the findings here suggest that the corroding environment actually represents a challenging condition to the SRB cells, forcing membrane adaptations to cope with the envelope stress imposed by the corrosion products and FeS particles. Flagella may be important for biofilm formation and settlement in niche micro-environments and its involvement in the MIC required further confirmation. Interestingly, the *P. piezophilus* biofilm incubated with mild steel was not energy-starved despite incubated in a carbon-limiting test condition, as evident by differential enrichment of electron transport complexes and ATP synthase. At the moment, it is unclear if the energy production is directly linked to the MIC but warrants further investigation. The increased energy production could be fueled by H_2 released from the abiotic corrosion or scavenging amino acids from lysed cells. While EMIC theory has attracted attention in the field of MIC, no indication of EMIC was found in this proteomic study as no extracellular electron transfer conduits (e.g., secreted cytochrome and heme or cysteine-rich proteins) were found to be differentially regulated in *P. piezophilus* when incubated with mild steel. This highlights that EMIC may not be a widespread mechanism in SRB but rather, some SRB may play an indirect role in causing MIC through H_2 utilization or inducing local breakage in the protective FeS layer during the dispersal/relocation of the motile cells. To our surprise, hydrostatic pressure has a minor impact on the overall proteomic profile, despite a worsened MIC outcome being observed when tested under the same condition. This suggest that protein activity rather than protein abundance could be the underlying cause of the increased pitting corrosion at elevated hydrostatic pressure. In summary, this proteomic study provides valuable insights into the physiology of deep-sea SRB *P. piezophilus* under corroding environments and in simulated deep-sea environments. The findings from this study shed light on the MIC physiologies of SRB in simulated deep-sea environment which is crucial for developing proper mitigation strategy against deep-sea MIC. Nevertheless, further investigation on more deep-sea SRB and/or shallow-water marine SRB at elevated hydrostatic pressure will undoubtedly provide a more holistic understanding of the mechanism and progression of deep-sea MIC.

Chapter 4

Exploring a 10-years deep-sea MIC via an enrichment culture approach: MIC characterization of a microbial consortium from a corroding mooring chain from 1988 m depth

4.1 Introduction

Deep sea represents not only a unique environment for material corrosion but also hosts a unique microbial ecosystem (Corinaldesi 2015). To thrive in this extreme environment, microbes developed unique adaptations to deal with the oligotrophic as well as high hydrostatic pressure conditions of the deep sea (Kaur et al. 2022). While microbiologically-influenced corrosion (MIC) is relatively well-studied in terrestrial and marine settings, there is very little known about deep-sea MIC. In Chapter 2, the MIC induced by both shallow-water and deep-sea SRB were investigated under simulated deep-sea condition. While the study provided evidence of the occurrence of deep-sea MIC, it oversimplifies the complexity of MIC in the field, which almost exclusively involves multi-species microbial communities that are under the influence of interspecies interaction, cooperation, and competition. Several dual species MIC studies have demonstrated that the outcome of MIC involving SRB could be complicated by the presence of other bacteria, resulting in either an enhancement or inhibition of the MIC, depending on the interacting partner involved (Liu and Cheng 2020, Lv et al. 2022).

Early studies of deep-sea corrosion have been conducted by deploying materials to the fields or by inspecting the corrosion of historical shipwrecks. While these studies provide insights into the environmental impact (e.g., oil spills) on the overall corrosion, the description of MIC is often observational (Mugge et al. 2019, Reinhart 1976, Venkatesan 2005). For example, rusticles are stalagmites-like corrosion products often found on corroding shipwrecks in the deep sea and are attributed to the iron extraction activity of iron metabolizing bacteria (Little et al. 2014). Yet, such claims remain questionable as those corrosion could also be explained by abiotic factors (Melchers 2021). As microbes are ubiquitous in marine environments, diagnosing MIC in the field, therefore, requires careful interpretation. The advancement of sequencing technology in recent years has encouraged environmental microbiome studies, yet little has been explored on the deep-sea corrosion microbiome.

From the limited studies available, it was demonstrated that the microbial communities from corroding sites were altered from the surrounding environment (Hamdan et al. 2021, Mugge et al. 2019, Rajala et al. 2022). As an example, Rajala et. al studied on a corroding mooring chain link that has been immersed in deep sea for 10 years and discovered a microbiome that was enriched in sulfate-reducing *Desulfovibrio* and sulfur-disproportionating *Desulfocapsa* that was distinct from the surrounding sediments. The author therefore proposed that sulfur cycling could be the main mechanism that drives the MIC of the mooring chain (Rajala et al. 2022). However, whether the sulfur-cycling microbiome (or the microbiome as a whole) are responsible for the MIC or just colonizing the metal surface is unknown due to the lack of control samples (a common limitation of field study). To validate the hypothesis, I have established enrichment cultures from the mooring chain as well as the sediment samples collected during the expedition to study their MIC behaviors in a more controlled experiment setup that simulates the deep-sea environment. In parallel to the corrosion assessment, the microbial activity and community composition were also evaluated to provide insights into the potential MIC microbes as well as to elucidates the underlying mechanisms contributing to corrosion..

4.2 Materials and Methods

4.2.1 Test medium preparation

A low-nutrient simulated seawater medium (designated as modified MOPS-ASW) that was modified from the MOPS-ASW used in Chapter 2 was used in this study for both culturing deep-sea enrichment cultures as well as conducting immersion tests. Briefly, the basal medium NCMA medium 1 artificial seawater (see Chapter 2.2.3 for recipe) was supplemented with 40 mM MOPS and oligotrophic medium R2A (at 20% strength). Volatile fatty acids acetate, lactate, and formate were added at 2 mM each. R2A was included at a reduced strength as it has been previously shown to support the growth of a diverse range of deep-sea microbes from the Mariana Trench, while volatile fatty acids were added to facilitate the growth of heterotrophs utilizing terminally degraded carbon sources (Glombitza et al. 2019, Zhao et al. 2020). After autoclave sterilization, the medium was sparged with N_2/CO_2 (95:5) gas, and the medium pH was adjusted to 7.8 using anoxic NaOH solution in anaerobic chamber.

4.2.2 Test specimen preparation

Mild steel ASTM A131, grade AH36 (UNS K01806, dimension = 10 mm x 10 mm x 2 mm) were obtained from Ebenezer NDT Services Pte Ltd, and CDC biofilm reactor disc polycarbonate coupons (12.7 mm diameter, 3.8 mm thickness) were obtained from Biosurface Technologies Corporation. Both the mild steel coupons and polycarbonate coupons were sequentially abraded with P420 (46 µm), P800 (22 µm), and P2000 (10 µm) sandpaper on all sides to standardize the surface roughness. The coupons were degreased with acetone and absolute ethanol and dried with a stream of N_2 gas. The initial weight of the mild steel coupons was obtained using XP2U weighting scale (Mettle Toledo) to a precision of ± 0.01 mg for weight-loss measurement. Before the corrosion test, coupons were sterilized by ultraviolet (UV) light on both sides for 20 min each.

4.2.3 Deep-sea enrichment cultures

Deep-sea samples, a corroding mooring chain link deployed for 10 years, and a sediment core from a nearby area were previously collected from Japan Sea at 1988 m depth during the KR18-15 expedition (Dive #812, Coordinate = 24° 31.3′ N, 126° 09.9′ E) in 2018 and stored immediately in a -80°C freezer (Rajala et al. 2022). Upon receiving in the lab, the corrosion crust of the mooring chain was scrapped for analysis and the remaining was aliquoted into cryotubes which were stored at -80 °C. On Nov 2022, the frozen samples were retrieved and ~0.5 g of mooring chain crust and sediment core were inoculated into 20 ml of modified MOPS-ASW each, under anoxic condition. The enrichment cultures were incubated in ProAmpac’s Kapak FoilPak (VWR) and pressurized to 15 MPa in a stainless-steel pressure vessel (HiP) with a pump controller (Teledyne ISCO). The incubation was initially performed at 4°C to mimic the deep-sea temperature. However, only slight growth was observed after > 30 days of incubation. Therefore, subsequent enrichment and test incubation were performed at room temperature. The enrichment cultures, now designated as 812MC (from the corroding mooring chain crust) and 812Sd (from the sediment core sample), were maintained regularly by transferring into fresh medium (50% v/v) every two weeks to dilute away the iron and sediment particles from the initial samples, as well as to obtain a larger volume of culture for the experiment. For each enrichment culture, a total of four parallel cultures of 50 ml each were obtained at transfer #5, which three of the cultures will be used as three biological replicates for the subsequent immersion test, and the remaining one culture was used to prepare glycerol stock and the continuation of the cultures.

4.2.4 Semi-continuous immersion test

The corrosion immersion tests were conducted in a semi-continuous incubation method to maintain an active microbial population during the test period. This is achieved by replenishing part of the test medium (25%) with fresh medium weekly, up to 28 days. This ensures a low (5% R2A strength and 0.5 mM for each of the volatile fatty acids) but consistent nutrient supply to the enrichment cultures that prevents the overgrowth of fastidious microbes and allows us to conduct MIC tests for a longer duration. The immersion test was prepared by diluting each replicate of the enrichment culture five times into fresh modified ASW medium, and distributed into four FoilPaks, two of which contained four pieces of AH36 mild steel coupons and two containing four pieces of polycarbonate coupons. In brief, a total of three biological replicates were prepared for each type of coupon per enrichment culture, and each biological replicate consists of two FoilPak (technical replicates) incubated with four mild steel or four polycarbonate coupons. After mixing, the bulk liquid was sampled for pH measurement (4 ml), iron assay (1 ml), sulfate assay (1 ml), sulfide assay (1 ml), as well as collecting planktonic fraction for DNA extraction (8 ml). The remaining volume after the initial sampling (week 0) was 60 ml. The FoilPaks were heat-sealed twice using impulse sealer before incubating at 15 MPa at room temperature.

Figure 4.1 shows the experiment workflow of the semi-continuous immersion test. The samples were depressurized and retrieved weekly for media replacement (15 ml, or 25% volume) with fresh medium (on Week 1, 2 ,3, and 4) inside the anaerobic chamber. The spent medium was used for DNA extraction to determine the planktonic microbial community composition (8 ml), sulfate and sulfide measurement (1 ml), iron measurement (1 ml, acidified to 1% HCl), and pH measurement (4 ml). On week 2 and week 4, four mild steel coupons and polycarbonate coupons were collected from each biological replicate for corrosion assessment (mild steel coupons only, one piece per replicate), electron microscopy (mild steel coupons only, one piece per replicate), and DNA extraction to determine the biofilm microbial composition (two pieces per replicate for mild steel coupons, and three pieces per replicate for polycarbonate coupons).

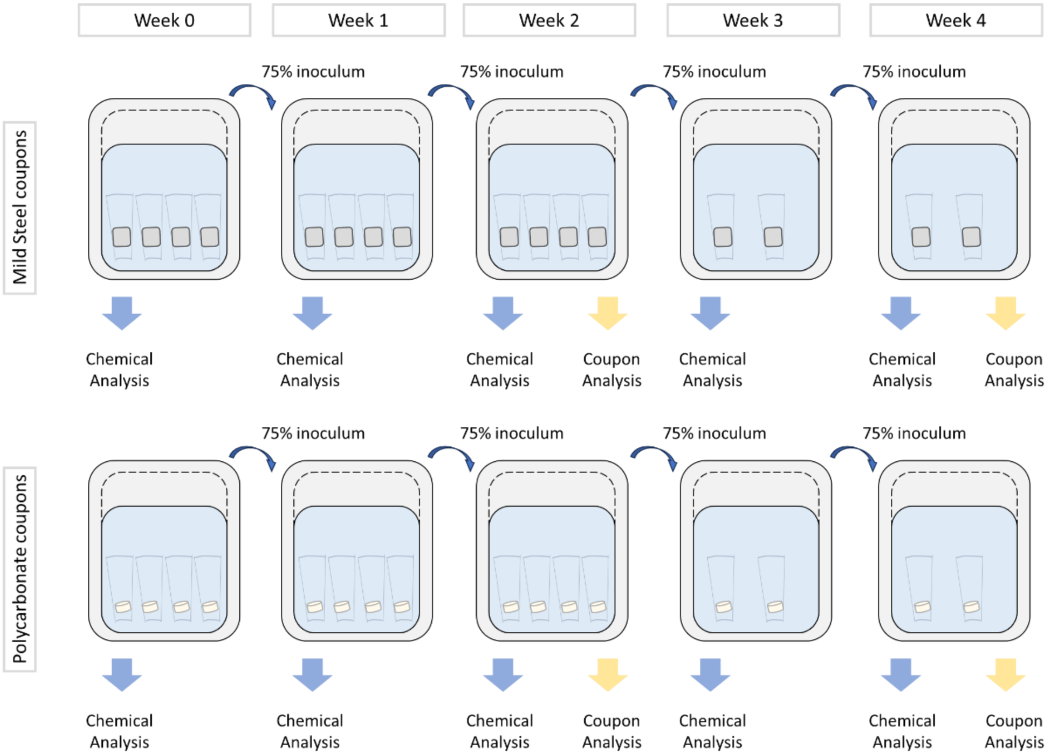

Figure 4.1. Schematic of the semi-continuous immersion test. Each samples contain four pieces of mild steels or polycarbonate coupons incubated in sterile artificial seawater, or with 812MC, or with 812Sd enrichment culture. Every 7 days, 25% of the spent medium will be replaced by fresh medium. Water samples were collected weekly for chemical analysis while the coupons were collected for analysis on week 2 and week 4.

4.2.5 Corrosion assessment

Before the immersion test, the mild steel coupons were weighted on a microbalance (Mettle Toledo XP2U) to obtain the initial weight of the test coupons. The coupons for weight loss measurement were submerged in 1% HCl with 0.35 g/L hexamethylenetetramine and gently sonicated in ElmaP waterbath sonicator at 37kHz, 80% power. The samples for weight-loss analysis were sonicated for 5 min as it was found to be sufficiently remove all the corrosion products in 812MC samples. Coupons were then rinsed three times with a large amount of Milli-Q water for 10 s each. The coupons were then dehydrated in absolute ethanol and dried under a stream of air. Weight-loss analysis was performed using Eq. 11 as described in Chapter 2 (Chapter 2.2.3). As a different batch of mild steel coupons was used in this chapter, I noticed that the weight loss was systematically lower (~ 0.01 mmpy) in comparison to the one obtained in Chapter 2.

The mild steel coupons were inspected under 3D Laser Scanning Microscope (Keyence VK-X1000) for localized corrosion. The coupon surface was scanned with 10 x objective lens and the deepest feature of each replicate was identified using Vol & Area function in the MultiFileAnalyzer software after tilt correction. For mild steel coupons with no macroscopic corrosion damages, the deepest feature was identified under 150 x objective lens and the deepest penetration rate was calculated using Eq. 12 as described in Chapter 2.

4.2.6 Scanning electron microscope (SEM)

Sample preparation and imaging procedures were performed as described in Chapter 2 (Chapter 2.2.6). Briefly, the mild steel coupons for SEM analysis were rinsed once with 1x PBS to remove loosely attached cells before fixed in N_2-sparged Sorenson buffer with 2.5% glutaraldehyde (pH 7.8) at 4 °C overnight. The coupons were washed once with Sorenson buffer and sequentially dehydrated in 30% (5 min), 50% (5 min), 70% (5 min), 80% (15 min), 95% ethanol (15 min), and twice in absolute ethanol (30 min each). The coupons were gently dried with a stream of N_2 and were kept in a N_2 atmosphere with silica desiccants until ready for SEM. Before imaging, the coupons were gold-coated (~5 nm thickness) and imaged with JEOL FE-SEM 7600F equipped with energy dispersive X-ray spectroscopy (EDS) detector at 15 kV accelerating voltage.

4.2.7 Chemical Analysis

Samples collected for sulfide analysis were fixed with zinc acetate at a final concentration of 0.2 M and stored in -80 °C freezer immediately. Samples collected for iron analysis (Fe_{bulk}) were acidified with hydrochloric acid to a final concentration of 1%. The spent 1% HCl cleaning solution for the weight loss was used for measuring the iron content in the corrosion products ($\text{Fe}_{\text{surface}}$). Sulfide and iron concentrations were measured using the copper sulfate method and 1,10-phenanthroline method, respectively as described in Chapter 2 (Chapter 2.2.4). The pH of the medium was monitored with SevenGo Duo portable pH meter (Mettler Toledo) in a separate aliquot.

4.2.8 DNA extraction

Planktonic cells (8 ml) were harvested by centrifuging the spent medium at 8000 x *g* for 10 min at 4 °C. The cell pellets were washed once with nucleic acid preservation buffer, followed by 1x PBS before storing the cell pellet in -80 °C freezer until ready for DNA extraction (Fu et al. 2011). Two pieces of mild steel or three pieces of polycarbonate coupons were used for extracting biofilm DNA. The coupons for DNA extraction were rinsed once with 1x PBS and preserved in 20 ml nucleic acid preservation buffer immediately upon retrieval. The coupons were sonicated in ElmaP waterbath sonicator (37 kHz, 80% Pwr, 5 min) and the detached cells were centrifuged at 8000 x *g* 10 min at 4 °C. The biofilm cell pellets were washed once with 1x PBS and stored in -80 °C freezer until ready for DNA extraction. DNeasy PowerSoil Pro kit was used to extract DNA from both planktonic and biofilm cells according to manufacturer protocol. DNA was eluted in 50 µl Solution C6 and the concentration and purity were checked using QubitTM dsDNA HS assay and Nanodrop 2000, respectively. Five nanograms of the eluted DNA were amplified with universal 16S rRNA gene primers 926F and 1392R with Illumina adaptor sequence using KAPA hotstart 2x mastermix in triplicate reaction for 25 cycles (Initial Denaturation: 95 °C for 3 min； Amplification cycle: 98 °C for 20s, 60 °C for 15s, 72 °C for 30 s, for a total of 25 cycles; Final extension: 72 °C for 1 min) (Matsuki et al. 2002). The PCR product from triplicate reactions were pooled and purified using AMPure bead XP (1.08x volume), washed with 70% ethanol and dried, before resuspending in 50 µl nuclease-free water. The concentration and purity of the purified PCR products were checked using QubitTM dsDNA HS assay (sensitivity ⩾ 0.002 µg/ml dsDNA) and Nanodrop 2000, respectively as well as in 2% TAE agarose gel.

4.2.9 Microbial community analysis

The purified PCR products were submitted to the sequencing facility of Macrogen Asia Pacific for paired-end Illumina Amplicon Sequencing (MiSeq 300). The sequencing reads were processed using the DADA2 workflow in RStudio (Callahan et al. 2016). Briefly, the sequencing primers were first trimmed, and low-quality bases were removed. The filtered reads were then subject to error learning and sample inference using DADA2. The pair-end reads were then merged, and chimera was removed. Taxonomy was assigned by matching the inferred amplicon sequence variants (ASVs) to SILVA 16S reference database v138.1 (Callahan et al. 2016, Yilmaz et al. 2014). Microbial taxonomy analysis was performed using the phyloseq package (McMurdie and Holmes 2013). The reads from each sample were rarefied to even depths and non-metric multidimensional scaling (NMDS) ordination was plotted using “bray” distance metric. For taxonomy plot showing the major taxa, ASVs that contribute to < 1% of the total reads were removed and the remaining ASVs were agglomerated at the genus level using tax_glom function in the phyloseq package. The taxa table was exported to GraphPad Prism software and plotted in mean ± SD out of three biological replicates. To compare the differential enrichment of the ASVs in the mooring chain versus the sediment cultures, and on mild steel versus polycarbonate surfaces, differential abundance analyses were performed using DESeq2 package (McMurdie and Holmes 2014). Due to the absence of different ASVs across different samples, samples were normalized based on “poscount” size factors were used instead of the default “ratio” to accommodate zero values in the dataset. Pair-wise comparisons were performed using DESeq function and an adjusted *p*-value < 0.05 was used as cut off.

4.3 Results

Two enrichment cultures, 812MC (from mooring chain) and 812Sd (from sediments) were established from the deep-sea samples previously collected during the KR18-15 expedition. After achieving stable growth, the 812MC and 812Sd enrichment cultures were subjected to immersion test with mild steel AH36 (i.e., 812MC + Mild Steel and 812Sd + Mild Steel) and polycarbonate coupons (i.e., 812MC + Polycarbonate and 812Sd + Polycarbonate) for corrosion assessment and microbial community assessment. Therefore, the result section was split into two parts, with Part I focused on assessing the MIC mediated by 812MC and 812Sd enrichment cultures compared to the corrosion in sterile medium, and Part II focused on the microbial analysis that studies if any specific microbes were enriched on the mild steel surface and correlate the microbial community composition of the enrichment cultures to their MIC behaviors.

Part I – Corrosion Assessment

4.3.1 812MC enrichment culture induced severe corrosion to mild steel AH36.

Upon retrieval from the immersion test, black corrosion products were noticeable on two sides of the mild steel coupons from 812MC sample in both week 2 and week 4. The affected area that was covered by the black corrosion products increased in size from week 2 to week 4 (Supplementary Figure 9). Visible corrosion damage and pits were observed underneath after removing the corrosion products (Figure 4.2). The deepest features were 18.28 ± 2.06 µm on week 2 and increased to 36.07 ± 4.12 µm on week 4, which corresponds to a penetration rate of ~ 0.47 mm/y (Figure 4.3). No signs of corrosion were observed in the areas that were not covered by the corrosion products. On the other hand, no corrosion products or visible corrosion damage were observed in the sterile sample or 812Sd + Mild Steel sample. Micron-size pits were observed on the surface of these samples occasionally but were rare and shallow (Supplementary Figure 10). Similarly, the corrosion rate measured from the weight-loss method was low in the sterile sample and 812Sd + Mild Steel sample and occurred mainly during the initial incubation period (Figure 4.4). Further incubation to week 4 only slightly increased the weight loss and hence, the corresponding corrosion rate decreased. In contrast, active corrosion was observed in 812MC + Mild Steel sample where the corrosion rate was maintained at ~ 0.016 mm/y throughout the incubation.

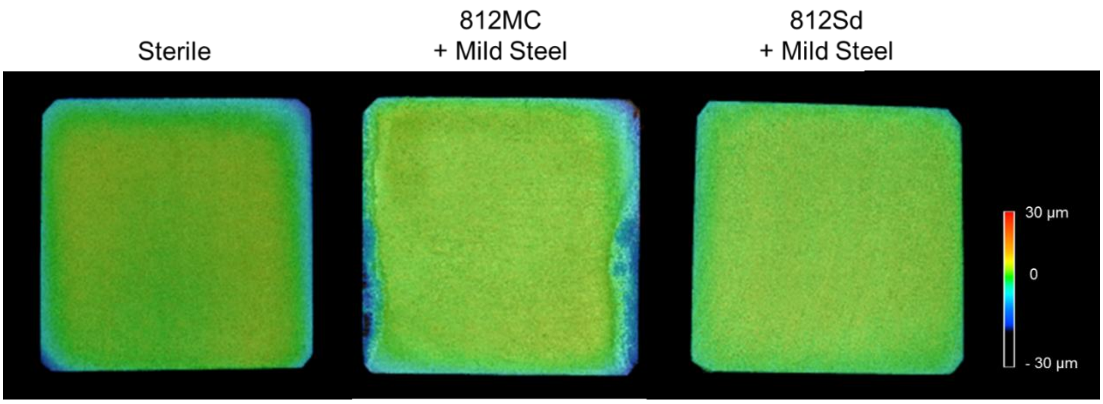

Figure 4.2. Height profile of the mild steel surface after 28 days incubation in sterile modified MOPS-ASW, with 812Sd enrichment cultures, or with 812MC enrichment cultures, after removal of corrosion products. The surfaces were colour-coded according to the surface topology.

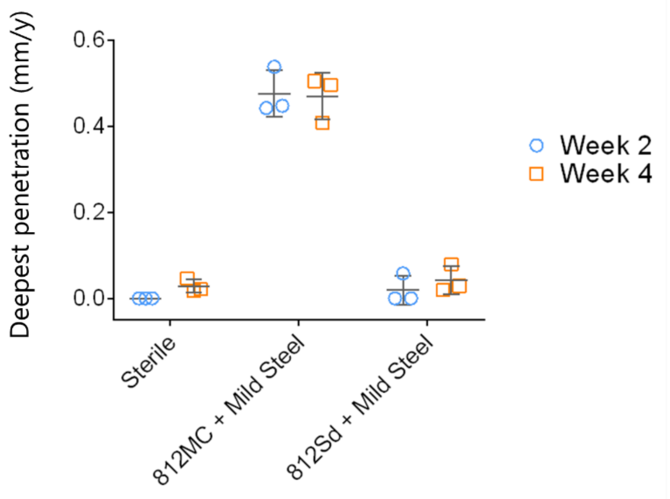

Figure 4.3. Localized corrosion analysis of the mild steel surface incubated in sterile modified MOPS-ASW, with 812Sd enrichment cultures, or with 812MC enrichment cultures. The maximum penetration rate was calculated based on the deepest features identified at week 2 and week 4, respectively.

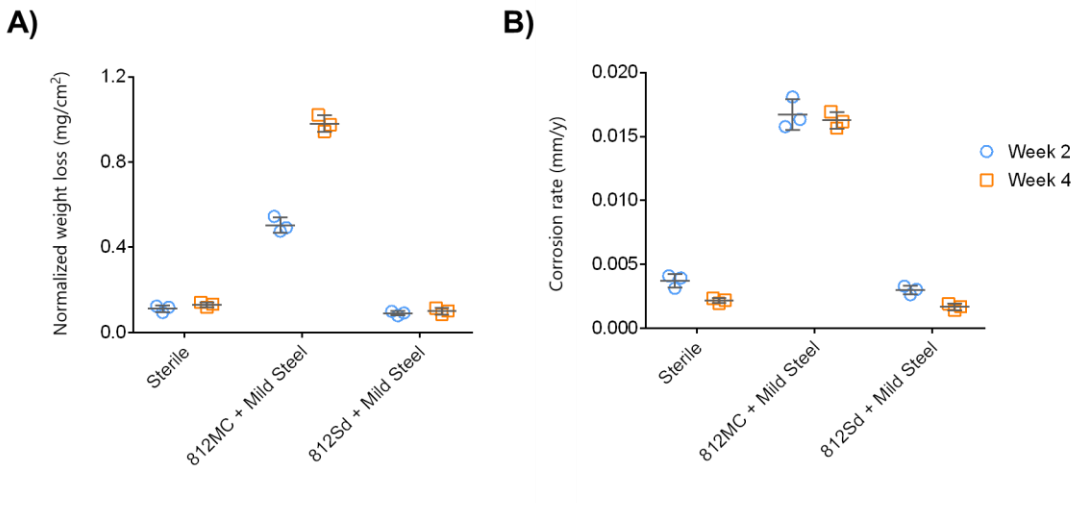

Figure 4.4. Weight-loss analysis of the mild steel coupons incubated in sterile modified MOPS-ASW, with 812MC enrichment culture or with 812Sd enrichment culture. The weight-loss results normalized to the surface area (A) and the corresponding corrosion rate in millimeter per year (mm/y) (B) from three biological replicates were presented.

4.3.2 Black corrosion products comprised of biofilm and mineral rich in sulfur element

Inspecting the surface morphology of the mild steel coupons from 812MC + Mild Steel sample under SEM revealed the black corrosion products were comprised of a mixture of "organic-looking" materials and large clumps of mineral aggregates rich in sulfur element (up to 27.8 weight% in some region measured by EDS) (Figure 4.5, Supplementary Figure 11). Microbes of diverse morphology were observed on the mineral aggregates, and thin filaments resembling "nanowire"-like structures or flagellar structures were occasionally observed (Supplementary Figure 12). The transition out of the area covered by the black corrosion products to the exposed surface was accompanied with a sharp loss of S peak (Supplementary Figure 13).

Microbial micro-colonies, individual vibrio-shaped microbes, and minerals, mainly oxides, were still observed in the area without black corrosion products. Similar vibrio-shaped microbes could also be found on the mild steel surface of the 812Sd sample, however, with no apparent three-dimensional biofilm structures (Figure 4.5). Little to no corrosion products were found on the surface of the mild steel coupon incubated with 812Sd but shallow depression features were occasionally observed. When incubated in the sterile test medium, the mild steel surface developed thin, plate-like oxides, which widen over time, and signs of general corrosion were observed on the base metal underneath (Figure 4.5).

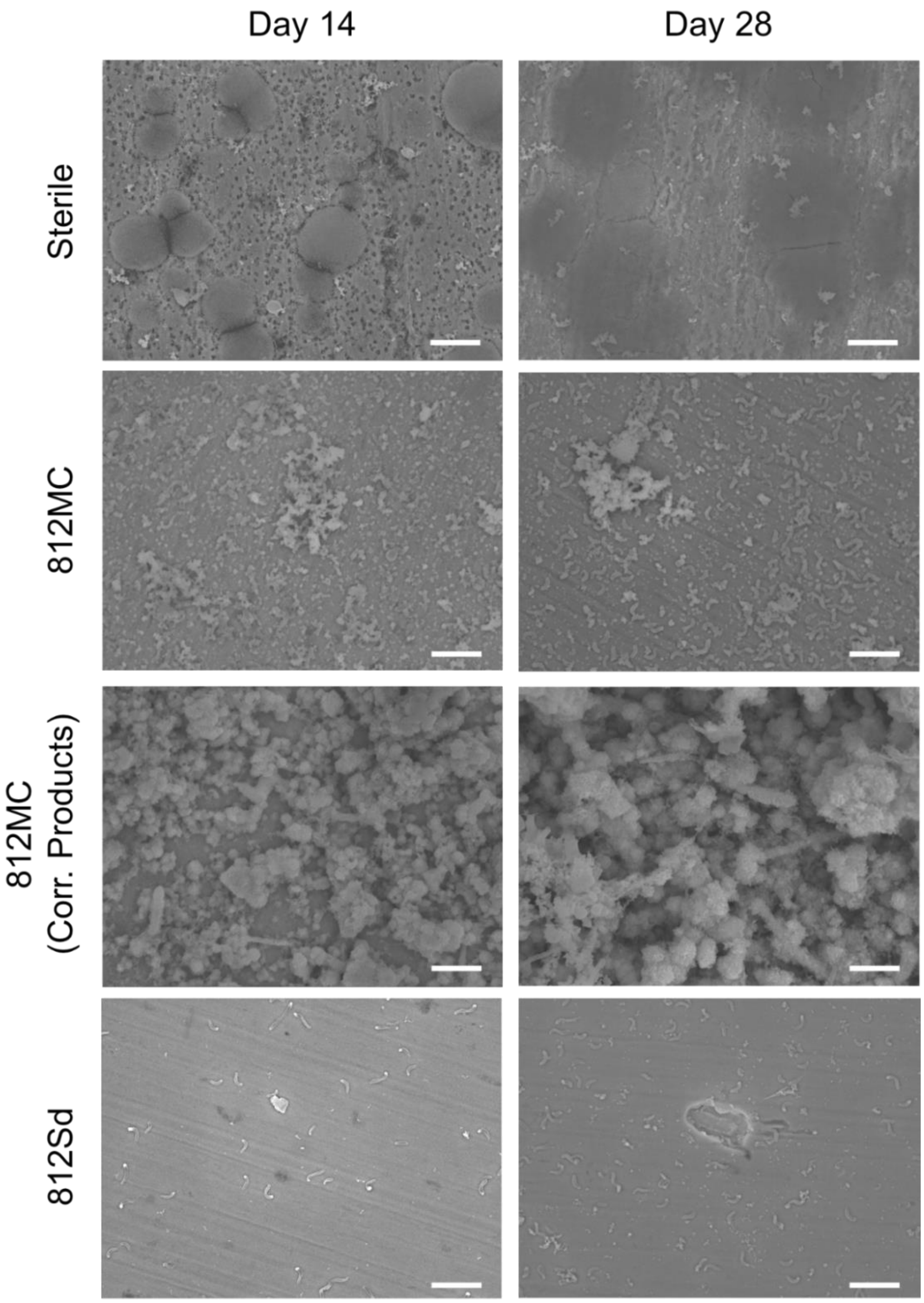

Figure 4.5. Scanning electron micrographs of the mild steel coupons after 28 days incubation in sterile modified MOPS-ASW, with mooring chain enrichment cultures 812MC or with sediment enrichment cultures 812Sd. Scale bar = 5 µm.

4.3.3 Active sulfide production but low iron dissolution in 812Sd enrichment culture

The concentration of sulfide and iron (Fe $_{\text{bulk}}$ and Fe $_{\text{surface}}$, measuring dissolved/particulate irons and the amount of iron in the corrosion products, respectively) were monitored to evaluate the microbial activity and the progress of corrosion. Sulfide was detected in 812MC enrichment cultures either incubated with mild steels or when incubated with polycarbonate surface, indicating an active sulfate-reducing activity in the samples (Figure 4.6A). Notably, sulfide was also detected in the 812Sd + Mild Steel sample despite the absence of a corrosion product layer on the mild steel. Nevertheless, very little Fe $_{\text{bulk}}$ was detected in the 812Sd + Mild Steel sample indicating that little iron dissolution has occurred, which is in accordance with the absence of corrosion products for this sample (Figure 4.6B). In the sterile sample, the Fe $_{\text{bulk}}$ increased from week 0 to week 1 but slightly declined afterward, suggesting that iron dissolution occurs mostly at the beginning of incubation. On the other hand, the Fe $_{\text{bulk}}$ steadily increased in 812MC + Mild Steel sample over the four weeks of incubation. The Fe $_{\text{surface}}$ was low (≤ 0.2 mg) in the sterile sample and 812Sd + Mild Steel sample which has no visible corrosion product (Figure 4.6C). Aligning with the macroscopic observation, the Fe $_{\text{surface}}$ in the 812MC sample increased from 0.64 ± 0.09 mg to 1.01 ± 0.09 mg from week 2 to week 4. The pH of both the enrichment culture samples was slightly lower than the sterile samples but overall, the medium pH remained neutral throughout the incubation (Figure 4.6D).

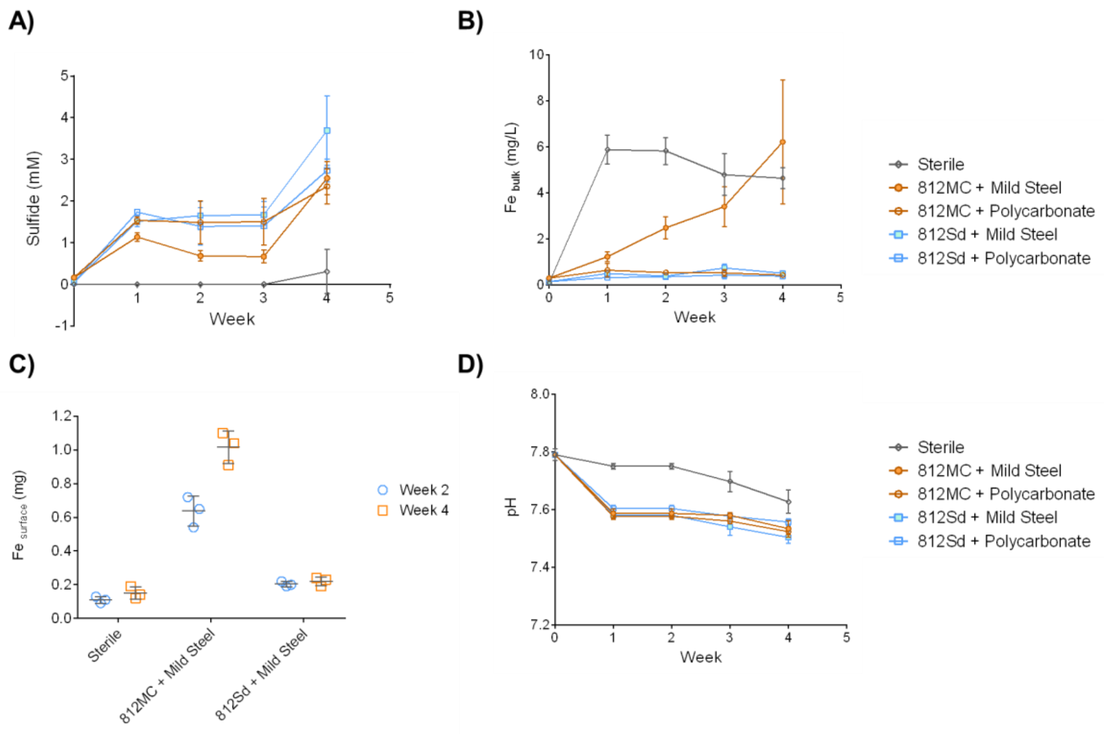

Figure 4.6. Chemical analysis and pH measurement of the immersion test samples. Sulfide production (A), iron dissolution, Fe $_{\text{bulk}}$ (B) and pH (D) were monitored weekly from the bulk liquid during the immersion test, whereas the Fe $_{\text{surface}}$, the iron content in the corrosion products were measured on week 2 and week 4 (C).

Part II – Microbial Analysis

4.3.4 Active microbial community in both 812MC and 812Sd enrichment cultures

As 16S rRNA gene copy number may vary between bacterial species, hence, the amount of the extracted DNA was used to estimate the total biomass in the enrichment cultures instead. In general, the planktonic biomass increased during the first week of incubation then maintained over the four weeks of incubation (Figure 4.7A). In both 812MC and 812Sd cultures, incubation with polycarbonate coupons (812MC + PC sample and 812Sd + PC sample) resulted in a slightly higher planktonic DNA concentration than when incubated with mild steels (812MC + MS and 812Sd + MS) (Figure 4.7A). On the other hand, the normalized biofilm DNA (ng/cm^2) was similar in 812MC samples regardless of surface types (812MC + MS and 812MC + PC) whereas in 812Sd samples, the normalized biofilm DNA in 812Sd + PC were ~4x higher than 812Sd + MS (Figure 4.7B).

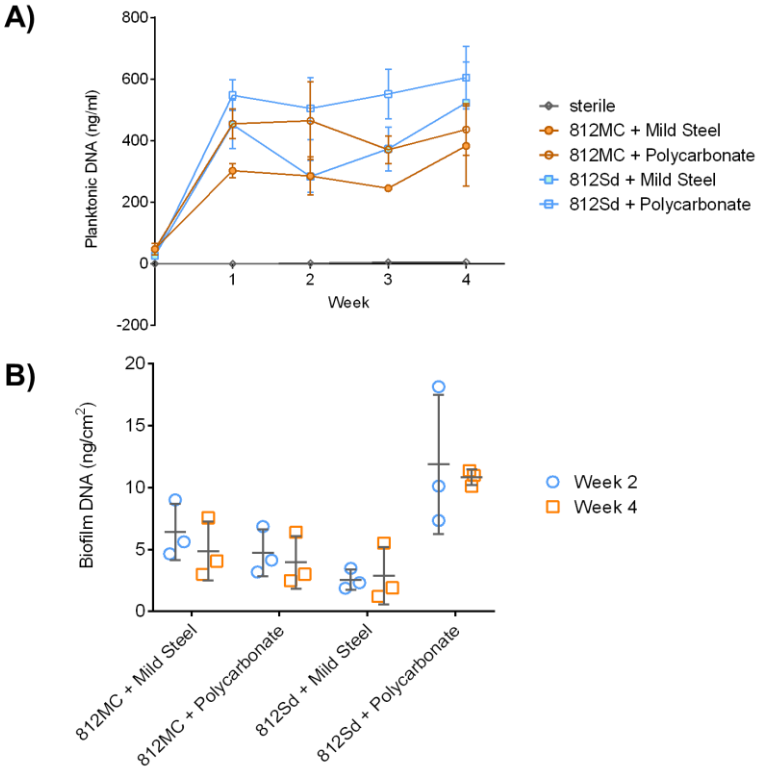

Figure 4.7. Biomass estimation of the samples based on the DNA content. The extracted planktonic DNA were normalized to the culture volume used for extraction (A), whereas biofilm DNA were normalized to the surface area of the coupons (B).

4.3.5 Microbial communities were dissimilar in 812MC and 812Sd enrichment cultures

To provide a better relationship between the microbial community and MIC, the microbial community composition was monitored before and throughout the immersion duration using amplicon sequencing targeting the V6 to V8 region of the 16S rRNA gene (Matsuki et al. 2002). An overview of the dissimilarities of microbial composition in the different samples was shown in the NMDS plot (Figure 4.8). The samples of different enrichment cultures (812MC vs 812Sd) were split along NMDS 1 axis whereas the samples from different cell fractions (planktonic vs biofilm) were split along NMDS 2. Substratum (Mild steel vs polycarbonate) and weeks also impact the biofilm community but to a lesser extent.

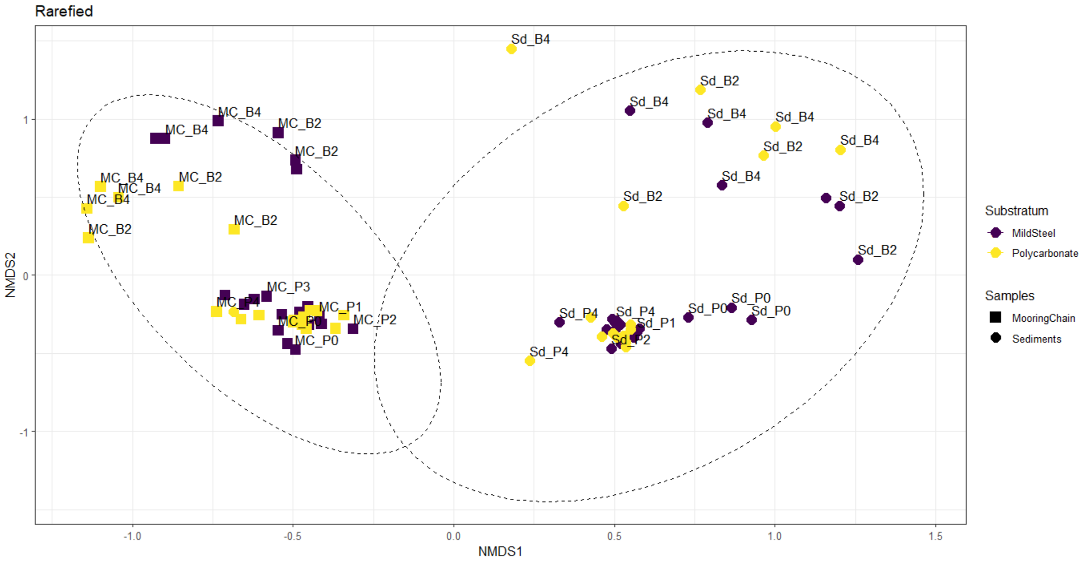

Figure 4.8. NMDS plot showing the dissimilarities between the samples. MC = 812MC enrichment culture, Sd = 812Sd enrichment culture; P = planktonic fraction, B = Biofilm fraction; Numeric number 0 to 4 indicates week 0 to week 4. Ellipses were drawn at 95% confidence level based on normal distribution assumptions.

4.3.6 Enrichment cultures were dominated by sulfate-reducing and fermentative bacteria

A closer inspection of the microbial community of the initial enrichment cultures and the planktonic cells throughout the immersion test revealed six major taxa in every sample albeit at different proportions (Figure 4.9). The major taxa are *Desulfovibrio* (sulfate-reducing taxa from class *Desulfovibrionales*) and *Exiguobacterium* (complex organic degrader, heavy metal resistant, facultative anaerobic taxa from class *Bacilli*), *Tepidibacter* (fermentative anaerobic taxa from class *Clostridia*), *Dethiosulfatibacter* (S^0 and thiosulfate-reducing, fermentative, amino acid metabolizing anaerobic taxa from class *Clostridia*), *Paramaledivibacter* (fermentative, amino acid metabolizing anaerobic taxa from class *Clostridia*) and *Draconibacterium* (fermentative, amino acid metabolizing anaerobic taxa from class *Clostridia*). Prior to the immersion tests, the initial enrichment cultures of the 812MC sample comprise mainly of genus *Exiguobacterium* (69.12 ± 7.51%) and *Desulfovibrio* (26.16 ± 6.43%) whereas 812Sd consists of mainly genus *Desulfovibrio* (78.22 ± 5.34%). While the exact ASV detected may vary between samples, at the genus level the microbial community composition gradually converges over the four weeks of incubation, regardless of the type of substratum (i.e., mild steel or polycarbonate).

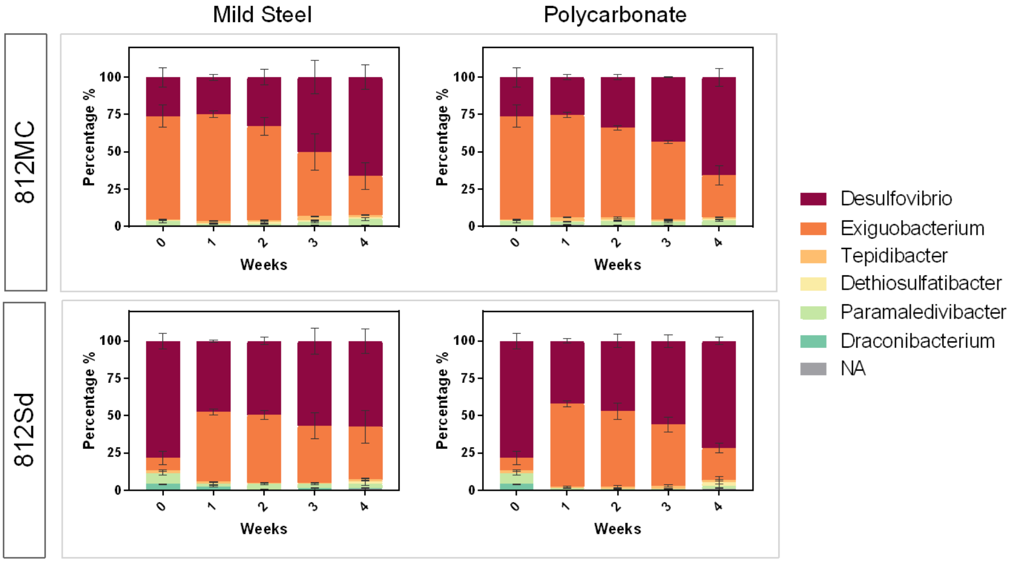

Figure 4.9. Distribution of major taxa in the planktonic community of the enrichment cultures incubated with mild steel and polycarbonate coupons across four weeks of incubation. Only ASVs contribute to >1% of the total reads were used to agglomerate at genus level. The genus were plotted in mean ± standard deviation obtained from three biological replicates.

4.3.7 *Tepidibacter* were specifically enriched in the mild steel biofilm of 812MC samples

Figure 4.10 shows the overview of the major taxa in the biofilm community in 812MC and 812Sd samples at week 2 and week 4. Despite corrosion is only observed in 812MC sample, the sulfate-reducing taxa *Desulfovibrio* was present in both the 812MC and 812Sd mild steel biofilm community (Figure 4.10). Furthermore, the *Desulfovibrio* was found more abundant in the mild steel biofilm of the non-corrosive 812Sd sample by 2.36- and 2.94-fold at week 2 and week 4, respectively, as measured by DESeq2 analysis (Figure 4.11). On the other hand, *Tepidibacter*, an anaerobic fermentative taxon that was not previously associated with MIC, was found enriched in the mild steel biofilm of the 812MC sample by 4.44- and 5.60-fold at week 2 and week 4, respectively. Notably, members from this genus have also been reported to utilize elemental sulfur (S^0) as an electron acceptor (Slobodkin et al. 2003, Tan et al. 2012). *Herbaspirillum* (nitrogen-fixing, non-fermenting facultative anaerobic taxa from class *Betaproteobacteria*) were detected in the mild steel biofilm of both 812MC and 812Sd samples at week 2. The remaining taxa that were differentially enriched are *Paramaledivibacter* and *Draconibacterium* in 812Sd samples, and *Vallitalea*, *Oceanirhabdus*, and two *Clostridia* with unassigned genus in 812MC samples (Figure 4.11).

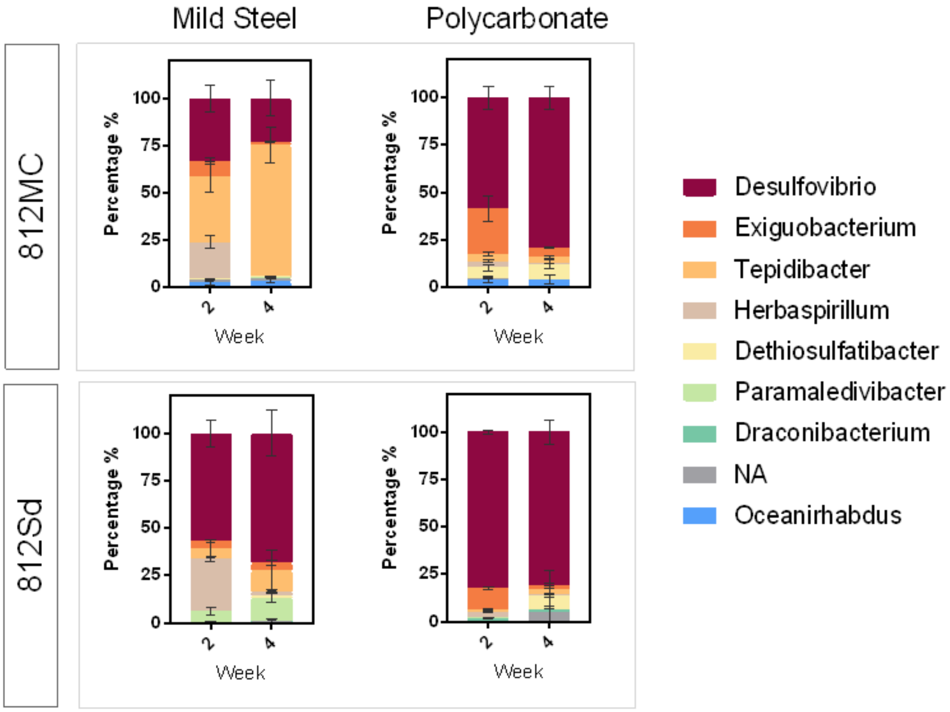

Figure 4.10. Distribution of major taxa in the biofilm community of the enrichment cultures incubated with mild steel and polycarbonate coupons at week 2 and week 4. Only ASVs contribute to >1% of the total reads were used to agglomerate at genus level. The genus were plotted in mean ± standard deviation obtained from three biological replicates.

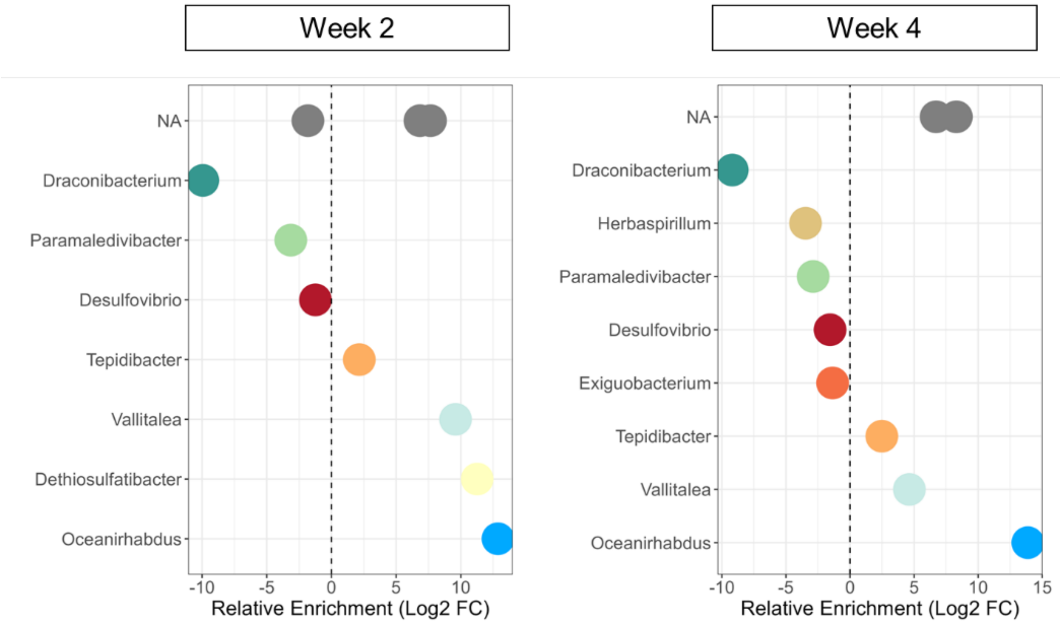

Figure 4.11. Differential abundance analysis of mild steel biofilm community at week 2 and week 4. The log 2-fold change of the enriched taxa (with adjusted p-value < 0.05) in 812MC sample against 812Sd sample as reference were plotted. Positive log2 FC indicates the taxa were enriched in 812MC mild steel biofilm whereas negative log2 FC indicates the taxa were enriched in 812Sd mild steel biofilm.

4.3.8 Polycarbonate biofilm community resembles mild steel biofilm community with altered proportion

The distribution of major taxa in the biofilm community of 812MC were more impacted by the type of substratum as compared to the biofilm community of the 812Sd sample (Figure 4.10). In 812MC sample, the polycarbonate biofilm was enriched with *Desulfovibrio* as compared to the mild steel, despite it was only statistically significant at week 4 when analyzed by DESeq2 (Figure 4.12). *Tepidibacter* that was highly enriched in the 812MC mild steel biofilm were 18.97- and 36.44-fold underrepresented in the polycarbonate biofilm at week 2 and week 4, respectively, suggesting a preference of this genus toward the mild steel substratum (or possibly, corrosion products). Interestingly, *Dethiosulfatibacter*, a thiosulfate/S^0-

reducing bacteria, was consistently enriched in the polycarbonate biofilm of 812MC samples at both week 2 and week 4 relative to the mild steel biofilm, whereas the same genus was only detected in a single replicate of the 812Sd sample (Takii et al. 2007) (Figure 4.12). On the other hand, most of the taxa were not impacted by switching the type of substratum to polycarbonate in the 812Sd sample. Similar to the 812MC sample, there is a higher percentage of *Desulfovibrio* detected on the polycarbonate surface as compared to the mild steel. However, the changes were not statistically significant when analyzed with DESeq2 (Figure 4.13). Notably, a few taxa were (almost) exclusively detected on one surface but not another therefore appeared to be highly enriched in the polycarbonate/mild steel biofilm community. For example, *Paramaledivibacter* was detected mainly in the mild steel biofilm whereas < 400 reads were detected in the polycarbonate surface. On the other hand, *Draconibacterium* was detected on the polycarbonate surface but much less on the mild steel surface (Figure 4.13).

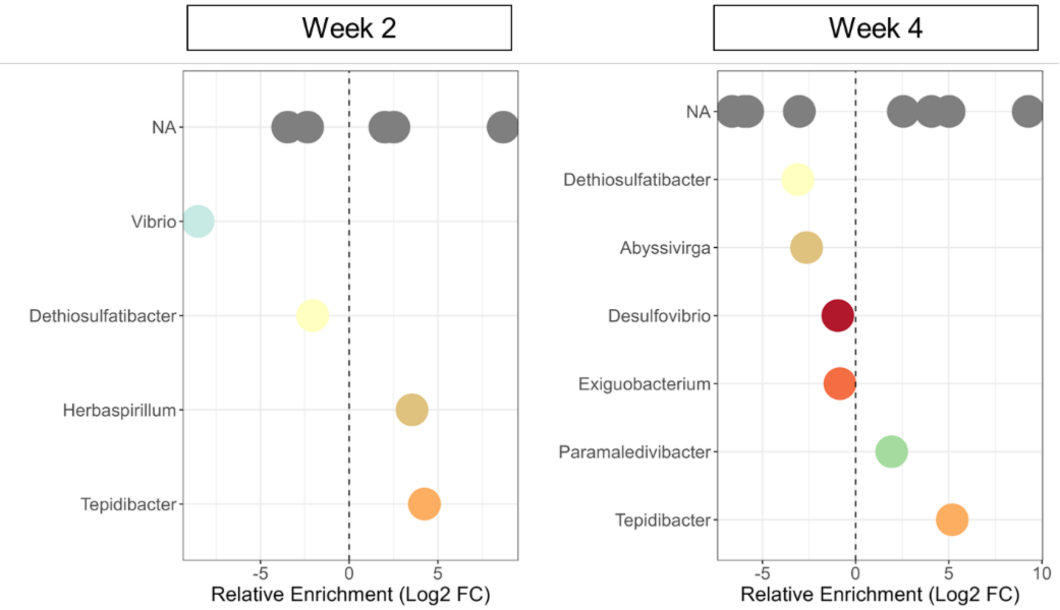

Figure 4.12 Differential abundance analysis of 812MC biofilm community at week 2 and week 4. The log 2-fold change of the enriched taxa (with adjusted p-value < 0.05) in mild steel biofilm against polycarbonate biofilm as reference were plotted. Positive log2 FC indicates the taxa were enriched in mild steel biofilm whereas negative log2 FC indicates the taxa were enriched in polycarbonate biofilm.

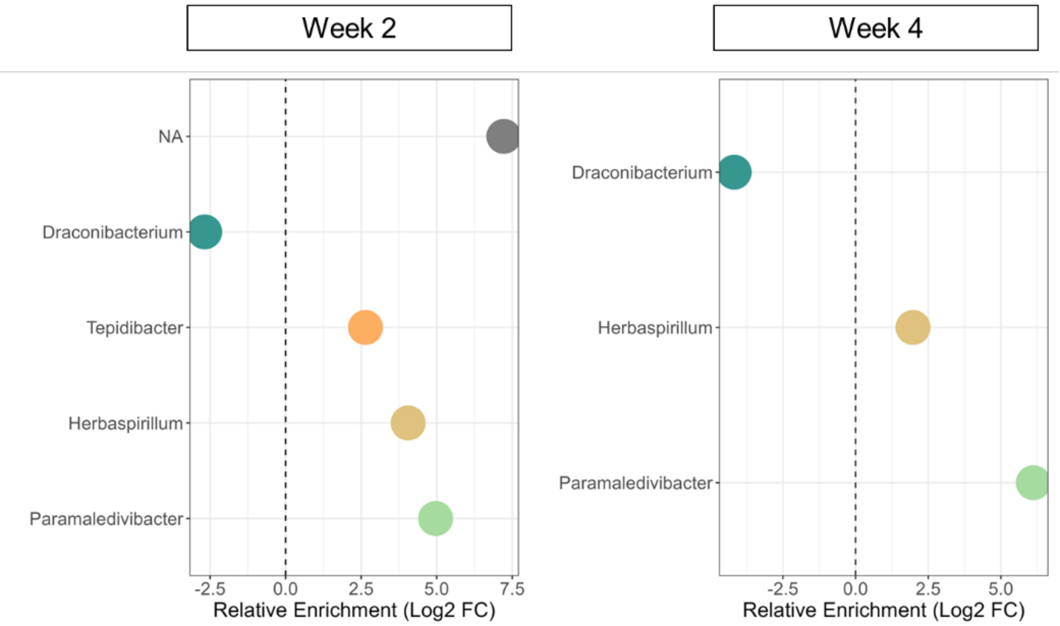

Figure 4.13. Differential abundance analysis of 812Sd biofilm community at week 2 and week 4. The log 2-fold change of the enriched taxa (with adjusted p-value < 0.05) in mild steel biofilm against polycarbonate biofilm as reference were plotted. Positive Log2 FC indicates the taxa were enriched in mild steel biofilm whereas negative Log2 FC indicates the taxa were enriched in polycarbonate biofilm.

4.4 Discussion

The impact of microbial community structure, particularly the deep-sea microbial community on the progression of MIC is little understood. Traditional axenic culture approach undermined the impact of the complex nature of the native community and their inter-species interactions whereas field studies suffer from the drawback of uncontrolled environments (especially long-term field studies) and lacking proper experimental control. Employing an enrichment culture approach hence allowed for a more targeted, hypothesis-driven approach to study how the deep-sea microbial community impacts MIC.

Intensive pitting corrosion of ~ 0.2 mm/year was reported for the original mooring chain link retrieved after 10 years of immersion at a depth of 1988 m (Rajala et al. 2022) . While the enrichment was performed without specific selection for the MIC traits, the microbial community enriched from the mooring chain retains the MIC traits and causes localized damage of up to 0.47 mm/year. The persistence of the MIC phenotype in the enrichment culture even in absence of trait selection indicates that the MIC capability may be intrinsic to the microbial community. In contrast, the microbial community enriched from a nearby sediment shows negligible corrosion similar to the sterile control. In the 812MC sample, the anodic dissolution occurs predominantly at the edge of the mild steel coupons, where it comes into contact with the coupon holder and forms a crevice. Yet, the sterile and 812Sd samples incubated under similar conditions did not exhibit such severe corrosion, suggesting that the corrosion is specifically caused by the microbial community in the 812MC samples. The formation of iron sulfide corrosion products layer may act as a physical barrier which suppress corrosion as observed in Chapter 2 (Figure 2.3). In this case however, the incomplete coverage of sulfur-rich corrosion products does not offer similar protection and therefore, the corrosion progress unimpeded. Notably, the accumulation of sulfur-rich corrosion products at the corroding regions indicate that the anodic site serves as a hotspot for the sulfide production. This implies a potential role of microbial sulfur in the aggressive iron dissolution (Figure 4.14). However, sulfide is also present in the bulk solution of 812Sd sample, yet no corrosion products nor severe corrosion were observed in the 812Sd sample. This suggests that sulfide alone is unlikely to be the primary causative agent of MIC (while corrosion mediated by iron sulfide is still possible after its formation), and an alternative mechanism must exist in the 812MC sample that initiates and aggravates the MIC.

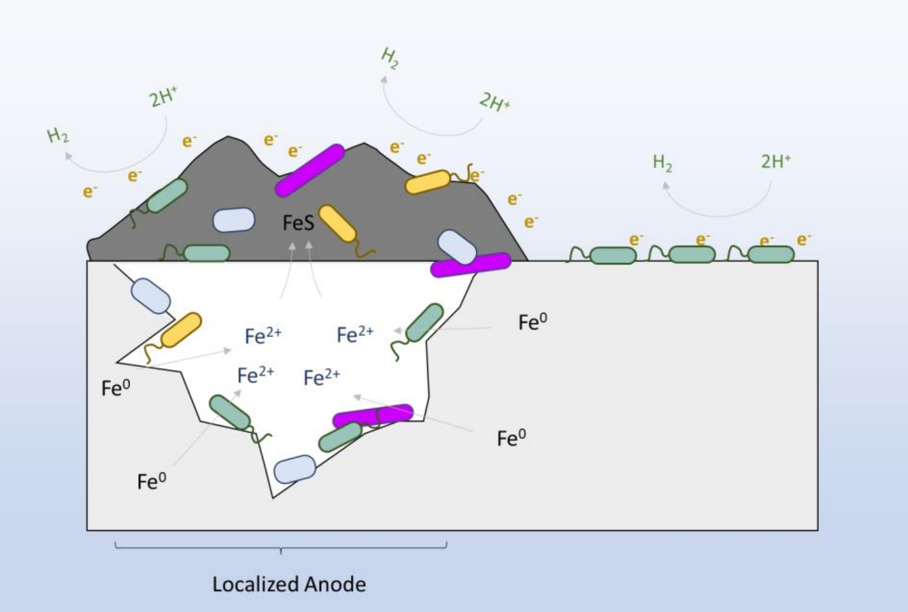

Figure 4.14. Schematic diagram of the MIC induced by the 812MC enrichment culture. The actively corroding anode coincides with the region with higher microbial diversity and accumulation of the sulfur-rich corrosion products.

Under SEM, it is clearly visible that microbes are attaching to the surface of mild steels in both the 812MC and 812Sd samples, however, a three-dimensional biofilm structure failed to develop in the latter sample (Figure 4.5). Thin filament structures or the so-called “nanowire”, which are commonly associated with extracellular electron transfer (despite lacking experimental evidence), were observed in the 812MC sample at the active corroding sites (Supplementary Figure 12) (Dou et al. 2019). Here, it is difficult to determine if the “nanowire” structures are indeed involved in the MIC in the 812MC sample, as those structures that are observed do not seem to attach directly to the base metal or the microbes. These filamentous structures may potentially be flagella which play a structural role in the biofilm in the presence of corrosion products as previously reported for *Desulfovibrio vulgaris* and the proteomic result from the Chapter 3 (Figure 3.11) (Clark et al. 2007).

The microbial community profile of the enrichment cultures of 812MC and 812Sd were altered from the original mooring chain and sediment community (Rajala et al. 2022). The alteration may be due to the culture viability arise from the differences in tolerance toward freezing/thawing steps during sample storage, variations in hydrostatic pressure and temperature changes during sample retrieval, and the culturing conditions (Bodor et al. 2020, Wang et al. 2021b). Despite having a similar microbial community composition (Figures 4.9 and 4.10), the sediment enrichment culture displayed a far less MIC activity than the mooring chain enrichment culture (Figure 4.4). This suggest that the corroding environment of the mooring chain may also play a role in selecting for MIC traits, which then persist through the enrichment procedures.

The major taxa in both 812 MC and 812Sd enrichment cultures consist of mainly sulfate-reducing bacteria and anaerobic/facultative anaerobic bacteria that have been previously isolated from deep-sea environments and capable of metabolizing complex carbohydrates and/or proteinaceous substrates such as starch and peptones that are presence in the medium (Crapart et al. 2007, Pi et al. 2013, Slobodkin et al. 2003). The lack of electron acceptors in the test medium other than sulfate encourages fermentative growth and the extensive fermentation might produce organic acid that reduces the pH sufficiently to promote MIC (Gu and Galicia 2012, Salgar-Chaparro et al. 2020). However, it is unlikely to explain the higher corrosivity in 812MC sample due to several reasons: i) the pH of the bulk liquid in both 812MC and 812Sd samples remained neutral (>7.5) throughout the incubation period, ii) the supply of fermentation substrates is limited, iii) fermentative bacteria are abundant in both 812MC and 812Sd samples, which theoretically, should result in noticeable general corrosion in both samples (Gu and Galicia 2012). However, it is possible that after the MIC initiated, the fermentation products built up underneath the corrosion products layer and aggravated the corrosion damage (Su et al. 2020, Wang and Melchers 2017). At the same time, *Desulfovibrio* could also benefits from the fermentation products such as hydrogen, lactic acid, and ethanol as alternative energy sources under the nutrient-limiting test condition, thereby maintaining an active sulfate-reducing population and sustaining MIC (Dar et al. 2008, Zhao et al. 2008).

The microbiome analysis from the previous study suggests that the mooring chain corrosion is linked to the sulfur cycling between sulfur-disproportionation *Desulfocapsa* and sulfate-reducing *Desulfovibrio* (Rajala et al. 2022). In this study, *Desulfocapsa* is absent in the enrichment cultures, potentially due to its long doubling time and a stringent growth requirement specifically on sulfur-disproportionation hence easily outcompeted by other heterotrophic bacteria (Finster et al. 1998). On the other hand, the sulfate-reducing *Desulfovibrio* is another potential candidate for the causative agent of MIC. The microbial analysis however shows that the genus *Desulfovibrio* is comprised mainly of a single ASV that is abundant in both the heavily corroded 812MC sample as well as the uncorroded 812Sd sample. Nevertheless, given that the 812MC cultures were established from a corroding mooring chain deployed for 10 years, it is plausible that through the extended time, the same ASV has acquired genetic and/or physiological adaptations that could potentially impact the MIC progression. It will be interesting to investigate if the same ASV isolated from the two enrichment cultures exhibit different MIC behaviors in a follow-up study. According to EMIC theory, some SRB may derive energy by directly oxidizing Fe^0 to sustain their growth and activity (Deng et al. 2020, Deng et al. 2015, Kato 2016). Therefore, biofilm formation on a Fe^0-based substratum should offer survival advantages as compared to an inert material such as polycarbonate, while such a study is still lacking in the literature. This does not seem to be the case here as the *Desulfovibrio* were enriched in the polycarbonate biofilm community rather than in mild steel biofilm, and with an estimated total biofilm biomass similar (for 812MC) or even higher (for 812Sd) on polycarbonate surface. Instead, genus such as *Herbaspirilllum* and *Tepidibacter* were found enriched specifically on the mild steel surface as compared to the polycarbonate (Figure 4.10). *Herbaspirilllum* is a nitrogen-fixing, microaerobic/facultative anaerobic soil bacteria which have been reported to secrete siderophore under iron limitation, while *Tepidibacter* is a spore-forming, fermentative bacteria, which has been previously isolated from crude oil-polluted soil as well as hydrothermal vent area (Slobodkin et al. 2003, Tan et al. 2012, Trovero et al. 2018). Unfortunately, the involvement of these two genera in MIC have not been reported.

It is worth noting that members from *Tepidibacter* (enriched in the 812MC + Mild Steel biofilm), as well as *Dethiosulfatibacter* (enriched in the 812MC + Polycarbonate biofilm) have been reported to utilize S^0 (but not sulfate) as terminal electron acceptor (Slobodkin et al. 2003, Takii et al. 2007). Elemental sulfur when come in direct contact with the mild steel, can cause severe localized corrosion damage and produces iron sulfide as the corrosion product which is indistinguishable from the SRB-mediated MIC or in any sulfide-containing environment (Bolney et al. 2021, Fang et al. 2008, Sherar et al. 2011). The consistent enrichment of two sulfur-metabolizing taxa (other than *Desulfovibrio*) in 812MC samples strongly indicates that that S^0 may be produced in the 812MC culture. Sulfide produced by the SRB may serves as the source for chemical or biological conversion to yield elemental sulfur (Cypionka et al. 1998, Steudel 1996). The S^0 is also proposed to be present on the corroding mooring chain in the original field study as a substrate utilized by *Desulfocapsa* for sulfur-disproportionation to produce sulfate and sulfide (Rajala et al. 2022). While further validation is needed, this study highlighted the potential involvement and role of S^0 in MIC caused by the mooring chain community.

4.5 Conclusion

Validating field MIC studies in a controlled laboratory setting has a promising potential in providing valuable insights into the MIC process, the potential culprit microbes, and their mechanisms in an environment of interest. Yet, such a validation study has not garnered adequate consideration in the past for typical MIC cases let alone deep-sea MIC. In this chapter, a MIC test was performed on the deep-sea enrichment cultures established from a corroding mooring chain after 10 years of deployment in a controlled environment that is difficult to study in the field. It was demonstrated that the mooring chain microbiome exhibits MIC behavior that is distinct from the abiotic corrosion as well as the corrosion induced by the sediment microbiome that has been enriched under similar conditions. The findings suggest that the MIC remains a threat to the deep-sea assets despite the extreme conditions. The corroding metals may serve as a hotspot for MIC microorganisms, where MIC-causing traits persist even after the removal of the corroding metal as observed in our enrichment culture. This also implies that the materials that do not exhibit corrosion immediately upon deployment may not be safe from aggressive corrosion after an extended incubation period, and extra caution should be taken to ensure sufficient test duration for material design and testing. The observation of accumulation of sulfur-rich corrosion products and an increased in microbial diversity at the corroding sites strongly suggest that MIC microbes aggravate corrosion by participate in stimulating anodic iron dissolution. While the microbial composition analysis via 16S rDNA amplicon confirmed the changes in the microbial community, many of the differentially abundant microbes are not known to be associated with MIC. Despite the sulfur disproportionation bacteria *Desulfocapsa* not being detected in the corrosive enrichment culture. Interestingly, *Tepidibacter* which is also capable of metabolizing elemental sulfur was found enriched in the corroding mild steel biofilm in this study. This unexpected finding highlights a potentially overlooked MIC mechanism that involves the highly corrosive elemental sulfur and warrants further investigation using X-ray characterization techniques. To better understand and explain the observed difference in the MIC outcome, a follow-up metagenomic comparison of the microbial community of the 812MC enrichment culture and 812Sd enrichment culture has been planned and is currently underway. In summary, while the objective to unravel the causative agent for the MIC and to identify the MIC mechanism remain unresolved, this study nevertheless establishes a groundwork for future MIC study in particular in deep-sea environment.

Chapter 5

Concluding remarks & future research recommendations

With the rising global interest in deep-sea resources, protection of deep-sea assets have become increasingly important considering the serious environmental and economic consequences in the case of failure. Whether the corrosion (including MIC) progresses similarly in deep sea as in terrestrial or typical marine setting has not been investigated in the past. While the involvement of MIC in deep-sea corrosion is expected due to the ubiquitous nature and adaptability of microbes, yet deep-sea MIC remains a largely unexplored territory of corrosion research. Furthermore, how hydrostatic pressure, – one of the key features of the deep sea, influences MIC has not been investigated, despite its fundamental role in microbial life in the deep sea. Through carefully designed experiments, this dissertation investigated these pressing research questions and provided an unprecedented overview of deep-sea MIC by a combination of corrosion assessment and microbial assessment.

Throughout this dissertation, MIC has been repeatedly demonstrated to be a threat in deep-sea environments, not only with axenic culture but also mixed-species cultures enriched field samples. Once the corrosion was initiated, the corroding micro-environment may promote MIC traits in the local microbial community. This is shown by the high MIC activity of the microbial community enriched from the corroding mooring chain but not in the microbial community enriched from the surrounding sediment. It is unclear if the interspecies interaction plays a role in accelerating MIC under such circumstances. The persistence of the MIC traits in the mooring chain microbial community even without specific selection during the enrichment procedure should also be a concern when evaluating MIC risk. The presence of SRB alone does not serve as a good indicator for MIC. This is repeatedly demonstrated in both Chapter 2 and Chapter 4, where their presence does not guarantee enhanced MIC activity (Figure 2.2 and 4.3). While SRB as a whole group of bacteria are commonly blamed as the causative agent of MIC, the presence of a specific species of the SRB (or bacteria species as a whole) plays a determining role in their potential MIC capability. On the other hand, in Chapter 4, many of the bacteria found in the highly corrosive mooring chain enrichment culture were not previously associated with MIC. These findings challenge the common practice in MIC research which focus on a limited number of highly corrosive SRB species and highlight the needs of expanding on our current model organism for MIC study. Hydrostatic pressure is a critical parameter in the deep sea, and the corrosion severity increased by at least two-fold at the hydrostatic pressure corresponding to the native habitat of the deep-sea SRB. However, the *P. piezophilus* proteome profile was not altered significantly when subjected to elevated hydrostatic pressure environment. Instead, the corrosion severity might be linked to the MIC protein activity or indirectly through the impact on the biofilm morphology. Bacteria from shallow waters might retain their MIC capability when subjected to elevated hydrostatic pressure and similarly deep-sea bacteria might persist to corrode mild steels even when incubated at atmospheric pressure (Figure 2.2 and 2.9). The inability of hydrostatic pressure to inhibit MIC poses a concern to the assets that are microbial contaminated before deployment for deep-sea operation.

The exact mechanism of SRB-induced MIC remained debatable even in the well-studied model such as *D. vulgaris* and *D. ferrophilus*. Whether deep-sea MIC possess different mechanisms to the typical MIC requires further investigation. Based on the current observations, the MIC activity is associated with actively corroding region (anodic site) rather than the passive region (cathodic site, as discussed in Chapter 2.4 and 4.4). Of which, proteomic results revealed active energy metabolism pathway in the biofilm of the deep-sea SRB *P. piezophilus* incubated with mild steel (discussed in Chapter 2.4). This, however, does not indicate the direct electron uptake as the main mechanism stimulating the anodic dissolution (Eq. 1), as the source of the electron donor remains unknown in this case and there was not any extracellular or membrane electron transfer proteins found enriched. Alternatively, the enhanced corrosion can be explained by chemical attack by elemental sulfur (discussed in Chapter 4.4) on the metal or mechanical disruption of the protective passive film by the flagella motility (discussed in Chapter 2), which were often overlooked in the MIC research.

Nevertheless, this research is not without limitations. Firstly, the experiments tested exclusively on the unprotected marine-grade mild steel AH36. In practical application, mild steels are rarely deployed without protective measures such as cathodic polarization or coating. To address this, future experiments will investigate the MIC on the mild steels protected with corrosion-resistant coating, such as nickel and zinc plating, under deep-sea condition. Additionally, the scope of the study will be expanded to include the mechanical properties of MIC-corroded steels to provide a more comprehensive evaluation of material performance. Secondly, longer corrosion test duration is needed to evaluate long-term material performance. However, this is currently impractical with the existing high-pressure batch experimental setup, as the test solution/nutrients are only introduced at the beginning of the experiment. Furthermore, the current experimental setup is not conducive to electrochemical analysis, an important technique for corrosion analysis. To address the constraints mentioned above, we plan to overcome these limitations in future experiments by employing a high-pressure flow reactor that has recently been developed in our laboratory. This advanced reactor system is anticipated to facilitate longer test durations and enable electrochemical analysis, providing a more comprehensive understanding of material performance in deep-sea conditions. In summary, this dissertation has provided an unprecedented understanding of the deep-sea MIC and has confirmed that MIC remains a critical risk to mild steel even in the extreme environment of deep sea. This dissertation has also provided new insights into the physiological responses and microbial community responses in the context of deep-sea MIC.

References

1. Abbas, M. and Shafiee, M. (2020) An overview of maintenance management strategies for corroded steel structures in extreme marine environments. Marine Structures 71, 102718.
2. Abe, F. (2007) Exploration of the effects of high hydrostatic pressure on microbial growth, physiology and survival: Perspectives from piezophysiology. Bioscience, Biotechnology, and Biochemistry 71(10), 2347-2357.
3. Abe, F. (2013) Dynamic structural changes in microbial membranes in response to high hydrostatic pressure analyzed using time-resolved fluorescence anisotropy measurement. Biophysical Chemistry 183, 3-8.
4. Akpanyung, K.V. and Loto, R.T. (2019) Pitting corrosion evaluation: a review. Journal of Physics: Conference Series 1378(2), 022088.
5. Alazard, D., Dukan, S., Urios, A., Verhé, F., Bouabida, N., Morel, F., Thomas, P., Garcia, J.-L. and Ollivier, B. (2003) *Desulfovibrio hydrothermalis* sp. nov., a novel sulfate-reducing bacterium isolated from hydrothermal vents. International Journal of Systematic and Evolutionary Microbiology 53(1), 173-178.
6. Alvarez-Ortega, C., Olivares, J. and Martínez, J.L. (2013) RND multidrug efflux pumps: what are they good for? Front Microbiol 4, 7.
7. Amano, C., Zhao, Z., Sintes, E., Reinthaler, T., Stefanschitz, J., Kisadur, M., Utsumi, M. and Herndl, G.J. (2022) Limited carbon cycling due to high-pressure effects on the deep-sea microbiome. Nature Geoscience 15(12), 1041-1047.
8. Amrani, A., Bergon, A., Holota, H., Tamburini, C., Garel, M., Ollivier, B., Imbert, J., Dolla, A. and Pradel, N. (2014) Transcriptomics reveal several gene expression

patterns in the piezophile *Desulfovibrio hydrothermalis* in response to hydrostatic pressure. PLOS ONE 9(9), e106831.

9. Amrani, A., van Helden, J., Bergon, A., Aouane, A., Ben Hania, W., Tamburini, C., Loriod, B., Imbert, J., Ollivier, B., Pradel, N. and Dolla, A. (2016) Deciphering the adaptation strategies of *Desulfovibrio piezophilus* to hydrostatic pressure through metabolic and transcriptional analyses. Environmental microbiology reports 8(4), 520-526.
10. ASTM (2003) Standard practice for preparing, cleaning, and evaluation corrosion test specimens. ASTM international.
11. Baena, S., Fardeau, M.L., Labat, M., Ollivier, B., Garcia, J.L. and Patel, B.K. (1998) *Desulfovibrio aminophilus* sp. nov., a novel amino acid degrading and sulfate reducing bacterium from an anaerobic dairy wastewater lagoon. Syst Appl Microbiol 21(4), 498-504.
12. Bale, S.J., Goodman, K., Rochelle, P.A., Marchesi, J.R., Fry, J.C., Weightman, A.J. and Parkes, R.J. (1997) *Desulfovibrio profundus* sp. nov., a novel barophilic sulfate-reducing bacterium from deep sediment layers in the Japan Sea. International Journal of Systematic and Evolutionary Microbiology 47(2), 515-521.
13. Bartlett, D.H. and Bidle, K.A. (1999) Enigmatic Microorganisms and Life in Extreme Environments. Seckbach, J. (ed), pp. 501-512, Springer Netherlands, Dordrecht.
14. Barton, L.L. and Fauque, G.D. (2009) Advances in Applied Microbiology, pp. 41-98, Academic Press.

15. Batmanghelich, F., Li, L. and Seo, Y. (2017) Influence of multispecies biofilms of *Pseudomonas aeruginosa* and *Desulfovibrio vulgaris* on the corrosion of cast iron. Corrosion Science 121, 94-104.
16. Beech, I.B. and Campbell, S.A. (2008) Accelerated low water corrosion of carbon steel in the presence of a biofilm harbouring sulphate-reducing and sulphur-oxidising bacteria recovered from a marine sediment. Electrochimica Acta 54(1), 14-21.
17. Beese, P., Venzlaff, H., Srinivasan, J., Garrelfs, J., Stratmann, M. and Mayrhofer, K.J.J. (2013) Monitoring of anaerobic microbially influenced corrosion via electrochemical frequency modulation. Electrochimica Acta 105, 239-247.
18. Bernardez, L.A., de Andrade Lima, L.R.P., de Jesus, E.B., Ramos, C.L.S. and Almeida, P.F. (2013) A kinetic study on bacterial sulfate reduction. Bioprocess and Biosystems Engineering 36(12), 1861-1869.
19. Beverskog, B. and Puigdomenech, I. (1996) Revised pourbaix diagrams for iron at 25–300 °C. Corrosion Science 38(12), 2121-2135.
20. Blackwood, D.J. (2020) An electrochemist perspective of microbiologically influenced corrosion, pp. 59-76.
21. Bodor, A., Bounedjoum, N., Vincze, G.E., Erdeiné Kis, Á., Laczi, K., Bende, G., Szilágyi, Á., Kovács, T., Perei, K. and Rákhely, G. (2020) Challenges of unculturable bacteria: environmental perspectives. Reviews in Environmental Science and Bio/Technology 19(1), 1-22.
22. Bolney, R., Grosch, M., Winkler, M., van Slageren, J., Weigand, W. and Robl, C. (2021) Mackinawite formation from elemental iron and sulfur. RSC Adv 11(51), 32464-32475.

23. Bosdriesz, E., Molenaar, D., Teusink, B. and Bruggeman, F.J. (2015) How fast-growing bacteria robustly tune their ribosome concentration to approximate growth-rate maximization. The FEBS Journal 282(10), 2029-2044.
24. Brown, S.A., Balmonte, J.P., Hoarfrost, A., Ghobrial, S. and Arnosti, C. (2022) Depth-related patterns in microbial community responses to complex organic matter in the western North Atlantic Ocean. Biogeosciences 19(24), 5617-5631.
25. Brutinel, E.D. and Gralnick, J.A. (2012) Shuttling happens: soluble flavin mediators of extracellular electron transfer in *Shewanella*. Applied Microbiology and Biotechnology 93(1), 41-48.
26. Cai, R. and Jiao, N. (2023) Recalcitrant dissolved organic matter and its major production and removal processes in the ocean. Deep Sea Research Part I: Oceanographic Research Papers 191, 103922.
27. Caines, S., Khan, F. and Shirokoff, J. (2013) Analysis of pitting corrosion on steel under insulation in marine environments. Journal of Loss Prevention in the Process Industries 26(6), 1466-1483.
28. Callahan, B.J., McMurdie, P.J., Rosen, M.J., Han, A.W., Johnson, A.J.A. and Holmes, S.P. (2016) DADA2: High-resolution sample inference from Illumina amplicon data. Nature Methods 13(7), 581-583.
29. Camacho-Sanchez, M., Burraco, P., Gomez-Mestre, I. and Leonard, J.A. (2013) Preservation of RNA and DNA from mammal samples under field conditions. Molecular Ecology Resources 13(4), 663-673.
30. Cao, J., Gayet, N., Zeng, X., Shao, Z., Jebbar, M. and Alain, K. (2016) *Pseudodesulfovibrio indicus* gen. nov., sp. nov., a piezophilic sulfate-reducing bacterium from the Indian Ocean and reclassification of four species of the genus

Desulfovibrio. International Journal of Systematic and Evolutionary Microbiology 66(10), 3904-3911.

31. Chan, K.-Y., Xu, L.-C. and Fang, H.H.P. (2002) Anaerobic electrochemical corrosion of mild steel in the presence of extracellular polymeric substances produced by a culture enriched in sulfate-reducing bacteria. Environmental Science & Technology 36(8), 1720-1727.
32. Chang, W., Li, Y., Li, Z., Lou, Y., Cui, T., Qian, H., Mol, A. and Zhang, D. (2022) The effect of riboflavin on the microbiologically influenced corrosion of pure iron by *Shewanella oneidensis* MR-1. Bioelectrochemistry 147, 108173.
33. Chatterjee, M., Fan, Y., Cao, F., Jones, A.A., Pilloni, G. and Zhang, X. (2021) Proteomic study of *Desulfovibrio ferrophilus* IS5 reveals overexpressed extracellular multi-heme cytochrome associated with severe microbiologically influenced corrosion. Scientific Reports 11(1), 1-11.
34. Clark, M.E., Edelmann, R.E., Duley, M.L., Wall, J.D. and Fields, M.W. (2007) Biofilm formation in *Desulfovibrio vulgaris* Hildenborough is dependent upon protein filaments. Environ Microbiol 9(11), 2844-2854.
35. Cocolin, L., Manzano, M., Cantoni, C. and Comi, G. (2001) Denaturing gradient gel electrophoresis analysis of the 16S rRNA gene V1 region to monitor dynamic changes in the bacterial population during fermentation of Italian sausages. Appl Environ Microbiol 67(11), 5113-5121.
36. Commichau, F.M., Gunka, K., Landmann, J.J. and Stülke, J. (2008) Glutamate metabolism in *Bacillus subtilis*: gene expression and enzyme activities evolved to avoid futile cycles and to allow rapid responses to perturbations of the system. J Bacteriol 190(10), 3557-3564.

37. Cordes, E.E., Jones, D.O.B., Schlacher, T.A., Amon, D.J., Bernardino, A.F., Brooke, S., Carney, R., DeLeo, D.M., Dunlop, K.M., Escobar-Briones, E.G., Gates, A.R., Génio, L., Gobin, J., Henry, L.-A., Herrera, S., Hoyt, S., Joye, M., Kark, S., Mestre, N.C., Metaxas, A., Pfeifer, S., Sink, K., Sweetman, A.K. and Witte, U. (2016) Environmental impacts of the deep-water oil and gas industry: A review to guide management strategies. Frontiers in Environmental Science 4.
38. Corinaldesi, C. (2015) New perspectives in benthic deep-sea microbial ecology. Frontiers in Marine Science 2.
39. Costello, M.J., Cheung, A. and De Hauwere, N. (2010) Surface area and the seabed area, volume, depth, slope, and topographic variation for the world's seas, oceans, and countries. Environmental Science & Technology 44(23), 8821-8828.
40. Crapart, S., Fardeau, M.L., Cayol, J.L., Thomas, P., Sery, C., Ollivier, B. and Combet-Blanc, Y. (2007) *Exiguobacterium profundum* sp. nov., a moderately thermophilic, lactic acid-producing bacterium isolated from a deep-sea hydrothermal vent. Int J Syst Evol Microbiol 57(Pt 2), 287-292.
41. Cullimore, D.R. and Johnston, L.A. (2008) Microbiology of concretions, sediments and mechanisms influencing the preservation of submerged archaeological artifacts. International Journal of Historical Archaeology 12(2), 120-132.
42. Cypionka, H., Smock, A.M. and Böttcher, M.E. (1998) A combined pathway of sulfur compound disproportionation in *Desulfovibrio desulfuricans*. FEMS Microbiology Letters 166(2), 181-186.
43. D'Amico, S., Collins, T., Marx, J.-C., Feller, G., Gerday, C. and Gerday, C. (2006) Psychrophilic microorganisms: challenges for life. EMBO reports 7(4), 385-389.

44. Dar, S.A., Kleerebezem, R., Stams, A.J.M., Kuenen, J.G. and Muyzer, G. (2008) Competition and coexistence of sulfate-reducing bacteria, acetogens and methanogens in a lab-scale anaerobic bioreactor as affected by changing substrate to sulfate ratio. Applied Microbiology and Biotechnology 78(6), 1045-1055.
45. Deng, X., Dohmae, N., Kaksonen, A.H. and Okamoto, A. (2020) Biogenic iron sulfide nanoparticles to enable extracellular electron uptake in sulfate-reducing bacteria. Angewandte Chemie International Edition 59(15), 5995-5999.
46. Deng, X., Nakamura, R., Hashimoto, K. and Okamoto, A. (2015) Electron extraction from an extracellular electrode by *Desulfovibrio ferrophilus* Strain IS5 without using hydrogen as an electron carrier. Electrochemistry 83(7), 529-531.
47. Dinh, H.T., Kuever, J., Mußmann, M., Hassel, A.W., Stratmann, M. and Widdel, F. (2004) Iron corrosion by novel anaerobic microorganisms. Nature 427(6977), 829-832.
48. Dittmar, T., Lennartz, S.T., Buck-Wiese, H., Hansell, D.A., Santinelli, C., Vanni, C., Blasius, B. and Hehemann, J.-H. (2021) Enigmatic persistence of dissolved organic matter in the ocean. Nature Reviews Earth & Environment 2(8), 570-583.
49. Dou, W., Liu, J., Cai, W., Wang, D., Jia, R., Chen, S. and Gu, T. (2019) Electrochemical investigation of increased carbon steel corrosion via extracellular electron transfer by a sulfate reducing bacterium under carbon source starvation. Corrosion Science 150, 258-267.
50. Eduok, U., Ohaeri, E. and Szpunar, J. (2019) Accelerated corrosion of pipeline steel in the presence of *Desulfovibrio desulfuricans* biofilm due to carbon source deprivation in CO2 saturated medium. Materials Science and Engineering: C 105, 110095.

51. Edyvean, R.G.J. (1991) Hydrogen sulphide — A corrosive metabolite. International Biodeterioration 27(2), 109-120.
52. Eklund, G.S. (1974) Initiation of pitting at sulfide inclusions in stainless steel. Journal of The Electrochemical Society 121(4), 467.
53. El Mendili, Y., Abdelouas, A. and Bardeau, J.-F. (2014) The corrosion behavior of carbon steel in sulfide aqueous media at 30°C. Journal of Materials Engineering and Performance 23(4), 1350-1357.
54. Emerson, S., Fischer, K., Reimers, C. and Heggie, D. (1985) Organic carbon dynamics and preservation in deep-sea sediments. Deep Sea Research Part A. Oceanographic Research Papers 32(1), 1-21.
55. Enning, D. and Garrelfs, J. (2014) Corrosion of iron by sulfate-reducing bacteria: new views of an old problem. Applied and Environmental Microbiology 80(4), 1226-1236.
56. Enning, D., Venzlaff, H., Garrelfs, J., Dinh, H.T., Meyer, V., Mayrhofer, K., Hassel, A.W., Stratmann, M. and Widdel, F. (2012) Marine sulfate-reducing bacteria cause serious corrosion of iron under electroconductive biogenic mineral crust. Environmental Microbiology 14(7), 1772-1787.
57. Erbacher, J. and Nelskamp, S. (2006) Comparison of benthic foraminifera inside and outside a sulphur-oxidizing bacterial mat from the present oxygen-minimum zone off Pakistan (NE Arabian Sea). Deep Sea Research Part I: Oceanographic Research Papers 53(5), 751-775.
58. Erfanian, A., Moayed, M.H., Mirjalili, M. and Pahlavan, S. (2022) Insight into the Elemental Sulfur Corrosion of Carbon Steel in Chloride Bearing Media Using Electrochemical and Non-electrochemical Techniques. Journal of the Taiwan Institute of Chemical Engineers 131, 104177.

59. Eschemann, A., Kühl, M. and Cypionka, H. (1999) Aerotaxis in *Desulfovibrio*. Environmental Microbiology 1(6), 489-494.

60. Fang, H., Young, D. and Nesic, S. (2008) Corrosion of mild steel in the presence of elemental sulfur, pp. NACE-08637.

61. Fang, J., Zhang, L. and Bazylinski, D.A. (2010) Deep-sea piezosphere and piezophiles: geomicrobiology and biogeochemistry. Trends in Microbiology 18(9), 413-422.

62. Farahati, R., Mousavi-Khoshdel, S.M., Ghaffarinejad, A. and Behzadi, H. (2020) Experimental and computational study of penicillamine drug and cysteine as water-soluble green corrosion inhibitors of mild steel. Progress in Organic Coatings 142, 105567.

63. Felbeck, H. and Somero, G.N. (1982) Primary production in deep-sea hydrothermal vent organisms: roles of sulfide-oxidizing bacteria. Trends in Biochemical Sciences 7(6), 201-204.

64. Finster, K., Liesack, W. and Thamdrup, B. (1998) Elemental sulfur and thiosulfate disproportionation by *Desulfocapsa sulfoexigens* sp. nov., a new anaerobic bacterium isolated from marine surface sediment. Applied and Environmental Microbiology 64(1), 119-125.

65. Flemming, H.-C., Wingender, J., Szewzyk, U., Steinberg, P., Rice, S.A. and Kjelleberg, S. (2016) Biofilms: an emergent form of bacterial life. Nature Reviews Microbiology 14(9), 563-575.

66. Fonknechten, N., Chaussonnerie, S., Tricot, S., Lajus, A., Andreesen, J.R., Perchat, N., Pelletier, E., Gouyvenoux, M., Barbe, V., Salanoubat, M., Le Paslier, D., Weissenbach, J., Cohen, G.N. and Kreimeyer, A. (2010) *Clostridium sticklandii*, a

specialist in amino acid degradation:revisiting its metabolism through its genome sequence. BMC Genomics 11(1), 555.

67. Frankel, G.S. (2016) Active Protective Coatings: New-Generation Coatings for Metals. Hughes, A.E., Mol, J.M.C., Zheludkevich, M.L. and Buchheit, R.G. (eds), pp. 17-32, Springer Netherlands, Dordrecht.
68. Fu, J.-j., Li, S.-n., Wang, Y., Liu, X.-d. and Lu, L.-d. (2011) Computational and electrochemical studies on the inhibition of corrosion of mild steel by *l*-cysteine and its derivatives. Journal of Materials Science 46(10), 3550-3559.
69. Fukasawa, K.M., Hata, T., Ono, Y. and Hirose, J. (2011) Metal preferences of zinc-binding motif on metalloproteases. J Amino Acids 2011, 574816.
70. Gaines, R.H. (1910) Bacterial activity as a corrosive influence in the soil. Journal of Industrial & Engineering Chemistry 2(4), 128-130.
71. Ge, T., Luo, C., Ren, P., Zhang, H., Chen, H., Chen, Z., Zhang, J. and Wang, X. (2022) Dissolved Organic Carbon Along a Meridional Transect in the Western North Pacific Ocean: Distribution, Variation and Controlling Processes. Frontiers in Marine Science 9.
72. Giering, S.L.C., Cavan, E.L., Basedow, S.L., Briggs, N., Burd, A.B., Darroch, L.J., Guidi, L., Irisson, J.-O., Iversen, M.H., Kiko, R., Lindsay, D., Marcolin, C.R., McDonnell, A.M.P., Möller, K.O., Passow, U., Thomalla, S., Trull, T.W. and Waite, A.M. (2020) Sinking organic particles in the ocean—Flux estimates from in situ optical devices. Frontiers in Marine Science 6.
73. Glombitza, C., Egger, M., Røy, H. and Jørgensen, B.B. (2019) Controls on volatile fatty acid concentrations in marine sediments (Baltic Sea). Geochimica et Cosmochimica Acta 258, 226-241.

74. Gross, M. and Jaenicke, R. (1994) Proteins under pressure. European Journal of Biochemistry 221(2), 617-630.
75. Gruber, N. (2008) The marine nitrogen cycle: overview and challenges. Nitrogen in the marine environment 2, 1-50.
76. Gu, T. and Galicia, B. (2012) Can acid producing bacteria be responsible for very fast MIC pitting?, pp. NACE-2012-1214.
77. Gu, T., Jia, R., Unsal, T. and Xu, D. (2019) Toward a better understanding of microbiologically influenced corrosion caused by sulfate reducing bacteria. Journal of Materials Science & Technology 35(4), 631-636.
78. Guan, F., Liu, Z., Dong, X., Zhai, X., Zhang, B., Duan, J., Wang, N., Gao, Y., Yang, L. and Hou, B. (2021) Synergistic effect of carbon starvation and exogenous redox mediators on corrosion of X70 pipeline steel induced by *Desulfovibrio singaporenus*. Science of The Total Environment 788, 147573.
79. Guo, X., Park, J.E., Gallart-Palau, X. and Sze, S.K. (2020) Oxidative Damage to the TCA Cycle Enzyme MDH1 Dysregulates Bioenergetic Enzymatic Activity in the Aged Murine Brain. Journal of Proteome Research 19(4), 1706-1717.
80. Hamdan, L.J., Hampel, J.J., Moseley, R.D., Mugge, R.L., Ray, A., Salerno, J.L. and Damour, M. (2021) Deep-sea shipwrecks represent island-like ecosystems for marine microbiomes. The ISME Journal 15(10), 2883-2891.
81. Hansell, D.A. and Orellana, M.V. (2021) Dissolved Organic Matter in the Global Ocean: A Primer. Gels 7(3).
82. Hou, X., Gao, L., Cui, Z. and Yin, J. (2018) Corrosion and protection of metal in the seawater desalination. IOP Conference Series: Earth and Environmental Science 108(2), 022037.

83. Huang, G., Chan, K.-Y. and Fang, H.H.P. (2004) Microbiologically Induced Corrosion of 70Cu-30Ni Alloy in Anaerobic Seawater. Journal of The Electrochemical Society 151(7), B434.
84. Huang, H.-W., Lung, H.-M., Yang, B.B. and Wang, C.-Y. (2014) Responses of microorganisms to high hydrostatic pressure processing. Food Control 40, 250-259.
85. Ichiye, T. (2018) Enzymes from piezophiles. Semin Cell Dev Biol 84, 138-146.
86. Iverson, W.P. (1966) Direct evidence for the cathodic depolarization theory of bacterial corrosion. Science 151(3713), 986-988.
87. Jia, R., Unsal, T., Xu, D., Lekbach, Y. and Gu, T. (2019) Microbiologically influenced corrosion and current mitigation strategies: A state of the art review. International Biodeterioration & Biodegradation 137, 42-58.
88. Jiao, N., Cai, R., Zheng, Q., Tang, K., Liu, J., Jiao, F., Wallace, D., Chen, F., Li, C., Amann, R., Benner, R. and Azam, F. (2018) Unveiling the enigma of refractory carbon in the ocean. National Science Review 5(4), 459-463.
89. Joo, J.o., Choi, J.-H., Kim, I.H., Kim, Y.-K. and Oh, B.-K. (2015) Effective bioremediation of Cadmium (II), nickel (II), and chromium (VI) in a marine environment by using *Desulfovibrio desulfuricans*. Biotechnology and Bioprocess Engineering 20(5), 937-941.
90. Jørgensen, B.B. (1982) Mineralization of organic matter in the sea bed—the role of sulphate reduction. Nature 296(5858), 643-645.
91. Jørgensen, B.B. and Boetius, A. (2007) Feast and famine — microbial life in the deep-sea bed. Nature Reviews Microbiology 5(10), 770-781.
92. Jørgensen, B.B., Findlay, A.J. and Pellerin, A. (2019) The biogeochemical sulfur cycle of marine sediments. Frontiers in Microbiology 10.

93. Kanehisa, M., Furumichi, M., Sato, Y., Kawashima, M. and Ishiguro-Watanabe, M. (2023) KEGG for taxonomy-based analysis of pathways and genomes. Nucleic Acids Res 51(D1), D587-d592.

94. Kato, S. (2016) Microbial extracellular electron transfer and its relevance to iron corrosion. Microbial Biotechnology 9(2), 141-148.

95. Kato, S., Yumoto, I. and Kamagata, Y. (2015) Isolation of acetogenic bacteria that induce biocorrosion by utilizing metallic iron as the sole electron donor. Applied and Environmental Microbiology 81(1), 67-73.

96. Kaur, J., Vishnu, A.L., Khipla, N. and Kaur, J. (2022) Survival Strategies in Cold-adapted Microorganisms. Goel, R., Soni, R., Suyal, D.C. and Khan, M. (eds), pp. 63-86, Springer Singapore, Singapore.

97. Khelaifia, S., Fardeau, M.L., Pradel, N., Aussignargues, C., Garel, M., Tamburini, C., Cayol, J.L., Gaudron, S., Gaill, F. and Ollivier, B. (2011) *Desulfovibrio piezophilus* sp. nov., a piezophilic, sulfate-reducing bacterium isolated from wood falls in the Mediterranean Sea. Int J Syst Evol Microbiol 61(Pt 11), 2706-2711.

98. Kip, N. and van Veen, J.A. (2015) The dual role of microbes in corrosion. The ISME Journal 9(3), 542-551.

99. Knisz, J., Eckert, R., Gieg, L.M., Koerdt, A., Lee, J.S., Silva, E.R., Skovhus, T.L., An Stepec, B.A. and Wade, S.A. (2023) Microbiologically influenced corrosion—more than just microorganisms. FEMS Microbiology Reviews 47(5), fuad041.

100. Koontz, L. (2014) Methods in Enzymology. Lorsch, J. (ed), pp. 3-10, Academic Press.

101. Koschinsky, A., Heinrich, L., Boehnke, K., Cohrs, J.C., Markus, T., Shani, M., Singh, P., Smith Stegen, K. and Werner, W. (2018) Deep-sea mining: Interdisciplinary research on potential environmental, legal, economic, and societal

implications. Integrated Environmental Assessment and Management 14(6), 672-691.

102. Krumholz, L.R., Bradstock, P., Sheik, C.S., Diao, Y., Gazioglu, O., Gorby, Y. and McInerney, M.J. (2015) Syntrophic growth of Desulfovibrio alaskensis requires genes for H2 and formate metabolism as well as those for flagellum and biofilm formation. Appl Environ Microbiol 81(7), 2339-2348.

103. Kühr, C.A.H.V.W. and Van der Vlugt, L.S. (1934) The graphitization of cast iron as an electrochemical process in anaerobic soils. Water 18, 147-165.

104. Kvarekvål, J. and Moloney, J. (2017) Trends in Oil and Gas Corrosion Research and Technologies. El-Sherik, A.M. (ed), pp. 113-147, Woodhead Publishing, Boston.

105. Lauro, F.M. and Bartlett, D.H. (2008) Prokaryotic lifestyles in deep sea habitats. Extremophiles 12(1), 15-25.

106. Lee, M.-S. (2004) Chemical equilibria in ferrous chloride acid solution. Metals and Materials International 10(4), 387-392.

107. Li, E., Wu, J., Zhang, D., Wang, P., Zhu, L., Li, C., Sun, Z. and Gao, Y. (2022a) Effect of autoinducer-2 on corrosion of Q235 carbon steel caused by sulfate reducing bacteria. Corrosion Science 200, 110220.

108. Li, H., Xu, D., Li, Y., Feng, H., Liu, Z., Li, X., Gu, T. and Yang, K. (2015a) Extracellular electron transfer Is a bottleneck in the microbiologically influenced corrosion of C1018 carbon steel by the biofilm of sulfate-reducing bacterium *Desulfovibrio vulgaris*. PLOS ONE 10(8), e0136183.

109. Li, M., Baker, B.J., Anantharaman, K., Jain, S., Breier, J.A. and Dick, G.J. (2015b) Genomic and transcriptomic evidence for scavenging of diverse organic compounds by widespread deep-sea archaea. Nature Communications 6(1), 8933.

110. Li, Z., Xue, W., Chen, Y., Yu, W. and Xiao, K. (2022b) Microstructure and grain boundary corrosion mechanism of pearlitic material. Journal of Materials Engineering and Performance 31(1), 483-494.

111. Li, Z., Yang, J., Guo, H., Kumseranee, S., Punpruk, S., Mohamed, M.E., Saleh, M.A. and Gu, T. (2022c) Mechanical property degradation of X80 pipeline steel due to microbiologically influenced corrosion caused by *Desulfovibrio vulgaris*. Frontiers in Bioengineering and Biotechnology 10.

112. Liang, D., Liu, X., Woodard, T.L., Holmes, D.E., Smith, J.A., Nevin, K.P., Feng, Y. and Lovley, D.R. (2021) Extracellular electron exchange capabilities of *Desulfovibrio ferrophilus* and *Desulfopila corrodens*. Environmental Science & Technology 55(23), 16195-16203.

113. Little, B.J., Gerke, T.L. and Lee, J.S. (2014) Mini-review: the morphology, mineralogy and microbiology of accumulated iron corrosion products. Biofouling 30(8), 941-948.

114. Liu, B., Fang, Z.-g., Wang, H.-b. and Wang, T. (2013) Effect of cross linking degree and adhesion force on the anti-corrosion performance of epoxy coatings under simulated deep sea environment. Progress in Organic Coatings 76(12), 1814-1818.

115. Liu, H. and Cheng, Y.F. (2020) Corrosion of X52 pipeline steel in a simulated soil solution with coexistence of Desulfovibrio desulfuricans and Pseudomonas aeruginosa bacteria. Corrosion Science 173, 108753.

116. Liu, H., Gu, T., Asif, M., Zhang, G. and Liu, H. (2017) The corrosion behavior and mechanism of carbon steel induced by extracellular polymeric substances of iron-oxidizing bacteria. Corrosion Science 114, 102-111.

117. Liu, R., Cui, Y., Liu, L. and Wang, F. (2021) Study on the mechanism of hydrostatic pressure promoting electrochemical corrosion of pure iron in 3.5% NaCl solution. Acta Materialia 203, 116467.

118. Liu, Y., Wang, Z. and Wei, Y. (2019) Influence of Seawater on the Carbon Steel Initial Corrosion Behavior. International Journal of Electrochemical Science 14(2), 1147-1162.

119. Liu, Y., Zhong, X., Wang, Z., Campbell, K.S., Zhou, L., Yuan, X., Yu, J., Li, L. and Hu, J. (2023) Permeating hydrogen generated from the elemental sulfur corrosion of low carbon steel. Corrosion Science 213, 110987.

120. Lovley, D.R. and Walker, D.J.F. (2019) *Geobacter* protein nanowires. Frontiers in Microbiology 10.

121. Lv, M., Du, M. and Li, Z. (2022) Investigation of mixed species biofilm on corrosion of X65 steel in seawater environment. Bioelectrochemistry 143, 107951.

122. Lyles, C., Le, H., Beasley, W., McInerney, M. and Suflita, J. (2014) Anaerobic hydrocarbon and fatty acid metabolism by syntrophic bacteria and their impact on carbon steel corrosion. Frontiers in Microbiology 5.

123. Ma, H., Cheng, X., Li, G., Chen, S., Quan, Z., Zhao, S. and Niu, L. (2000) The influence of hydrogen sulfide on corrosion of iron under different conditions. Corrosion Science 42(10), 1669-1683.

124. Marciales, A., Peralta, Y., Haile, T., Crosby, T. and Wolodko, J. (2019) Mechanistic microbiologically influenced corrosion modeling—A review. Corrosion Science 146, 99-111.

125. Martin, D., Bartlett, D.H. and Roberts, M.F. (2002) Solute accumulation in the deep-sea bacterium *Photobacterium profundum*. Extremophiles 6(6), 507-514.

126. Matsuki, T., Watanabe, K., Fujimoto, J., Miyamoto, Y., Takada, T., Matsumoto, K., Oyaizu, H. and Tanaka, R. (2002) Development of 16S rRNA-gene-targeted group-specific primers for the detection and identification of predominant bacteria in human feces. Appl Environ Microbiol 68(11), 5445-5451.

127. May Kerrie, L., Lehman Kelly, M., Mitchell Angela, M. and Grabowicz, M. (2019) A stress response monitoring lipoprotein trafficking to the outer membrane. mBio 10(3), 10.1128/mbio.00618-00619.

128. McMurdie, P.J. and Holmes, S. (2013) phyloseq: An R package for reproducible interactive analysis and graphics of microbiome census data. PLOS ONE 8(4), e61217.

129. McMurdie, P.J. and Holmes, S. (2014) Waste not, want not: Why rarefying microbiome data Is inadmissible. PLOS Computational Biology 10(4), e1003531.

130. Melchers, R.E. (2005) Effect of immersion depth on marine corrosion of mild steel. Corrosion 61(09).

131. Melchers, R.E. (2021) Long-term corrosion of steels in deep, cold, low oxygen sea waters. Corrosion Engineering, Science and Technology 56(8), 736-741.

132. Miller, J.D., Warren, B.J. and Chabot, L.G. (2012) Microbiologically influenced corrosion of Gulf of Mexico mooring chain at 6,000 feet depths, pp. 649-658.

133. Mori, K., Tsurumaru, H. and Harayama, S. (2010) Iron corrosion activity of anaerobic hydrogen-consuming microorganisms isolated from oil facilities. Journal of Bioscience and Bioengineering 110(4), 426-430.

134. Muehlenbachs, L., Cohen, M.A. and Gerarden, T. (2013) The impact of water depth on safety and environmental performance in offshore oil and gas production. Energy Policy 55, 699-705.

135. Mugge, R.L., Brock, M.L., Salerno, J.L., Damour, M., Church, R.A., Lee, J.S. and Hamdan, L.J. (2019) Deep-sea biofilms, historic shipwreck preservation and the Deepwater Horizon spill. Frontiers in Marine Science 6.

136. Muyzer, G. and Stams, A.J.M. (2008) The ecology and biotechnology of sulphate-reducing bacteria. Nature Reviews Microbiology 6(6), 441-454.

137. Nair, R.R., Silveira, C.M., Diniz, M.S., Almeida, M.G., Moura, J.J.G. and Rivas, M.G. (2015) Changes in metabolic pathways of *Desulfovibrio alaskensis* G20 cells induced by molybdate excess. JBIC Journal of Biological Inorganic Chemistry 20(2), 311-322.

138. NOAA World Ocean Atlas, National Ocean Service.

139. Ogata, H., Lubitz, W. and Higuchi, Y. (2016) Structure and function of [NiFe] hydrogenases. The Journal of Biochemistry 160(5), 251-258.

140. Padilla-Viveros, A., Garcia-Ochoa, E. and Alazard, D. (2006) Comparative electrochemical noise study of the corrosion process of carbon steel by the sulfate-reducing bacterium Desulfovibrio alaskensis under nutritionally rich and oligotrophic culture conditions. Electrochimica Acta 51(18), 3841-3847.

141. Pankhania, I.P., Moosavi, A.N. and Hamilton, W.A. (1986) Utilization of cathodic hydrogen by *Desulfovibrio vulgaris* (Hildenborough). Microbiology 132(12), 3357-3365.

142. Pawlowicz, R. (2013) Key physical variables in the ocean: Temperature, salinity, and density, Nature Education Knowledge.

143. Pi, R.-X., Zhang, W.-W., Fang, M.-X., Zhang, Y.-Z., Li, T.-T., Wu, M. and Zhu, X.-F. (2013) *Oceanirhabdus sediminicola* gen. nov., sp. nov., an anaerobic bacterium isolated from sea sediment. International Journal of Systematic and Evolutionary Microbiology 63(Pt_11), 4277-4283.

144. Pirbadian, S., Barchinger, S.E., Leung, K.M., Byun, H.S., Jangir, Y., Bouhenni, R.A., Reed, S.B., Romine, M.F., Saffarini, D.A., Shi, L., Gorby, Y.A., Golbeck, J.H. and El-Naggar, M.Y. (2014) *Shewanella oneidensis* MR-1 nanowires are outer membrane and periplasmic extensions of the extracellular electron transport components. Proceedings of the National Academy of Sciences 111(35), 12883-12888.

145. Popoola, L.T., Grema, A.S., Latinwo, G.K., Gutti, B. and Balogun, A.S. (2013) Corrosion problems during oil and gas production and its mitigation. International Journal of Industrial Chemistry 4(1), 35.

146. Popov, B.N. (2015) Corrosion Engineering. Popov, B.N. (ed), pp. 29-92, Elsevier, Amsterdam.

147. Pradel, N., Ji, B., Gimenez, G., Talla, E., Lenoble, P., Garel, M., Tamburini, C., Fourquet, P., Lebrun, R., Bertin, P., Denis, Y., Pophillat, M., Barbe, V., Ollivier, B. and Dolla, A. (2013) The first genomic and proteomic characterization of a deep-sea sulfate reducer: Insights into the piezophilic lifestyle of *Desulfovibrio piezophilus*. PLOS ONE 8(1), e55130.

148. Price, M.N., Ray, J., Wetmore, K.M., Kuehl, J.V., Bauer, S., Deutschbauer, A.M. and Arkin, A.P. (2014) The genetic basis of energy conservation in the sulfate-reducing bacterium *Desulfovibrio alaskensis* G20. Frontiers in Microbiology 5.

149. Price, S.J. and Figueira, R.B. (2017) Corrosion protection systems and fatigue corrosion in offshore wind structures: Current status and future perspectives. Coatings 7(2), 25.

150. Pu, Y., Tian, Y., Hou, S., Dou, W. and Chen, S. (2023) Carbon starvation considerably accelerated nickel corrosion by Desulfovibrio vulgaris. Bioelectrochemistry 153, 108453.

151. Puentes-Cala, E., Tapia-Perdomo, V., Espinosa-Valbuena, D., Reyes-Reyes, M., Quintero-Santander, D., Vasquez-Dallos, S., Salazar, H., Santamaría-Galvis, P., Silva-Rodríguez, R. and Castillo-Villamizar, G. (2022) Microbiologically influenced corrosion: The gap in the field. Frontiers in Environmental Science 10.

152. Pusparizkita, Y.M., Fardilah, V.A., Aslan, C., Jamari, J. and Bayuseno, A.P. (2023) Understanding of low-carbon steel marine corrosion through simulation in artificial seawater. AIMS Materials Science 10(3), 499-516.

153. Pyenson, H. and Tracy, P.H. (1945) A 1,10—Phenanthroline Method for the Determination of Iron in Powdered Milk. Journal of Dairy Science 28(5), 401-412.

154. Qureshi, M.H., Kato, C. and Horikoshi, K. (1998) Purification of a *ccb*-type quinol oxidase specifically induced in a deep-sea barophilic bacterium, *Shewanella* sp. strain DB-172F. Extremophiles 2(2), 93-99.

155. Rajala, P., Cheng, D.Q., Rice, S.A. and Lauro, F.M. (2022) Sulfate-dependant microbially induced corrosion of mild steel in the deep sea: a 10-year microbiome study. Microbiome 10(1), 4.

156. Rasmussen, J.J., Vegge, C.S., Frøkiær, H., Howlett, R.M., Krogfelt, K.A., Kelly, D.J. and Ingmer, H. (2013) *Campylobacter jejuni* carbon starvation protein A (CstA) is involved in peptide utilization, motility and agglutination, and has a role in stimulation of dendritic cells. Journal of Medical Microbiology 62(8), 1135-1143.

157. Refait, P., Grolleau, A.-M., Jeannin, M., Rémazeilles, C. and Sabot, R. (2020) Corrosion of Carbon Steel in Marine Environments: Role of the Corrosion Product Layer, pp. 198-218.

158. Reinhart, F.M. (1976) Corrosion of metals and alloys in the deep ocean, Civil Engineering Lab (Navy) Port Hueneme CA.

159. Salgar-Chaparro, S.J., Darwin, A., Kaksonen, A.H. and Machuca, L.L. (2020) Carbon steel corrosion by bacteria from failed seal rings at an offshore facility. Scientific Reports 10(1), 12287.

160. Sass, A.M., Eschemann, A., Kühl, M., Thar, R., Sass, H. and Cypionka, H. (2002) Growth and chemosensory behavior of sulfate-reducing bacteria in oxygen—sulfide gradients. FEMS Microbiology Ecology 40(1), 47-54.

161. Sena Martins, M., Serra, N. and Stammer, D. (2015) Spatial and temporal scales of sea surface salinity variability in the Atlantic Ocean. Journal of Geophysical Research: Oceans 120(6), 4306-4323.

162. Sharma, S., Zhou, R., Wan, L., Feng, S., Song, K., Xu, C., Li, Y. and Liao, M. (2021) Mechanism of LolCDE as a molecular extruder of bacterial triacylated lipoproteins. Nat Commun 12(1), 4687.

163. Sherar, B.W.A., Power, I.M., Keech, P.G., Mitlin, S., Southam, G. and Shoesmith, D.W. (2011) Characterizing the effect of carbon steel exposure in sulfide containing solutions to microbially induced corrosion. Corrosion Science 53(3), 955-960.

164. Sliem, M.H., Fayyad, E.M., Abdullah, A.M., Younan, N.A., Al-Qahtani, N., Nabhan, F.F., Ramesh, A., Laycock, N., Ryan, M.P., Maqbool, M. and Arora, D. (2021) Monitoring of under deposit corrosion for the oil and gas industry: A review. Journal of Petroleum Science and Engineering 204, 108752.

165. Slobodkin, A.I., Tourova, T.P., Kostrikina, N.A., Chernyh, N.A., Bonch-Osmolovskaya, E.A., Jeanthon, C. and Jones, B.E. (2003) *Tepidibacter thalassicus* gen. nov., sp. nov., a novel moderately thermophilic, anaerobic, fermentative bacterium from a deep-sea hydrothermal vent. Int J Syst Evol Microbiol 53(Pt 4), 1131-1134.

166. Sowards, J.W. and Mansfield, E. (2014) Corrosion of copper and steel alloys in a simulated underground storage-tank sump environment containing acid-producing bacteria. Corrosion Science 87, 460-471.

167. Steudel, R. (1996) Mechanism for the formation of elemental sulfur from aqueous sulfide in chemical and microbiological desulfurization processes. Industrial & Engineering Chemistry Research 35(4), 1417-1423.

168. Stipaničev, M., Turcu, F., Esnault, L., Schweitzer, E.W., Kilian, R. and Basseguy, R. (2013) Corrosion behavior of carbon steel in presence of sulfate-reducing bacteria in seawater environment. Electrochimica Acta 113, 390-406.

169. Stott, J.F.D. and Abdullahi, A.A. (2018) Reference Module in Materials Science and Materials Engineering, Elsevier.

170. Su, H., Tang, R., Peng, X., Gao, A. and Han, Y. (2020) Corrosion behavior and mechanism of carbon steel influenced by interior deposit microflora of an in-service pipeline. Bioelectrochemistry 132, 107406.

171. Sun, H., Liu, L., Li, Y. and Wang, F. (2013) Effect of hydrostatic pressure on the corrosion behavior of a low alloy steel. Journal of The Electrochemical Society 160(3), C89.

172. Sweeton, F.H. and Baes, C.F. (1970) The solubility of magnetite and hydrolysis of ferrous ion in aqueous solutions at elevated temperatures. The Journal of Chemical Thermodynamics 2(4), 479-500.

173. Takii, S., Hanada, S., Tamaki, H., Ueno, Y., Sekiguchi, Y., Ibe, A. and Matsuura, K. (2007) *Dethiosulfatibacter aminovorans* gen. nov., sp. nov., a novel thiosulfate-reducing bacterium isolated from coastal marine sediment via sulfate-reducing enrichment with casamino acids. Int J Syst Evol Microbiol 57(Pt 10), 2320-2326.

174. Tamby, A., Sinninghe Damsté, J.S. and Villanueva, L. (2022) Microbial membrane lipid adaptations to high hydrostatic pressure in the marine environment. Front Mol Biosci 9, 1058381.

175. Tamura, H. (2008) The role of rusts in corrosion and corrosion protection of iron and steel. Corrosion Science 50(7), 1872-1883.

176. Tan, H.-Q., Wu, X.-Y., Zhang, X.-Q., Wu, M. and Zhu, X.-F. (2012) *Tepidibacter mesophilus* sp. nov., a mesophilic fermentative anaerobe isolated from soil polluted by crude oil, and emended description of the genus *Tepidibacter*. International Journal of Systematic and Evolutionary Microbiology 62(1), 66-70.

177. Tang, H.-Y., Yang, C., Ueki, T., Pittman, C.C., Xu, D., Woodard, T.L., Holmes, D.E., Gu, T., Wang, F. and Lovley, D.R. (2021) Stainless steel corrosion via direct iron-to-microbe electron transfer by *Geobacter* species. The ISME Journal 15(10), 3084-3093.

178. Tian, F., He, X., Bai, X. and Yuan, C. (2020) Electrochemical corrosion behaviors and mechanism of carbon steel in the presence of acid-producing bacterium *Citrobacter farmeri* in artificial seawater. International Biodeterioration & Biodegradation 147, 104872.

179. Torres-Beltrán, M., Vargas-Gastélum, L., Magdaleno-Moncayo, D., Riquelme, M., Herguera-García, J.C., Prieto-Davó, A. and Lago-Lestón, A. (2021) The metabolic core of the prokaryotic community from deep-sea sediments of the

southern Gulf of Mexico shows different functional signatures between the continental slope and abyssal plain. PeerJ 9, e12474.

180. Tran, T.T.T., Kannoorpatti, K., Padovan, A. and Thennadil, S. (2021) A study of bacteria adhesion and microbial corrosion on different stainless steels in environment containing *Desulfovibrio vulgaris*. Royal Society Open Science 8(1), 201577.

181. Traverso, P. and Canepa, E. (2014) A review of studies on corrosion of metals and alloys in deep-sea environment. Ocean Engineering 87, 10-15.

182. Treude, T., Smith, C.R., Wenzhöfer, F., Carney, E., Bernardino, A.F., Hannides, A.K., Krüger, M. and Boetius, A. (2009) Biogeochemistry of a deep-sea whale fall: sulfate reduction, sulfide efflux and methanogenesis. Marine Ecology Progress Series 382, 1-21.

183. Tripathi, A.K., Thakur, P., Saxena, P., Rauniyar, S., Gopalakrishnan, V., Singh, R.N., Gadhamshetty, V., Gnimpieba, E.Z., Jasthi, B.K. and Sani, R.K. (2021) Gene sets and mechanisms of sulfate-reducing bacteria biofilm formation and quorum sensing with impact on corrosion. Frontiers in Microbiology 12.

184. Trovero, M.F., Scavone, P., Platero, R., de Souza, E.M., Fabiano, E. and Rosconi, F. (2018) *Herbaspirillum seropedicae* differentially expressed genes in response to iron availability. Frontiers in Microbiology 9.

185. Tsurumaru, H., Ito, N., Mori, K., Wakai, S., Uchiyama, T., Iino, T., Hosoyama, A., Ataku, H., Nishijima, K., Mise, M., Shimizu, A., Harada, T., Horikawa, H., Ichikawa, N., Sekigawa, T., Jinno, K., Tanikawa, S., Yamazaki, J., Sasaki, K., Yamazaki, S., Fujita, N. and Harayama, S. (2018) An extracellular [NiFe] hydrogenase mediating iron corrosion is encoded in a genetically unstable genomic island in *Methanococcus maripaludis*. Scientific Reports 8(1), 15149.

186. Tyler, R.H., Boyer, T.P., Minami, T., Zweng, M.M. and Reagan, J.R. (2017) Electrical conductivity of the global ocean. Earth, Planets and Space 69(1), 156.

187. Ueki, T. and Lovley, D.R. (2022) *Desulfovibrio vulgaris* as a model microbe for the study of corrosion under sulfate-reducing conditions. mLife 1(1), 13-20.

188. Ueki, T., Woodard Trevor, L. and Lovley Derek, R. (2022) Genetic manipulation of *Desulfovibrio ferrophilus* and evaluation of Fe(III) oxide reduction mechanisms. Microbiology Spectrum 10(6), e03922-03922.

189. Umoren, S.A., Solomon, M.M. and Saji, V.S. (2022) Polymeric Materials in Corrosion Inhibition. Umoren, S.A., Solomon, M.M. and Saji, V.S. (eds), pp. 83-102, Elsevier.

190. Unsal, T., Jia, R., Kumseranee, S., Punpruk, S. and Gu, T. (2019) Laboratory investigation of microbiologically influenced corrosion of carbon steel in hydrotest using enriched artificial seawater inoculated with an oilfield biofilm consortium. Engineering Failure Analysis 100, 544-555.

191. Unsal, T., Xu, L., Jia, R., Kijkla, P., Kumseranee, S., Punpruk, S., Mohamed, M.E., Saleh, M.A. and Gu, T. (2023) Microbiologically influenced corrosion of titanium by Desulfovibrio vulgaris biofilm under organic carbon starvation. Bioelectrochemistry 149, 108307.

192. Venkatesan, R. (2005) Studies on corrosion of some structural materials in deep sea environment.

193. Venkatesan, R., Venkatasamy, M.A., Bhaskaran, T.A., Dwarakadasa, E.S. and Ravindran, M. (2002) Corrosion of ferrous alloys in deep sea environments. British Corrosion Journal 37(4), 257-266.

194. Wang, D., Kijkla, P., Mohamed, M.E., Saleh, M.A., Kumseranee, S., Punpruk, S. and Gu, T. (2021a) Aggressive corrosion of carbon steel by *Desulfovibrio*

ferrophilus IS5 biofilm was further accelerated by riboflavin. Bioelectrochemistry 142, 107920.

195. Wang, D., Liu, J., Jia, R., Dou, W., Kumseranee, S., Punpruk, S., Li, X. and Gu, T. (2020) Distinguishing two different microbiologically influenced corrosion (MIC) mechanisms using an electron mediator and hydrogen evolution detection. Corrosion Science 177, 108993.
196. Wang, F., Li, M., Huang, L. and Zhang, X.-H. (2021b) Cultivation of uncultured marine microorganisms. Marine Life Science & Technology 3(2), 117-120.
197. Wang, G., Wu, Q., Li, X.-Z., Xu, J., Xu, Y., Shi, W.-H. and Wang, S.-L. (2019) Microscopic Analysis of Steel Corrosion Products in Seawater and Sea-Sand Concrete.
198. Wang, J., Liu, H., Mohamed, M.E.-S., Saleh, M.A. and Gu, T. (2022) Mitigation of sulfate reducing Desulfovibrio ferrophilus microbiologically influenced corrosion of X80 using THPS biocide enhanced by Peptide A. Journal of Materials Science & Technology 107, 43-51.
199. Wang, L., Bradstock, P., Li, C., McInerney, M.J. and Krumholz, L.R. (2016) The role of Rnf in ion gradient formation in *Desulfovibrio alaskensis*. PeerJ 4, e1919.
200. Wang, X. and Melchers, R.E. (2017) Long-term under-deposit pitting corrosion of carbon steel pipes. Ocean Engineering 133, 231-243.
201. Wang, Y., Cheng, G., Wu, W., Qiao, Q., Li, Y. and Li, X. (2015) Effect of pH and chloride on the micro-mechanism of pitting corrosion for high strength pipeline steel in aerated NaCl solutions. Applied Surface Science 349, 746-756.

202. Weimer Paul, J., Van Kavelaar Margaret, J., Michel Charles, B. and Ng Thomas, K. (1988) Effect of Phosphate on the Corrosion of Carbon Steel and on the Composition of Corrosion Products in Two-Stage Continuous Cultures of Desulfovibrio desulfuricans. Applied and Environmental Microbiology 54(2), 386-396.

203. Wikieł, A.J., Datsenko, I., Vera, M. and Sand, W. (2014) Impact of Desulfovibrio alaskensis biofilms on corrosion behaviour of carbon steel in marine environment. Bioelectrochemistry 97, 52-60.

204. Williamson, A.J., Carlson, H.K., Kuehl, J.V., Huang, L.L., Iavarone, A.T., Deutschbauer, A. and Coates, J.D. (2018) Dissimilatory Sulfate Reduction Under High Pressure by Desulfovibrio alaskensis G20. Frontiers in Microbiology 9.

205. Winning, I.G., Taylor, A. and Ronceray, M. (2010) Corrosion mitigation - The corrosion engineers options, pp. SPE-130299-MS.

206. Wiśniewski, J.R., Zougman, A., Nagaraj, N. and Mann, M. (2009) Universal sample preparation method for proteome analysis. Nature Methods 6(5), 359-362.

207. Woodard Trevor, L., Ueki, T. and Lovley Derek, R. (2023) H_2 is a major intermediate in *Desulfovibrio vulgaris* corrosion of iron. mBio 14(2), e00076-00023.

208. Wu, T., Hu, E., Xu, S., Chen, M., Guo, P., Dai, Z., Feng, T., Zhou, L., Tang, W., Zhan, L., Fu, X., Liu, S., Bo, X. and Yu, G. (2021) clusterProfiler 4.0: A universal enrichment tool for interpreting omics data. Innovation (Camb) 2(3), 100141.

209. Xu, D. and Gu, T. (2014) Carbon source starvation triggered more aggressive corrosion against carbon steel by the *Desulfovibrio vulgaris* biofilm. International Biodeterioration & Biodegradation 91, 74-81.

210. Yang, Z.X., Kan, B., Li, J.X., Su, Y.J. and Qiao, L.J. (2017) Hydrostatic pressure effects on stress corrosion cracking of X70 pipeline steel in a simulated deep-sea environment. International Journal of Hydrogen Energy 42(44), 27446-27457.

211. Yilmaz, P., Parfrey, L.W., Yarza, P., Gerken, J., Pruesse, E., Quast, C., Schweer, T., Peplies, J., Ludwig, W. and Glöckner, F.O. (2014) The SILVA and "All-species Living Tree Project (LTP)" taxonomic frameworks. Nucleic Acids Research 42(D1), D643-D648.

212. Zakowski, K., Narozny, M., Szocinski, M. and Darowicki, K. (2014) Influence of water salinity on corrosion risk-the case of the southern Baltic Sea coast. Environ Monit Assess 186(8), 4871-4879.

213. Zhang, W., Brown, B., Young, D., Bota, G., Nesic, S. and Singer, M. (2021) Pitting mechanism of mild steel in marginally sour environments—Part I: A parametric study based on formation of protective layers. Corrosion Science 183, 109305.

214. Zhao, X., Liu, J., Zhou, S., Zheng, Y., Wu, Y., Kogure, K. and Zhang, X.-H. (2020) Diversity of culturable heterotrophic bacteria from the Mariana Trench and their ability to degrade macromolecules. Marine Life Science & Technology 2(2), 181-193.

215. Zhao, Y., Ren, N. and Wang, A. (2008) Contributions of fermentative acidogenic bacteria and sulfate-reducing bacteria to lactate degradation and sulfate reduction. Chemosphere 72(2), 233-242.

216. Zhou, C., Zheng, S., Chen, C. and Lu, G. (2013) The effect of the partial pressure of H2S on the permeation of hydrogen in low carbon pipeline steel. Corrosion Science 67, 184-192.

217. Zhou, E., Wang, J., Moradi, M., Li, H., Xu, D., Lou, Y., Luo, J., Li, L., Wang, Y., Yang, Z., Wang, F. and Smith, J.A. (2020) Methanogenic archaea and sulfate reducing bacteria induce severe corrosion of steel pipelines after hydrostatic testing. Journal of Materials Science & Technology 48, 72-83.

Supplementary Figures

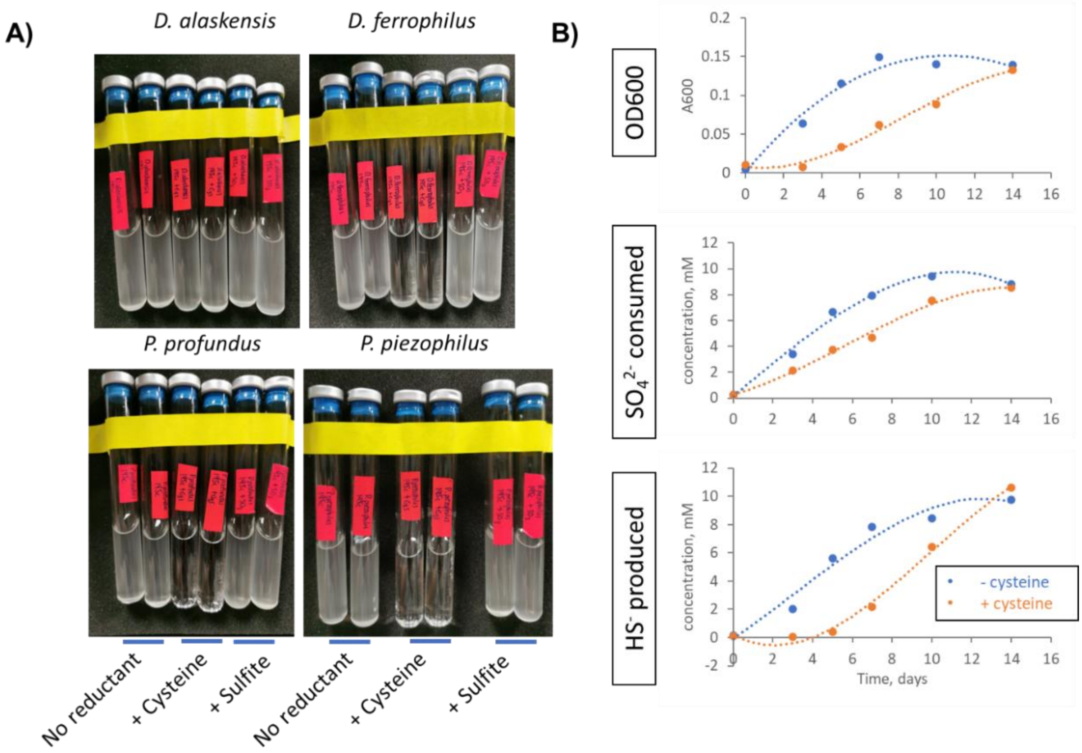

Supplementary Figure 1. Impacts of cysteine on SRB growth. The SRB were grown in DSMZ 195c without any reductant, added with 3.2 mM cysteine-HCl or 2 mM sodium sulfite for 72 h (A). With the exception of *D. alaskensis*, the addition of cysteine-HCl resulted in significant delay in growth. Monitoring of growth, sulfate-reduction, and sulfide production of *P. piezophilus* cultured in MOPS-ASW added with 20 mM sodium-DL-lactate for 14 days at room temperature in the presence or absence of cysteine-HCl (B).

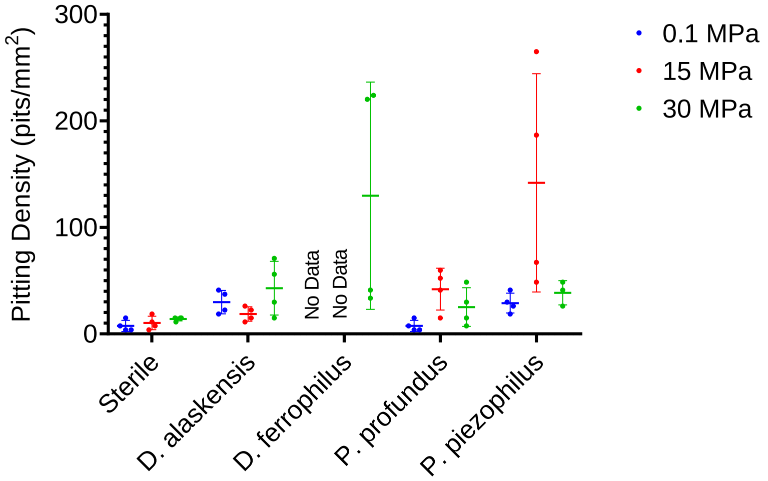

Supplementary Figure 2. Pitting density of the mild steel incubated with different SRB at 0.1 MPa, 15 MPa and 30 MPa. Data are presented in mean ± standard deviation from each independent replicates.

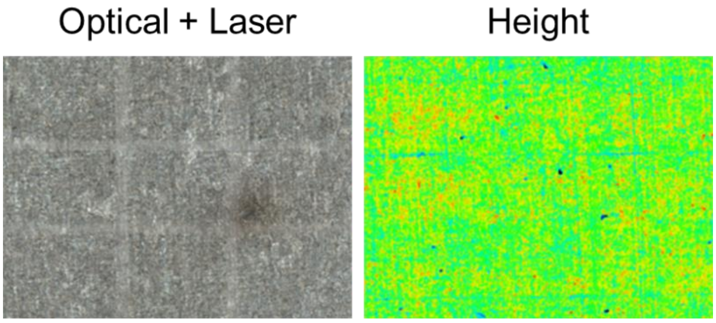

Supplementary Figure 3. Surface of mild steel coupons after 14 days incubation in sterile MOPS-ASW added with 1 mM sodium sulfide. Scale bar = 50 µm.

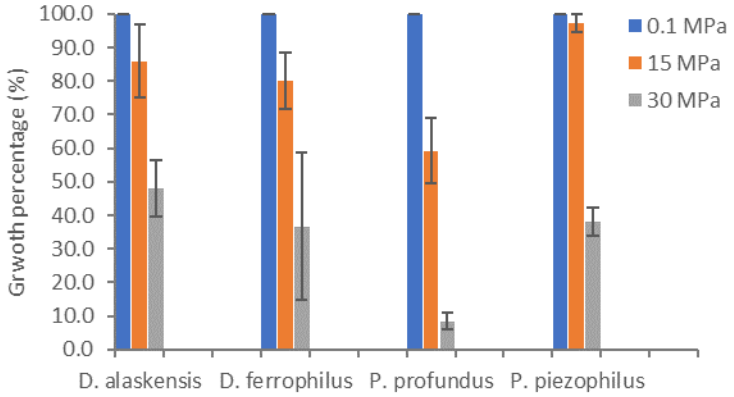

Supplementary Figure 4. Impact of hydrostatic pressure on SRB growth in nutrient-rich medium. Percentage of SRB growth (OD_{600}) in DSMZ 195c cultured at different hydrostatic pressure for 72 h, relative to 0.1 MPa. Data is presented as mean ± standard deviation from three independent experiments.

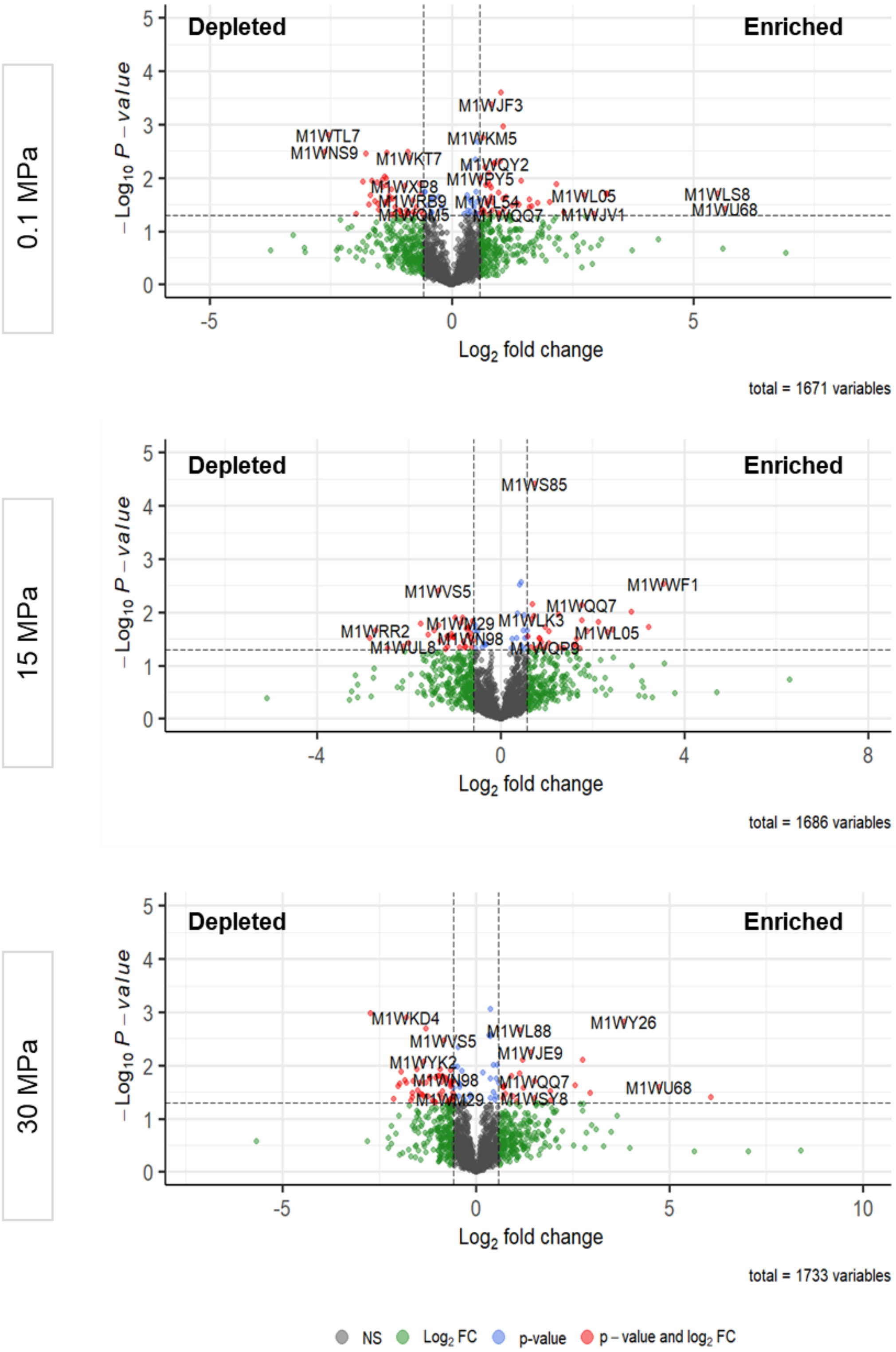

Supplementary Figure 5. Differential abundant proteins in the planktonic fraction of *P. piezophilus* incubated with mild steel coupons relative to epoxy coupon at 0.1 MPa, 15

MPa, and 30 MPa. Differentially abundant proteins highlighted in red were identified using cut-off of fold change ≥ 1.5 (log2 fold change ≥ 0.585) and *p*-value < 0.05.

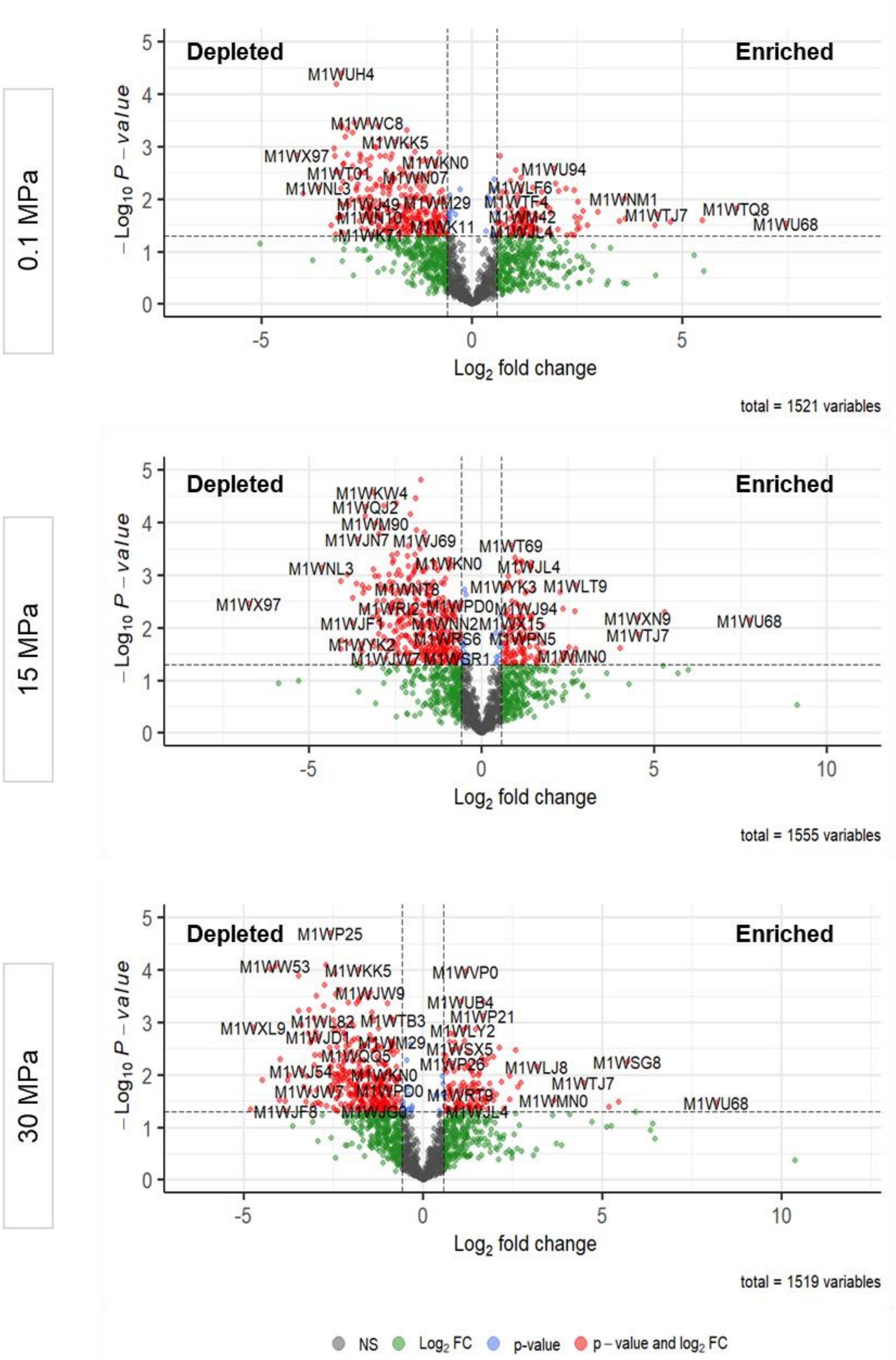

Supplementary Figure 6. Differential abundant proteins in the biofilm fraction of *P. piezophilus* incubated with mild steel coupons relative to epoxy coupon at 0.1 MPa, 15 MPa, and 30 MPa. Differentially abundant proteins highlighted in red were identified using cut-off of fold change ≥ 1.5 (log2 fold change ≥ 0.585) and *p*-value < 0.05.

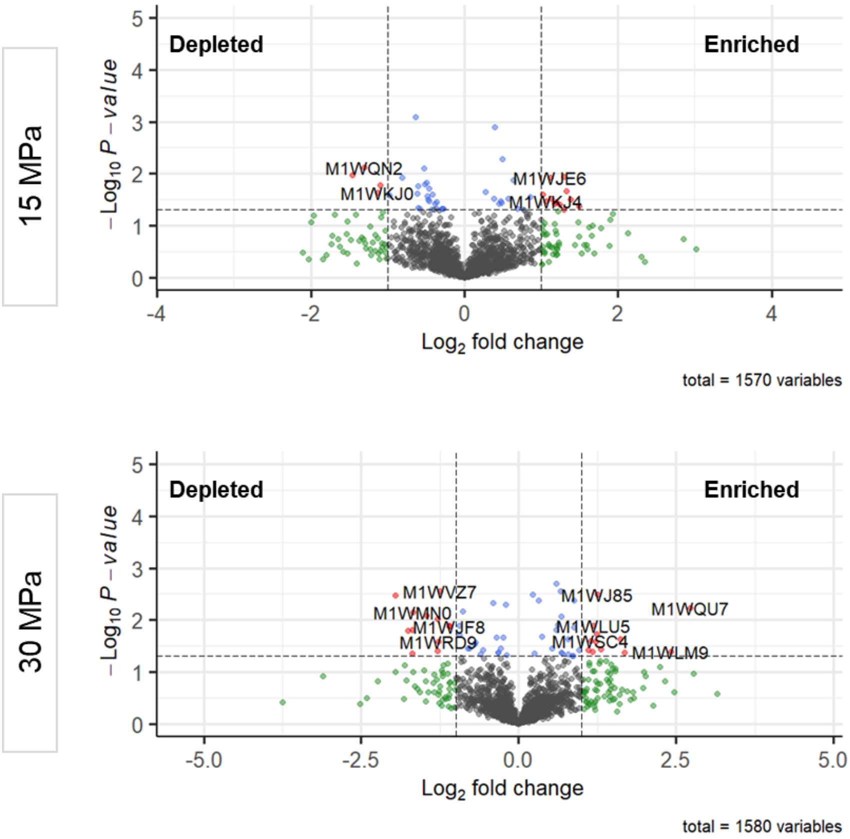

Supplementary Figure 7. Differential abundant proteins in the planktonic fraction of *P. piezophilus* incubated with mild steel coupons at elevated hydrostatic pressure relative to 0.1 MPa. Differentially abundant proteins highlighted in red were identified using cut-off of fold change ≥ 1.5 (log2 fold change ≥ 0.585) and *p*-value < 0.05.

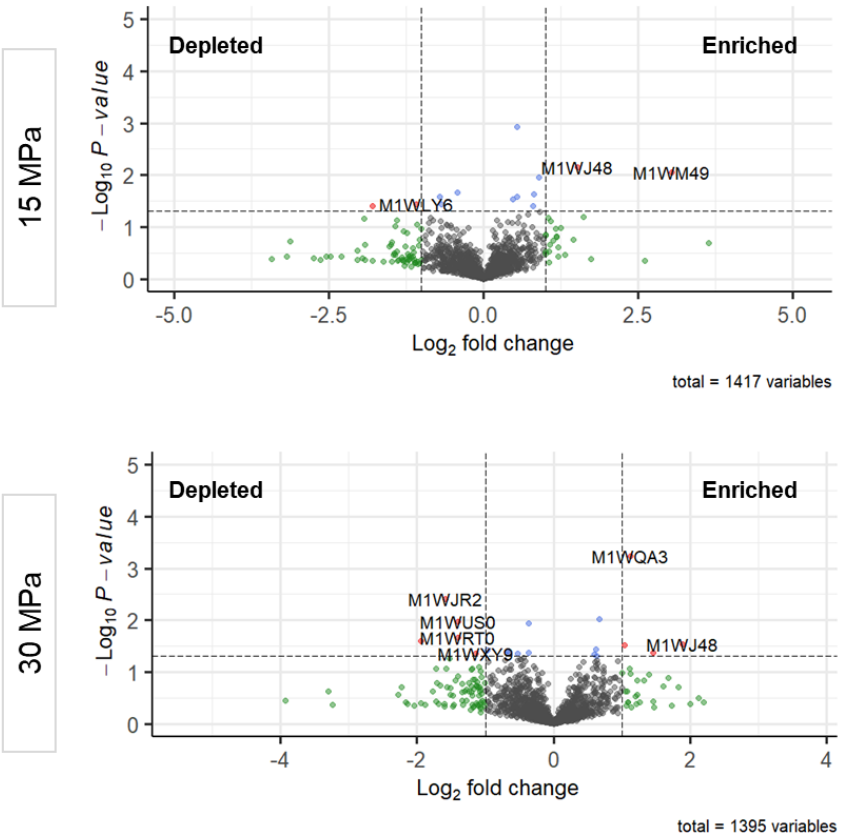

Supplementary Figure 8. Differential abundant proteins in the biofilm fraction of *P. piezophilus* incubated with mild steel coupons at elevated hydrostatic pressure relative to 0.1 MPa. Differentially abundant proteins highlighted in red were identified using cut-off of fold change ≥ 1.5 (log2 fold change ≥ 0.585) and *p*-value < 0.05.

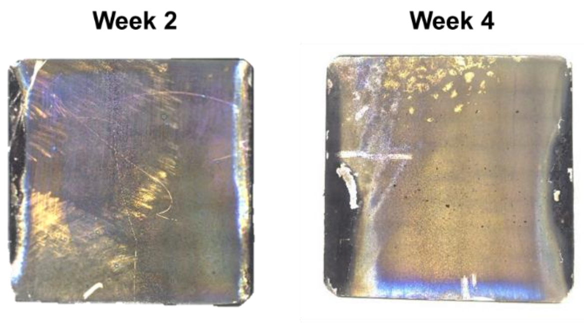

Supplementary Figure 9. Mild steel coupons incubated with 812MC enrichment cultures for 14 and 28 days, respectively. The affected area that covered by the black corrosion products grew in size from week 2 to week 4.

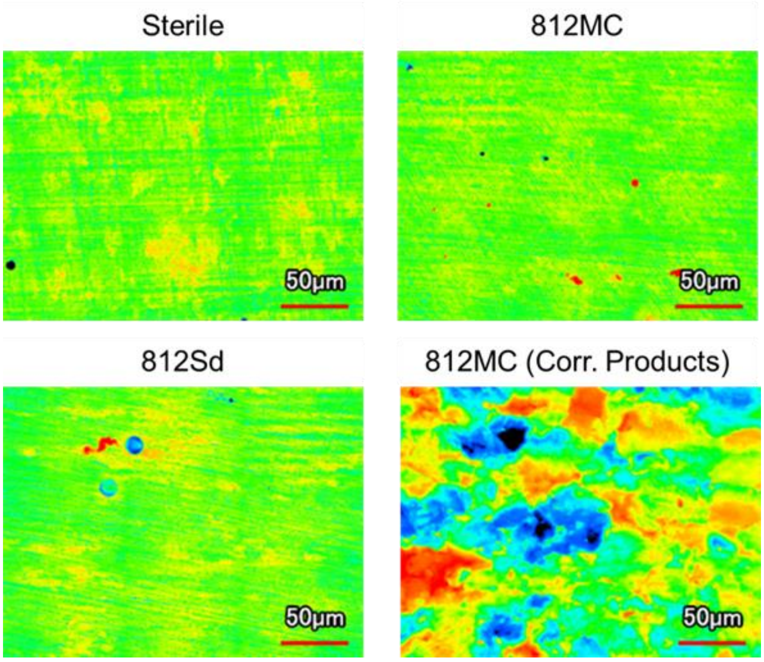

Supplementary Figure 10. Representative images of the height profile of the mild steel surface after 28 days incubation in sterile modified MOPS-ASW, with 812Sd enrichment cultures, or with 812MC enrichment cultures (in an exposed surface and area underneath the corrosion product).

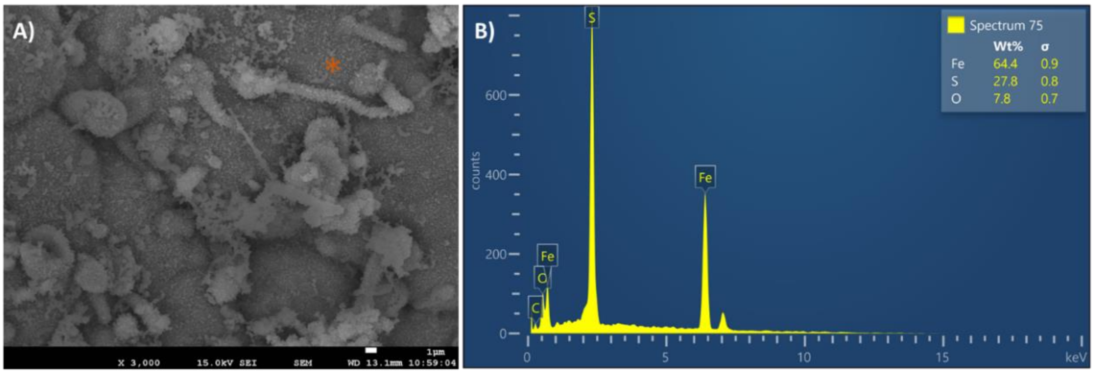

Supplementary Figure 11. Elemental analysis by EDS on the mild steel incubated with 812MC enrichment culture. Representative SEM micrograph (A) and the EDS spectrum (B) at point marked by the orange asterisk in (A).

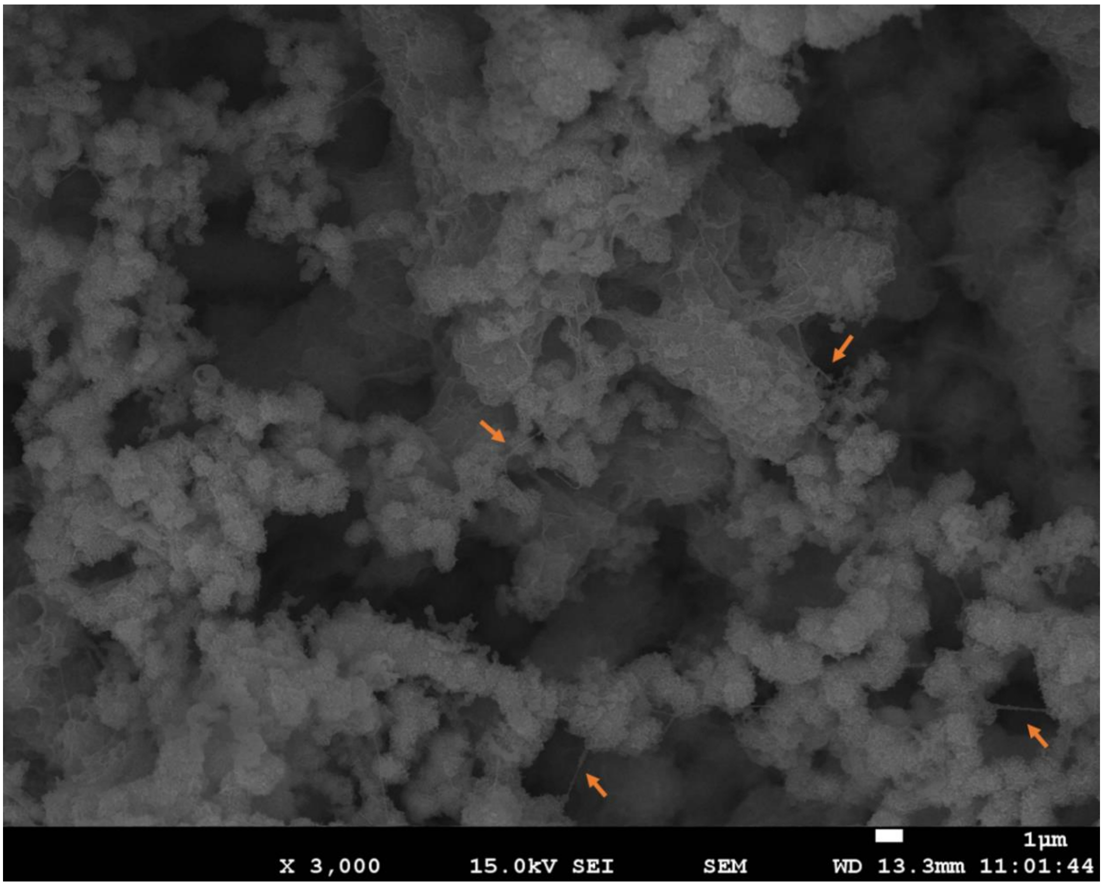

Supplementary Figure 12. Representative SEM micrograph of mild steel incubated with 812MC enrichment cultures. "Nanowire"-like structures were marked by arrows.

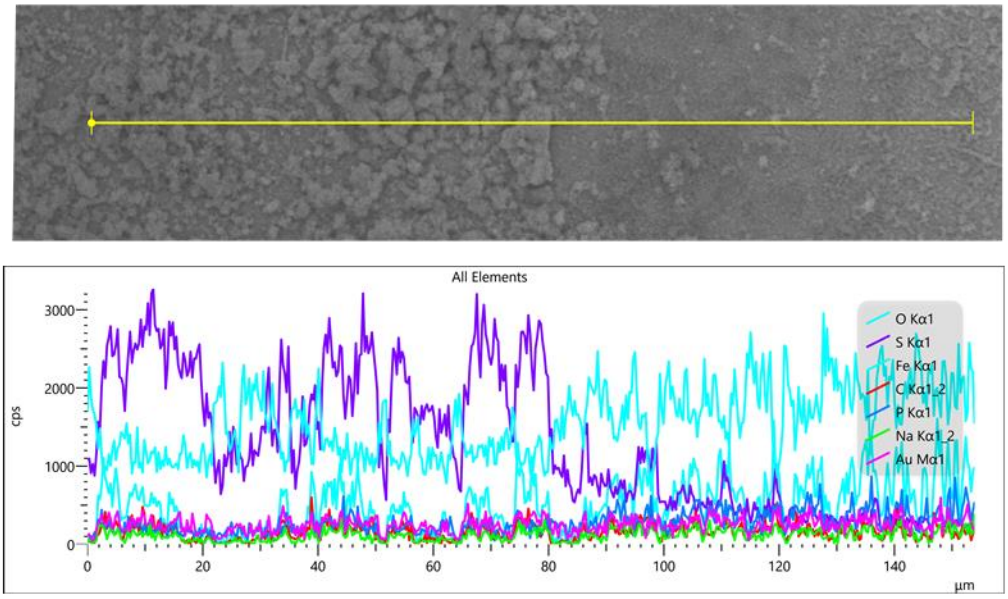

Supplementary Figure 13. Transition between area covered by the black corrosion products to the exposed surface. A line EDS analysis were performed along the horizontal lines indicated in the SEM micrograph and the elemental analysis is shown below.

Supplementary Tables

Supplementary Table 1. Test for the effect of different experiment setup on abiotic corrosion and MIC

Purpose	**Condition tested**	**SRB tested**	**Replicate 1**	**Replicate 2**	**Replicate 3**
Test for abiotic corrosion inhibition/acceleration	MOPS-ASW	Sterile	0.0121	0.0151	
	MOPS-ASW (Initial DO = 0.1 mg/L)	Sterile	0.0122	0.0185	
	MOPS-ASW (Initial DO = 6.4 mg/L)	Sterile	0.0447	0.0338	
	MOPS-ASW + 1 mM sdium sulfide	Sterile	0.0088	0.0095	
	MOPS-ASW + 1% *P. piezophilus* culture filtrate	Sterile	0.0053	0.0004	
Test for effect of cysteine on abiotic corrosion and MIC	MOPS-ASW + 3.2 mM cysteine-HCl (pH adjusted)	Sterile	0.0026	0.0033	
	MOPS-ASW + 3.2 mM cysteine-HCl (pH adjusted)	P. piezophilus	0.0082	0.0060	
Test for effect of starting cell density and with and without carbon sources	MOPS-ASW (no lactate)	Sterile	0.0139	0.0135	0.0138
	MOPS-ASW (no lactate)	*P. profundus (OD600 0.05)*	0.0024	0.0027	0.0033
	MOPS-ASW (no lactate)	*P. profundus (OD600 0.1)*	0.0019	0.0161	0.0025
	MOPS-ASW (20 mM lactate)	Sterile	0.0132	0.0132	0.0135
	MOPS-ASW (20 mM lactate)	*P. profundus (OD600 0.05)*	0.0011	0.0017	0.0016
	MOPS-ASW (20 mM lactate)	*P. profundus (OD600 0.1)*	0.0002	0.0002	0.0001
Test for effect of starting cell density and with and without carbon sources	MOPS-ASW (no lactate)	Sterile	0.0121	0.0151	
	MOPS-ASW (no lactate)	*P. piezophilus (OD600 0.05)*	0.0030	0.0038	
	MOPS-ASW (no lactate)	*P. piezophilus (OD600 0.1)*	0.0030	0.0027	
	MOPS-ASW (20 mM lactate)	Sterile	0.0154		
	MOPS-ASW (20 mM lactate)	*P. piezophilus (OD600 0.05)*	0.0017	0.0019	

Supplementary Table 2. List of differentially abundant proteins in *P. piezophilus* planktonic cells when incubated with mild steel AH36 at 0.1 MPa.

KEGG ID	Protein Description	*p*-value	log2fc
Enriched proteins			
BN4_20225	PEP-CTERM protein-sorting domain-containing protein	0.038	5.651
BN4_11148	ATPase	0.020	5.495
BN4_10001	Chromosomal replication initiator protein DnaA	0.020	3.204
BN4_20205	PAS domain-containing protein	0.021	3.192
BN4_11299	Putative Iron-sulfur flavoprotein	0.047	2.935
BN4_20444	Dinitrogenase iron-molybdenum cofactor biosynthesis protein	0.021	2.735
BN4_12083	Putative Predicted Fe-S oxidoreductase	0.044	2.312
BN4_11086	ATP-dependent protease subunit HslV	0.013	2.162
BN4_20178	Molybdenum ABC transporter, periplasmic molybdate-binding protein	0.028	2.022
BN4_12803	Uncharacterized protein	0.029	1.766
BN4_11159	Thioredoxin-like fold domain-containing protein	0.033	1.650
BN4_10816	Probable 2-phosphosulfolactate phosphatase	0.035	1.608
BN4_11927	Ribonuclease 3	0.025	1.604
BN4_10029	2-aminoadipate transaminase	0.011	1.439
BN4_11032	Threonine aldolase	0.031	1.379
BN4_11729	SCP2 domain-containing protein	0.029	1.346
BN4_10549	RNA polymerase sigma-54 factor	0.032	1.241
BN4_11879	Aldehyde oxidoreductase	0.050	1.172
BN4_11610	Acyl carrier protein	0.023	1.116
BN4_12781	Uncharacterized protein	0.038	1.069
BN4_20446	Cobyrinic acid ac-diamide synthase	0.001	1.067
BN4_20445	Cobyrinic acid ac-diamide synthase	0.024	1.060
BN4_12512	DUF4292 domain-containing protein	0.000	1.012
BN4_20331	Stress responsive alpha-beta barrel domain protein	0.005	1.004
BN4_10778	FAD dependent oxidoreductase	0.049	0.990
BN4_12629	Protein dsrD	0.045	0.970
BN4_11481	SEC-C motif domain protein	0.019	0.969
BN4_10720	Adenylate kinase	0.005	0.884
BN4_12299	Phosphate butyryltransferase	0.005	0.875
BN4_10985	Putative RNA-binding protein rbpA	0.028	0.840
BN4_11727	CinA domain protein	0.041	0.820
BN4_11665	Rubrerythrin	0.023	0.815
BN4_11622	Nitrogen-fixing NifU domain protein	0.015	0.812
BN4_10558	Dinitrogenase iron-molybdenum cofactor biosynthesis domain-containing protein	0.000	0.812
BN4_11045	Multifunctional fusion protein	0.013	0.775
BN4_10115	3-isopropylmalate dehydrogenase	0.008	0.772
BN4_10303	Lon protease	0.012	0.751
BN4_11354	Aminotransferase class-III	0.049	0.744
BN4_10030	FAD-dependent pyridine nucleotide-disulphide oxidoreductase	0.027	0.733

BN4_10506	Acetylornithine aminotransferase	0.030	0.729
BN4_12510	Putative ribose-5-phosphate isomerase B	0.014	0.711
BN4_10007	Ribosome-recycling factor	0.006	0.683
BN4_10600	Extracellular solute-binding protein family 3	0.040	0.661
BN4_20137	Transglutaminase-like domain-containing protein	0.044	0.652
BN4_12628	Sulfite reductase, dissimilatory-type subunit beta	0.002	0.638
BN4_10974	Tetratricopeptide repeat-like domain-containing protein	0.038	0.611
BN4_10112	2-isopropylmalate synthase	0.010	0.600
BN4_10709	Lipoprotein	0.046	0.593
Depleted proteins			
BN4_20518	OmpA/MotB domain protein	0.020	-0.637
BN4_20468	50S ribosomal protein L3	0.041	-0.937
BN4_20428	Anaerobic cobalt chelatase	0.049	-1.246
BN4_20417	Metal dependent phosphohydrolase	0.022	-1.298
BN4_20379	Imidazoleglycerol-phosphate dehydratase	0.049	-1.044
BN4_20321	SPBc2 prophage-derived DNA-binding protein HU 2	0.014	-1.358
BN4_20318	17 kDa surface antigen	0.011	-1.430
BN4_20186	Glycogen debranching enzyme	0.003	-1.336
BN4_20184	Putative alpha-amylase	0.029	-1.342
BN4_20112	Periplasmic solute binding protein	0.025	-1.277
BN4_20109	Nickel transport complex, NikM subunit, transmembrane	0.004	-0.871
BN4_12765	Elongation factor 4	0.024	-1.222
BN4_12605	Putative AsmA family protein	0.014	-0.968
BN4_12557	Redox-sensing transcriptional repressor Rex	0.041	-1.085
BN4_12487	CBS domain containing protein	0.002	-2.558
BN4_12467	Formate dehydrogenase accessory protein	0.035	-0.738
BN4_12443	histidine kinase	0.011	-1.657
BN4_12366	Metal dependent phosphohydrolase	0.012	-1.547
BN4_12315	histidine kinase	0.043	-1.069
BN4_12294	TPM domain-containing protein	0.021	-1.685
BN4_12219	ATP-dependent 6-phosphofructokinase	0.030	-1.528
BN4_12209	Coenzyme A biosynthesis bifunctional protein CoaBC	0.026	-0.798
BN4_12141	Glycosyl transferase group 1	0.049	-0.944
BN4_12024	Putative RNA methylase	0.031	-1.714
BN4_11959	Putative signal transduction protein	0.012	-1.839
BN4_11819	Enolase	0.048	-0.773
BN4_11709	Probable transaldolase	0.042	-0.639
BN4_11686	Phosphoenolpyruvate-protein phosphotransferase	0.029	-1.372
BN4_11658	Putative ABC-type protease/lipase transport system, ATPase and permease components	0.048	-1.185
BN4_11512	DUF885 domain-containing protein	0.003	-0.901
BN4_11234	Saccharopine dehydrogenase NADP binding domain-containing protein	0.003	-1.782
BN4_11232	AB hydrolase-1 domain-containing protein	0.047	-1.979
BN4_10979	Uncharacterized protein	0.043	-0.801
BN4_10903	Uncharacterized protein	0.016	-1.244

BN4_10901	DUF1722 domain-containing protein	0.015	-1.440
BN4_10851	Permease	0.027	-1.594
BN4_10815	histidine kinase	0.013	-0.658
BN4_10776	Sigma54 specific transcriptional regulator, Fis family	0.043	-0.904
BN4_10730	Metal dependent phosphohydrolase	0.010	-1.365
BN4_10526	DNA-binding protein HU-beta	0.003	-2.623
BN4_10369	Acetolactate synthase small subunit	0.048	-0.605
BN4_10286	Pseudouridine synthase	0.035	-1.177
BN4_10219	Protein tolR	0.040	-1.512
BN4_10216	BFN domain-containing protein	0.009	-1.387

Supplementary Table 3. List of differentially abundant proteins in *P. piezophilus* planktonic cells when incubated with mild steel AH36 at 15 MPa.

KEGG ID	Protein Description	p.value	log2fc
Enriched proteins			
BN4_11873	Related to coenzyme F390 synthetase	0.003	3.548
BN4_12811	Uncharacterized solute-binding protein SYNAS_25580	0.019	3.215
BN4_20357	Lipoprotein	0.010	2.850
BN4_11482	4-hydroxy-3-methylbut-2-en-1-yl diphosphate synthase (flavodoxin)	0.021	2.435
BN4_20444	Dinitrogenase iron-molybdenum cofactor biosynthesis protein	0.024	2.326
BN4_11376	Putative heavy-metal chelation domain-containing protein	0.015	2.128
BN4_11830	GTP cyclohydrolase 1 type 2 homolog	0.023	1.882
BN4_11879	Aldehyde oxidoreductase	0.007	1.776
BN4_20084	Bacterial Pleckstrin homology domain-containing protein	0.014	1.761
BN4_10701	2-amino-4-hydroxy-6-hydroxymethyldihydropteridine pyrophosphokinase	0.047	1.726
BN4_10158	YibE/F family protein	0.032	1.655
BN4_20210	histidine kinase	0.040	1.643
BN4_12677	Methyltransferase type 11	0.041	1.592
BN4_11339	Uncharacterized protein	0.047	1.382
BN4_10472	SurA domain protein	0.011	1.270
BN4_10763	Ribosome maturation factor RimP	0.046	1.267
BN4_20495	Transcriptional regulator, LysR family	0.023	1.054
BN4_20351	Acetoin:2,6-dichlorophenolindophenol oxidoreductase subunit beta	0.038	1.049
BN4_10191	Cyclic pyranopterin monophosphate synthase	0.019	0.975
BN4_11864	Oxidoreductase FAD/NAD(P)-binding domain protein	0.045	0.973
BN4_20355	Alkylhydroperoxidase like protein, AhpD family	0.037	0.880
BN4_11798	High-affinity branched-chain amino acid transport ATP-binding protein BraG	0.031	0.848
BN4_10538	Flagellar synthesis regulator FleN	0.044	0.840
BN4_12326	PDZ domain-containing protein	0.030	0.834
BN4_12825	FMN-dependent alpha-hydroxy acid dehydrogenase	0.050	0.755
BN4_20052	Putative two component, sigma54 specific, transcriptional regulator, Fis family	0.012	0.719
BN4_12815	Riboflavin biosynthesis protein RibBA	0.007	0.694
BN4_10778	FAD dependent oxidoreductase	0.013	0.677
BN4_10064	Extracellular solute-binding protein family 3	0.046	0.666
BN4_10033	Putative enzyme	0.028	0.601
Depleted proteins			
BN4_10741	GTPase Der	0.034	-0.606
BN4_11634	Flavodoxin	0.014	-0.616
BN4_12307	Metal dependent phosphohydrolase	0.045	-0.635
BN4_20183	Phosphorylase	0.030	-0.650
BN4_12155	Transcriptional coactivator p15 (PC4) C-terminal domain-containing protein	0.024	-0.665
BN4_10193	Uncharacterized protein	0.018	-0.691

BN4_12207	HTH merR-type domain-containing protein	0.020	-0.700
BN4_11369	5-methyltetrahydropteroyltriglutamate--homocysteine methyltransferase	0.028	-0.718
BN4_20333	Putative Surface antigen msp4 family protein	0.021	-0.739
BN4_12180	Amphi-Trp domain-containing protein	0.044	-0.765
BN4_12813	Transcription antitermination protein NusB	0.046	-0.773
BN4_11721	Uncharacterized protein	0.036	-0.814
BN4_20430	Putative CheA signal transduction histidine kinase	0.013	-0.828
BN4_11650	OmpA/MotB domain protein	0.016	-0.860
BN4_11070	Methyl-accepting chemotaxis sensory transducer with Cache sensor (Modular protein)	0.045	-0.886
BN4_10738	Chemotaxis protein methyltransferase	0.013	-0.989
BN4_11234	Saccharopine dehydrogenase NADP binding domain-containing protein	0.030	-1.023
BN4_10580	Fumarate reductase respiratory complex transmembrane subunit	0.029	-1.029
BN4_11027	Putative Methyl-accepting chemotaxis protein	0.029	-1.064
BN4_20429	histidine kinase	0.025	-1.065
BN4_10394	Tetratricopeptide TPR_2 repeat protein	0.032	-1.135
BN4_12745	histidine kinase	0.045	-1.159
BN4_10582	succinate dehydrogenase	0.028	-1.169
BN4_12297	Chemotaxis protein methyltransferase	0.048	-1.201
BN4_12558	Phosphate regulon transcriptional regulatory protein phoB	0.034	-1.323
BN4_10171	50S ribosomal protein L31	0.017	-1.342
BN4_11478	Uncharacterized protein	0.004	-1.349
BN4_12754	Alcohol dehydrogenase zinc-binding domain protein	0.022	-1.450
BN4_11822	Type III pantothenate kinase	0.026	-1.582
BN4_12477	Acriflavin resistance protein	0.016	-1.747
BN4_20472	30S ribosomal protein S19	0.038	-2.003
BN4_10325	Methyl-accepting chemotaxis sensory transducer with Pas/Pac sensor	0.044	-2.118
BN4_10092	Uncharacterized protein	0.048	-2.457
BN4_12484	PAS/PAC sensor signal transduction histidine kinase (Modular protein)	0.022	-2.716
BN4_10539	Integration host factor subunit beta	0.030	-2.847

Supplementary Table 4. List of differentially abundant proteins in *P. piezophilus* planktonic cells when incubated with mild steel AH36 at 30 MPa.

KEGG ID	Protein Description	p.value	log2fc
Enriched proteins			
BN4_12642	Adenylyl-sulfate kinase	0.039	6.060
BN4_20225	PEP-CTERM protein-sorting domain-containing protein	0.025	4.733
BN4_20016	FAD-dependent pyridine nucleotide-disulphide oxidoreductase	0.001	3.828
BN4_10728	Tyrosine recombinase XerC	0.033	2.940
BN4_10004	1-deoxy-D-xylulose 5-phosphate reductoisomerase	0.008	2.749
BN4_11981	DUF116 domain-containing protein	0.023	2.552
BN4_10038	Radical SAM domain protein	0.045	1.914
BN4_12444	Deoxyribodipyrimidine photo-lyase	0.031	1.911
BN4_11952	Uncharacterized protein	0.041	1.511
BN4_11879	Aldehyde oxidoreductase	0.020	1.503
BN4_10538	Flagellar synthesis regulator FleN	0.006	1.413
BN4_12566	Uncharacterized protein	0.026	1.222
BN4_11547	Putative sugar transporter subunit: ATP-binding component of ABC superfamily transporter	0.008	1.203
BN4_10018	Carboxymuconolactone decarboxylase-like domain-containing protein	0.014	1.127
BN4_10200	Outer membrane chaperone Skp (OmpH)	0.002	1.120
BN4_20136	Periplasmic solute binding protein	0.047	1.039
BN4_10761	Flagellar basal-body rod protein FlgG	0.038	0.948
BN4_20047	Tyrosine-protein kinase	0.016	0.917
BN4_11805	Uncharacterized protein	0.034	0.757
BN4_12575	Metallophosphoesterase	0.024	0.731
BN4_20049	PEP-CTERM system associated protein	0.025	0.725
BN4_12218	PfkB domain protein	0.041	0.691
BN4_11966	Ornithine aminotransferase	0.025	0.688
Depleted proteins			
BN4_12645	N-acylneuraminate-9-phosphate synthase	0.043	-0.590
BN4_10054	FeoA family protein	0.020	-0.594
BN4_11929	DRTGG domain protein	0.033	-0.604
BN4_10971	Uncharacterized protein	0.038	-0.607
BN4_11796	UspA domain protein	0.022	-0.653
BN4_10327	Protein-glutamate methylesterase/protein-glutamine glutaminase	0.012	-0.655
BN4_20064	Acriflavin resistance protein	0.019	-0.655
BN4_11510	acylphosphatase	0.025	-0.659
BN4_12005	Glycosyl transferase family 2	0.021	-0.664
BN4_11650	OmpA/MotB domain protein	0.042	-0.668
BN4_11001	Response regulator receiver protein	0.044	-0.683
BN4_10784	Glycine cleavage system H protein	0.048	-0.742
BN4_20183	Phosphorylase	0.018	-0.775
BN4_20239	Nitroreductase	0.017	-0.790
BN4_11478	Uncharacterized protein	0.003	-0.838

BN4_11234	Saccharopine dehydrogenase NADP binding domain-containing protein	0.030	-0.868
BN4_10905	PSP1 domain protein	0.040	-0.871
BN4_20265	Molybdopterin molybdenumtransferase	0.016	-0.872
BN4_10860	Hemerythrin-like metal-binding protein	0.021	-0.893
BN4_11104	site-specific DNA-methyltransferase (adenine-specific)	0.012	-0.934
BN4_12467	Formate dehydrogenase accessory protein	0.035	-0.943
BN4_11291	DNA repair protein RecN	0.016	-0.956
BN4_12348	tRNA (adenine(58)-N(1))-methyltransferase TrmI	0.016	-0.998
BN4_11303	50S ribosomal protein L27	0.017	-1.044
BN4_12207	HTH merR-type domain-containing protein	0.048	-1.050
BN4_12430	Type IV pilus assembly PilZ	0.048	-1.091
BN4_11911	Glycosyl transferase family 1 domain-containing protein	0.046	-1.132
BN4_10581	succinate dehydrogenase	0.017	-1.194
BN4_20113	ABC transporter related	0.016	-1.204
BN4_10505	Deoxyuridine 5'-triphosphate nucleotidohydrolase	0.038	-1.249
BN4_10351	Cytokinin riboside 5'-monophosphate phosphoribohydrolase	0.002	-1.294
BN4_10584	Putative fumarate hydratase subunit beta	0.021	-1.297
BN4_20339	Dinitrogenase iron-molybdenum cofactor biosynthesis domain-containing protein	0.038	-1.349
BN4_20321	SPBc2 prophage-derived DNA-binding protein HU 2	0.008	-1.350
BN4_20107	Ferrous iron transport protein B	0.035	-1.394
BN4_10181	Flagellar synthesis regulator FleN	0.034	-1.443
BN4_12558	Phosphate regulon transcriptional regulatory protein phoB	0.021	-1.463
BN4_12419	Diguanylate cyclase/phosphodiesterase with PAS/PAC sensor(S)	0.030	-1.503
BN4_12215	Sporulation initiation inhibitor protein soj	0.012	-1.539
BN4_10647	Ferric uptake regulation protein	0.020	-1.631
BN4_10298	Uncharacterized protein	0.039	-1.644
BN4_11233	Leucine carboxyl methyltransferase	0.033	-1.657
BN4_10076	Protein TonB	0.045	-1.678
BN4_12171	Integration host factor subunit alpha	0.001	-1.800
BN4_12345	Thioredoxin domain protein	0.021	-1.811
BN4_10526	DNA-binding protein HU-beta	0.019	-1.850
BN4_10582	succinate dehydrogenase	0.013	-1.941
BN4_11235	Saccharopine dehydrogenase NADP binding domain-containing protein	0.022	-1.981
BN4_12487	CBS domain containing protein	0.024	-2.016
BN4_10053	Ferrous iron transport protein B	0.042	-2.134
BN4_10539	Integration host factor subunit beta	0.001	-2.734

Supplementary Table 5. List of differentially abundant proteins in *P. piezophilus* biofilm cells when incubated with mild steel AH36 at 0.1 MPa.

KEGG ID	Protein Description	p.value	log2fc
Enriched proteins			
BN4_20225	PEP-CTERM protein-sorting domain-containing protein	0.030	7.460
BN4_12587	Basal-body rod modification protein FlgD	0.020	6.290
BN4_12588	Flagellar hook-length control protein	0.030	5.470
BN4_10535	Apolipoprotein N-acyltransferase	0.030	4.710
BN4_12412	Flagellar hook protein FlgE	0.020	4.400
BN4_20177	Molybdenum transport system permease	0.030	4.340
BN4_10601	Polar amino acid ABC transporter, inner membrane subunit	0.020	3.640
BN4_20368	CcmD family protein	0.010	3.620
BN4_20045	PEP-CTERM protein-sorting domain-containing protein	0.030	3.510
BN4_20524	Flagellar hook-associated protein 2	0.020	3.000
BN4_12247	Type I restriction modification DNA specificity domain-containing protein	0.030	2.740
BN4_12031	Na+/H+ antiporter NhaC	0.020	2.630
BN4_10296	Uncharacterized protein	0.020	2.570
BN4_20520	MJ0042 family finger-like protein	0.040	2.550
BN4_10761	Flagellar basal-body rod protein FlgG	0.010	2.520
BN4_10312	CDP-diacylglycerol--glycerol-3-phosphate 3-phosphatidyltransferase	0.030	2.500
BN4_10455	Magnesium transporter MgtE	0.040	2.490
BN4_12365	Methyl-accepting chemotaxis sensory transducer	0.020	2.440
BN4_10804	NADH/Ubiquinone/plastoquinone (Complex I)	0.010	2.420
BN4_10349	Methyl-accepting chemotaxis sensory transducer	0.010	2.230
BN4_10207	Ribonuclease BN	0.010	2.050
BN4_10063	Polar amino acid ABC transporter, inner membrane subunit	0.040	2.040
BN4_10609	Putative glutamine ABC transporter permease protein glnM	0.000	1.980
BN4_20330	Methyl-accepting chemotaxis sensory transducer with Pas/Pac sensor	0.000	1.950
BN4_20319	histidine kinase	0.040	1.870
BN4_11203	Glucans biosynthesis protein G	0.020	1.870
BN4_11791	Methyl-accepting chemotaxis sensory transducer with Pas/Pac sensor	0.010	1.850
BN4_10197	Lipoprotein releasing system, transmembrane protein, LolC/E family	0.040	1.800
BN4_11641	Phosphate transporter	0.010	1.770
BN4_10947	Tmc complex, transmembrane protein	0.010	1.670
BN4_20382	Small-conductance mechanosensitive channel	0.010	1.660
BN4_11772	histidine kinase	0.040	1.620
BN4_10810	NADH-quinone oxidoreductase subunit H	0.020	1.610
BN4_10639	histidine kinase	0.010	1.550
BN4_10660	Binding-protein-dependent transport systems inner membrane component	0.040	1.510
BN4_11048	Acriflavin resistance protein	0.020	1.500
BN4_20155	HAMP domain-containing protein	0.020	1.490
BN4_12041	Uncharacterized protein	0.020	1.490
BN4_10811	NADH-quinone oxidoreductase subunit D	0.040	1.480

BN4_20351	Acetoin:2,6-dichlorophenolindophenol oxidoreductase subunit beta	0.040	1.480
BN4_11562	Pyridine nucleotide-disulphide oxidoreductase dimerisation region	0.010	1.430
BN4_10812	NADH dehydrogenase (Ubiquinone) 30 kDa subunit (Modular protein)	0.030	1.420
BN4_10034	Binding-protein-dependent transport systems inner membrane component	0.030	1.420
BN4_20337	Sodium/sulphate symporter	0.030	1.420
BN4_12822	Metallophosphoesterase	0.030	1.410
BN4_11606	Cell division protein FtsZ	0.040	1.410
BN4_20019	histidine kinase	0.040	1.390
BN4_11668	Chemoreceptor protein A	0.020	1.350
BN4_10261	MotA/TolQ/ExbB proton channel	0.030	1.340
BN4_11735	Putative ABC transporter permease protein HI_1086	0.030	1.330
BN4_10003	Zinc metalloprotease	0.020	1.320
BN4_11895	Cytochrome c oxidase subunit 2	0.030	1.300
BN4_10483	tRNA threonylcarbamoyladenosine biosynthesis protein TsaE	0.030	1.290
BN4_11526	VENN motif-containing domain-containing protein	0.030	1.280
BN4_20297	Methyl-accepting chemotaxis sensory transducer	0.030	1.270
BN4_10842	ATP-dependent zinc metalloprotease FtsH	0.020	1.260
BN4_12315	histidine kinase	0.020	1.250
BN4_20046	Secretion ATPase, PEP-CTERM locus subfamily	0.040	1.240
BN4_11420	Membrane protein insertase YidC	0.020	1.240
BN4_20430	Putative CheA signal transduction histidine kinase	0.020	1.230
BN4_11715	Methyl-accepting chemotaxis sensory transducer	0.020	1.210
BN4_11948	Na(+)/H(+) antiporter NhaA	0.040	1.210
BN4_12591	Diguanylate cyclase	0.030	1.210
BN4_10864	Outer membrane homotrimeric porin	0.040	1.190
BN4_20504	ABC-type transport auxiliary lipoprotein component domain-containing protein	0.020	1.190
BN4_12733	Inner membrane protein ybhL	0.020	1.170
BN4_12213	Band 7 domain-containing protein	0.030	1.170
BN4_11823	Methyl-accepting chemotaxis sensory transducer	0.030	1.170
BN4_20296	Methyl-accepting chemotaxis sensory transducer with Cache sensor	0.020	1.170
BN4_11805	Uncharacterized protein	0.000	1.160
BN4_12162	Putative signal transduction protein	0.010	1.160
BN4_10542	inorganic diphosphatase	0.010	1.150
BN4_20023	Transmembrane protein	0.020	1.150
BN4_10498	Protein-export membrane protein SecF	0.040	1.150
BN4_11676	Uncharacterized protein	0.020	1.150
BN4_12529	ATP synthase subunit beta	0.020	1.140
BN4_10573	Putative Vibriobactin receptor	0.030	1.120
BN4_11005	Peptidyl-prolyl cis-trans isomerase	0.040	1.120
BN4_20305	Electron transfer flavoprotein alpha/beta-subunit	0.020	1.090
BN4_10449	Protein-export membrane protein SecG	0.010	1.070
BN4_11242	Putative Receptor-mostly Fe transport	0.040	1.060
BN4_12292	LemA family protein	0.010	1.060
BN4_11408	Maturation element for hydrogenase 2	0.020	1.050

BN4_12636	Peptidyl-prolyl cis-trans isomerase	0.000	1.030
BN4_11923	histidine kinase	0.030	1.030
BN4_10934	histidine kinase	0.040	1.020
BN4_11732	Arginine biosynthesis bifunctional protein ArgJ	0.040	1.000
BN4_10742	Methyl-accepting chemotaxis sensory transducer	0.030	0.990
BN4_10885	Nickel transport complex, NikM subunit, transmembrane	0.030	0.990
BN4_12264	Flagellar hook-associated protein 3	0.020	0.980
BN4_12734	Inner membrane protein YccF	0.030	0.980
BN4_10696	Uncharacterized protein	0.040	0.950
BN4_10232	Basic membrane lipoprotein	0.020	0.930
BN4_12799	Nicotinate-nucleotide--dimethylbenzimidazole phosphoribosyltransferase	0.000	0.910
BN4_12641	Extracellular ligand-binding receptor	0.020	0.900
BN4_10484	Aspartokinase	0.030	0.890
BN4_11737	Mammalian cell entry related domain protein	0.010	0.860
BN4_10429	Extracellular ligand-binding receptor	0.010	0.830
BN4_20370	Extracellular ligand-binding receptor	0.030	0.790
BN4_10492	Extracellular solute-binding protein family 3	0.010	0.710
BN4_10476	Chemotaxis protein CheW	0.030	0.690
BN4_12549	Alkyl hydroperoxide reductase/ Thiol specific antioxidant/ Mal allergen	0.040	0.670
BN4_11570	Phosphoribosylformylglycinamidine cyclo-ligase	0.010	0.670
BN4_10112	2-isopropylmalate synthase	0.000	0.660
BN4_11852	PpiC-type peptidyl-prolyl cis-trans isomerase	0.030	0.650
BN4_11291	DNA repair protein RecN	0.020	0.620
BN4_12436	Rhodanese domain protein	0.030	0.600
Depleted proteins			
BN4_12637	High-affinity branched-chain amino acid transport ATP-binding protein BraG	0.020	-0.620
BN4_11418	LUD domain-containing protein	0.040	-0.620
BN4_20060	Alkyl hydroperoxide reductase/ Thiol specific antioxidant/ Mal allergen	0.020	-0.630
BN4_20103	Ferric uptake regulation protein	0.010	-0.650
BN4_12489	histidine kinase	0.020	-0.650
BN4_10878	Rhodanese domain protein	0.010	-0.670
BN4_12170	Protein hit	0.040	-0.690
BN4_11556	Type-3 glutamine synthetase	0.030	-0.700
BN4_11803	NADP-dependent L-serine/L-allo-threonine dehydrogenase ydfG	0.010	-0.710
BN4_10368	Acetolactate synthase	0.040	-0.710
BN4_12172	Sporulation domain protein	0.020	-0.730
BN4_11437	3-dehydroquinate synthase homolog	0.030	-0.750
BN4_12354	Diguanylate phosphodiesterase	0.040	-0.760
BN4_11636	Dihydroxy-acid dehydratase	0.010	-0.770
BN4_12202	Pyruvate ferredoxin/flavodoxin oxidoreductase	0.010	-0.770
BN4_12643	Long-chain-fatty-acid--CoA ligase	0.000	-0.780
BN4_11793	Arginine--tRNA ligase	0.030	-0.780
BN4_11924	Uncharacterized protein	0.030	-0.790
BN4_12727	Alanine--tRNA ligase	0.020	-0.790

BN4_10246	DNA polymerase III subunit gamma/tau	0.020	-0.800
BN4_20518	OmpA/MotB domain protein	0.030	-0.800
BN4_11650	OmpA/MotB domain protein	0.010	-0.810
BN4_12524	ATP synthase subunit b	0.030	-0.810
BN4_11555	Putative enzyme	0.030	-0.820
BN4_20314	50S ribosomal subunit assembly factor BipA	0.020	-0.820
BN4_10844	Argininosuccinate synthase	0.000	-0.860
BN4_20254	L-seryl-tRNA(Sec) selenium transferase	0.020	-0.860
BN4_12509	transketolase	0.020	-0.870
BN4_12203	Thiamine pyrophosphate protein domain protein TPP-binding	0.040	-0.870
BN4_12653	Chaperonin GroEL	0.000	-0.870
BN4_20439	Carbamoyl-phosphate synthase small chain	0.020	-0.870
BN4_20331	Stress responsive alpha-beta barrel domain protein	0.030	-0.890
BN4_10734	Cell division coordinator CpoB	0.030	-0.890
BN4_20514	siroheme decarboxylase	0.020	-0.900
BN4_11443	Anthranilate phosphoribosyltransferase	0.040	-0.900
BN4_20288	IMP cyclohydrolase	0.020	-0.920
BN4_11972	Amine oxidase	0.040	-0.920
BN4_10786	glycine dehydrogenase (aminomethyl-transferring)	0.020	-0.940
BN4_11367	Surface carbohydrate biosynthesis protein	0.030	-0.960
BN4_10029	2-aminoadipate transaminase	0.040	-0.960
BN4_11381	FAD-dependent pyridine nucleotide-disulphide oxidoreductase	0.000	-0.980
BN4_12214	Protein CapI	0.030	-0.980
BN4_11097	CoA-binding domain protein	0.030	-0.990
BN4_20336	Transferase hexapeptide repeat containing protein	0.010	-1.000
BN4_11700	Signal recognition particle protein	0.010	-1.010
BN4_11407	isocitrate dehydrogenase (NADP(+))	0.040	-1.020
BN4_12510	Putative ribose-5-phosphate isomerase B	0.010	-1.020
BN4_10217	Polymerase/histidinol phosphatase N-terminal domain-containing protein	0.030	-1.030
BN4_10238	Deoxyguanosinetriphosphate triphosphohydrolase-like protein	0.030	-1.040
BN4_10266	Biotin/lipoyl attachment domain-containing protein	0.020	-1.060
BN4_12487	CBS domain containing protein	0.040	-1.060
BN4_20516	Delta-aminolevulinic acid dehydratase	0	-1.06
BN4_12015	endopeptidase La	0.04	-1.07
BN4_12628	Sulfite reductase, dissimilatory-type subunit beta	0.03	-1.07
BN4_10666	Response regulator receiver protein	0.03	-1.07
BN4_11663	Rubredoxin-oxygen oxidoreductase	0.01	-1.09
BN4_20393	Chaperone protein ClpB	0.02	-1.1
BN4_12019	Universal stress protein	0.01	-1.11
BN4_11172	GCN5-related N-acetyltransferase	0.02	-1.11
BN4_12825	FMN-dependent alpha-hydroxy acid dehydrogenase	0	-1.12
BN4_10311	Iron-sulfur cluster carrier protein	0.01	-1.13
BN4_10062	Amino-acid transporter subunit ATP-binding component of ABC superfamily	0.01	-1.13
BN4_20375	Inosine-5'-monophosphate dehydrogenase	0.01	-1.14

BN4_12610	Putative Chemotaxis protein CheX	0	-1.15
BN4_10640	Transcriptional regulatory protein zraR	0.03	-1.15
BN4_11705	Short-chain dehydrogenase/reductase SDR	0.02	-1.16
BN4_11438	Bifunctional chorismate mutase/prephenate dehydratase	0.01	-1.16
BN4_11004	tryptophan--tRNA ligase	0.01	-1.17
BN4_12036	Periplasmic [NiFe] hydrogenase large subunit	0.03	-1.19
BN4_11974	Lipoprotein	0	-1.19
BN4_12059	GDP-mannose 3,5-epimerase	0.04	-1.2
BN4_11983	Aspartate carbamoyltransferase	0.03	-1.23
BN4_11702	Serine--tRNA ligase	0.02	-1.23
BN4_10847	Putative enzyme with nucleoside triphosphate hydrolase domain	0.01	-1.23
BN4_11977	Aspartate--tRNA(Asp/Asn) ligase	0.02	-1.23
BN4_10762	Flagellar basal-body rod protein FlgF	0.04	-1.25
BN4_20512	Ribulose-phosphate 3-epimerase	0.02	-1.26
BN4_11844	Hydantoinase/oxoprolinase	0	-1.26
BN4_10017	Uncharacterized protein	0.02	-1.29
BN4_11078	50S ribosomal protein L25	0	-1.29
BN4_11881	cysteine desulfurase	0.02	-1.3
BN4_12560	Spore coat polysaccharide biosynthesis protein spsC	0.02	-1.3
BN4_11984	Dihydroorotase	0.01	-1.31
BN4_11436	2-amino-3,7-dideoxy-D-threo-hept-6-ulosonate synthase	0.01	-1.31
BN4_12748	Glutamine--tRNA ligase	0.02	-1.33
BN4_20033	Catalase	0	-1.34
BN4_10865	Histidinol dehydrogenase	0.01	-1.34
BN4_11327	Putative succinate-semialdehyde dehydrogenase [NADP+]	0.01	-1.35
BN4_11439	3-phosphoshikimate 1-carboxyvinyltransferase	0	-1.36
BN4_11183	Putative xanthine dehydrogenase subunit D (XDHasesubunit D)	0.03	-1.39
BN4_10837	UTP--glucose-1-phosphate uridylyltransferase	0.02	-1.39
BN4_10738	Chemotaxis protein methyltransferase	0.02	-1.4
BN4_10555	CTP synthase	0.03	-1.4
BN4_12753	GAK system CofD-like protein	0.03	-1.41
BN4_10681	2-hydroxyglutaryl-CoA dehydratase (HgdB-like)	0.02	-1.41
BN4_10720	Adenylate kinase	0.01	-1.42
BN4_10827	Thiamine-phosphate synthase	0.03	-1.43
BN4_11080	Transcriptional regulator, CarD family	0.02	-1.43
BN4_20079	Nitrate reductase	0.04	-1.43
BN4_12283	Fumarate hydratase class II	0.01	-1.44
BN4_11611	3-oxoacyl-[acyl-carrier-protein] reductase	0	-1.45
BN4_11546	Extracellular solute-binding protein family 1	0.04	-1.46
BN4_10778	FAD dependent oxidoreductase	0.01	-1.47
BN4_20258	UDP-N-acetylglucosamine 1-carboxyvinyltransferase	0.02	-1.48
BN4_10911	Holliday junction branch migration complex subunit RuvA	0.01	-1.49
BN4_12061	UDP-glucose 6-dehydrogenase	0.02	-1.49
BN4_11049	Efflux transporter, RND family, MFP subunit	0	-1.5
BN4_10416	Exopolyphosphatase-related protein	0	-1.5

BN4_11622	Nitrogen-fixing NifU domain protein	0.02	-1.5
BN4_10061	Polysaccharide biosynthesis protein CapD-like domain-containing protein	0.03	-1.5
BN4_10599	Amino-acid transporter subunit ATP-binding component of ABC superfamily	0.03	-1.51
BN4_11589	Metal dependent phosphohydrolase	0	-1.53
BN4_12341	CBS domain containing membrane protein	0.01	-1.54
BN4_11054	Phosphoesterase RecJ domain protein	0.04	-1.55
BN4_20338	CBS domain containing membrane protein	0	-1.55
BN4_11914	Intracellular protease, PfpI family	0.03	-1.56
BN4_11077	Ribose-phosphate pyrophosphokinase	0.02	-1.56
BN4_10740	Protein-glutamate methylesterase/protein-glutamine glutaminase	0.04	-1.56
BN4_12570	Cell division protein ZapB	0.02	-1.56
BN4_12569	Bifunctional protein GlmU	0.01	-1.57
BN4_10401	Heat shock protein HSP20	0.01	-1.57
BN4_10611	Amino-acid transporter subunit ATP-binding component of ABC superfamily	0.01	-1.58
BN4_10282	FAD dependent oxidoreductase	0.02	-1.58
BN4_10301	ATP-dependent Clp protease proteolytic subunit	0.01	-1.59
BN4_20469	50S ribosomal protein L4	0.02	-1.6
BN4_10320	Thioredoxin reductase	0.02	-1.61
BN4_10623	Uncharacterized protein	0.03	-1.62
BN4_10556	Phosphoribosylformylglycinamidine synthase 1	0.04	-1.63
BN4_10136	Aldehyde ferredoxin oxidoreductase	0	-1.63
BN4_11631	Riboflavin biosynthesis protein RibD	0.02	-1.63
BN4_11472	Molybdopterin synthase catalytic subunit	0.02	-1.64
BN4_10397	Cysteine desulfurase	0.03	-1.65
BN4_10339	4-hydroxy-tetrahydrodipicolinate reductase	0.02	-1.65
BN4_12531	Aspartate aminotransferase A	0	-1.65
BN4_10551	Lipopolysaccharide transport periplasmic protein LptA	0.02	-1.67
BN4_10274	Imidazole glycerol phosphate synthase subunit HisH	0.04	-1.68
BN4_10305	ADP-ribosylation/Crystallin J1	0.01	-1.68
BN4_11865	Rubrerythrin	0.01	-1.71
BN4_20508	Transcriptional regulator, AsnC family	0.01	-1.73
BN4_11364	NeuB family protein	0	-1.73
BN4_12231	Putative Phenylacetate-coenzyme A ligase	0.02	-1.74
BN4_12030	Putative UspA domain protein	0.01	-1.77
BN4_11928	CoA-binding domain protein	0.03	-1.78
BN4_10992	Aminotransferase class V	0.02	-1.79
BN4_10267	Uncharacterized protein	0.03	-1.79
BN4_11829	C4-type zinc ribbon domain-containing protein	0.03	-1.81
BN4_11490	Polyprenyl synthetase	0.03	-1.82
BN4_12526	ATP synthase subunit delta	0	-1.83
BN4_11069	DUF3088 domain-containing protein	0.02	-1.83
BN4_10252	Pyruvate ferredoxin/flavodoxin oxidoreductase, beta subunit	0	-1.83
BN4_20460	50S ribosomal protein L10	0	-1.87

BN4_11446	Tryptophan synthase beta chain	0.02	-1.87
BN4_11628	Zinc resistance-associated protein	0.03	-1.9
BN4_10352	Beta-lactamase domain protein	0.04	-1.91
BN4_10902	DUF1722 domain-containing protein	0	-1.91
BN4_12047	Aldehyde ferredoxin oxidoreductase	0.03	-1.91
BN4_11588	CBS domain containing protein	0	-1.92
BN4_10647	Ferric uptake regulation protein	0.03	-1.92
BN4_11314	Molybdenum storage protein subunit beta	0.01	-1.92
BN4_10440	Pseudouridine synthase	0	-1.93
BN4_10243	Homoserine dehydrogenase	0	-1.94
BN4_20431	Response regulator receiver protein	0.02	-1.94
BN4_10541	4-hydroxy-tetrahydrodipicolinate synthase	0.01	-1.96
BN4_20186	Glycogen debranching enzyme	0.04	-1.96
BN4_12644	Putative transcriptional regulator	0.01	-1.97
BN4_11961	Protein vdlD	0.01	-1.99
BN4_11738	Toluene tolerance family protein	0.04	-1.99
BN4_10658	ABC transporter related	0.03	-2
BN4_12246	Virulence protein	0.03	-2.01
BN4_11131	Transcriptional regulator, AraC family	0.02	-2.01
BN4_10941	Response regulator receiver protein	0.02	-2.03
BN4_10463	Cupin 2 conserved barrel domain protein	0.01	-2.03
BN4_20480	50S ribosomal protein L5	0.04	-2.03
BN4_11368	3-oxoacyl-[acyl-carrier-protein] reductase	0	-2.05
BN4_10869	50S ribosomal protein L9	0	-2.06
BN4_11970	RNA methyltransferase, TrmH family, group 3	0.04	-2.09
BN4_11798	High-affinity branched-chain amino acid transport ATP-binding protein BraG	0.01	-2.09
BN4_12121	Rubrerythrin	0.01	-2.12
BN4_10081	Putative pectate lyase protein	0.04	-2.12
BN4_20416	TPR repeat-containing protein	0.01	-2.13
BN4_10095	Glucose-1-phosphate thymidylyltransferase	0.01	-2.13
BN4_11093	Hmc complex, High-molecular-weight cytochrome c, 15 heme	0.01	-2.14
BN4_10971	Uncharacterized protein	0.01	-2.18
BN4_12434	Transcriptional regulator, AsnC family	0	-2.18
BN4_20470	50S ribosomal protein L23	0.02	-2.18
BN4_11405	DUF306 domain-containing protein	0	-2.19
BN4_12101	SIR2-like domain-containing protein	0	-2.19
BN4_20246	Extracellular solute-binding protein family 1	0.02	-2.19
BN4_12664	FG-GAP repeat protein	0.02	-2.2
BN4_11505	Orotate phosphoribosyltransferase	0.03	-2.22
BN4_10346	Ribosomal silencing factor RsfS	0.03	-2.23
BN4_10231	Xanthine-guanine phosphoribosyltransferase	0.02	-2.23
BN4_10244	Aminotransferase	0.02	-2.23
BN4_10600	Extracellular solute-binding protein family 3	0.01	-2.24
BN4_20451	Response regulator receiver modulated CheW protein	0	-2.24
BN4_11421	Single-stranded nucleic acid binding R3H domain protein	0.02	-2.25

BN4_20483	50S ribosomal protein L6	0.04	-2.25
BN4_11511	Response regulator receiver modulated CheW protein	0	-2.27
BN4_10782	Putative nickel-responsive regulator	0.01	-2.28
BN4_10860	Hemerythrin-like metal-binding protein	0.01	-2.29
BN4_20385	Uracil phosphoribosyltransferase	0.01	-2.3
BN4_11901	EF-hand domain-containing protein	0	-2.31
BN4_11354	Aminotransferase class-III	0.01	-2.35
BN4_11385	TRAP dicarboxylate transporter-DctP subunit	0.02	-2.36
BN4_10899	Amidophosphoribosyltransferase	0.01	-2.38
BN4_20109	Nickel transport complex, NikM subunit, transmembrane	0.03	-2.39
BN4_11929	DRTGG domain protein	0	-2.39
BN4_20486	50S ribosomal protein L30	0.03	-2.4
BN4_10610	ABC transporter glutamine-binding protein glnH	0.02	-2.41
BN4_20484	50S ribosomal protein L18	0.01	-2.42
BN4_10486	Glyceraldehyde-3-phosphate dehydrogenase	0.01	-2.42
BN4_11949	Diguanylate cyclase/phosphodiesterase with PAS/PAC sensor(S)	0.03	-2.42
BN4_10064	Extracellular solute-binding protein family 3	0.02	-2.43
BN4_10132	ABC transporter, periplasmic substrate-binding protein	0.02	-2.44
BN4_12467	Formate dehydrogenase accessory protein	0	-2.44
BN4_20321	SPBc2 prophage-derived DNA-binding protein HU 2	0.01	-2.44
BN4_20440	3-deoxy-manno-octulosonate cytidylyltransferase	0	-2.44
BN4_12576	Tyrosine--tRNA ligase	0.01	-2.45
BN4_10036	Extracellular solute-binding protein family 5	0.01	-2.45
BN4_10170	Sulfite reductase, dissimilatory-type subunit gamma	0.01	-2.48
BN4_12171	Integration host factor subunit alpha	0.02	-2.48
BN4_11833	Methyltransferase type 11	0	-2.49
BN4_10437	Elongation factor P	0.01	-2.49
BN4_10351	Cytokinin riboside 5'-monophosphate phosphoribohydrolase	0.02	-2.5
BN4_12225	HTH tetR-type domain-containing protein	0.04	-2.51
BN4_10755	FlgN protein	0	-2.51
BN4_11487	Peptidase M23	0.02	-2.53
BN4_20458	50S ribosomal protein L11	0.01	-2.56
BN4_11296	Putative Nitroreductase	0	-2.57
BN4_10979	Uncharacterized protein	0.01	-2.6
BN4_11659	Response regulator rpfG	0.02	-2.61
BN4_11442	Anthranilate synthase component II	0.01	-2.61
BN4_10850	NLPA lipoprotein	0.04	-2.63
BN4_10345	Nitroreductase	0	-2.65
BN4_11316	Acetylglutamate kinase	0	-2.65
BN4_10007	Ribosome-recycling factor	0	-2.66
BN4_10494	Glutaredoxin (Modular protein)	0	-2.67
BN4_10369	Acetolactate synthase small subunit	0	-2.67
BN4_20239	Nitroreductase	0.03	-2.68
BN4_12471	Molybdopterin-guanine dinucleotide biosynthesis protein B	0.01	-2.69
BN4_10929	Glyoxylate reductase	0.01	-2.7

BN4_12629	Protein dsrD	0.01	-2.72
BN4_10582	succinate dehydrogenase	0.01	-2.75
BN4_11075	Periplasmic serine endoprotease DegP-like	0.01	-2.75
BN4_12297	Chemotaxis protein methyltransferase	0	-2.8
BN4_12480	Heat shock protein Hsp20	0	-2.83
BN4_10787	Dihydrolipoyl dehydrogenase	0	-2.84
BN4_20482	30S ribosomal protein S8	0.01	-2.87
BN4_10200	Outer membrane chaperone Skp (OmpH)	0	-2.88
BN4_11402	ABC transporter related protein	0.01	-2.93
BN4_20438	TPR repeat-containing protein	0	-2.96
BN4_10448	Triosephosphate isomerase	0	-2.97
BN4_10795	Chorismate synthase	0.01	-2.98
BN4_11947	Tetratricopeptide TPR_2 repeat protein	0	-3.01
BN4_12180	Amphi-Trp domain-containing protein	0	-3.04
BN4_10539	Integration host factor subunit beta	0.04	-3.06
BN4_20473	50S ribosomal protein L22	0	-3.07
BN4_11754	Putative 6-phosphogluconate dehydrogenase YqeC	0	-3.07
BN4_12092	Putative RNA-binding protein rbpA	0.02	-3.1
BN4_10737	Response regulator receiver protein	0	-3.1
BN4_11795	Histidinol-phosphate aminotransferase	0	-3.1
BN4_10103	2,3-bisphosphoglycerate-dependent phosphoglycerate mutase	0	-3.1
BN4_20031	Pyridoxamine 5'-phosphate oxidase-related FMN-binding	0.01	-3.11
BN4_11166	Isoquinoline 1-oxidoreductase subunit alpha	0.02	-3.11
BN4_11396	Uncharacterized protein	0.01	-3.12
BN4_20457	Transcription termination/antitermination protein NusG	0	-3.16
BN4_10960	Peptidyl-prolyl cis-trans isomerase	0.02	-3.17
BN4_10389	PilZ domain-containing protein	0.02	-3.2
BN4_10833	SH3b domain-containing protein	0	-3.23
BN4_12558	Phosphate regulon transcriptional regulatory protein phoB	0	-3.24
BN4_11955	Cupin fold metalloprotein, WbuC family	0	-3.26
BN4_10298	Uncharacterized protein	0	-3.28
BN4_20212	Periplasmic phosphate binding protein	0.03	-3.35
BN4_10421	FMN dependent NADH:quinone oxidoreductase	0.01	-3.65
BN4_10953	Transcriptional regulator, MarR family	0.01	-4.02
BN4_12378	Nitrogen regulatory protein P-II	0	-4.16

Supplementary Table 6. List of differentially abundant proteins in *P. piezophilus* biofilm cells when incubated with mild steel AH36 at 15 MPa.

KEGG ID	Protein Description	p.value	log2fc
Enriched proteins			
BN4_20225	PEP-CTERM protein-sorting domain-containing protein	0.01	7.76
BN4_11750	Small-conductance mechanosensitive channel	0.01	5.29
BN4_12412	Flagellar hook protein FlgE	0.01	4.54
BN4_12588	Flagellar hook-length control protein	0.01	4.51
BN4_12331	C_GCAxxG_C_C family protein	0.02	4.00
BN4_12383	Uncharacterized protein	0.04	3.29
BN4_11203	Glucans biosynthesis protein G	0.00	2.73
BN4_20177	Molybdenum transport system permease	0.02	2.71
BN4_20160	Formate dehydrogenase subunit beta	0.00	2.71
BN4_12585	Flagellar hook protein FlgE	0.03	2.64
BN4_11880	Molybdopterin molybdenumtransferase	0.04	2.60
BN4_10717	Glutamyl-tRNA reductase	0.02	2.54
BN4_12703	MscS Mechanosensitive ion channel	0.03	2.43
BN4_11084	Chloride channel core	0.04	2.40
BN4_12191	Transcriptional regulator, LysR family	0.03	2.39
BN4_10753	Flagellar hook-associated protein 3	0.00	2.35
BN4_11499	Phosphoadenosine phosphosulfate reductase	0.04	2.30
BN4_20524	Flagellar hook-associated protein 2	0.00	2.27
BN4_10761	Flagellar basal-body rod protein FlgG	0.05	2.09
BN4_10701	2-amino-4-hydroxy-6-hydroxymethyldihydropteridine pyrophosphokinase	0.03	1.80
BN4_20442	D-alanine--D-alanine ligase	0.01	1.79
BN4_11332	Periplasmic heavy metal sensor	0.02	1.75
BN4_20241	histidine kinase	0.04	1.75
BN4_11013	Phosphoglucomutase	0.03	1.67
BN4_12678	Methyltransferase type 11	0.04	1.63
BN4_10312	CDP-diacylglycerol--glycerol-3-phosphate 3-phosphatidyltransferase	0.04	1.59
BN4_12546	Signal peptide peptidase SppA, 36K type	0.02	1.59
BN4_10045	Uncharacterized protein	0.05	1.58
BN4_12556	ATP synthase subunit c	0.01	1.58
BN4_12733	Inner membrane protein ybhL	0.04	1.56
BN4_12260	Methyl-accepting chemotaxis sensory transducer with Cache sensor	0.02	1.54
BN4_12294	TPM domain-containing protein	0.00	1.51
BN4_10063	Polar amino acid ABC transporter, inner membrane subunit	0.02	1.50
BN4_10534	CBS domain containing protein	0.01	1.46
BN4_11895	Cytochrome c oxidase subunit 2	0.01	1.44
BN4_10137	Uncharacterized protein	0.00	1.44
BN4_11791	Methyl-accepting chemotaxis sensory transducer with Pas/Pac sensor	0.00	1.44
BN4_10697	Phosphoenolpyruvate synthase	0.04	1.43
BN4_11552	Uncharacterized protein	0.01	1.41

BN4_10864	Outer membrane homotrimeric porin	0.00	1.39
BN4_10236	Extracellular solute-binding protein family 3	0.01	1.39
BN4_20227	Ion-translocating oxidoreductase complex subunit B	0.02	1.38
BN4_11027	Putative Methyl-accepting chemotaxis protein	0.02	1.35
BN4_11715	Methyl-accepting chemotaxis sensory transducer	0.01	1.34
BN4_10639	histidine kinase	0.04	1.34
BN4_10261	MotA/TolQ/ExbB proton channel	0.00	1.30
BN4_11805	Uncharacterized protein	0.00	1.30
BN4_11668	Chemoreceptor protein A	0.00	1.27
BN4_12632	Oligosaccharyl transferase STT3 subunit	0.04	1.25
BN4_10455	Magnesium transporter MgtE	0.02	1.24
BN4_20283	Flagellar M-ring protein	0.03	1.24
BN4_20372	High-affinity branched-chain amino acid transport system permease protein BraE	0.01	1.24
BN4_11597	Phospho-N-acetylmuramoyl-pentapeptide-transferase	0.04	1.23
BN4_10207	Ribonuclease BN	0.03	1.23
BN4_20019	histidine kinase	0.03	1.21
BN4_20305	Electron transfer flavoprotein alpha/beta-subunit	0.03	1.20
BN4_20029	Methyl-accepting transducer domain-containing protein	0.02	1.19
BN4_11242	Putative Receptor-mostly Fe transport	0.02	1.19
BN4_11102	Restriction modification system DNA specificity domain	0.03	1.18
BN4_12503	Inner membrane protein, binds b-type hemes	0.05	1.18
BN4_12525	ATP synthase subunit b	0.01	1.18
BN4_10154	Ion-translocating oxidoreductase complex subunit G	0.01	1.18
BN4_10608	Polar amino acid ABC transporter, inner membrane subunit	0.04	1.18
BN4_10885	Nickel transport complex, NikM subunit, transmembrane	0.02	1.17
BN4_10542	inorganic diphosphatase	0.00	1.17
BN4_11732	Arginine biosynthesis bifunctional protein ArgJ	0.01	1.15
BN4_11420	Membrane protein insertase YidC	0.00	1.14
BN4_11408	Maturation element for hydrogenase 2	0.00	1.14
BN4_10802	NADH-quinone oxidoreductase subunit N	0.02	1.14
BN4_11005	Peptidyl-prolyl cis-trans isomerase	0.01	1.14
BN4_12768	DUF697 domain-containing protein	0.02	1.13
BN4_10816	Probable 2-phosphosulfolactate phosphatase	0.03	1.13
BN4_12636	Peptidyl-prolyl cis-trans isomerase	0.00	1.12
BN4_11735	Putative ABC transporter permease protein HI_1086	0.01	1.10
BN4_11806	Quinone-interacting membrane-bount oxidoreductase. b-heme and FeS protein	0.01	1.10
BN4_12713	Protein ynjB	0.02	1.08
BN4_11074	Methyl-accepting chemotaxis sensory transducer	0.01	1.08
BN4_20231	Electron transport complex, RnfD subunit	0.01	1.07
BN4_11389	Outer membrane protein beta-barrel domain-containing protein	0.01	1.06
BN4_10810	NADH-quinone oxidoreductase subunit H	0.00	1.06
BN4_12799	Nicotinate-nucleotide--dimethylbenzimidazole phosphoribosyltransferase	0.00	1.04
BN4_12040	Sulfate exporter family transporter	0.02	1.04

BN4_11467	DUF748 domain-containing protein	0.00	1.03
BN4_12529	ATP synthase subunit beta	0.05	1.01
BN4_10316	Lipoprotein	0.03	1.01
BN4_11823	Methyl-accepting chemotaxis sensory transducer	0.00	1.00
BN4_11328	Antibiotic biosynthesis monooxygenase	0.02	1.00
BN4_12413	Outer membrane chaperone Skp (OmpH)	0.05	0.99
BN4_10974	Tetratricopeptide repeat-like domain-containing protein	0.00	0.97
BN4_10614	Molybdopterin-containing protein family	0.00	0.96
BN4_10326	histidine kinase	0.03	0.96
BN4_12490	Putative Methyl-accepting chemotaxis sensory transducer	0.01	0.96
BN4_10112	2-isopropylmalate synthase	0.05	0.96
BN4_20229	Ion-translocating oxidoreductase complex subunit E	0.02	0.94
BN4_10947	Tmc complex, transmembrane protein	0.01	0.93
BN4_10615	Pentaheme cytochrome c	0.03	0.92
BN4_10667	histidine kinase	0.05	0.90
BN4_12031	Na+/H+ antiporter NhaC	0.01	0.90
BN4_11821	Methyl-accepting chemotaxis sensory transducer	0.03	0.88
BN4_10098	Outer membrane efflux protein	0.04	0.88
BN4_12213	Band 7 domain-containing protein	0.01	0.88
BN4_10742	Methyl-accepting chemotaxis sensory transducer	0.01	0.87
BN4_20296	Methyl-accepting chemotaxis sensory transducer with Cache sensor	0.01	0.87
BN4_12708	Methyl-accepting chemotaxis sensory transducer	0.00	0.87
BN4_12077	Putative SnoG	0.00	0.86
BN4_12276	Sulfate transporter	0.03	0.85
BN4_20242	Carbon starvation protein CstA	0.05	0.85
BN4_20119	YtxH domain-containing protein	0.01	0.84
BN4_10484	Aspartokinase	0.01	0.83
BN4_11676	Uncharacterized protein	0.02	0.83
BN4_10476	Chemotaxis protein CheW	0.01	0.82
BN4_12323	Putative metal dependent phosphohydrolase	0.01	0.79
BN4_12482	Methyl-accepting chemotaxis sensory transducer	0.00	0.78
BN4_10754	Flagellar hook-associated protein 1	0.04	0.78
BN4_10232	Basic membrane lipoprotein	0.00	0.77
BN4_12292	LemA family protein	0.00	0.77
BN4_10580	Fumarate reductase respiratory complex transmembrane subunit	0.00	0.77
BN4_10842	ATP-dependent zinc metalloprotease FtsH	0.02	0.75
BN4_11291	DNA repair protein RecN	0.01	0.75
BN4_12758	Putative PAS/PAC sensor protein	0.03	0.74
BN4_11948	Na(+)/H(+) antiporter NhaA	0.03	0.74
BN4_11470	Diguanylate cyclase/phosphodiesterase with PAS/PAC sensor(S)	0.05	0.73
BN4_10991	Putative Methyl-accepting chemotaxis sensory transducer	0.01	0.71
BN4_12387	Zinc transporter ZupT	0.03	0.71
BN4_20051	PilZ domain-containing protein	0.03	0.70
BN4_20450	Hydrogenase expression/formation protein hypE	0.04	0.69
BN4_20370	Extracellular ligand-binding receptor	0.02	0.68

BN4_20430	Putative CheA signal transduction histidine kinase	0.01	0.68
BN4_12641	Extracellular ligand-binding receptor	0.00	0.67
BN4_12208	Putative lipoprotein	0.01	0.67
BN4_10706	Histidine triad (HIT) protein	0.02	0.67
BN4_20326	Phosphate acetyltransferase	0.00	0.65
BN4_12784	HesB/YadR/YfhF-family protein	0.05	0.65
BN4_10090	Uncharacterized protein	0.01	0.65
BN4_10365	YggT family protein	0.02	0.64
BN4_10806	NADH/Ubiquinone/plastoquinone (Complex I)	0.03	0.61
BN4_20429	histidine kinase	0.04	0.59
Depleted proteins			
BN4_11022	Chaperonin GroEL	0.00	-0.60
BN4_11760	Carbon monoxide dehydrogenase	0.00	-0.60
BN4_12775	Aminotransferase	0.03	-0.60
BN4_12286	DNA repair ATPase	0.04	-0.61
BN4_10009	Elongation factor Ts	0.01	-0.62
BN4_20314	50S ribosomal subunit assembly factor BipA	0.01	-0.62
BN4_12354	Diguanylate phosphodiesterase	0.02	-0.63
BN4_11924	Uncharacterized protein	0.03	-0.63
BN4_10192	Beta-lactamase domain protein	0.02	-0.66
BN4_11808	Quinone-interacting membrane bound oxidoreductase, Flavin protein	0.00	-0.68
BN4_11812	sulfate adenylyltransferase	0.04	-0.69
BN4_11977	Aspartate--tRNA(Asp/Asn) ligase	0.04	-0.70
BN4_11865	Rubrerythrin	0.03	-0.70
BN4_12144	Acetoacetate metabolism regulatory protein AtoC	0.04	-0.71
BN4_11250	Isoprenylcysteine carboxylmethyltransferase family protein	0.03	-0.71
BN4_10785	Probable glycine dehydrogenase (decarboxylating) subunit 1	0.04	-0.72
BN4_12508	Fructose-1,6-bisphosphatase	0.05	-0.73
BN4_11936	Valine--tRNA ligase	0.00	-0.75
BN4_10900	Carbamoyl-phosphate synthase large chain	0.03	-0.76
BN4_12801	Porphobilinogen deaminase	0.04	-0.76
BN4_12020	Glutamine synthetase	0.03	-0.77
BN4_10904	Methionine--tRNA ligase	0.01	-0.77
BN4_20306	Electron transfer flavoprotein alpha/beta-subunit	0.05	-0.77
BN4_20331	Stress responsive alpha-beta barrel domain protein	0.01	-0.78
BN4_10196	Lysine--tRNA ligase	0.04	-0.79
BN4_11430	S-adenosylmethionine synthase	0.04	-0.81
BN4_10115	3-isopropylmalate dehydrogenase	0.01	-0.81
BN4_20304	Electron transfer flavoprotein-ubiquinone oxidoreductase	0.02	-0.81
BN4_11796	UspA domain protein	0.03	-0.81
BN4_10594	Pyruvate-flavodoxin oxidoreductase	0.04	-0.82
BN4_10273	Imidazole glycerol phosphate synthase subunit HisF	0.00	-0.82
BN4_11803	NADP-dependent L-serine/L-allo-threonine dehydrogenase ydfG	0.01	-0.82
BN4_11994	Diaminopimelate epimerase	0.01	-0.82
BN4_20328	LUD domain-containing protein	0.02	-0.82

BN4_11437	3-dehydroquinate synthase homolog	0.01	-0.83
BN4_10973	Gamma-glutamyl phosphate reductase	0.00	-0.83
BN4_12202	Pyruvate ferredoxin/flavodoxin oxidoreductase	0.03	-0.83
BN4_12727	Alanine--tRNA ligase	0.04	-0.84
BN4_10193	Uncharacterized protein	0.04	-0.84
BN4_10975	Indolepyruvate oxidoreductase subunit IorA	0.00	-0.85
BN4_11601	UDP-N-acetylmuramate--L-alanine ligase	0.04	-0.85
BN4_12172	Sporulation domain protein	0.00	-0.85
BN4_10270	Betaine aldehyde dehydrogenase	0.05	-0.85
BN4_20416	TPR repeat-containing protein	0.04	-0.85
BN4_20373	High-affinity branched-chain amino acid transport ATP-binding protein LivG	0.02	-0.87
BN4_20036	Probable alpha-L-glutamate ligase	0.01	-0.87
BN4_20494	50S ribosomal protein L17	0.01	-0.89
BN4_11636	Dihydroxy-acid dehydratase	0.01	-0.90
BN4_11686	Phosphoenolpyruvate-protein phosphotransferase	0.04	-0.90
BN4_20103	Ferric uptake regulation protein	0.03	-0.90
BN4_10360	Sec-independent protein translocase protein TatA	0.01	-0.93
BN4_12815	Riboflavin biosynthesis protein RibBA	0.02	-0.94
BN4_10343	Amino acid-binding ACT domain protein	0.00	-0.94
BN4_12786	Bifunctional protein PyrR	0.00	-0.95
BN4_12653	Chaperonin GroEL	0.00	-0.96
BN4_11851	Aconitate hydratase A	0.02	-0.96
BN4_20336	Transferase hexapeptide repeat containing protein	0.00	-0.96
BN4_11065	Putative RNA-binding protein rbpE	0.01	-0.96
BN4_11665	Rubrerythrin	0.00	-0.96
BN4_10409	SufBD protein	0.01	-0.97
BN4_11438	Bifunctional chorismate mutase/prephenate dehydratase	0.02	-0.97
BN4_12509	transketolase	0.02	-0.98
BN4_11418	LUD domain-containing protein	0.02	-0.98
BN4_10203	Acyl-[acyl-carrier-protein]--UDP-N-acetylglucosamine O-acyltransferase	0.02	-0.98
BN4_12765	Elongation factor 4	0.04	-0.99
BN4_10976	Indolepyruvate ferredoxin oxidoreductase	0.03	-0.99
BN4_10511	Carboxy-terminal-processing protease	0.03	-1.01
BN4_20030	DUF169 domain-containing protein	0.00	-1.01
BN4_11080	Transcriptional regulator, CarD family	0.01	-1.02
BN4_12080	GHMP kinase	0.02	-1.02
BN4_12562	ATP phosphoribosyltransferase	0.01	-1.02
BN4_10217	Polymerase/histidinol phosphatase N-terminal domain-containing protein	0.00	-1.02
BN4_20491	30S ribosomal protein S11	0.04	-1.03
BN4_11239	Secretion protein HlyD	0.04	-1.05
BN4_10710	Diaminopimelate decarboxylase	0.02	-1.05
BN4_20393	Chaperone protein ClpB	0.01	-1.05
BN4_11818	Bifunctional protein FolD	0.01	-1.05
BN4_12003	DNA topoisomerase 1	0.03	-1.05

BN4_20490	30S ribosomal protein S13	0.04	-1.06
BN4_11887	6-phosphofructokinase 6	0.00	-1.06
BN4_10556	Phosphoribosylformylglycinamidine synthase 1	0.01	-1.07
BN4_12583	Transcriptional regulator, XRE family	0.03	-1.08
BN4_10653	CoB--CoM heterodisulfide reductase	0.03	-1.09
BN4_20512	Ribulose-phosphate 3-epimerase	0.02	-1.09
BN4_11407	isocitrate dehydrogenase (NADP(+))	0.00	-1.10
BN4_10734	Cell division coordinator CpoB	0.02	-1.10
BN4_10305	ADP-ribosylation/Crystallin J1	0.04	-1.11
BN4_10344	Phenylacetate-coenzyme A ligase	0.00	-1.12
BN4_10776	Sigma54 specific transcriptional regulator, Fis family	0.03	-1.12
BN4_12610	Putative Chemotaxis protein CheX	0.01	-1.13
BN4_12444	Deoxyribodipyrimidine photo-lyase	0.02	-1.13
BN4_12204	Ketoisovalerate oxidoreductase subunit vorB	0.00	-1.14
BN4_12637	High-affinity branched-chain amino acid transport ATP-binding protein BraG	0.01	-1.14
BN4_20439	Carbamoyl-phosphate synthase small chain	0.05	-1.14
BN4_11702	Serine--tRNA ligase	0.02	-1.14
BN4_12762	N-acetyl-gamma-glutamyl-phosphate reductase	0.01	-1.15
BN4_11935	uroporphyrinogen-III C-methyltransferase	0.01	-1.15
BN4_10815	histidine kinase	0.02	-1.16
BN4_10858	UbiD family decarboxylase	0.02	-1.17
BN4_10837	UTP--glucose-1-phosphate uridylyltransferase	0.03	-1.17
BN4_10652	Glycerol kinase	0.00	-1.17
BN4_10611	Amino-acid transporter subunit ATP-binding component of ABC superfamily	0.00	-1.17
BN4_11443	Anthranilate phosphoribosyltransferase	0.01	-1.18
BN4_12628	Sulfite reductase, dissimilatory-type subunit beta	0.00	-1.18
BN4_11717	Glutamate-1-semialdehyde 2,1-aminomutase	0.01	-1.18
BN4_10768	Phosphoesterase RecJ domain protein	0.04	-1.19
BN4_10075	Tetratricopeptide domain protein	0.03	-1.20
BN4_12742	Ketose-bisphosphate aldolase class-II	0.02	-1.20
BN4_10301	ATP-dependent Clp protease proteolytic subunit	0.03	-1.20
BN4_20475	50S ribosomal protein L16	0.02	-1.21
BN4_10961	Acyl-CoA synthetase yngI	0.02	-1.21
BN4_12059	GDP-mannose 3,5-epimerase	0.03	-1.21
BN4_11755	Glucose-6-phosphate 1-dehydrogenase	0.01	-1.22
BN4_12825	FMN-dependent alpha-hydroxy acid dehydrogenase	0.00	-1.24
BN4_10555	CTP synthase	0.02	-1.24
BN4_10666	Response regulator receiver protein	0.01	-1.24
BN4_12382	CoA-binding domain protein	0.05	-1.25
BN4_10161	Thioredoxin-disulfide reductase	0.00	-1.25
BN4_12047	Aldehyde ferredoxin oxidoreductase	0.04	-1.25
BN4_20516	Delta-aminolevulinic acid dehydratase	0.00	-1.27
BN4_10311	Iron-sulfur cluster carrier protein	0.03	-1.27
BN4_11578	Protein rrf2	0.01	-1.27

BN4_12214	Protein CapI	0.01	-1.28
BN4_11077	Ribose-phosphate pyrophosphokinase	0.03	-1.30
BN4_11655	RapA2 cadherin-like domain-containing protein	0.04	-1.33
BN4_12431	PhoH family protein	0.02	-1.33
BN4_11966	Ornithine aminotransferase	0.01	-1.34
BN4_11439	3-phosphoshikimate 1-carboxyvinyltransferase	0.01	-1.34
BN4_10894	Peptidase U32	0.05	-1.34
BN4_11131	Transcriptional regulator, AraC family	0.00	-1.34
BN4_11093	Hmc complex, High-molecular-weight cytochrome c, 15 heme	0.00	-1.34
BN4_10778	FAD dependent oxidoreductase	0.00	-1.35
BN4_10381	Metal dependent phosphohydrolase	0.02	-1.36
BN4_10274	Imidazole glycerol phosphate synthase subunit HisH	0.02	-1.36
BN4_11631	Riboflavin biosynthesis protein RibD	0.03	-1.37
BN4_11589	Metal dependent phosphohydrolase	0.02	-1.37
BN4_10596	Superoxide dismutase	0.00	-1.37
BN4_11081	Transcription termination factor Rho	0.04	-1.38
BN4_12461	3-methyl-2-oxobutanoate hydroxymethyltransferase	0.00	-1.38
BN4_20186	Glycogen debranching enzyme	0.02	-1.39
BN4_11381	FAD-dependent pyridine nucleotide-disulphide oxidoreductase	0.00	-1.39
BN4_10692	Response regulator receiver protein	0.04	-1.39
BN4_10405	acetolactate synthase	0.00	-1.40
BN4_11622	Nitrogen-fixing NifU domain protein	0.02	-1.40
BN4_10536	Peptide chain release factor 2	0.00	-1.41
BN4_10738	Chemotaxis protein methyltransferase	0.03	-1.41
BN4_20477	30S ribosomal protein S17	0.00	-1.42
BN4_11663	Rubredoxin-oxygen oxidoreductase	0.01	-1.42
BN4_11472	Molybdopterin synthase catalytic subunit	0.01	-1.42
BN4_10720	Adenylate kinase	0.01	-1.43
BN4_12530	ATP synthase epsilon chain	0.04	-1.44
BN4_10366	Cell-division initiation protein DivIVA	0.01	-1.44
BN4_11327	Putative succinate-semialdehyde dehydrogenase [NADP+]	0.03	-1.44
BN4_10463	Cupin 2 conserved barrel domain protein	0.04	-1.45
BN4_20473	50S ribosomal protein L22	0.01	-1.46
BN4_10377	Phosphatidylglycerol lysyltransferase C-terminal domain-containing protein	0.05	-1.46
BN4_10384	Methylenetetrahydrofolate--tRNA-(uracil-5-)-methyltransferase TrmFO	0.02	-1.46
BN4_10553	3-deoxy-D-manno-octulosonate 8-phosphate phosphatase KdsC	0.01	-1.48
BN4_10288	Signal recognition particle receptor FtsY	0.01	-1.48
BN4_10786	glycine dehydrogenase (aminomethyl-transferring)	0.00	-1.48
BN4_20459	50S ribosomal protein L1	0.02	-1.49
BN4_12362	Flavoredoxin	0.00	-1.51
BN4_10243	Homoserine dehydrogenase	0.00	-1.51
BN4_11190	N-acyl-D-amino-acid deacylase	0.00	-1.52
BN4_11872	XshC-Cox1-family protein	0.04	-1.52
BN4_12118	Phosphoribosylamine--glycine ligase	0.03	-1.52
BN4_12684	Methyltransferase domain-containing protein	0.03	-1.52

BN4_11914	Intracellular protease, PfpI family	0.01	-1.53
BN4_12088	Glutamine-dependent NAD(+) synthetase	0.01	-1.53
BN4_11972	Amine oxidase	0.02	-1.53
BN4_10352	Beta-lactamase domain protein	0.00	-1.53
BN4_10827	Thiamine-phosphate synthase	0.04	-1.54
BN4_10828	Thiamine biosynthesis protein ThiF	0.00	-1.54
BN4_11314	Molybdenum storage protein subunit beta	0.00	-1.54
BN4_20273	Translation initiation factor IF-3	0.01	-1.54
BN4_11086	ATP-dependent protease subunit HslV	0.04	-1.55
BN4_12510	Putative ribose-5-phosphate isomerase B	0.02	-1.57
BN4_10267	Uncharacterized protein	0.01	-1.57
BN4_10317	Fructose-1,6-bisphosphatase class 1	0.03	-1.58
BN4_20033	Catalase	0.00	-1.58
BN4_12341	CBS domain containing membrane protein	0.00	-1.59
BN4_10551	Lipopolysaccharide transport periplasmic protein LptA	0.00	-1.60
BN4_12019	Universal stress protein	0.00	-1.61
BN4_20246	Extracellular solute-binding protein family 1	0.03	-1.61
BN4_11183	Putative xanthine dehydrogenase subunit D (XDHasesubunit D)	0.03	-1.62
BN4_10136	Aldehyde ferredoxin oxidoreductase	0.00	-1.62
BN4_11364	NeuB family protein	0.03	-1.63
BN4_10942	Response regulator receiver protein	0.03	-1.63
BN4_10600	Extracellular solute-binding protein family 3	0.04	-1.64
BN4_10339	4-hydroxy-tetrahydrodipicolinate reductase	0.00	-1.64
BN4_12526	ATP synthase subunit delta	0.00	-1.65
BN4_10503	glutamate synthase (NADPH)	0.00	-1.67
BN4_11766	histidine kinase	0.00	-1.67
BN4_10416	Exopolyphosphatase-related protein	0.01	-1.68
BN4_10610	ABC transporter glutamine-binding protein glnH	0.04	-1.69
BN4_11481	SEC-C motif domain protein	0.01	-1.69
BN4_20508	Transcriptional regulator, AsnC family	0.01	-1.70
BN4_11405	DUF306 domain-containing protein	0.01	-1.70
BN4_11448	TPR repeat-containing protein	0.03	-1.70
BN4_20465	30S ribosomal protein S7	0.00	-1.73
BN4_10538	Flagellar synthesis regulator FleN	0.02	-1.73
BN4_11436	2-amino-3,7-dideoxy-D-threo-hept-6-ulosonate synthase	0.00	-1.73
BN4_20468	50S ribosomal protein L3	0.01	-1.73
BN4_11804	Diguanylate cyclase DosC	0.03	-1.74
BN4_12414	Hpt protein	0.01	-1.75
BN4_10755	FlgN protein	0.01	-1.75
BN4_20258	UDP-N-acetylglucosamine 1-carboxyvinyltransferase	0.00	-1.75
BN4_10640	Transcriptional regulatory protein zraR	0.03	-1.75
BN4_10408	ABC transporter related protein	0.01	-1.75
BN4_10396	Cysteine synthase	0.01	-1.76
BN4_20338	CBS domain containing membrane protein	0.00	-1.78
BN4_11049	Efflux transporter, RND family, MFP subunit	0.01	-1.78

BN4_11695	50S ribosomal protein L19	0.01	-1.79
BN4_10865	Histidinol dehydrogenase	0.02	-1.79
BN4_12726	50S ribosomal protein L13	0.04	-1.80
BN4_10876	Threonine synthase	0.00	-1.84
BN4_11798	High-affinity branched-chain amino acid transport ATP-binding protein BraG	0.01	-1.85
BN4_12774	Iron-sulfur cluster carrier protein	0.00	-1.85
BN4_12231	Putative Phenylacetate-coenzyme A ligase	0.00	-1.85
BN4_11881	cysteine desulfurase	0.02	-1.86
BN4_20483	50S ribosomal protein L6	0.00	-1.87
BN4_11511	Response regulator receiver modulated CheW protein	0.00	-1.88
BN4_11659	Response regulator rpfG	0.02	-1.88
BN4_20460	50S ribosomal protein L10	0.01	-1.88
BN4_12101	SIR2-like domain-containing protein	0.00	-1.90
BN4_11749	Secondary thiamine-phosphate synthase enzyme	0.00	-1.92
BN4_12036	Periplasmic [NiFe] hydrogenase large subunit	0.00	-1.92
BN4_10231	Xanthine-guanine phosphoribosyltransferase	0.02	-1.92
BN4_11574	Putative cytoplasmic protein	0.01	-1.92
BN4_10200	Outer membrane chaperone Skp (OmpH)	0.00	-1.93
BN4_12531	Aspartate aminotransferase A	0.00	-1.93
BN4_11054	Phosphoesterase RecJ domain protein	0.02	-1.93
BN4_11069	DUF3088 domain-containing protein	0.02	-1.94
BN4_10252	Pyruvate ferredoxin/flavodoxin oxidoreductase, beta subunit	0.00	-1.95
BN4_11396	Uncharacterized protein	0.00	-1.95
BN4_20485	30S ribosomal protein S5	0.00	-1.95
BN4_10740	Protein-glutamate methylesterase/protein-glutamine glutaminase	0.04	-1.96
BN4_11611	3-oxoacyl-[acyl-carrier-protein] reductase	0.00	-1.96
BN4_12307	Metal dependent phosphohydrolase	0.01	-1.97
BN4_10582	succinate dehydrogenase	0.05	-1.99
BN4_10960	Peptidyl-prolyl cis-trans isomerase	0.00	-2.00
BN4_20487	50S ribosomal protein L15	0.00	-2.01
BN4_12030	Putative UspA domain protein	0.00	-2.01
BN4_11023	Co-chaperonin GroES	0.00	-2.02
BN4_12302	UspA domain protein	0.02	-2.03
BN4_20002	Ferredoxin-nitroreductase protein	0.03	-2.06
BN4_11984	Dihydroorotase	0.05	-2.06
BN4_10061	Polysaccharide biosynthesis protein CapD-like domain-containing protein	0.00	-2.06
BN4_11583	RNA methyltransferase, TrmA family	0.01	-2.07
BN4_20451	Response regulator receiver modulated CheW protein	0.01	-2.08
BN4_11949	Diguanylate cyclase/phosphodiesterase with PAS/PAC sensor(S)	0.02	-2.09
BN4_12664	FG-GAP repeat protein	0.01	-2.09
BN4_10929	Glyoxylate reductase	0.00	-2.10
BN4_10770	30S ribosomal protein S15	0.00	-2.10
BN4_10121	Methylenetetrahydrofolate reductase	0.00	-2.10
BN4_12551	Hypoxanthine phosphoribosyltransferase	0.05	-2.11
BN4_20334	histidine kinase	0.01	-2.12

BN4_10869	50S ribosomal protein L9	0.00	-2.13
BN4_11833	Methyltransferase type 11	0.01	-2.13
BN4_12644	Putative transcriptional regulator	0.00	-2.13
BN4_10238	Deoxyguanosinetriphosphate triphosphohydrolase-like protein	0.01	-2.14
BN4_10769	tRNA pseudouridine synthase B	0.00	-2.15
BN4_10036	Extracellular solute-binding protein family 5	0.04	-2.15
BN4_10541	4-hydroxy-tetrahydrodipicolinate synthase	0.00	-2.16
BN4_11510	acylphosphatase	0.01	-2.16
BN4_10064	Extracellular solute-binding protein family 3	0.03	-2.16
BN4_11961	Protein vdlD	0.01	-2.19
BN4_10583	Putative fumarate hydratase subunit alpha	0.03	-2.21
BN4_10168	Methyltransferase small	0.01	-2.22
BN4_20035	Succinylglutamate desuccinylase/aspartoacylase	0.02	-2.22
BN4_20476	50S ribosomal protein L29	0.01	-2.23
BN4_20479	50S ribosomal protein L24	0.00	-2.24
BN4_20478	50S ribosomal protein L14	0.01	-2.25
BN4_10060	UDP-4-amino-4, 6-dideoxy-N-acetyl-beta-L-altrosamine transaminase	0.00	-2.26
BN4_11505	Orotate phosphoribosyltransferase	0.00	-2.31
BN4_10985	Putative RNA-binding protein rbpA	0.01	-2.32
BN4_12310	histidine kinase	0.01	-2.32
BN4_10389	PilZ domain-containing protein	0.00	-2.33
BN4_11421	Single-stranded nucleic acid binding R3H domain protein	0.01	-2.33
BN4_10320	Thioredoxin reductase	0.00	-2.34
BN4_12434	Transcriptional regulator, AsnC family	0.01	-2.37
BN4_12576	Tyrosine--tRNA ligase	0.00	-2.38
BN4_10941	Response regulator receiver protein	0.03	-2.38
BN4_11900	Cytochrome c-553	0.01	-2.39
BN4_11368	3-oxoacyl-[acyl-carrier-protein] reductase	0.00	-2.41
BN4_11929	DRTGG domain protein	0.01	-2.41
BN4_10327	Protein-glutamate methylesterase/protein-glutamine glutaminase	0.00	-2.41
BN4_12317	Substrate-binding region of ABC-type glycine betaine transport system	0.02	-2.42
BN4_12085	Acylneuraminate cytidylyltransferase (Modular protein)	0.02	-2.43
BN4_12056	UDP-glucose 4-epimerase	0.05	-2.44
BN4_20391	Curved DNA-binding protein	0.00	-2.44
BN4_10401	Heat shock protein HSP20	0.03	-2.44
BN4_10506	Acetylornithine aminotransferase	0.01	-2.45
BN4_12569	Bifunctional protein GlmU	0.00	-2.45
BN4_10529	Purine nucleoside phosphorylase	0.01	-2.45
BN4_10397	Cysteine desulfurase	0.00	-2.45
BN4_10494	Glutaredoxin (Modular protein)	0.02	-2.46
BN4_10095	Glucose-1-phosphate thymidylyltransferase	0.00	-2.47
BN4_10091	Recombination-associated protein RdgC	0.01	-2.47
BN4_12358	Putative phage repressor	0.00	-2.49
BN4_20112	Periplasmic solute binding protein	0.02	-2.53
BN4_10899	Amidophosphoribosyltransferase	0.01	-2.53

BN4_11316	Acetylglutamate kinase	0.00	-2.55
BN4_20309	Uncharacterized protein	0.02	-2.55
BN4_20480	50S ribosomal protein L5	0.00	-2.55
BN4_20431	Response regulator receiver protein	0.02	-2.56
BN4_11906	Regulatory protein ada	0.00	-2.56
BN4_10992	Aminotransferase class V	0.00	-2.58
BN4_11487	Peptidase M23	0.02	-2.58
BN4_12217	Putative chromosome-partitioning protein parB	0.00	-2.58
BN4_10901	DUF1722 domain-containing protein	0.00	-2.60
BN4_10268	Single-stranded DNA-binding protein	0.00	-2.60
BN4_10737	Response regulator receiver protein	0.00	-2.61
BN4_10658	ABC transporter related	0.00	-2.63
BN4_11354	Aminotransferase class-III	0.00	-2.64
BN4_20486	50S ribosomal protein L30	0.00	-2.66
BN4_11075	Periplasmic serine endoprotease DegP-like	0.00	-2.67
BN4_12281	Response regulator receiver protein	0.01	-2.67
BN4_10244	Aminotransferase	0.00	-2.69
BN4_11795	Histidinol-phosphate aminotransferase	0.00	-2.69
BN4_11713	Lipoprotein	0.03	-2.70
BN4_12207	HTH merR-type domain-containing protein	0.02	-2.75
BN4_11369	5-methyltetrahydropteroyltriglutamate--homocysteine methyltransferase	0.04	-2.77
BN4_12092	Putative RNA-binding protein rbpA	0.00	-2.80
BN4_10369	Acetolactate synthase small subunit	0.00	-2.80
BN4_10437	Elongation factor P	0.00	-2.84
BN4_11385	TRAP dicarboxylate transporter-DctP subunit	0.02	-2.84
BN4_11325	Rho termination factor N-terminal domain-containing protein	0.01	-2.89
BN4_11742	dITP/XTP pyrophosphatase	0.02	-2.89
BN4_20482	30S ribosomal protein S8	0.01	-2.90
BN4_20457	Transcription termination/antitermination protein NusG	0.00	-2.90
BN4_10817	UDP-glucuronate decarboxylase	0.00	-2.93
BN4_20484	50S ribosomal protein L18	0.00	-2.93
BN4_10221	Protein tolB	0.01	-2.96
BN4_12813	Transcription antitermination protein NusB	0.00	-2.98
BN4_10486	Glyceraldehyde-3-phosphate dehydrogenase	0.00	-2.98
BN4_20428	Anaerobic cobalt chelatase	0.01	-2.99
BN4_11928	CoA-binding domain protein	0.01	-2.99
BN4_11060	Phenylacetate-coenzyme A ligase	0.00	-2.99
BN4_12171	Integration host factor subunit alpha	0.01	-3.03
BN4_20470	50S ribosomal protein L23	0.00	-3.04
BN4_11955	Cupin fold metalloprotein, WbuC family	0.00	-3.08
BN4_10007	Ribosome-recycling factor	0.00	-3.08
BN4_12180	Amphi-Trp domain-containing protein	0.02	-3.11
BN4_10466	Transcriptional regulator, Crp/Fnr family	0.02	-3.13
BN4_10103	2,3-bisphosphoglycerate-dependent phosphoglycerate mutase	0.00	-3.14
BN4_10170	Sulfite reductase, dissimilatory-type subunit gamma	0.01	-3.15

BN4_10584	Putative fumarate hydratase subunit beta	0.05	-3.21
BN4_10351	Cytokinin riboside 5'-monophosphate phosphoribohydrolase	0.00	-3.26
BN4_11478	Uncharacterized protein	0.00	-3.35
BN4_11038	Bacterial Pleckstrin homology domain-containing protein	0.00	-3.40
BN4_10953	Transcriptional regulator, MarR family	0.00	-3.43
BN4_20321	SPBc2 prophage-derived DNA-binding protein HU 2	0.02	-3.45
BN4_10286	Pseudouridine synthase	0.00	-3.46
BN4_11303	50S ribosomal protein L27	0.03	-3.47
BN4_12480	Heat shock protein Hsp20	0.02	-3.52
BN4_12629	Protein dsrD	0.05	-3.53
BN4_10979	Uncharacterized protein	0.00	-3.58
BN4_10539	Integration host factor subunit beta	0.00	-3.63
BN4_10548	Ribosome hibernation promoting factor	0.01	-3.73
BN4_20433	Sua5/YciO/YrdC/YwlC family protein	0.00	-3.75
BN4_11730	DUF3124 domain-containing protein	0.02	-3.82
BN4_10795	Chorismate synthase	0.00	-3.89
BN4_11716	siroheme decarboxylase	0.02	-4.05
BN4_10448	Triosephosphate isomerase	0.00	-4.08
BN4_10523	GatB/YqeY domain-containing protein	0.02	-4.09
BN4_10421	FMN dependent NADH:quinone oxidoreductase	0.00	-4.64
BN4_12378	Nitrogen regulatory protein P-II	0.00	-6.75

Supplementary Table 7. List of differentially abundant proteins in *P. piezophilus* biofilm cells when incubated with mild steel AH36 at 30 MPa.

KEGG ID	Protein Description	p.value	log2fc
Enriched proteins			
BN4_20225	PEP-CTERM protein-sorting domain-containing protein	0.03	8.18
BN4_20127	RND efflux system, outer membrane lipoprotein, NodT family	0.01	5.70
BN4_12588	Flagellar hook-length control protein	0.03	5.46
BN4_11203	Glucans biosynthesis protein G	0.04	5.20
BN4_12412	Flagellar hook protein FlgE	0.01	4.48
BN4_12585	Flagellar hook protein FlgE	0.03	3.65
BN4_10753	Flagellar hook-associated protein 3	0.01	3.19
BN4_12143	ATP-grasp domain-containing protein	0.01	2.74
BN4_20529	Shikimate kinase	0.02	2.66
BN4_12787	Shikimate kinase	0.00	2.59
BN4_10069	HicB-like antitoxin of toxin-antitoxin system domain-containing protein	0.01	2.43
BN4_20024	Phosphoenolpyruvate synthase	0.03	2.43
BN4_10983	Cold shock-like protein CspC (Modular protein)	0.04	2.25
BN4_20339	Dinitrogenase iron-molybdenum cofactor biosynthesis domain-containing protein	0.01	2.19
BN4_20524	Flagellar hook-associated protein 2	0.00	2.13
BN4_11360	Amidohydrolase-related domain-containing protein	0.02	2.04
BN4_11328	Antibiotic biosynthesis monooxygenase	0.03	1.97
BN4_20233	Pentaheme cytochrome c	0.00	1.96
BN4_10885	Nickel transport complex, NikM subunit, transmembrane	0.02	1.95
BN4_12041	Uncharacterized protein	0.02	1.93
BN4_12613	Auxin Efflux Carrier	0.03	1.86
BN4_11389	Outer membrane protein beta-barrel domain-containing protein	0.01	1.86
BN4_10236	Extracellular solute-binding protein family 3	0.00	1.83
BN4_20351	Acetoin:2,6-dichlorophenolindophenol oxidoreductase subunit beta	0.04	1.79
BN4_12387	Zinc transporter ZupT	0.03	1.78
BN4_12365	Methyl-accepting chemotaxis sensory transducer	0.01	1.75
BN4_20378	Sec-independent protein translocase protein TatC	0.03	1.72
BN4_12556	ATP synthase subunit c	0.03	1.72
BN4_11467	DUF748 domain-containing protein	0.03	1.70
BN4_20330	Methyl-accepting chemotaxis sensory transducer with Pas/Pac sensor	0.01	1.70
BN4_10237	ABC transmembrane type-1 domain-containing protein	0.00	1.68
BN4_11552	Uncharacterized protein	0.02	1.68
BN4_10727	Peptidyl-prolyl cis-trans isomerase	0.00	1.67
BN4_12352	DNA helicase	0.04	1.65
BN4_11693	Oxidoreductase domain protein	0.00	1.63
BN4_20177	Molybdenum transport system permease	0.03	1.63
BN4_20229	Ion-translocating oxidoreductase complex subunit E	0.01	1.57
BN4_11581	Metal transport protein HI_1621	0.04	1.56
BN4_12733	Inner membrane protein ybhL	0.01	1.56

BN4_10534	CBS domain containing protein	0.01	1.55
BN4_10172	DUF1385 domain-containing protein	0.02	1.54
BN4_12505	Diguanylate cyclase with PAS/PAC sensor	0.04	1.54
BN4_10864	Outer membrane homotrimeric porin	0.05	1.53
BN4_10542	inorganic diphosphatase	0.02	1.53
BN4_12260	Methyl-accepting chemotaxis sensory transducer with Cache sensor	0.02	1.52
BN4_10810	NADH-quinone oxidoreductase subunit H	0.04	1.51
BN4_10792	Uncharacterized protein	0.03	1.50
BN4_20241	histidine kinase	0.02	1.48
BN4_10639	histidine kinase	0.02	1.46
BN4_10216	BFN domain-containing protein	0.00	1.46
BN4_10990	Stress induced hydrophobic peptide	0.01	1.43
BN4_12133	histidine kinase	0.04	1.42
BN4_11562	Pyridine nucleotide-disulphide oxidoreductase dimerisation region	0.02	1.40
BN4_11142	TNase-like domain-containing protein	0.01	1.40
BN4_10804	NADH/Ubiquinone/plastoquinone (Complex I)	0.01	1.40
BN4_12294	TPM domain-containing protein	0.02	1.38
BN4_11735	Putative ABC transporter permease protein HI_1086	0.02	1.38
BN4_11676	Uncharacterized protein	0.05	1.35
BN4_12160	Lipid A export ATP-binding/permease protein MsbA	0.01	1.34
BN4_10197	Lipoprotein releasing system, transmembrane protein, LolC/E family	0.03	1.34
BN4_12264	Flagellar hook-associated protein 3	0.01	1.34
BN4_12636	Peptidyl-prolyl cis-trans isomerase	0.03	1.33
BN4_10754	Flagellar hook-associated protein 1	0.04	1.33
BN4_20292	Glycerol-3-phosphate acyltransferase	0.04	1.32
BN4_20305	Electron transfer flavoprotein alpha/beta-subunit	0.04	1.32
BN4_12040	Sulfate exporter family transporter	0.04	1.28
BN4_11791	Methyl-accepting chemotaxis sensory transducer with Pas/Pac sensor	0.01	1.27
BN4_11220	Putative iron(III) compound receptor	0.04	1.27
BN4_11948	Na(+)/H(+) antiporter NhaA	0.01	1.26
BN4_20231	Electron transport complex, RnfD subunit	0.00	1.25
BN4_11074	Methyl-accepting chemotaxis sensory transducer	0.02	1.25
BN4_12716	histidine kinase	0.02	1.24
BN4_11005	Peptidyl-prolyl cis-trans isomerase	0.02	1.23
BN4_11732	Arginine biosynthesis bifunctional protein ArgJ	0.04	1.21
BN4_11408	Maturation element for hydrogenase 2	0.00	1.21
BN4_10947	Tmc complex, transmembrane protein	0.00	1.20
BN4_11932	MATE efflux family protein	0.02	1.19
BN4_10261	MotA/TolQ/ExbB proton channel	0.00	1.16
BN4_11668	Chemoreceptor protein A	0.01	1.16
BN4_11420	Membrane protein insertase YidC	0.00	1.12
BN4_12503	Inner membrane protein, binds b-type hemes	0.01	1.11
BN4_11102	Restriction modification system DNA specificity domain	0.04	1.10
BN4_10044	Uncharacterized protein	0.02	1.08
BN4_10816	Probable 2-phosphosulfolactate phosphatase	0.04	1.07

BN4_20430	Putative CheA signal transduction histidine kinase	0.00	1.06
BN4_12529	ATP synthase subunit beta	0.02	1.05
BN4_20228	Ion-translocating oxidoreductase complex subunit A	0.02	1.05
BN4_20382	Small-conductance mechanosensitive channel	0.00	1.03
BN4_10934	histidine kinase	0.04	1.00
BN4_20096	Diguanylate cyclase with PAS/PAC sensor	0.01	1.00
BN4_10223	Phosphatidylglycerophosphatase A	0.04	0.99
BN4_10169	YcaO domain-containing protein	0.03	0.99
BN4_10974	Tetratricopeptide repeat-like domain-containing protein	0.03	0.99
BN4_12606	DUF4197 domain-containing protein	0.04	0.96
BN4_20242	Carbon starvation protein CstA	0.05	0.96
BN4_11806	Quinone-interacting membrane-bount oxidoreductase. b-heme and FeS protein	0.02	0.95
BN4_12810	Lipoprotein	0.03	0.94
BN4_11805	Uncharacterized protein	0.03	0.92
BN4_12525	ATP synthase subunit b	0.04	0.90
BN4_11823	Methyl-accepting chemotaxis sensory transducer	0.00	0.90
BN4_12292	LemA family protein	0.00	0.88
BN4_11095	histidine kinase	0.00	0.87
BN4_12031	Na+/H+ antiporter NhaC	0.01	0.86
BN4_11144	Dipeptide ABC transporter, solute-binding protein	0.01	0.85
BN4_10742	Methyl-accepting chemotaxis sensory transducer	0.01	0.84
BN4_12199	Homocysteine biosynthesis enzyme sulfur-incorporation domain-containing protein	0.05	0.83
BN4_20296	Methyl-accepting chemotaxis sensory transducer with Cache sensor	0.01	0.82
BN4_20108	Uncharacterized protein	0.02	0.81
BN4_12708	Methyl-accepting chemotaxis sensory transducer	0.00	0.81
BN4_10706	Histidine triad (HIT) protein	0.02	0.79
BN4_11821	Methyl-accepting chemotaxis sensory transducer	0.00	0.77
BN4_12490	Putative Methyl-accepting chemotaxis sensory transducer	0.05	0.76
BN4_10365	YggT family protein	0.02	0.76
BN4_10483	tRNA threonylcarbamoyladenosine biosynthesis protein TsaE	0.02	0.75
BN4_20323	L-lactate permease	0.02	0.75
BN4_11559	Transcription elongation factor GreA	0.00	0.74
BN4_12213	Band 7 domain-containing protein	0.04	0.74
BN4_10482	CBS domain containing membrane protein	0.02	0.71
BN4_12713	Protein ynjB	0.03	0.70
BN4_10853	Thiol peroxidase	0.01	0.69
BN4_10609	Putative glutamine ABC transporter permease protein glnM	0.02	0.69
BN4_20023	Transmembrane protein	0.01	0.66
BN4_10239	Lipoprotein	0.05	0.64
BN4_10090	Uncharacterized protein	0.00	0.64
BN4_10003	Zinc metalloprotease	0.05	0.64
BN4_12641	Extracellular ligand-binding receptor	0.01	0.61
BN4_10441	UPF0033 domain-containing protein	0.01	0.60
BN4_11291	DNA repair protein RecN	0.04	0.60

BN4_11614	DUF177 domain-containing protein	0.00	0.59
Depleted proteins			
BN4_12627	Sulfite reductase, dissimilatory-type subunit alpha	0.03	-0.62
BN4_10115	3-isopropylmalate dehydrogenase	0.01	-0.66
BN4_10633	Putative Chromosome partitioning ATPase-like protein	0.01	-0.67
BN4_11844	Hydantoinase/oxoprolinase	0.01	-0.68
BN4_10273	Imidazole glycerol phosphate synthase subunit HisF	0.03	-0.68
BN4_11430	S-adenosylmethionine synthase	0.00	-0.71
BN4_10009	Elongation factor Ts	0.02	-0.72
BN4_11605	Cell division protein FtsA	0.01	-0.73
BN4_11994	Diaminopimelate epimerase	0.04	-0.74
BN4_11556	Type-3 glutamine synthetase	0.01	-0.75
BN4_11055	DNA polymerase I	0.03	-0.75
BN4_11636	Dihydroxy-acid dehydratase	0.01	-0.76
BN4_11441	Anthranilate synthase component 1	0.04	-0.76
BN4_20303	Acyl-CoA dehydrogenase domain protein	0.04	-0.78
BN4_10876	Threonine synthase	0.04	-0.79
BN4_10904	Methionine--tRNA ligase	0.04	-0.80
BN4_10303	Lon protease	0.00	-0.82
BN4_10973	Gamma-glutamyl phosphate reductase	0.00	-0.82
BN4_11700	Signal recognition particle protein	0.01	-0.82
BN4_12172	Sporulation domain protein	0.00	-0.82
BN4_20288	IMP cyclohydrolase	0.01	-0.83
BN4_11650	OmpA/MotB domain protein	0.00	-0.84
BN4_10395	serine O-acetyltransferase	0.04	-0.85
BN4_20518	OmpA/MotB domain protein	0.03	-0.86
BN4_10192	Beta-lactamase domain protein	0.00	-0.87
BN4_10710	Diaminopimelate decarboxylase	0.00	-0.87
BN4_12581	Transcriptional regulator, XRE family	0.04	-0.88
BN4_10217	Polymerase/histidinol phosphatase N-terminal domain-containing protein	0.00	-0.89
BN4_10014	Elongation factor G	0.00	-0.89
BN4_10736	histidine kinase	0.03	-0.90
BN4_11022	Chaperonin GroEL	0.02	-0.90
BN4_20309	Uncharacterized protein	0.00	-0.91
BN4_11924	Uncharacterized protein	0.02	-0.92
BN4_11843	Histone deacetylase	0.04	-0.92
BN4_12362	Flavoredoxin	0.00	-0.93
BN4_12510	Putative ribose-5-phosphate isomerase B	0.01	-0.93
BN4_11418	LUD domain-containing protein	0.01	-0.94
BN4_10517	Nucleoside diphosphate kinase	0.01	-0.94
BN4_10302	ATP-dependent Clp protease ATP-binding subunit ClpX	0.02	-0.95
BN4_12610	Putative Chemotaxis protein CheX	0.04	-0.95
BN4_20496	Chorismate dehydratase	0.02	-0.95
BN4_12286	DNA repair ATPase	0.04	-0.96

BN4_20434	histidine kinase	0.02	-0.98
BN4_10344	Phenylacetate-coenzyme A ligase	0.05	-0.99
BN4_12202	Pyruvate ferredoxin/flavodoxin oxidoreductase	0.00	-0.99
BN4_11080	Transcriptional regulator, CarD family	0.03	-1.00
BN4_12686	CMP-N-acetlyneuraminic acid synthetase	0.01	-1.00
BN4_20416	TPR repeat-containing protein	0.02	-1.01
BN4_12643	Long-chain-fatty-acid--CoA ligase	0.01	-1.02
BN4_10768	Phosphoesterase RecJ domain protein	0.04	-1.03
BN4_10300	Trigger factor	0.01	-1.03
BN4_12003	DNA topoisomerase 1	0.03	-1.04
BN4_20336	Transferase hexapeptide repeat containing protein	0.02	-1.04
BN4_12214	Protein CapI	0.04	-1.04
BN4_20306	Electron transfer flavoprotein alpha/beta-subunit	0.03	-1.05
BN4_12509	transketolase	0.01	-1.06
BN4_10844	Argininosuccinate synthase	0.05	-1.07
BN4_12543	Phosphate-specific transport system accessory protein PhoU	0.03	-1.07
BN4_10402	endopeptidase La	0.04	-1.08
BN4_12653	Chaperonin GroEL	0.01	-1.08
BN4_11856	Two component, sigma54 specific, transcriptional regulator, Fis family	0.04	-1.08
BN4_10961	Acyl-CoA synthetase yngI	0.03	-1.08
BN4_10839	YbbR family protein	0.04	-1.08
BN4_12203	Thiamine pyrophosphate protein domain protein TPP-binding	0.05	-1.08
BN4_10289	Asparagine--tRNA ligase	0.04	-1.09
BN4_10828	Thiamine biosynthesis protein ThiF	0.05	-1.09
BN4_12637	High-affinity branched-chain amino acid transport ATP-binding protein BraG	0.01	-1.10
BN4_10665	Putative signal transduction protein	0.01	-1.11
BN4_11472	Molybdopterin synthase catalytic subunit	0.03	-1.11
BN4_10070	Glutamate synthase (NADPH)	0.03	-1.12
BN4_11555	Putative enzyme	0.02	-1.13
BN4_10173	Peptide chain release factor 1	0.03	-1.14
BN4_10785	Probable glycine dehydrogenase (decarboxylating) subunit 1	0.01	-1.14
BN4_20310	OsmC family protein	0.01	-1.14
BN4_12825	FMN-dependent alpha-hydroxy acid dehydrogenase	0.01	-1.14
BN4_12144	Acetoacetate metabolism regulatory protein AtoC	0.03	-1.15
BN4_11250	Isoprenylcysteine carboxylmethyltransferase family protein	0.04	-1.16
BN4_10975	Indolepyruvate oxidoreductase subunit IorA	0.01	-1.17
BN4_12775	Aminotransferase	0.01	-1.17
BN4_10400	Response regulator receiver modulated diguanylate cyclase/phosphodiesterase with PAS/PAC sensor(S)	0.02	-1.17
BN4_10681	2-hydroxyglutaryl-CoA dehydratase (HgdB-like)	0.01	-1.18
BN4_20389	Phosphonopyruvate decarboxylase-related protein	0.04	-1.18
BN4_20516	Delta-aminolevulinic acid dehydratase	0.00	-1.18
BN4_12283	Fumarate hydratase class II	0.02	-1.18
BN4_11171	L-lysine 2,3-aminomutase	0.02	-1.18
BN4_20314	50S ribosomal subunit assembly factor BipA	0.04	-1.18

BN4_10443	aminomethyltransferase	0.02	-1.19
BN4_10518	Pyrroline-5-carboxylate reductase	0.05	-1.19
BN4_11239	Secretion protein HlyD	0.02	-1.20
BN4_10109	Uncharacterized protein	0.03	-1.20
BN4_12690	Asparagine synthase (Glutamine-hydrolyzing)	0.05	-1.21
BN4_11887	6-phosphofructokinase 6	0.01	-1.23
BN4_10463	Cupin 2 conserved barrel domain protein	0.04	-1.24
BN4_12562	ATP phosphoribosyltransferase	0.02	-1.24
BN4_11663	Rubredoxin-oxygen oxidoreductase	0.00	-1.24
BN4_12136	Transcriptional regulatory protein flbD	0.02	-1.24
BN4_12019	Universal stress protein	0.00	-1.25
BN4_11234	Saccharopine dehydrogenase NADP binding domain-containing protein	0.03	-1.25
BN4_11327	Putative succinate-semialdehyde dehydrogenase [NADP+]	0.01	-1.25
BN4_10305	ADP-ribosylation/Crystallin J1	0.03	-1.26
BN4_11574	Putative cytoplasmic protein	0.04	-1.26
BN4_10786	glycine dehydrogenase (aminomethyl-transferring)	0.00	-1.27
BN4_11078	50S ribosomal protein L25	0.01	-1.28
BN4_11443	Anthranilate phosphoribosyltransferase	0.00	-1.28
BN4_12059	GDP-mannose 3,5-epimerase	0.02	-1.29
BN4_12815	Riboflavin biosynthesis protein RibBA	0.03	-1.29
BN4_11049	Efflux transporter, RND family, MFP subunit	0.02	-1.29
BN4_20289	GTPase HflX	0.02	-1.30
BN4_20030	DUF169 domain-containing protein	0.03	-1.30
BN4_10168	Methyltransferase small	0.01	-1.32
BN4_12727	Alanine--tRNA ligase	0.04	-1.32
BN4_11622	Nitrogen-fixing NifU domain protein	0.02	-1.33
BN4_10837	UTP--glucose-1-phosphate uridylyltransferase	0.00	-1.33
BN4_20393	Chaperone protein ClpB	0.00	-1.33
BN4_10246	DNA polymerase III subunit gamma/tau	0.02	-1.34
BN4_11972	Amine oxidase	0.03	-1.34
BN4_11491	1-deoxy-D-xylulose-5-phosphate synthase	0.00	-1.35
BN4_12120	Aminotransferase class IV	0.01	-1.35
BN4_10594	Pyruvate-flavodoxin oxidoreductase	0.05	-1.35
BN4_20258	UDP-N-acetylglucosamine 1-carboxyvinyltransferase	0.01	-1.35
BN4_11004	tryptophan--tRNA ligase	0.04	-1.35
BN4_10253	Energy-dependent translational throttle protein EttA	0.03	-1.36
BN4_10581	succinate dehydrogenase	0.05	-1.36
BN4_12020	Glutamine synthetase	0.04	-1.36
BN4_11578	Protein rrf2	0.02	-1.39
BN4_10666	Response regulator receiver protein	0.00	-1.39
BN4_11655	RapA2 cadherin-like domain-containing protein	0.00	-1.39
BN4_20439	Carbamoyl-phosphate synthase small chain	0.04	-1.40
BN4_10610	ABC transporter glutamine-binding protein glnH	0.04	-1.40
BN4_10366	Cell-division initiation protein DivIVA	0.01	-1.40
BN4_11851	Aconitate hydratase A	0.00	-1.41

BN4_12061	UDP-glucose 6-dehydrogenase	0.05	-1.41
BN4_11966	Ornithine aminotransferase	0.01	-1.41
BN4_20399	Protein GrpE	0.02	-1.42
BN4_10720	Adenylate kinase	0.03	-1.42
BN4_12742	Ketose-bisphosphate aldolase class-II	0.00	-1.42
BN4_12514	RNA polymerase sigma factor	0.00	-1.42
BN4_11818	Bifunctional protein FolD	0.00	-1.43
BN4_12728	Protein RecA	0.03	-1.43
BN4_12088	Glutamine-dependent NAD(+) synthetase	0.04	-1.44
BN4_10311	Iron-sulfur cluster carrier protein	0.04	-1.44
BN4_10556	Phosphoribosylformylglycinamidine synthase 1	0.02	-1.46
BN4_11381	FAD-dependent pyridine nucleotide-disulphide oxidoreductase	0.00	-1.47
BN4_12204	Ketoisovalerate oxidoreductase subunit vorB	0.00	-1.47
BN4_11439	3-phosphoshikimate 1-carboxyvinyltransferase	0.01	-1.48
BN4_12118	Phosphoribosylamine--glycine ligase	0.05	-1.49
BN4_12382	CoA-binding domain protein	0.01	-1.50
BN4_20485	30S ribosomal protein S5	0.03	-1.51
BN4_12461	3-methyl-2-oxobutanoate hydroxymethyltransferase	0.01	-1.51
BN4_11548	Aldose 1-epimerase	0.01	-1.52
BN4_10513	Flagellar motor switch protein FliM	0.00	-1.52
BN4_11407	isocitrate dehydrogenase (NADP(+))	0.02	-1.53
BN4_11589	Metal dependent phosphohydrolase	0.01	-1.53
BN4_11914	Intracellular protease, PfpI family	0.02	-1.53
BN4_12438	HTH merR-type domain-containing protein	0.05	-1.54
BN4_20032	Glutamine amidotransferase class-I	0.01	-1.54
BN4_10036	Extracellular solute-binding protein family 5	0.02	-1.55
BN4_10971	Uncharacterized protein	0.01	-1.55
BN4_11588	CBS domain containing protein	0.05	-1.55
BN4_10555	CTP synthase	0.01	-1.56
BN4_11547	Putative sugar transporter subunit: ATP-binding component of ABC superfamily transporter	0.02	-1.57
BN4_11069	DUF3088 domain-containing protein	0.04	-1.58
BN4_11949	Diguanylate cyclase/phosphodiesterase with PAS/PAC sensor(S)	0.02	-1.58
BN4_10611	Amino-acid transporter subunit ATP-binding component of ABC superfamily	0.00	-1.61
BN4_10301	ATP-dependent Clp protease proteolytic subunit	0.01	-1.62
BN4_11236	Polyketide synthase thioesterase domain-containing protein	0.02	-1.63
BN4_12748	Glutamine--tRNA ligase	0.02	-1.64
BN4_10623	Uncharacterized protein	0.01	-1.64
BN4_10136	Aldehyde ferredoxin oxidoreductase	0.00	-1.64
BN4_10267	Uncharacterized protein	0.02	-1.65
BN4_12341	CBS domain containing membrane protein	0.00	-1.65
BN4_11596	UDP-N-acetylmuramoyl-tripeptide--D-alanyl-D-alanine ligase	0.04	-1.65
BN4_20508	Transcriptional regulator, AsnC family	0.02	-1.66
BN4_10734	Cell division coordinator CpoB	0.04	-1.66
BN4_10346	Ribosomal silencing factor RsfS	0.01	-1.67

BN4_11183	Putative xanthine dehydrogenase subunit D (XDHasesubunit D)	0.01	-1.67
BN4_10243	Homoserine dehydrogenase	0.01	-1.68
BN4_10782	Putative nickel-responsive regulator	0.03	-1.70
BN4_12085	Acylneuraminate cytidylyltransferase (Modular protein)	0.05	-1.70
BN4_12700	Putative enzyme	0.03	-1.70
BN4_10795	Chorismate synthase	0.03	-1.70
BN4_10738	Chemotaxis protein methyltransferase	0.00	-1.71
BN4_20375	Inosine-5'-monophosphate dehydrogenase	0.03	-1.72
BN4_11302	50S ribosomal protein L21	0.03	-1.72
BN4_20035	Succinylglutamate desuccinylase/aspartoacylase	0.04	-1.72
BN4_20440	3-deoxy-manno-octulosonate cytidylyltransferase	0.02	-1.73
BN4_10892	Dihydroorotate dehydrogenase	0.03	-1.73
BN4_10865	Histidinol dehydrogenase	0.00	-1.73
BN4_10942	Response regulator receiver protein	0.01	-1.74
BN4_20414	Guanylate kinase	0.01	-1.76
BN4_20465	30S ribosomal protein S7	0.04	-1.77
BN4_11438	Bifunctional chorismate mutase/prephenate dehydratase	0.00	-1.77
BN4_10416	Exopolyphosphatase-related protein	0.01	-1.78
BN4_10396	Cysteine synthase	0.01	-1.78
BN4_20460	50S ribosomal protein L10	0.01	-1.79
BN4_12774	Iron-sulfur cluster carrier protein	0.01	-1.79
BN4_20338	CBS domain containing membrane protein	0.00	-1.79
BN4_10858	UbiD family decarboxylase	0.04	-1.80
BN4_10320	Thioredoxin reductase	0.01	-1.80
BN4_11448	TPR repeat-containing protein	0.04	-1.80
BN4_11018	Uncharacterized protein	0.03	-1.81
BN4_12207	HTH merR-type domain-containing protein	0.05	-1.81
BN4_11505	Orotate phosphoribosyltransferase	0.00	-1.82
BN4_12623	Putative Diguanylate cyclase	0.02	-1.83
BN4_12813	Transcription antitermination protein NusB	0.02	-1.83
BN4_20484	50S ribosomal protein L18	0.02	-1.83
BN4_12231	Putative Phenylacetate-coenzyme A ligase	0.02	-1.83
BN4_11974	Lipoprotein	0.02	-1.84
BN4_10390	4Fe-4S ferredoxin iron-sulfur binding domain protein	0.02	-1.84
BN4_11511	Response regulator receiver modulated CheW protein	0.01	-1.85
BN4_10585	Malate dehydrogenase (Oxaloacetate-decarboxylating) (NADP(+))	0.00	-1.86
BN4_11436	2-amino-3,7-dideoxy-D-threo-hept-6-ulosonate synthase	0.00	-1.86
BN4_11755	Glucose-6-phosphate 1-dehydrogenase	0.03	-1.87
BN4_10553	3-deoxy-D-manno-octulosonate 8-phosphate phosphatase KdsC	0.02	-1.88
BN4_20483	50S ribosomal protein L6	0.02	-1.88
BN4_10619	MazG family protein	0.02	-1.88
BN4_11421	Single-stranded nucleic acid binding R3H domain protein	0.04	-1.90
BN4_12117	HTH merR-type domain-containing protein	0.02	-1.91
BN4_20531	Flavin-dependent thymidylate synthase	0.02	-1.92
BN4_11233	Leucine carboxyl methyltransferase	0.01	-1.92

BN4_20033	Catalase	0.00	-1.92
BN4_10274	Imidazole glycerol phosphate synthase subunit HisH	0.00	-1.94
BN4_20391	Curved DNA-binding protein	0.02	-1.96
BN4_20334	histidine kinase	0.01	-1.96
BN4_11583	RNA methyltransferase, TrmA family	0.03	-1.97
BN4_10652	Glycerol kinase	0.01	-1.97
BN4_12047	Aldehyde ferredoxin oxidoreductase	0.00	-1.97
BN4_20479	50S ribosomal protein L24	0.04	-1.98
BN4_11368	3-oxoacyl-[acyl-carrier-protein] reductase	0.00	-1.99
BN4_11023	Co-chaperonin GroES	0.00	-2.00
BN4_11695	50S ribosomal protein L19	0.03	-2.00
BN4_11075	Periplasmic serine endoprotease DegP-like	0.02	-2.00
BN4_11961	Protein vdlD	0.01	-2.02
BN4_11314	Molybdenum storage protein subunit beta	0.02	-2.04
BN4_10770	30S ribosomal protein S15	0.01	-2.04
BN4_10899	Amidophosphoribosyltransferase	0.02	-2.05
BN4_20478	50S ribosomal protein L14	0.04	-2.05
BN4_12644	Putative transcriptional regulator	0.00	-2.06
BN4_10408	ABC transporter related protein	0.04	-2.06
BN4_10941	Response regulator receiver protein	0.02	-2.07
BN4_11702	Serine--tRNA ligase	0.01	-2.07
BN4_12030	Putative UspA domain protein	0.01	-2.08
BN4_10327	Protein-glutamate methylesterase/protein-glutamine glutaminase	0.01	-2.09
BN4_10869	50S ribosomal protein L9	0.00	-2.09
BN4_12531	Aspartate aminotransferase A	0.05	-2.12
BN4_20385	Uracil phosphoribosyltransferase	0.00	-2.14
BN4_20480	50S ribosomal protein L5	0.02	-2.15
BN4_20451	Response regulator receiver modulated CheW protein	0.00	-2.15
BN4_12569	Bifunctional protein GlmU	0.00	-2.15
BN4_10554	2-dehydro-3-deoxyphosphooctonate aldolase	0.01	-2.16
BN4_20212	Periplasmic phosphate binding protein	0.04	-2.16
BN4_20239	Nitroreductase	0.00	-2.17
BN4_12576	Tyrosine--tRNA ligase	0.00	-2.17
BN4_11367	Surface carbohydrate biosynthesis protein	0.00	-2.18
BN4_12645	N-acylneuraminate-9-phosphate synthase	0.01	-2.18
BN4_10935	Methyl-accepting chemotaxis sensory transducer with Pas/Pac sensor	0.01	-2.20
BN4_12434	Transcriptional regulator, AsnC family	0.01	-2.20
BN4_10252	Pyruvate ferredoxin/flavodoxin oxidoreductase, beta subunit	0.00	-2.21
BN4_10985	Putative RNA-binding protein rbpA	0.01	-2.22
BN4_10401	Heat shock protein HSP20	0.01	-2.22
BN4_20482	30S ribosomal protein S8	0.01	-2.22
BN4_11405	DUF306 domain-containing protein	0.01	-2.23
BN4_11354	Aminotransferase class-III	0.01	-2.26
BN4_11316	Acetylglutamate kinase	0.01	-2.26
BN4_11881	cysteine desulfurase	0.04	-2.28

BN4_11510	acylphosphatase	0.00	-2.29
BN4_12459	Putative phage repressor	0.02	-2.29
BN4_20431	Response regulator receiver protein	0.00	-2.31
BN4_12217	Putative chromosome-partitioning protein parB	0.01	-2.32
BN4_12302	UspA domain protein	0.01	-2.33
BN4_11166	Isoquinoline 1-oxidoreductase subunit alpha	0.01	-2.34
BN4_11611	3-oxoacyl-[acyl-carrier-protein] reductase	0.01	-2.35
BN4_10369	Acetolactate synthase small subunit	0.00	-2.36
BN4_10244	Aminotransferase	0.01	-2.36
BN4_11364	NeuB family protein	0.05	-2.36
BN4_11872	XshC-Cox1-family protein	0.02	-2.37
BN4_11083	Riboflavin biosynthesis protein	0.02	-2.38
BN4_20457	Transcription termination/antitermination protein NusG	0.01	-2.39
BN4_10506	Acetylornithine aminotransferase	0.03	-2.40
BN4_10397	Cysteine desulfurase	0.00	-2.40
BN4_10911	Holliday junction branch migration complex subunit RuvA	0.03	-2.40
BN4_12049	Glycosyl transferase group 1	0.02	-2.41
BN4_10541	4-hydroxy-tetrahydrodipicolinate synthase	0.00	-2.43
BN4_11045	Multifunctional fusion protein	0.05	-2.44
BN4_20186	Glycogen debranching enzyme	0.01	-2.44
BN4_11983	Aspartate carbamoyltransferase	0.00	-2.46
BN4_10860	Hemerythrin-like metal-binding protein	0.01	-2.46
BN4_10992	Aminotransferase class V	0.00	-2.46
BN4_20458	50S ribosomal protein L11	0.01	-2.49
BN4_12307	Metal dependent phosphohydrolase	0.00	-2.49
BN4_20449	Hydrogenase maturation factor	0.04	-2.49
BN4_20063	Efflux transporter, RND family, MFP subunit	0.01	-2.49
BN4_11296	Putative Nitroreductase	0.00	-2.50
BN4_11029	Uncharacterized protein	0.02	-2.52
BN4_11038	Bacterial Pleckstrin homology domain-containing protein	0.00	-2.52
BN4_12471	Molybdopterin-guanine dinucleotide biosynthesis protein B	0.02	-2.55
BN4_10121	Methylenetetrahydrofolate reductase	0.01	-2.55
BN4_10352	Beta-lactamase domain protein	0.01	-2.56
BN4_20321	SPBc2 prophage-derived DNA-binding protein HU 2	0.02	-2.58
BN4_12101	SIR2-like domain-containing protein	0.00	-2.58
BN4_11795	Histidinol-phosphate aminotransferase	0.00	-2.59
BN4_11104	site-specific DNA-methyltransferase (adenine-specific)	0.01	-2.61
BN4_12480	Heat shock protein Hsp20	0.02	-2.65
BN4_11631	Riboflavin biosynthesis protein RibD	0.04	-2.69
BN4_10929	Glyoxylate reductase	0.00	-2.73
BN4_10486	Glyceraldehyde-3-phosphate dehydrogenase	0.00	-2.76
BN4_10170	Sulfite reductase, dissimilatory-type subunit gamma	0.00	-2.79
BN4_12551	Hypoxanthine phosphoribosyltransferase	0.04	-2.85
BN4_20421	Ribosomal small subunit Rsm22	0.00	-2.88
BN4_11235	Saccharopine dehydrogenase NADP binding domain-containing protein	0.03	-2.91

BN4_10448	Triosephosphate isomerase	0.00	-2.91
BN4_10351	Cytokinin riboside 5'-monophosphate phosphoribohydrolase	0.01	-2.93
BN4_10539	Integration host factor subunit beta	0.02	-2.97
BN4_10095	Glucose-1-phosphate thymidylyltransferase	0.00	-2.97
BN4_11754	Putative 6-phosphogluconate dehydrogenase YqeC	0.00	-2.99
BN4_10007	Ribosome-recycling factor	0.00	-2.99
BN4_11595	UDP-N-acetylmuramoyl-L-alanyl-D-glutamate--2,6-diaminopimelate ligase	0.04	-2.99
BN4_10103	2,3-bisphosphoglycerate-dependent phosphoglycerate mutase	0.00	-3.02
BN4_10049	2-amino-3,7-dideoxy-D-threo-hept-6-ulosonate synthase	0.00	-3.03
BN4_12171	Integration host factor subunit alpha	0.01	-3.03
BN4_10694	Response regulator receiver protein	0.04	-3.09
BN4_10979	Uncharacterized protein	0.00	-3.12
BN4_10437	Elongation factor P	0.00	-3.13
BN4_11369	5-methyltetrahydropteroyltriglutamate--homocysteine methyltransferase	0.02	-3.16
BN4_11929	DRTGG domain protein	0.00	-3.18
BN4_12467	Formate dehydrogenase accessory protein	0.00	-3.20
BN4_12180	Amphi-Trp domain-containing protein	0.01	-3.24
BN4_12092	Putative RNA-binding protein rbpA	0.03	-3.27
BN4_12297	Chemotaxis protein methyltransferase	0.02	-3.33
BN4_10583	Putative fumarate hydratase subunit alpha	0.00	-3.38
BN4_10061	Polysaccharide biosynthesis protein CapD-like domain-containing protein	0.01	-3.39
BN4_10817	UDP-glucuronate decarboxylase	0.00	-3.46
BN4_12358	Putative phage repressor	0.00	-3.48
BN4_10787	Dihydrolipoyl dehydrogenase	0.01	-3.73
BN4_11955	Cupin fold metalloprotein, WbuC family	0.01	-3.78
BN4_10584	Putative fumarate hydratase subunit beta	0.05	-3.82
BN4_10953	Transcriptional regulator, MarR family	0.03	-3.84
BN4_10523	GatB/YqeY domain-containing protein	0.01	-3.99
BN4_20438	TPR repeat-containing protein	0.03	-4.01
BN4_11434	Nitrogen regulatory protein P-II	0.01	-4.49
BN4_12558	Phosphate regulon transcriptional regulatory protein phoB	0.00	-4.74
BN4_10512	Divergent polysaccharide deacetylase family protein	0.05	-4.81

Supplementary Table 8. List of differentially abundant proteins in the planktonic cells incubated at 15 MPa with mild steel AH36.

KEGG ID	Protein Description	p.value	log2fc
Enriched proteins			
M1WYT0	Chorismate dehydratase	0.04	1.49
M1WJA6	Elongation factor G	0.03	1.38
M1WSY5	Metal dependent phosphohydrolase	0.02	1.33
M1WJ80	Cyclic pyranopterin monophosphate synthase	0.01	1.30
M1WSG4	Uncharacterized protein	0.05	1.29
M1WUC8	1,4-dihydroxy-6-naphtoate synthase	0.04	1.24
M1WS50	4-hydroxy-3-methylbut-2-en-1-yl diphosphate synthase (flavodoxin)	0.04	1.20
M1WTP3	Redox-sensing transcriptional repressor Rex	0.04	1.17
M1WLN9	Transcriptional regulator, MarR family	0.03	1.13
M1WJE6	GatB/YqeY domain-containing protein	0.01	1.12
M1WKJ4	Molybdopterin-guanine dinucleotide biosynthesis protein B	0.03	1.07
M1WRG9	Diguanylate phosphodiesterase	0.02	1.02
M1WT82	Helicase HerA central domain-containing protein	0.03	0.85
M1WJ99	Pseudouridine synthase	0.05	0.77
M1WVG7	Peptidase M20	0.05	0.69
M1WVI1	Polyketide synthase thioesterase domain-containing protein	0.01	0.64
Depleted proteins			
M1WSJ3	Protein CreA	0.05	-0.60
M1WUS0	succinate dehydrogenase	0.02	-0.61
M1WQP9	Oxidoreductase FAD/NAD(P)-binding domain protein	0.02	-0.61
M1WWL8	Peptidase M24	0.00	-0.63
M1WJ60	Recombination-associated protein RdgC	0.01	-0.81
M1WX89	Putative phage repressor	0.03	-0.98
M1WK39	tRNA (guanine-N(1)-)-methyltransferase	0.02	-1.10
M1WKJ0	TPM domain-containing protein	0.02	-1.13
M1WQN2	RNA polymerase sigma-54 factor	0.01	-1.31
M1WQH6	TRAP transporter solute receptor, TAXI family (Modular protein)	0.01	-1.46

Supplementary Table 9. List of differentially abundant proteins in the planktonic cells incubated at 30 MPa with mild steel AH36.

KEGG ID	Protein Description	p.value	log2fc
Enriched proteins			
M1WQU7	Putative signal transduction protein	0.01	2.73
M1WLM9	Uncharacterized protein	0.04	2.42
M1WP15	Replication-associated recombination protein A	0.04	1.68
M1WLS8	ATPase	0.02	1.61
M1WMA7	Sulfate exporter family transporter	0.04	1.31
M1WJ85	BFN domain-containing protein	0.00	1.25
M1WKH3	Metal dependent phosphohydrolase	0.02	1.24
M1WQU8	Transcriptional regulatory protein zraR	0.03	1.22
M1WLU5	Leucine carboxyl methyltransferase	0.01	1.19
M1WNN5	Tetratricopeptide repeat protein	0.04	1.17
M1WSC4	Putative Tetratricopeptide TPR_2 repeat protein	0.02	1.15
M1WXS5	N-acylneuraminate-9-phosphate synthase	0.04	1.11
M1WYN9	Aspartyl/glutamyl-tRNA(Asn/Gln) amidotransferase subunit C	0.04	0.95
M1WJE9	Flagellar synthesis regulator FleN	0.00	0.88
M1WPB3	Transcriptional regulator, NifA subfamily, Fis Family	0.01	0.87
M1WMW7	1-deoxy-D-xylulose 5-phosphate reductoisomerase	0.05	0.87
M1WKZ2	Imidazoleglycerol-phosphate dehydratase	0.05	0.85
M1WMD3	Protein hit	0.05	0.79
M1WJE6	GatB/YqeY domain-containing protein	0.02	0.78
M1WV01	NADH-quinone oxidoreductase subunit D	0.04	0.69
M1WJ99	Pseudouridine synthase	0.04	0.68
M1WVK9	Uncharacterized protein	0.01	0.68
M1WX16	PfkB domain protein	0.00	0.66
M1WLB4	ATP-dependent Clp protease ATP-binding subunit ClpA	0.01	0.63
M1WL06	Hydrogenase maturation factor	0.00	0.60
M1WLF1	Nucleoside diphosphate kinase	0.02	0.60
Depleted proteins			
M1WMU4	DUF4140 domain-containing protein	0.05	-0.61
M1WLH9	ABC transporter related	0.03	-0.69
M1WNH9	Cytokinin riboside 5'-monophosphate phosphoribohydrolase	0.03	-0.69
M1WK39	tRNA (guanine-N(1)-)-methyltransferase	0.04	-0.77
M1WNZ3	Glycerol kinase	0.03	-0.81
M1WQP9	Oxidoreductase FAD/NAD(P)-binding domain protein	0.01	-0.89
M1WUS0	succinate dehydrogenase	0.02	-0.94
M1WK85	Flagellin	0.01	-0.95
M1WP08	Response regulator receiver protein	0.01	-1.10
M1WJF8	Putative fumarate hydratase subunit beta	0.01	-1.11
M1WVZ7	UDP-N-acetylmuramoylalanine--D-glutamate ligase	0.00	-1.25
M1WRD9	Type I restriction enzyme endonuclease subunit	0.03	-1.28

M1WXL9	Phosphate regulon transcriptional regulatory protein phoB	0.04	-1.28
M1WSS1	TPR repeat-containing protein	0.01	-1.29
M1WMZ4	Uncharacterized protein	0.01	-1.46
M1WMN0	Flagellar hook protein FlgE	0.01	-1.68
M1WK80	EF-hand domain-containing protein	0.04	-1.69
M1WNV9	succinate dehydrogenase	0.02	-1.69
M1WSG6	Uncharacterized protein	0.02	-1.75
M1WQH6	TRAP transporter solute receptor, TAXI family (Modular protein)	0.00	-1.95

Supplementary Table 10. List of differentially abundant proteins in the biofilm cells incubated at 15 MPa with mild steel AH36.

KEGG ID	Protein Description	p.value	log2fc
Enriched proteins			
M1WM49	Small-conductance mechanosensitive channel	0.01	3.04
M1WJ48	Response regulator receiver protein	0.01	1.53
M1WLT9	Glucans biosynthesis protein G	0.01	0.89
M1WQN8	Hydantoinase/oxoprolinase	0.02	0.82
M1WRH4	Putative RNA-binding protein rbpE	0.04	0.80
Depleted proteins			
M1WLG2	Putative Vibriobactin receptor	0.04	-0.68
M1WW52	Oxidoreductase domain protein	0.03	-0.71
M1WLY6	Prephenate dehydrogenase	0.04	-1.09
M1WTF8	UspA domain protein	0.04	-1.79

Supplementary Table 11. List of differentially abundant proteins in the biofilm cells incubated at 30 MPa with mild steel AH36.

KEGG ID	Protein Description	p.value	log2fc
Enriched proteins			
M1WJ48	Response regulator receiver protein	0.03	1.89
M1WKA8	Uncharacterized protein	0.04	1.46
M1WQA3	DUF177 domain-containing protein	0.00	1.12
M1WTM2	Type IV pilus assembly PilZ	0.03	1.04
M1WY64	Diguanylate cyclase with PAS/PAC sensor	0.01	0.67
M1WYD0	PEP-CTERM protein-sorting domain-containing protein	0.05	0.63
M1WTU0	Co-chaperonin GroES	0.04	0.63
M1WUJ7	MotA/TolQ/ExbB proton channel	0.05	0.59
Depleted proteins			
M1WUL3	Trigger factor	0.04	-0.65
M1WKV3	Putative alpha-amylase	0.04	-0.68
M1WXY2	Hydrogenase maturation factor HypA	0.04	-0.96
M1WXY9	Lipoprotein	0.04	-1.14
M1WRT0	RNA polymerase sigma factor	0.02	-1.40
M1WUS0	succinate dehydrogenase	0.01	-1.40
M1WJR2	site-specific DNA-methyltransferase (adenine-specific)	0.00	-1.59
M1WP81	Dihydroorotate dehydrogenase	0.02	-1.95

Supplementary Table 12. Distribution of differentially abundant proteins in the planktonic population of *P. piezophilus* incubated with mild steel according to KEGG pathway. Pathways with statistically significant enrichment/depletion were highlighted in bold.

	Differentially Enriched			**Differentially Depleted**		
Pathway	**0.1 MPa**	**15 MPa**	**30 MPa**	**0.1 MPa**	**15 MPa**	**30 MPa**
dpi00010 Glycolysis / Gluconeogenesis	0	0	0	2	0	0
dpi00020 Citrate cycle (TCA cycle)	0	0	0	0	2	**3**
dpi00030 Pentose phosphate pathway	1	0	0	2	0	0
dpi00051 Fructose and mannose metabolism	1	0	0	1	0	0
dpi00052 Galactose metabolism	0	0	0	1	0	0
dpi00190 Oxidative phosphorylation	0	0	0	0	2	2
dpi00220 Arginine biosynthesis	1	0	0	0	0	0
dpi00230 Purine metabolism	1	0	2	0	0	0
dpi00240 Pyrimidine metabolism	0	0	1	0	0	1
dpi00250 Alanine, aspartate and glutamate metabolism	0	0	1	0	0	0
dpi00260 Glycine, serine and threonine metabolism	1	0	0	0	0	1
dpi00270 Cysteine and methionine metabolism	0	0	0	0	1	0
dpi00290 Valine, leucine and isoleucine biosynthesis	2	0	0	1	0	0
dpi00300 Lysine biosynthesis	2	0	0	0	0	0
dpi00330 Arginine and proline metabolism	0	0	1	0	0	0
dpi00340 Histidine metabolism	0	0	0	1	0	0
dpi00450 Selenocompound metabolism	0	0	0	0	1	0
dpi00500 Starch and sucrose metabolism	0	0	0	1	1	1
dpi00520 Amino sugar and nucleotide sugar metabolism	0	0	0	0	0	1
dpi00540 Lipopolysaccharide biosynthesis	0	0	1	0	0	0

dpi00620 Pyruvate metabolism	1	0	0	0	2	4
dpi00627 Aminobenzoate degradation	0	0	0	0	0	1
dpi00630 Glyoxylate and dicarboxylate metabolism	0	0	0	0	0	1
dpi00633 Nitrotoluene degradation	1	0	0	0	0	0
dpi00650 Butanoate metabolism	1	0	0	1	2	2
dpi00660 C5-Branched dibasic acid metabolism	1	0	0	1	0	0
dpi00680 Methane metabolism	1	0	0	2	0	0
dpi00730 Thiamine metabolism	1	0	0	0	0	0
dpi00740 Riboflavin metabolism	0	1	0	0	0	0
dpi00760 Nicotinate and nicotinamide metabolism	1	0	0	0	0	0
dpi00770 Pantothenate and CoA biosynthesis	0	0	0	2	1	0
dpi00785 Lipoic acid metabolism	0	0	0	0	0	1
dpi00790 Folate biosynthesis	0	3	0	0	0	1
dpi00860 Porphyrin metabolism	1	1	0	1	0	0
dpi00900 Terpenoid backbone biosynthesis	0	1	1	0	0	0
dpi00910 Nitrogen metabolism	0	0	1	0	0	0
dpi00920 Sulfur metabolism	1	0	1	0	0	0
dpi01100 Metabolic pathways	13	5	6	8	5	9
dpi01110 Biosynthesis of secondary metabolites	9	3	3	6	4	5
dpi01120 Microbial metabolism in diverse environments	6	1	2	3	2	4
dpi01200 Carbon metabolism	1	0	0	3	0	2
dpi01210 2-Oxocarboxylic acid metabolism	4	0	0	1	0	0
dpi01230 Biosynthesis of amino acids	5	0	1	5	1	0
dpi01232 Nucleotide metabolism	1	0	0	0	0	1
dpi01240 Biosynthesis of cofactors	3	4	0	2	1	1
dpi01250 Biosynthesis of nucleotide sugars	0	0	1	0	0	1

dpi02010 ABC transporters	1	2	2	3	0	1
dpi02020 Two-component system	2	0	0	1	7	2
dpi02024 Quorum sensing	0	2	0	0	0	0
dpi02030 Bacterial chemotaxis	0	0	0	0	6	1
dpi02040 Flagellar assembly	1	0	1	1	0	0
dpi02060 Phosphotransferase system (PTS)	0	0	0	1	0	0
dpi03010 Ribosome	0	0	0	1	2	1
dpi03018 RNA degradation	0	0	0	2	0	0
dpi04122 Sulfur relay system	0	1	0	0	0	0

Supplementary Table 13. Distribution of differentially abundant proteins in the biofilm population of *P. piezophilus* incubated with mild steel according to KEGG pathway. Pathways with statistically significant enrichment/depletion are highlighted in bold.

	Differentially Enriched			**Differentially Depleted**		
Pathway	**0.1 MPa**	**15 MPa**	**30 MPa**	**0.1 MPa**	**15 MPa**	**30 MPa**
dpi00010 Glycolysis / Gluconeogenesis	0	2	1	9	13	14
dpi00020 Citrate cycle (TCA cycle)	0	1	0	7	9	**12**
dpi00030 Pentose phosphate pathway	0	1	0	8	**14**	**10**
dpi00040 Pentose and glucuronate interconversions	0	0	0	3	2	2
dpi00051 Fructose and mannose metabolism	0	0	0	3	**8**	6
dpi00052 Galactose metabolism	0	1	0	1	2	3
dpi00053 Ascorbate and aldarate metabolism	0	0	0	3	2	3
dpi00061 Fatty acid biosynthesis	0	0	0	3	3	4
dpi00071 Fatty acid degradation	0	0	0	1	1	2
dpi00130 Ubiquinone and other terpenoid-quinone biosynthesis	0	0	0	0	1	2
dpi00190 Oxidative phosphorylation	**6**	**8**	5	3	4	2
dpi00220 Arginine biosynthesis	1	1	1	5	**7**	**8**
dpi00230 Purine metabolism	1	1	0	7	10	9
dpi00240 Pyrimidine metabolism	0	0	0	7	8	9
dpi00250 Alanine, aspartate and glutamate metabolism	0	0	0	8	8	**11**
dpi00260 Glycine, serine and threonine metabolism	1	1	0	6	7	8
dpi00261 Monobactam biosynthesis	1	1	0	2	3	1
dpi00270 Cysteine and methionine metabolism	1	1	1	2	7	8
dpi00280 Valine, leucine and isoleucine degradation	0	0	0	1	0	1
dpi00290 Valine, leucine and isoleucine biosynthesis	1	1	0	3	4	3
dpi00300 Lysine biosynthesis	1	1	0	4	6	**7**

dpi00310 Lysine degradation	0	0	0	3	1	3
dpi00330 Arginine and proline metabolism	0	0	0	1	4	5
dpi00332 Carbapenem biosynthesis	0	0	0	0	1	1
dpi00340 Histidine metabolism	0	0	0	3	5	5
dpi00350 Tyrosine metabolism	0	0	0	3	4	4
dpi00360 Phenylalanine metabolism	0	0	0	2	5	4
dpi00380 Tryptophan metabolism	0	0	0	2	1	2
dpi00400 Phenylalanine, tyrosine and tryptophan biosynthesis	0	0	1	9	8	8
dpi00401 Novobiocin biosynthesis	0	0	0	2	3	3
dpi00430 Taurine and hypotaurine metabolism	0	1	0	0	0	0
dpi00450 Selenocompound metabolism	0	0	0	3	6	4
dpi00470 D-Amino acid metabolism	0	1	0	1	3	3
dpi00480 Glutathione metabolism	0	0	0	2	3	3
dpi00500 Starch and sucrose metabolism	0	1	0	1	1	1
dpi00520 Amino sugar and nucleotide sugar metabolism	0	1	0	7	8	10
dpi00521 Streptomycin biosynthesis	0	1	0	1	1	1
dpi00523 Polyketide sugar unit biosynthesis	0	0	0	1	1	1
dpi00525 Acarbose and validamycin biosynthesis	0	0	0	1	1	1
dpi00540 Lipopolysaccharide biosynthesis	0	0	0	1	3	3
dpi00541 O-Antigen nucleotide sugar biosynthesis	0	0	0	6	5	6
dpi00543 Exopolysaccharide biosynthesis	0	0	0	0	0	1
dpi00550 Peptidoglycan biosynthesis	0	2	0	1	2	3
dpi00561 Glycerolipid metabolism	0	0	1	0	1	1
dpi00564 Glycerophospholipid metabolism	1	1	2	0	0	0
dpi00620 Pyruvate metabolism	1	4	1	7	8	11
dpi00627 Aminobenzoate degradation	0	0	0	0	1	1

dpi00630 Glyoxylate and dicarboxylate metabolism	0	1	0	5	6	9
dpi00633 Nitrotoluene degradation	0	0	0	1	2	1
dpi00640 Propanoate metabolism	0	1	0	3	1	1
dpi00650 Butanoate metabolism	0	1	0	6	7	7
dpi00660 C5-Branched dibasic acid metabolism	0	0	0	2	3	2
dpi00670 One carbon pool by folate	0	0	0	0	2	4
dpi00680 Methane metabolism	0	4	2	2	8	6
dpi00730 Thiamine metabolism	0	0	0	3	4	4
dpi00740 Riboflavin metabolism	0	0	0	1	2	3
dpi00750 Vitamin B6 metabolism	0	0	0	0	1	1
dpi00760 Nicotinate and nicotinamide metabolism	0	0	0	1	2	3
dpi00770 Pantothenate and CoA biosynthesis	0	0	0	3	4	4
dpi00780 Biotin metabolism	0	0	0	2	2	2
dpi00785 Lipoic acid metabolism	0	0	0	2	2	4
dpi00790 Folate biosynthesis	0	1	0	0	1	2
dpi00860 Porphyrin metabolism	1	2	0	3	7	2
dpi00900 Terpenoid backbone biosynthesis	0	0	0	1	0	1
dpi00910 Nitrogen metabolism	0	1	1	1	1	2
dpi00920 Sulfur metabolism	0	1	0	2	4	4
dpi00970 Aminoacyl-tRNA biosynthesis	0	0	0	8	7	7
dpi01100 Metabolic pathways	11	23	12	84	126	127
dpi01110 Biosynthesis of secondary metabolites	4	7	4	54	80	82
dpi01120 Microbial metabolism in diverse environments	1	10	3	31	52	48
dpi01200 Carbon metabolism	0	3	1	19	32	34
dpi01210 2-Oxocarboxylic acid metabolism	3	3	1	7	11	9
dpi01212 Fatty acid metabolism	0	0	0	3	3	4

dpi01230 Biosynthesis of amino acids	3	3	2	**28**	**42**	**44**
dpi01232 Nucleotide metabolism	0	0	0	6	8	9
dpi01240 Biosynthesis of cofactors	1	4	1	19	28	28
dpi01250 Biosynthesis of nucleotide sugars	0	1	0	9	11	14
dpi01501 beta-Lactam resistance	0	1	0	0	0	0
dpi01502 Vancomycin resistance	0	2	0	0	0	1
dpi01503 Cationic antimicrobial peptide (CAMP) resistance	0	1	0	1	2	1
dpi02010 ABC transporters	**10**	8	9	10	7	3
dpi02020 Two-component system	**13**	**21**	**14**	14	15	15
dpi02024 Quorum sensing	6	5	4	7	8	8
dpi02030 Bacterial chemotaxis	**10**	**17**	**11**	8	8	11
dpi02040 Flagellar assembly	**7**	**9**	**8**	1	1	1
dpi02060 Phosphotransferase system (PTS)	0	0	0	0	1	0
dpi03010 Ribosome	0	0	0	12	**29**	15
dpi03018 RNA degradation	0	0	1	1	4	3
dpi03030 DNA replication	3	0	0	1	1	1
dpi03060 Protein export	3	1	2	1	2	1
dpi03070 Bacterial secretion system	0	2	2	1	2	1
dpi03430 Mismatch repair	0	0	0	1	1	1
dpi03440 Homologous recombination	0	0	0	2	1	3
dpi04122 Sulfur relay system	0	0	0	2	2	2